An Investigation of Materials and Printing Methods on the Response of 3D Printed Supercapacitors

A thesis presented for the degree of Doctor of Philosophy to the National University of Ireland, Cork

November 2024

Thesis Presented by:

Matthew Ferguson, B.Sc. (Hons)

School of Chemistry

University College Cork, Ireland

Thesis Supervisor:

Prof. Colm O'Dwyer

Declaration

This statement certifies that the work presented in this thesis is my own research. No part of this thesis has been submitted previously for consideration for any other degree at University College Cork or any other research institute. All work presented here was performed under the supervision of Prof. Colm O'Dwyer, with all other contributions from other authors appropriately referenced. Prior to submission, I have read and understood the terms and conditions regarding plagiarism as outlined by University College Cork.

Signed

Matthew Ferguson

Acknowledgements

First and foremost, my sincerest thanks to Prof. Colm O'Dwyer, whose guidance and supervision over the past several years has been vital for the completion of this thesis. Many fantastic opportunities and experiences, including the chance to attend two international conferences, have only arisen thanks to his dedication and hard work to making this PhD process as rewarding and constructive as possible. For all these reasons and more, I am immensely grateful.

A huge thanks as well to every member of the Applied Nanoscience Group, and many others throughout the Kane Building, who were always willing to give up their time to help whenever I needed it. There are too many people to name, but your contributions to this work have not gone unnoticed and are very much appreciated. To many others that I have gotten to know over the past few years, whether through work or just hanging out at lunch, my experience has been made so much more positive and enjoyable because of you all.

A special thank you to Mom, Dad, Anna, Ciara, all my friends and family, and, of course, Bonnie (for her boundless enthusiasm and energy). To Amy, for your years of support, friendship, company, für alles, ganz herzlichen Dank!

Publications

- **Ferguson, M.**; Egorov, V.; Zhang, Y.; Gulzar, U.; O'Dwyer, C., The Influence of 3D Printing Methods and Materials on the Response of Printed Symmetric Carbon Supercapacitors. *ECS Advances* 2024, *3* (3), 032501.
- Zhang, Y.; Grant, A.; Carroll, A.; Gulzar, U.; **Ferguson, M.**; Roy, A.; Nicolosi, V.; O'Dwyer, C., Water-Soluble Binders That Improve Electrochemical Sodium-Ion Storage Properties in a $NaTi_2(PO_4)_3$ Anode. *Journal of the Electrochemical Society* 2023, *170* (5), 050529.
- **Ferguson, M.**; Egorov, V.; Zhang, Y.; Gulzar, U.; O'Dwyer, C., Solvent pre-soaking of FDM printed conductive PLA current collectors improves the response of 3D-printed carbon supercapacitors. (*Submitted).*
- Gulzar, U.; Lonergan, A.; Zhang, Y.; Grant, A.; Carroll A.; **Ferguson, M.**; O'Dwyer, C. Understanding the morphological properties of sulfur electrodes for high capacity and high-power lithium-sulfur batteries. *Journal of the Electrochemical Society (Submitted).*

Oral Presentations

- 3D Printed Symmetric Carbon Supercapacitors: A Study Comparing Electrochemical Performance and Cycle Life Depending on 3D Printing Technique and Materials.
  A01-0006 26th May 2024, 245th ECS Meeting, San Francisco, California, USA, 26th – 30th May 2024.
- Electrochemical Performance and Characterisation of Chemically Treated Conductive PLA Fused Deposition Modelling (FDM) Current Collectors within Additively Manufactured (3D-Printed) Symmetric Carbon Supercapacitors.
  A05-0771 28th May 2024, 245th ECS Meeting, San Francisco, California, USA, 26th – 30th May 2024.

Poster Presentations

- The influence of 3D printing methods and materials on the response of printed symmetric carbon supercapacitors.
  E-MRS 2023 Spring Meeting, Strasbourg, France, 29th May – 2nd June 2023.
- 3D Printed Symmetric Carbon Supercapacitors: A study comparing electrochemical performance and cycle life depending on 3D printing technique and materials.
  74th Irish Universities Chemistry Research Colloquium, Galway, Ireland, 14th – 15th June 2023.

Thesis Abstract and Overview

The motivation behind this thesis project was to explore the design and manufacturing of supercapacitor energy storage devices using 3D-printing. Compared to conventional batteries (such as the ubiquitous lithium-ion battery), supercapacitor devices possess the distinct advantages of higher specific power (power output per unit mass of active material) and extremely long cycle lives (potentially in the millions of charge-discharge cycles), but also come with the drawback of lower specific energy (amount of energy stored per unit mass of active material). The materials used to make supercapacitors (usually porous carbon materials for the electrodes and simple acid/base or salt electrolytes) also tend to be far more abundant, cheaper, environmentally friendly, and non-toxic when compared to their battery counterparts. Due to these characteristics, supercapacitors have been implemented in a great number of different technologies, being ideally suited for situations that require high bursts of power, long service life, and high thermal stability. Regenerative braking, energy grid storage, handheld power tools, light rail, and street lighting are a few examples. The possibility for flexible, biocompatible, and non-toxic supercapacitors makes them an ideal energy storage device within wearable electronics and medical implants.

Additive manufacturing (more commonly known as 3D-printing) has seen a massive upsurge in popularity within scientific research in the past decade. Attracted by the multitude of benefits it offers (unmatched ease of prototyping and customisation, the ability to create highly complex components, huge reduction in waste material), many areas of science, medicine, and engineering now routinely utilise 3D-printing in their work and research. Within the context of supercapacitor devices, 3D-printing enables manufacturing of highly complex electrode architectures, geometric freedom to explore new form-factors, ease of prototyping, and reduction in part-specific tooling requirements.

The aim of this thesis was to provide a detailed examination of the behaviours and performances of symmetric supercapacitor devices made using two different 3D-printing methods: Vat Polymerisation (Vat-P) and Fused Deposition Modelling (FDM). In doing so, we hope to provide useful insight into the factors and conditions that affect the performance and cell stability of our 3D-printed supercapacitor devices, with special consideration to the nature of the 3D-printing method used to manufacture the supercapacitor cells. Multiple 3D-printing methods are seldom directly compared within a single study in the literature. Over the course of this thesis, various active materials are loaded into the 3D-printed supercapacitor devices, with their electrochemical performances being extensively tested via cyclic voltammetry and galvanostatic charge-discharge tests. The structures and morphologies of the 3D-printed current collectors and electrode slurries are examined using Raman spectroscopy and scanning electron microscopy (SEM) throughout the thesis. Simple carbon-based electrodes are first tested, before moving onto more complex electrodes implementing conductive additives and pseudo-capacitive metal oxide inverse opal structures.

Chapter 1 serves as the introduction and literature review of this thesis. The chapter first introduces the basic concepts of energy storage, batteries, and the various forms of supercapacitors; highlighting the energy storage mechanisms and performance metrics that differentiate them. This chapter then reviews a variety of carbon-based electrode materials, as well as conductive polymers, MXenes, metal oxides, and inverse opal structures also used as supercapacitor active materials. Attention is drawn to the synergistic effects of varying electrode materials. The history and working principles of various 3D-printing technologies are then introduced, before concentrating on the two methods utilised in this thesis (Vat-P and FDM). The raw materials, performance metrics, and pros and cons of these two 3D-printing technologies are discussed and compared at length. The chapter ends with a review of 3D-printed supercapacitor devices from the literature, underlining the great strides that have been

made over the past decade, while outlining some challenges to be overcome in future research outputs.

Chapter 2 details the experimental procedures, materials characterisation techniques, and electrochemical analyses used throughout the thesis. The 3D-printing processes for both Vat-P and FDM, electrode slurry formation, and cell assembly are outlined in detail. The theory of the characterisation techniques and electrochemical analyses are briefly introduced, following which the specific settings and procedures used in this work are detailed.

Chapter 3 is the first results chapter, introducing the 3D-printed supercapacitor cell framework studied throughout this thesis. In this chapter, we analyse and compare the electrochemical response, and intrinsic limitations of symmetric carbon-based supercapacitors made using two 3D-printing techniques (Vat-P and FDM). Two cell types are made in this study, one with metallized Vat-P-printed current collectors, the other with conductive PLA (polylactic acid) FDM-printed current collectors in a similarly designed printed coin cell. Simple carbon-based electrodes (SWNT, GNP, and a 50:50 by mass mixture of the two) are first tested within these cells. The metallized Vat-P current collector cells possess superior conductivity and more ideally rectangular CV responses, but initially suffer from very poor cycle lives. The conductive PLA current collector cells have far higher internal resistance, less ideal CV responses, and have poorer structural robustness (due to the nature of the 3D-printing technique) but possess excellent cycle lives. The second half of the chapter addresses the shortcomings of the Vat-P cells' cycle lives and explores more complex carbon-based electrodes, introducing conductive additives (Super-P) and bindings agents (PVDF). The cycle lives of the metallized Vat-P cells are greatly improved by reducing the voltage window to limit metal delamination.

Chapter 4 expands upon our study of conductive PLA current collectors made using FDM 3D-printing. In the previous chapter, though possessing exceptional cycle lives, the cells which incorporate these conductive PLA current collectors suffer from extremely high internal resistance, hindering their electrochemical performance. As such, several different chemical treatments (DMF-short, DMF-long, KOH-long) were undertaken on the conductive PLA current collectors, aiming to improve the conductivity via surface modification. Following this, the current collectors were loaded with a 50:50 SWNT:GNP by mass ratio electrode slurry. This works shows how DMF treatment methods resulted in little change in electrochemical performance compared to the untreated FDM current collector cells. Pre-treatment in a solution of KOH identical to the cell electrolyte markedly improves the current collector conductivity (showing a tenfold reduction in internal resistance and an improved CV response). Galvanostatic charge-discharge tests reveal the effect of long-term cycling, showing the worsened cycling stability for the KOH-treated current collector cells when compared to the untreated current collector cells.

Chapter 5 is the last results chapter of the thesis, where we introduce pseudo-capacitive manganese oxide inverse-opals to our carbon-based electrode slurries. By drawing upon pseudo-capacitive energy storage mechanisms, we aim to improve the specific capacitance and specific energy values for the 3D-printed supercapacitor cells, while also analysing how long-term cycling is affected. As manganese oxides possess low electronic conductivity, several different carbons are investigated to enhance electron transport throughout the electrode materials. MO-IO-carbon composite slurries prepared in a similar manner and composition to previous chapters showed disappointing electrochemical response, being consistently inferior to other cells in Chapter 3. However, improved electrochemical performances were obtained by employing a different electrode slurry preparation method and exploring new compositions of MO-IO-carbon electrode slurries.

Table of Contents

Chapter 1

Introduction and Literature Review

Abstract

With the world facing an unprecedented energy crisis, improving our ability to store energy in reliable, efficient, and long-lasting storage devices remains a critical research area in materials sciences. Within the field of energy storage devices, supercapacitors provide several advantages over conventional batteries, possessing superior specific power and cycle life, though suffer from lower specific energy, the improvement of which is a primary focus for many supercapacitor researchers. 3D-printing (also known as additive manufacturing) has been applied to many areas of materials science, including that of energy storage devices and supercapacitors. 3D-printing of energy storage devices allows for unparalleled levels of customisation, ease of prototyping, freedom of design, as well as eliminating waste material during the manufacturing process. Many studies have utilised 3D-printing methods to manufacture energy storage devices, but directly comparing more than one 3D-printing method within a single study is far more seldom researched. Here, the basics of energy storage devices and supercapacitors are outlined, as well as the different active electrode materials used within these devices. Following this, the concepts of 3D-printing will be introduced, with emphasis placed on the two methods used within this thesis. A discussion outlining the considerations to be taken for using 3D-printing to make energy storage devices will be presented, followed by a review of the progress and outlook on 3D-printed supercapacitors in the literature.

1.1 Introduction to Energy Storage Devices and Supercapacitors

Electrochemical energy storage devices are ubiquitous in today's world, and our society is only becoming more reliant upon them as time goes on. Many countries are making great strides to decrease (or even eliminate) their dependence on fossil fuels, switching instead to renewable sources for their energy needs. Perhaps the biggest disadvantage of renewable energy is the inconsistent energy output (less solar energy on overcast days, less wind energy on calm days, etc.), which is often incongruous with the demand for energy at a given time. This places a great urgency on our ability to effectively and efficiently store generated energy for later use when it is needed. Electrochemical energy storage devices (such as batteries and supercapacitors) remain one of the most widely used and effective means of doing so. At the most fundamental level, energy storage devices contain energy through reversible redox reactions (batteries), the formation of electronic double-layers (electronic double-layer capacitors, or EDLCs), or a combination of the two (pseudo-capacitors) [1]. Each of these mechanisms for electrochemical energy storage have their own unique benefits and downfalls, which will be discussed throughout this work.

Batteries remain the most widely used and well-known form of electrochemical energy storage device in today's world, with most portable electronic devices most likely containing some form of primary (single use) or secondary (rechargeable) battery device [2]. The first ever secondary battery device can be traced back to 1859, when French physicist Gaston Planté invented the lead-acid cell [3]. Further improvements and advances in battery technology followed throughout the 19th and 20th centuries, culminating in the commercialisation of the first lithium-ion battery by Sony Co. in 1991 [4], having overcome the safety and performance issues plaguing lithium battery systems developed over the past few decades [5, 6]. This commercialisation completely transformed the field of portable electronics, paving the way for

the plethora of handheld electronic devices that in many ways shape and define our modern society, greatly impacting communication, entertainment, and access to information [7].

The basic setup for a battery (as well as supercapacitors, as will be discussed later) consists of two electrodes (an anode and cathode, or positive and negative electrode, as will be explained), a separator, an electrolyte, and two current collectors [8]. Using lithium-ion batteries as our example for the battery system, the basic energy storage mechanism of a battery involves the reversible intercalation and de-intercalation of lithium ions into, and then back out of, the battery active materials [9]. The electrolyte solution (usually a lithium salt dissolved in an organic solvent) facilitates the flow of lithium ions from one electrode to another [10]. The separator is ionically porous, allowing for lithium ions to flow freely, but is also electronically insulating and prevents the two electrodes from physical contact with one another [11]. The current collectors serve to collect the flow of electrons to and from the electrodes and the external circuit to which the battery is connected [12].

For battery electrodes, the anode is defined as the electrode where oxidation is taking place, and the cathode is defined as the electrode where reduction is taking place. As such, depending on whether the battery is being charged and discharged, the electrodes can be either an anode or a cathode. To make things simpler, the electrodes can be designated as the positive electrode ($LiCoO_2$) and negative electrode (graphite). When a battery is being charged, electrons are forced from the positive electrode to the negative electrode via an external circuit (as the separator prevents electron flow within the cell) [13]. As the positive electrode material ($LiCoO_2$) is losing electrons in the charging process, it acts as the anode (oxidation). The negative electrode material (graphite) gains surplus electrons and a net negative charge [14]. The positively charged lithium ions resulting from the oxidation reaction are attracted to the negative charge, and they flow through the separator to intercalate within the negative electrode material, resulting in a reduction reaction at the negative electrode cathode [15].

For the discharging process, the electrons spontaneously leave the negative electrode, now acting as the anode (oxidation), flowing through the external circuit, back to the positive electrode, which gains a net negative charge. The lithium ions are once again free after the oxidation reaction at the negative electrode anode, and they flow back to the positive electrode cathode where a reduction reaction restores the positive electrode material to its original, lower energy level form [16, 17]. An illustration of this process can be seen in Figure 1.1 (a). The spontaneous electron flow (and resulting current) of a discharging battery system is what powers countless electronic devices worldwide. Compared to other forms of energy storage discussed here (supercapacitors), batteries have the advantage of superior specific energy (more energy stored per unit mass of active materials) and lower self-discharge, but suffer from lower specific power (low power output per unit mass of active material), slow charging times, instability in air, and far lower charge-discharge cycling stability [18–20]. The cycling instability of battery systems is a consequence of several physical and electrochemical mechanisms, such as solid-electrolyte interface (SEI) layer formation, lithium plating, electrode phase-changes, and particle fractures [21, 22].

From the first commercialization to the present day, many researchers focus on modifications to the existing lithium-ion storage system to further improve the performance metrics of the batteries, and to ameliorate the disadvantages and degradation mechanisms discussed earlier [23]. $LiCoO_2$ (LCO), first patented by Goodenough (a recent Nobel Prize recipient) et al. [24, 25], has remained the most commonly used cathode material for lithium-ion batteries for decades, thanks to the superior air stability and good electrochemical properties (high open circuit voltage ~4 V, good electronic conductivity, low self-discharge) compared to materials studied previously (such as $NaCoO_2$) [26, 27]. However, other materials such as high voltage spinel electrodes, Li–sulfur, Li–air, Li–CO_2, and Li-rich and Ni-rich transition metal oxides (TMOs) have all been investigated for use within lithium-ion batteries,

possessing higher charge capacity, lower cost, and lower toxicity than the conventional LCO material [28, 29].

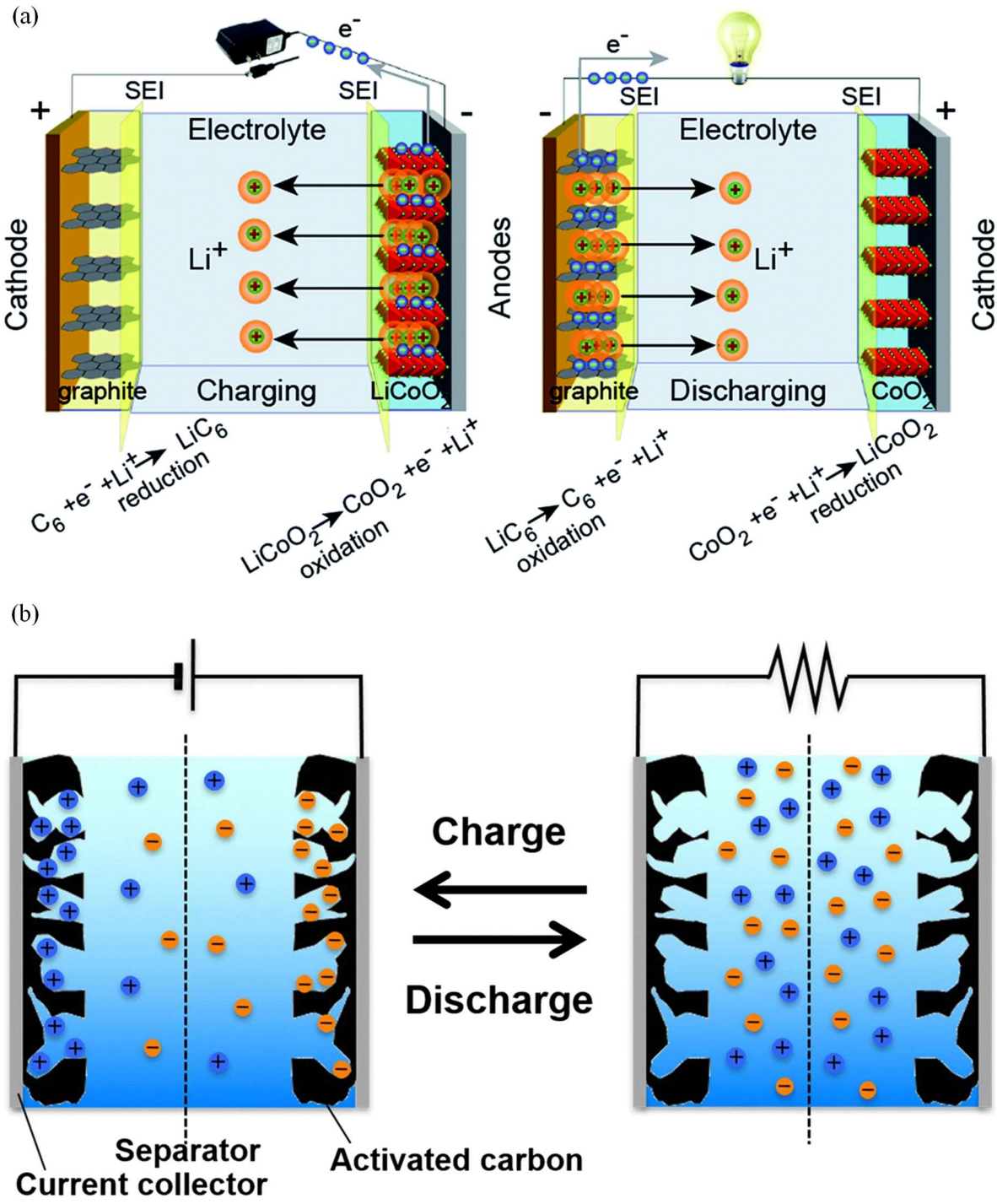

Figure 1.1 (a) Charging and discharging schematic for a Li-ion battery with a $LiCoO_2$ positive electrode and a graphite negative electrode. Reproduced with permission [30]. Copyright 2016, the Royal Society of Chemistry. (b) Charging and discharging schematic for a carbon-based EDLC. Reproduced with permission [31]. Copyright 2019, Springer Nature.

Sony's original lithium-ion battery contained graphene-based anode materials for lithium-ion intercalation and de-intercalation, which continue to be widely used to this day [32]. A great number of alternative anode materials, such as those based on silicon, TMOs, and alloys, have been investigated for potential advancements over the standard lithium-ion battery materials [33, 34].

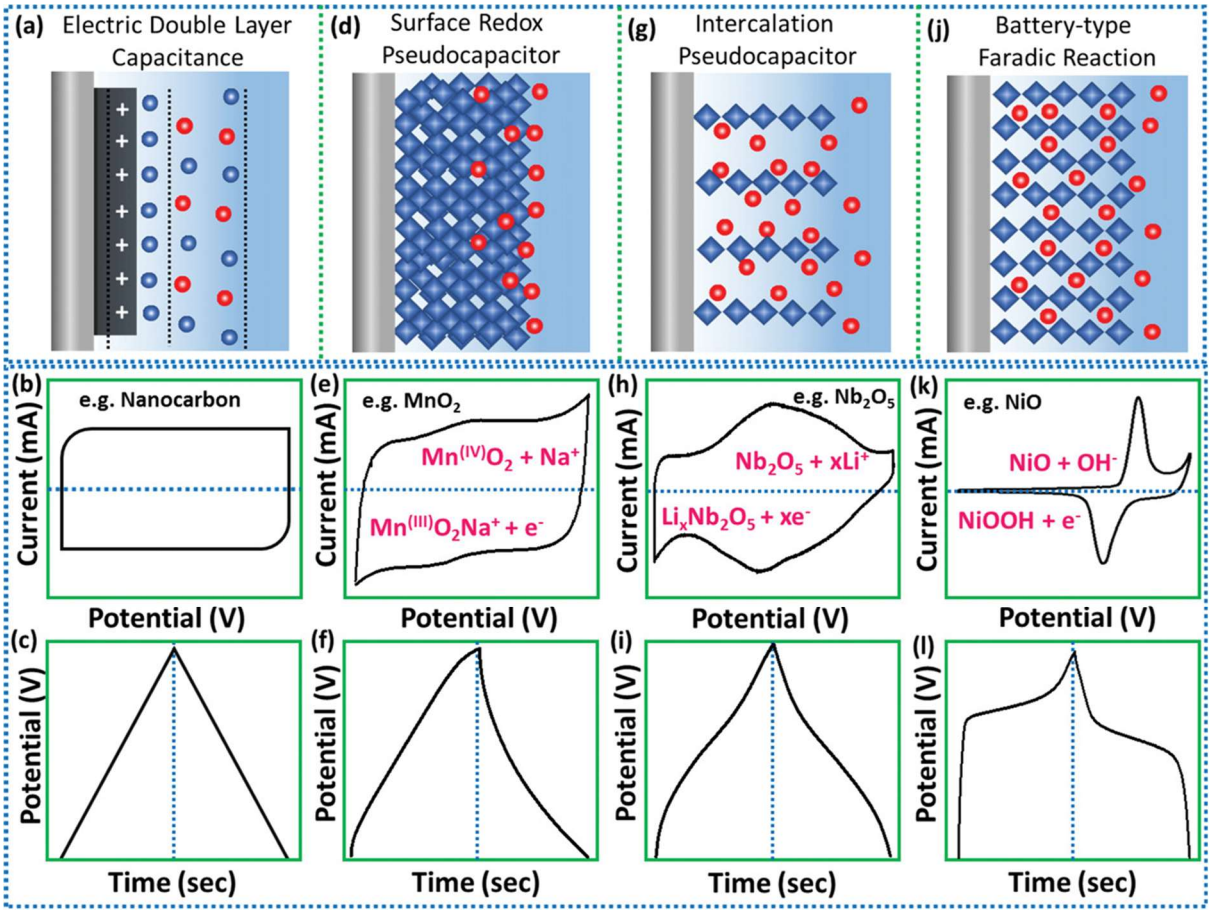

Figure 1.2 Schematics for different energy storage mechanism with their corresponding signatures from cyclic voltammetry and galvanostatic charge-discharge electrochemical testing; (a–c) electric double layer capacitance, (d–f) surface redox pseudo-capacitance, (g–i) intercalation pseudo-capacitance, and (j–l) battery-type faradaic reaction. Reproduced with permission [39]. Copyright 2020, John Wiley and Sons.

In recent years, concerns have been raised about global lithium production being unable to match the ever-increasing demand for lithium-ion batteries required to power our electronic devices and the growing industry of electronic vehicles (EVs) [35, 36]. As such, many studies

and projects have been looking into developing viable alternatives to lithium-ion batteries, such as sodium-ion and potassium-ion batteries [37, 38], though the details of these studies are beyond the scope of this project.

Supercapacitors (also known as ultracapacitors) are another form of electrochemical energy storage device used frequently in modern technologies. This form of energy storage device is the focus of this project. Like batteries, the basic setup of a supercapacitor consists of two electrodes, two current collectors, a separator, and an electrolyte solution. Electronic double-layer capacitors (EDLCs) are a form of supercapacitor which store energy via the formation of electric double-layers, first described by Hermann von Helmholtz in 1853 [40]. The first somewhat recognisable supercapacitor device (consisting of porous carbon-based electrodes in H_2SO_4 electrolyte solution) was patented by H.I. Becker as a "Low Voltage Electrolytic Capacitor" in 1957 [41, 42]. The first EDLC device was invented in 1961 by the Standard Oil Company, Cleveland, Ohio (SOHIO) [43], but there was very low demand for a device of its kind at the time [44]. The prototype was licensed by Nippon Electrical Company (NIC), who released the first commercially viable EDLC to be used for computer memory backup in 1975, sold with the name "supercapacitor" [45].

Depending on their charge storage mechanism, supercapacitors can be classified as EDLCs, pseudo-capacitors, or hybrid-capacitors. EDLCs store energy through the formation of electric double-layers on the electrode surface, without any redox reactions taking place [46–48]. When an EDLC is charged, electrons are forced from the positive electrode, through an external circuit, to accumulate at the negative electrode. The resulting net positive and negative charges at each electrode electrostatically attract the negatively and positively charged electrolyte ions respectively, which migrate (through an ionically conductive, but electronically insulating separator) to the electrode surfaces, forming electronic double-layers [49, 50]. During discharging the opposite process occurs, with the excess electrons at the negative

electrode flowing back out through the external circuit to the positive electrode. The neutral charge at both electrodes is restored, both double layers disintegrate, and the electrolyte ions diffuse back into the bulk electrolyte.

The simplicity of this near-instantaneous charge storage mechanism without any redox reactions has the advantages of extremely rapid charging and discharging, superior specific power compared to battery type devices (as shown in Figure 1.3), as well as exceptional charge-discharge cycle life stability. Conventional batteries usually degrade after several thousand cycles, but EDLC devices can last for hundreds of thousands, or even millions of charge-discharge cycles [51–54]. The main disadvantage of this charge storage mechanism is inferior specific energy and specific capacitance. Given that the electric double-layer only forms at the surface of the electrodes, the amount of charge stored by the device is limited by the surface area of the electrode materials used. The surface area of the electrodes can be enhanced by using more porous materials (porous carbons are usually used for EDLC electrodes) [55–57], by activating the electrode materials (through chemical or physical treatments) to increase their porosity [58–60], and/or by carefully choosing the electrolyte used so the ions more effectively and efficiently fit into the pores and channels of the electrodes [61–63]. Other disadvantages include high self-discharge for EDLC devices [64, 65], as well as their higher cost per unit kWh compared to lithium-ion batteries (though other cost parameters, such as cost per charge-discharge cycle, are much more favourable for EDLCs).

The word pseudo-capacitance is derived from a phrase used by David C. Grahame in 1941, where he used the term “pseudo-capacity” to describe the “excess capacity which arises from the reversible electro-reduction of an ion” to distinguish it from the double-layer capacity with which he was primarily concerned [66]. Pseudo-capacitors store energy via rapid, reversible redox reactions at the electrode surface, or intercalation-type reversible redox reactions that usually occur at or near the surface of the electrodes [67, 68]. These reactions

can also occur within the bulk of certain layered or tunneled electrode active materials [69]. As the pseudo-capacitive energy storage mechanism is not limited to just the surface of the electrodes, they possess superior specific energy and specific capacitance to EDLCs. However, as redox processes are occurring as part of the charge storage mechanism, the cycling stabilities of pseudo-capacitors are lower than EDLCs [70]. Lower power density and more expensive electrode materials when compared to EDLCs are other issues that researchers are focusing on improving [71, 67]. The differences in energy storage mechanism and typical electrochemical responses for EDLCs, surface redox pseudo-capacitors, intercalation pseudo-capacitors, and batteries are shown in Figure 1.2.

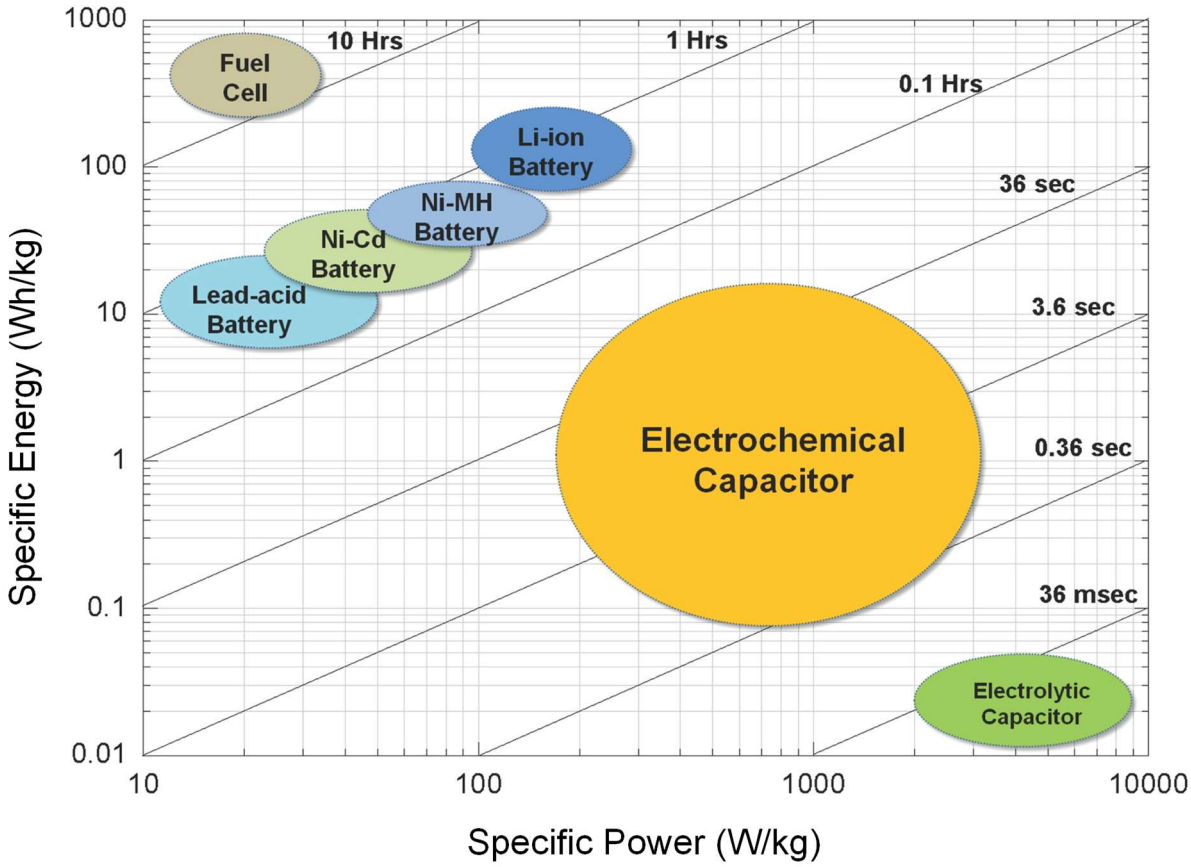

Figure 1.3 A Ragone plot, comparing the energy density and power density of several electrochemical energy storage devices. Though conventional batteries have the advantage of higher energy density, they cannot compete with supercapacitors when it comes to power density and cycle life. Reproduced with permission [53]. Copyright 2015, John Wiley and Sons.

A hybrid-supercapacitor can also be made, combining EDLC materials with pseudo-capacitive/battery-type materials within a single device [72]. This can be done either symmetrically, where both electrodes contain EDLC and pseudo-capacitive/battery-type active materials, or asymmetrically, where one electrode contains only EDLC materials and the other contains only pseudo-capacitive/battery-type materials [73]. A synergy of the EDLC materials and pseudo-capacitive/battery-type materials can be obtained, resulting in a device that improves upon the performance issues of each material type (i.e., lower specific energy for EDLCs, lower specific power and poorer cycle lives for pseudo-capacitors and batteries) [39, 74].

Supercapacitors have been implemented in a great variety of industries and technologies (examples of which are shown in Figure 1.4), being ideally suited for situations that require high bursts of power, long service life, high thermal stability, bendability, and non-toxicity. One such application is renewable and hybrid energy storage, where supercapacitors are used for storing energy in the source and grid, stabilizing the fluctuating loads of these power supplies [75, 76]. The fast-charging nature of supercapacitors makes them an ideal device to use for regenerative braking, whereby the energy produced from braking a vehicle or other moving mechanical components is used to charge attached supercapacitor devices, rather than being lost as heat energy [77–79]. This helps recycle some energy back into powering the system and reduces the energy consumption overall. Handheld power tools [80], specific military technologies [81], microgrids [82], streetlights [83], and light rail [84–86] have all successfully implemented supercapacitors to power and/or reduce energy consumption for these technologies. The possibility for flexible [87, 88] and micro-supercapacitor devices [89, 90] (the likes of which is not possible for conventional batteries), as well as the options for non-toxic, biocompatible, and environmentally friendly materials makes them idea for medical implants and wearable electronics [91–94]. Studies have even investigated piezoelectric

materials to develop supercapacitor medical implants and wearable devices that harvest and store energy from the human body's natural movements [95–97].

Figure 1.4 Examples of technologies that implement supercapacitors [98]. Copyright 2022, MDPI.

1.2 Carbon-Based Energy Storage Materials

When it comes to EDLC devices, the importance of porosity cannot be overstated; as the formation of electric double-layers is limited to the surface of the electrodes only, using a highly porous electrode material vastly increases the surface area in which a double-layer can form, thereby increasing the capacitance of the EDLC device [99, 100]. The electrolyte ions having fast access to the full surface area of the electrodes also insures the excellent specific

power and fast charging that are characteristic for EDLCs [101, 102]. Pores are classified based on their size as follows: macropores (>50 nm), mesopores (2-50 nm), and micropores (<2 nm) [103].

As mentioned before, porous and high-surface area conductive carbon materials are often used as electrode active materials for EDLC devices (examples of which are shown in Figure 1.5). The general advantages of these materials for this purpose are abundant; they are highly electronically conductive, possess a high specific surface area (SSA), are chemically stable, lightweight, non-toxic, safe, and found from an abundance of renewable and waste-derived sources [104–106].

The first carbon material to be discussed here (as it is the most used carbon electrode material for EDLC devices) is activated carbon (AC), a highly porous, amorphous family of carbon materials often derived from organic sources (wood, coconut shells, food waste, seeds, etc.) [107]. The raw materials are often carbonized at an elevated temperature in an inert atmosphere (<800ºC) and then activated to increase their porosity, usually by chemical exposure or physical means [108]. The raw materials, carbonization temperatures, and activation method used to obtain the AC all have an influence on the overall morphology and pore size distribution for the final material [109].

ACs have the advantages of being derived from highly abundant and eco-friendly sources [110], being relatively cheap to produce, having exceptionally high surface areas, and electrochemical stability [111]. SSA values for activated carbons usually fall within the range of 1,000-2,000 m^2/g [112], though this is sometimes exceeded (an SSA of ~3,000 m^2/g was recently reported by Boulanger et al. [113]). The drawbacks of activated carbon materials are the relatively lower electronic conductivity and a non-optimised pore structure that leaves much of the surface area inaccessible to electrolyte ions [114], resulting in limited capacitance

and rate performance [115]. The former problem can be ameliorated by forming a composite electrode of AC with other materials [116, 117], as will be discussed later in more detail. The inaccessible pores and microchannels can be accessed by further treatment methods, such as laser ablation.

Another commonly used carbon material for supercapacitor electrodes (and the most utilised throughout this project) is carbon nanotubes (CNTs). First discovered by Suomo Ijima in 1991 [118], this carbon allotrope consists of sheets of graphene (single-atom thick sheets of graphitic sp^2 carbon [119]) rolled into a tube shape [120]. CNTs can be further classified into single-walled carbon nanotubes (SWNTs), which consist of standalone graphite tubes, and multi-walled carbon nanotubes (MWNTs), which consist of several graphitic tubes of different diameters wrapped around one another [121].

SWNTs (first synthesised and reported independently in 1993 by both Iijima et. al. [122] and Bethune et. al. [123]) were the CNT material used in this project. Synthesis methods for SWNTs include laser ablation [124], arc-discharge [125], and chemical vapour deposition [126]. Compared to MWNTs, SWNTs are generally more challenging to synthesise in bulk [127], but can reach higher electric conductivities (ranging from 10^2 to 10^6 S/cm, while MWNTs range from 10^3 to 10^5 S/cm [128]), provide better mechanical properties [129], and don't possess the inter-layer interference of electronic properties that occur in MWNTs [130]. The significantly higher cost per unit mass (relative to other carbon-based electrode materials) [131, 132] and a relatively lower accessible surface area compared to AC (usually determined to be several hundred m^2/g) [133–135] are the main drawbacks of using SWNTs as supercapacitor electrode materials.

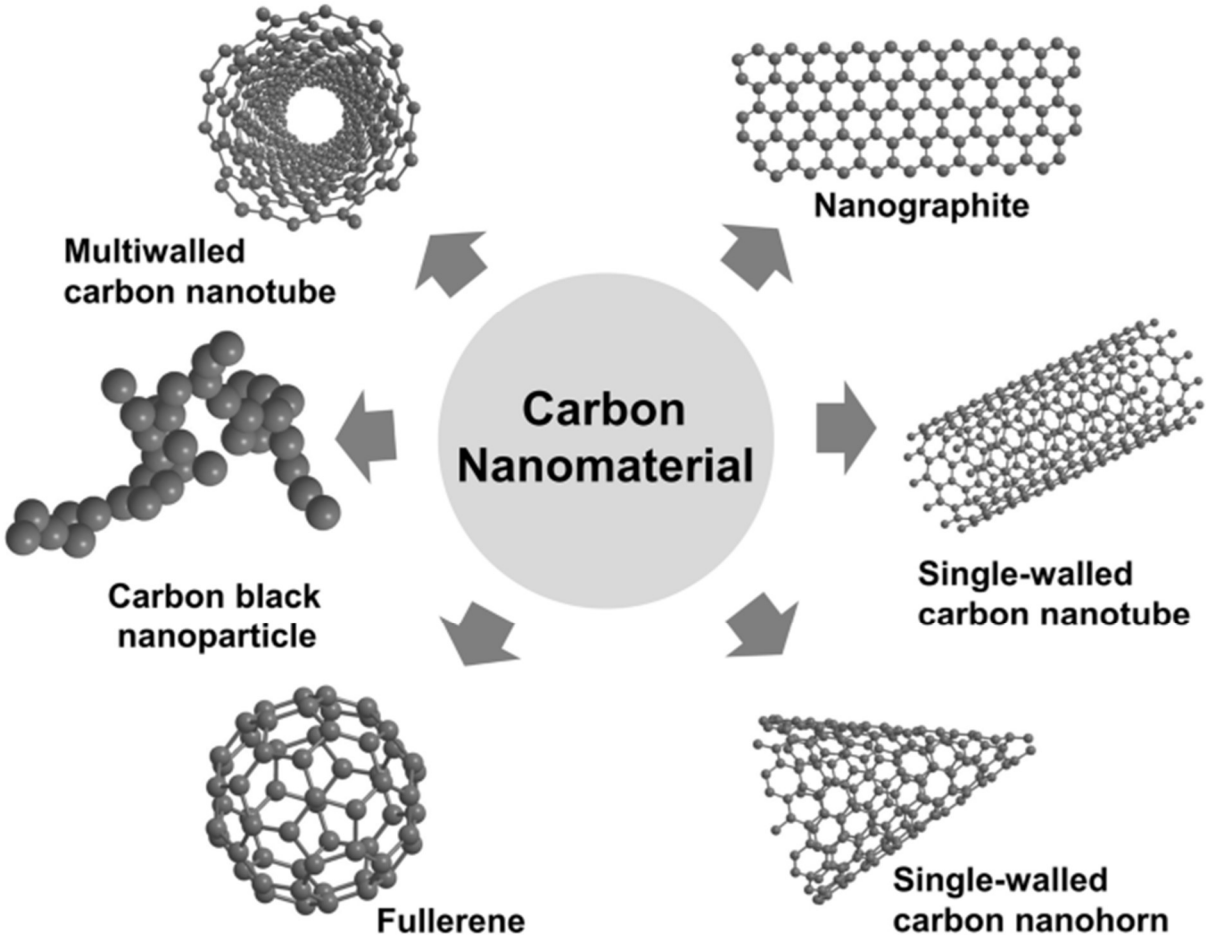

Figure 1.5 Several examples of different carbon allotrope nanomaterials, some of which (SWNTs, MWNTs, carbon black, graphite) are commonly used as electrode materials for supercapacitors [136]. Copyright 2019, Springer Nature.

Another carbon material used extensively in this project is graphene nanoplatelets. Graphene, consisting of a one-atom (0.34 nm) thick layer graphitic sp^2 carbon [137], is one of the most significant discoveries of the 21st century in materials sciences. Single-sheet graphene can possess metal-like electric conductivity, electron mobilities exceeding 200,000 $cm^2/(Vs)$ [138], a theoretical surface area of 2,630 m^2/g [139], and optical transparency, all exceptionally useful features for uses in photonics, nanocomposites, opto-electronics, and protective coatings [140, 141]. However, the mass production of single-layer pure graphene sheets is extremely difficult, with very high cost and slow fabrication rates [142].

Graphene nanoplatelets (GNPs) are a relatively low-cost and high production rate alternative to pure single-layered graphene, while still possessing many useful and interesting properties. GNPs consist of mixtures of single-layer graphene, few-layer graphene (2-10 layers) [143], and thicker graphite nano/micro-platelets, with GNP thickness therefore ranging from 0.34 nm to 100 nm in the same batch [144, 145]. GNPs possess an SSA generally ranging from ~500-750 m^2/g [146, 147] and high electronic conductivity (~10^5 S/cm parallel to the graphene plane, and ~1 S/cm in the transversal direction [148]). The tendency of the graphitic aromatic polycyclic layers to stack due to strong π-π interactions [149] limits the total accessible SSA by electrolyte ions. Exfoliation using metal nanoparticles [150] or dispersion with other carbon-based materials [151] can be used to separate the graphitic layers, increasing the SSA available for double-layer formation.

Super-P (or carbon black) is a commercially available conducting agent, often implemented as an additive to energy storage electrode composites [152–154]. The material has a powdered morphology with an average particle size of ~40 nm [155]. Fibrous electrode materials and additives (such as CNTs and carbon fibres, CFs) effectively form long-range conductive pathways within electrode composites (conductive "highways") but can have limited contact with other electrode active materials. A dispersion of super-P particles throughout can effectively form many short-range conductive pathways (conductive "local roads"), which works synergistically with the fibrous materials to facilitate short-range and long-range electron transport throughout the electrode active materials [156, 157] (see Figure 1.6 (c)).

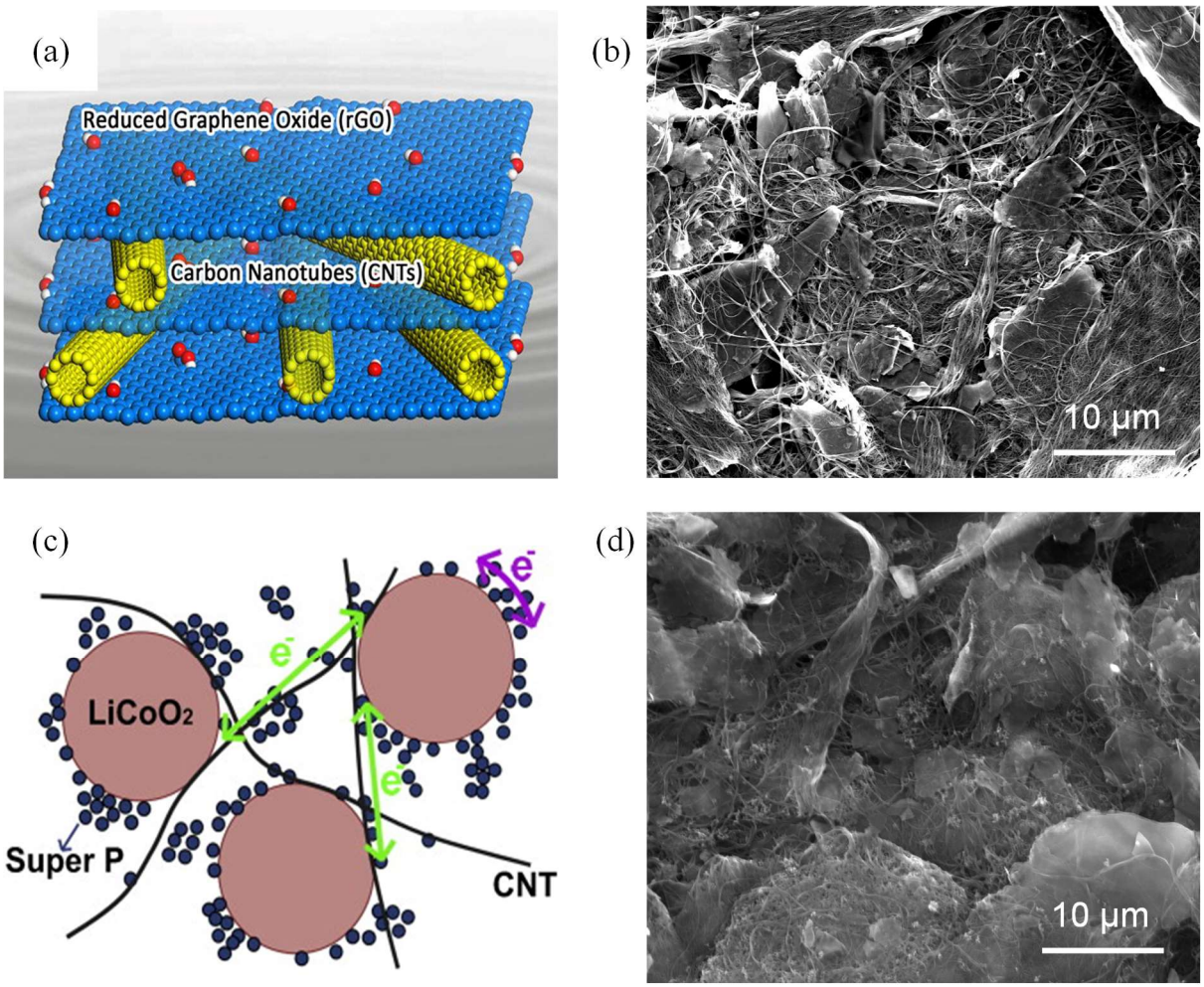

Figure 1.6 (a) Schematic showing the separation of graphene layers via dispersion of carbon nanotubes, preventing the restacking of the graphene layers and increasing the surface area of the electrode material available for double-layer formation. Reproduced with permission [158]. Copyright 2015, Elsevier. (b) SEM image of GNPs interspersed with SWNTs used for carbon-based electrodes throughout this work. (c) Illustration of the synergistic conductive CNT "highways" (green arrows) and Super-P "local roads" (purple arrow), facilitating long-range and short-range electron transport throughout the active material. Reproduced with permission [157]. Copyright 2013, Elsevier. (d) SEM image of GNP/SWNT/Super-P composite used for carbon-based electrodes in Chapter 3 of this work.

For much carbon-based supercapacitor research, including that presented in this project, understanding the synergy between carbon materials of different morphologies is essential for designing effective carbon composite materials that maximise the electrochemical performance of supercapacitor devices. The most used carbon composite electrode in this work consists of a 50:50 by mass ratio of GNPs and SWNTs. As discussed previously, polycyclic graphitic aromatic sheets tend to stack, cutting off much of the SSA for double-layer formation. In this

work (as with other research outputs [159–161]), fibrous SWNTs are used to separate the GNPs, with the aim of increasing the SSA, and improving electrochemical performance by extension (see Figure 1.6 (a) and (b)). The benefit of using SWNTs is twofold, as the material also functions as the fibrous, electronically conductive "highways" mentioned previously. Later, super-P is also introduced to the carbon composite, with the aim of providing the benefits of short-range, "local road" conductive channels discussed earlier (see Figure 1.6 (c) and (d)).

1.3 Beyond Carbon-Based Energy Storage Materials

While possessing exceptional cycling stabilities, high specific power, and inert chemistries, the biggest drawback for carbon-based EDLC devices is their low specific energy (energy stored per unit mass active material) relative to other forms of energy storage devices. The addition of pseudo-capacitive active materials can help boost the specific energies of supercapacitor devices, but often causes the specific power and cycling stability to suffer [162]. Transition metal oxides (TMOs) [163] and conductive polymers [164] are the most commonly used pseudo-capacitive materials, with transition metal nitrides/sulfides/carbides, MXenes, and metal organic frameworks (MOFs) also being researched as promising alternatives [67].

In 1971, Trasatti and Buzzanca reported the first study on the pseudo-capacitive charge storage behavior of TMOs (in their case, a ruthenium oxide, RuO_2 thin film in sulfuric acid) [165]. A later study in 1995 by Zheng et. al. studied nanostructured hydrous RuO_2 electrodes, achieving a very high capacitance value of 720 F/g at a voltage window of 1 V in 0.5 M H_2SO_4 electrolyte solution [166]. The metal oxide is reversibly oxidised/reduced reversibly through a proton exchange mechanism, $RuO_2 + xH^+ + xe^- \Leftrightarrow RuO_{2-x}(OH)_x$ $(0 \leq x \leq 2)$ [167]. The high capacitance values achieved can be attributed to the structural water molecules aiding in proton transport. Nano-structuring of RuO_2 can also increase the interfacial surface area between the

TMO electrode and the electrolyte, meaning more active sites are accessible for charge transfer reactions [168]. The environmental toxicity and extremely high price of ruthenium (approximately €13,750/kg as of July 9, 2024 [169]) limits the greater implementation of RuO_2 electrodes in energy storage [170].

However, the favourable electrochemical properties of hydrous RuO_2 encouraged researchers to investigate other metal oxides for similar pseudo-capacitive energy storage properties. One such metal oxide is manganese dioxide (MnO_2), whose pseudo-capacitive behaviours in an amorphous, hydrous form was reported in 1999 by Lee and Goodenough. In their study, an electrode of amorphous $MnO_2.xH_2O$ achieved a specific capacitance of ~200 F/g in 2 M aqueous KCl electrolyte at a voltage window of 1.2 V (-0.2 and +1.0 V versus SCE) [171]. This material has the advantages of being environmentally inert and cheaper than RuO_2 [172]. It is also effective when used in neutral electrolyte solutions [173, 174]. In one such study testing MnO_2 electrodes in aqueous KCl electrolyte, it was determined that the charge storage mechanism for MnO_2 involves fast reversible redox reactions through both the potassium ions ($MnO_2 + xK^+ + xe^- \Leftrightarrow MnO_{2-x}(OK)_x$) and protons from the protic solvent ($MnO_2 + xH^+ + xe^- \Leftrightarrow MnO_{2-x}(OH)_x$), depending on availability of the cations [175]. This is a very useful characteristic given that many metal oxides are unstable in acidic solutions [176].

The lower capacitance and conductivity [177] values relative to RuO_2 are the main drawback of MnO_2 [178]. The low electronic conductivity can be mitigated by forming composite electrodes of MnO_2 with other electrode materials, such as carbon [179, 180]. Several other transition metal oxide species such as nickel oxide [181], vanadium oxide [182], and cobalt oxide [183] have also been investigated extensively for their pseudocapacitive properties, with each presenting their own unique pros and cons [184].

Another class of materials often implemented into pseudo-capacitive energy storage devices is conductive polymers [185]. Polymers are generally known to be electronic insulators and are often used for that purpose, but researchers in the latter half of the 20th century began to unearth semiconducting properties of certain doped polymers. One such discovery was made by Hideki Shirakawa and co-workers via a "fortuitous error" of using an excessive amount of organometallic catalyst for polymerising acetylene [186]. This inadvertently formed doped polyacetylene, which displayed semiconducting properties. Further research with collaborators from the University of Pennsylvania led to a publication in 1977 which showed that the electronic conductivity of doped polyacetylene could be tuned over eleven orders of magnitude (from insulating to metallic behaviour) by the concentration of dopant [187]. Alan Heeger, Alan MacDiarmid, and Hideki Shirakawa were jointly awarded the 2000 Nobel Prize in Chemistry "for the discovery and development of conductive polymers" [188].

Since then, other conductive polymers have been researched and synthesised: a few examples are polyaniline, polypyrrole, polythiophene, PEDOT, polyphenylene vinylene (structures are shown in Figure 1.7 (a)). As with other pseudo-capacitive materials, conductive polymers undergo fast and reversible redox reactions to store charge throughout the conductive polymer electrode, boosting the specific energy while limiting the specific power due to sluggish ion diffusion within the bulk of the electrode [164]. Conductive polymers possess the unique advantages of having hugely variable conductivities, flexibility, low-cost, light weight, and abundancy of raw materials [189], but also have poor cycling stability and low specific capacitance [190].

As discussed in earlier sections, a necessity of high-functioning supercapacitor devices is that the electrolyte can access as much of the electrode surface area as possible, for both the formation of electronic double-layers for EDLC devices, and reversible surface/near-surface redox reactions in the case of pseudo-capacitors. As such, a group of interesting and relatively

novel materials called MXenes provide many highly advantageous characteristics for supercapacitor energy storage. First discovered at Drexel University in 2011 [191], MXenes are a class of 2D transition metal carbides/nitrides of the general formula $M_{n+1}X_nT_x$ with M being a transition metal, X being carbon or nitrogen, and T being a surface termination group (e.g. -OH, -O, -Cl, -F, etc.), with *n* varying from 1 to 4 [192, 193]. The MXene first discovered in Drexel University was $Ti_3C_2T_x$, with over 25 other forms being synthesised since then [194]. See Figure 1.7 (b) for an illustration of the structure of several MXene materials.

MXenes exhibit excellent electronic conductivity (up to ~9,880 cm^{-1} for $Ti_3C_2T_x$ thin-films [195]), rich surface chemistry, a high surface area layered structure with tunable interlayer distance (depending on the synthesis route [196]), and charge transfer capabilities due to the variable oxidation state of the transition metal. A study reported by Lukatskaya et. al. demonstrated the promising electrochemical properties of MXenes by designing a macroporous $Ti_3C_2T_x$ film which delivered a specific capacitance of up to 210 F/g at a scan rate of 10 V/s (surpassing the best carbon supercapacitors reported at the time), and showing that MXene hydrogels can match the volumetric capacitance of RuO_2, achieving values of ~1,500 F/cm^3 [197].

Despite the excellent properties displayed by MXenes, several challenges remain to be overcome before wider ultilisation in energy storage is possible. The harsh chemical etching procedures used to synthesise MXenes can lead to defects and vacancies which are vulnerable to oxidation in water or oxygen, causing the crystalline MXene structure to degrade into TMOs and amorphous carbon [198]. Specific procedures for controlling oxygen kinetics in MXenes and storing MXene products in argon-atmosphere are being implemented to prevent this [199].

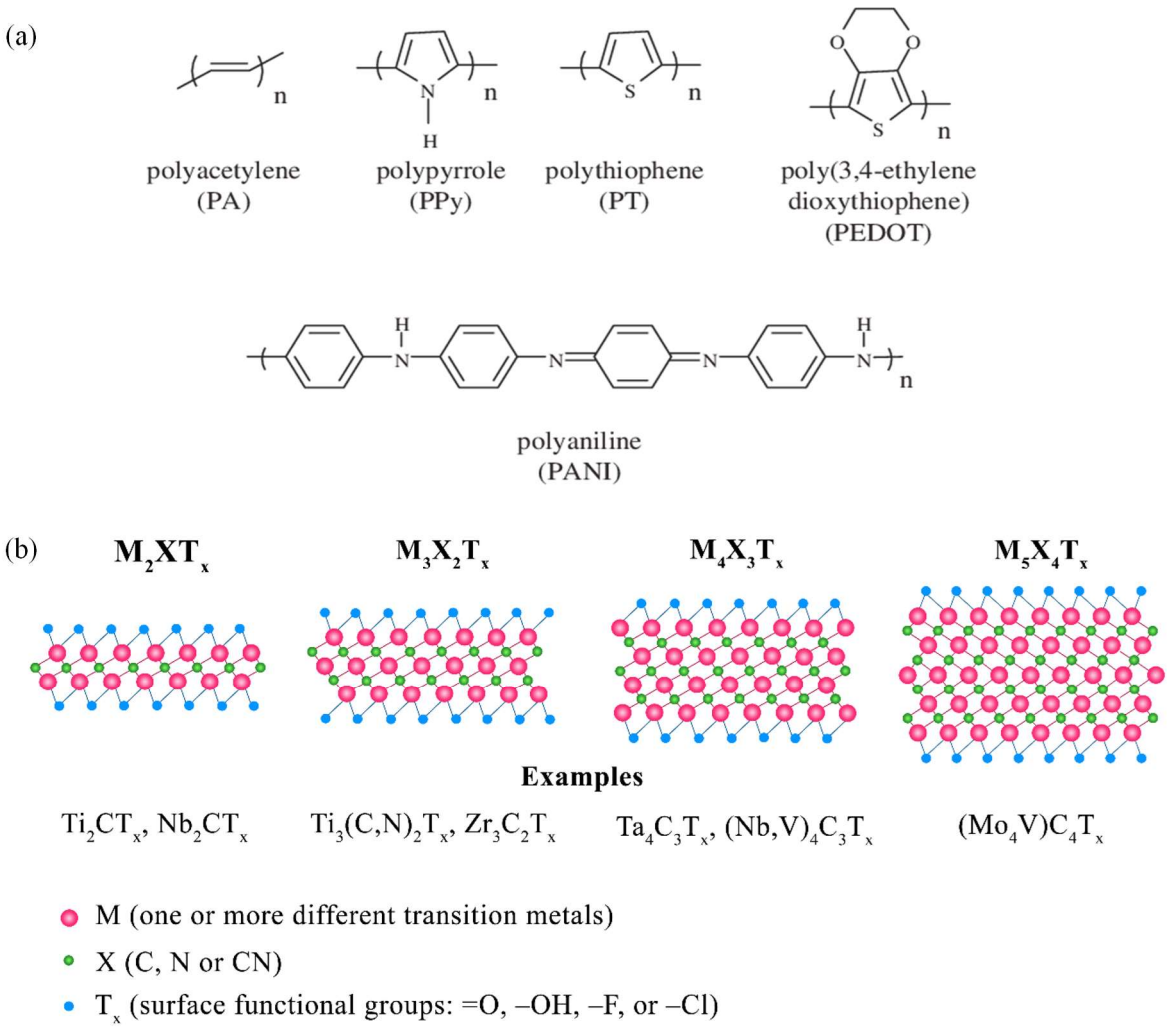

Figure 1.7 (a) Chemical structures of some of the most common conductive polymers. Reused with permission [200]. Copyright 2010, The Royal Society. (b) Chemical structures and formulae for a single layer of MXenes [201]. Copyright 2021, MDPI.

Inverse opals are highly uniform porous structures implemented in Chapter 5 of this work. Naturally occurring opal is an example of a colloidal crystal, consisting of nanoscale monodisperse amorphous silica spheres arranged in a face-centred cubic (fcc) arrangement [202]. Inverse opals are the reverse of this structure, with fcc packed spherical pores and the space around these pores filled with material. Generally, inverse opals are obtained first by depositing a sacrificial colloidal crystal opal template (the dimensions and arrangements of which will dictate the final inverse opal structure), such as polystyrene spheres. The precursor material is then infiltrated into the template in fluid form and/or dissolved in a solvent, filling

the gaps between the spheres before being chemically or physically solidified. Finally, the opal template is removed, using a method dependent on the material of the template [203, 204]. Figure 1.8 (a) shows a general schematic for inverse-opal synthesis. Further stabilisation and modification steps may be required, depending on the materials used and the desired level of ordered porosity [205]. Using this synthesis method (or variations thereof) inverse opal structures have been made from a variety of materials: such as metal oxides, metals, carbons, semiconductors, and polymers [206].

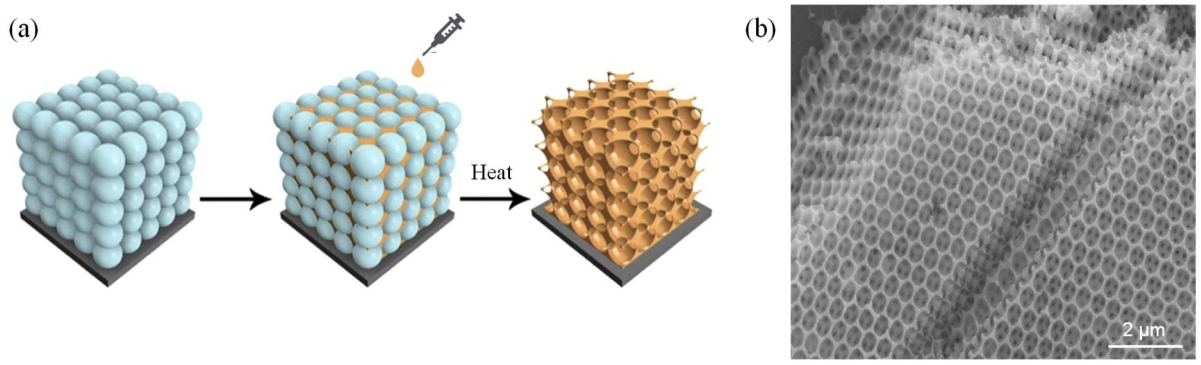

Figure 1.8 (a) Outline of a typical synthesis method for obtaining inverse opal structured materials. (b) SEM image of a NiO-based inverse opal, with the distinctive morphology clearly visible.

For energy storage devices, inverse opals offer the advantages of a highly ordered, porous electrode structure that has a far more controllable SSA and pore size than randomly arranged slurry electrode materials (see Figure 1.8 (b)). This would aid in electrolyte insertion and improve the interfacial contact between the electrolyte and electrode materials. For EDLC systems, this would increase the SSA available for double-layer formation [207]. For batteries and intercalation type pseudo-capacitance, this would improve mass transport properties and rate capabilities [208], but also negatively affect the volumetric energy density, given that only 26% of the fcc inverse opal structure is filled with material. Additional layer coatings and structures onto the inverse opal material have been researched to improve the volumetric

energy density [209]. The synthesis and characterisation of the MnO_2 inverse opal-carbon composite studied in this work will be discussed in greater detail in Chapters 2 and 5.

1.4 Introduction to Additive Manufacturing and 3D-Printing

This section will give a brief overview of the history of 3D-printing technologies, different types of 3D-printing currently used, and the applications of 3D-printing in modern technology. The traditional method for industrial manufacturing is subtractive, beginning with a large block of starting materials, parts of which are removed to obtain the final desired shape. Everything from stonemasonry, forestry, mining, and wood carving uses this manufacturing method. The reverse of this, building layer by layer to obtain a three-dimensional final output, is known as additive manufacturing (AM), which has not been as widely utilised in manufacturing [210]. With the invention and advances in 3D-printing in recent decades, AM has become more widespread with many industries taking advantage of the multiple benefits this method provides: ease of prototyping, ability to create highly complex components, reduction of waste materials [211].

The first reported approaches to 3D-printing technologies can be traced to the early 1980s, when two independent studies, conducted by Hideo Kodama in 1981 [212] and Alan J. Herbert in 1982 [213], investigated photopolymer prototyping systems to manufacture components layer-by-layer. In 1983 Charles “Chuck” Hull printed a small cup using a photopolymerisable liquid resin which was solidified layer-by-layer with UV-light [214]. This process would come to be called stereolithography (SLA), a term coined by Hull. In 1984, Hull applied for the first patent for commercial SLA technology [215], which was granted in 1986. In the same year his patent was granted, he co-founded the company 3D Systems, which would go on to design and manufacture multiple 3D-printer devices, producing printed components

made of polymers, ceramics, metals, composites, and others [216]. In 1988, Scott Crump invented fused deposition modelling (FDM) [217], a 3D-printing technology that uses a continuous filament of thermo-polymer which is melted and extruded by a heated nozzle to build the printed component layer-by-layer [218]. In 1989, he and his wife, Lisa Crump, founded Stratasys [219], which commercialised the FDM technology invented by Crump. FDM remains the most widely used 3D-printing method at the consumer level. Both SLA (more generally known as Vat-Polymerisation, Vat-P) and FDM 3D-printing were used in this work, and both methods will be discussed in greater detail later.

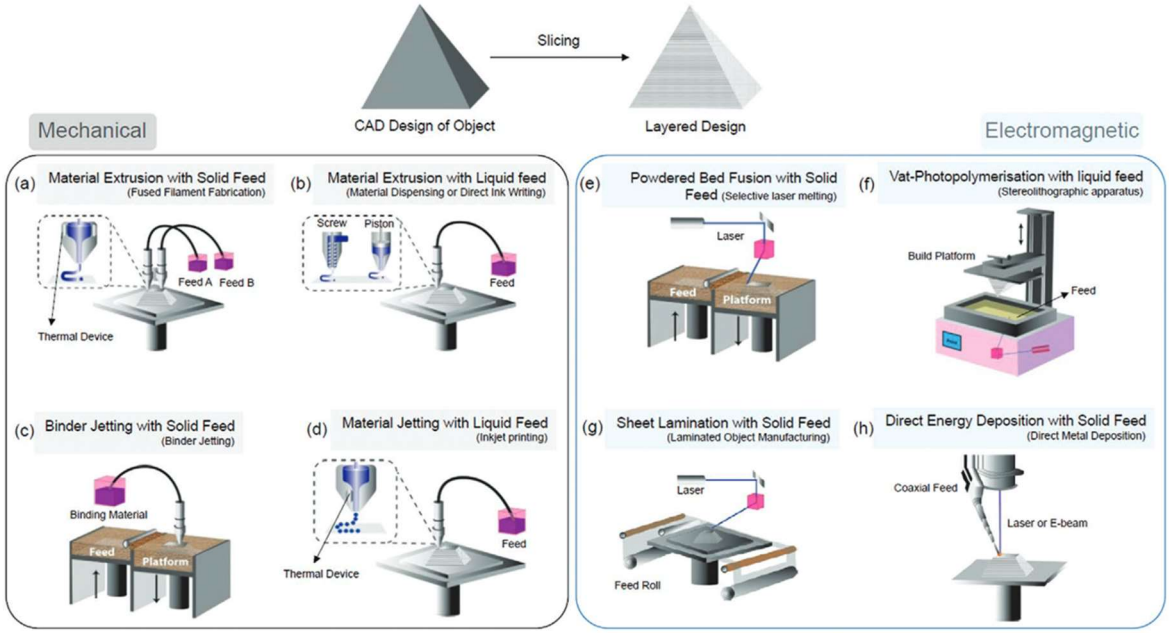

Figure 1.9 Schematics for a variety of 3D-printing methods discussed throughout this section. Both (a) Material Extrusion with Solid Feed and (f) Vat-Photopolymerisation with Liquid Feed methods are used extensively throughout this work. Reproduced with permission [220]. Copyright 2020, John Wiley and Sons.

Since the inventions of SLA and FDM in the 1980s, multiple other 3D-printing methods have been developed (some of which are illustrated in Figure 1.9). Related to SLA 3D-printing is Digital Light Processing (DLP) and Liquid Crystal Display (LCD), which also use light to cure photopolymer resins. The difference between these methods is the light source. SLA uses

a precise mobile laser to trace each layer. DLP uses a digital projector, and LCD uses a liquid crystal mask system (liquid crystals change molecular arrangement and optical transparency when an electric field is applied [221]). The DLP and LCD systems allow an entire layer of the printed component to be cured instantly [222, 223] rather than traced slowly by a mobile laser, which shortens the overall printing times. DLP is, however, limited to printing small objects (e.g. jewellery and dental implants) due to the small size of the projection (to guarantee high precision) [224]. LCD is cheap and accurate but suffers from a short service life due to light leakage from the liquid crystal mask system, which can cause unwanted extra polymerisation of the resin material [225].

Direct Ink Writing (DIW) is an extrusion-based 3D-printing method (like FDM). Instead of using a heated nozzle which melts a solid reel of thermoplastic, DIW uses a pressure-driven system to extrude viscoelastic ink to build the printed component layer-by-layer [226, 227]. The main advantage of DIW over other 3D-printing methods is that any precursor ink material can be printed using this method (inks containing metals, ceramics, plastics, composites, carbons, etc.) if the ink precursor possesses the rheological properties (apparent viscosity, shear thinning, viscoelasticity, etc.) required for printing [228]. This contrasts the far more limited choice of materials for other 3D-printing methods (e.g. photopolymers for Vat-P, thermoplastics for FDM), making DIW a highly versatile 3D-printing method.

Material Jetting (MJ) is a very advanced 3D-printing technique which combines elements of photopolymer curing and extrusion-based methods. The raw material is a photopolymer resin which is heated to obtain optimal viscosity. The material is extruded out of a printhead as tiny droplets, which are “jetted” to the desired location, at which point they are cured by a UV lamp attached to the printer [229]. As well as having very high accuracy, MJ has the distinct advantage of simultaneous multi-material printing facilitated by multiple

printheads [230]. MJ has therefore been used to print highly complex multicoloured models and components possessing different physical properties within one print [231, 232].

Another category of 3D-printing technology is Laser Powder Bed Fusion (LPBF), a generic term for several 3D-printing methods (selective laser sintering, selective laser melting, selective heat sintering, direct metal laser sintering, electron beam melting [233]) which use powder as their raw materials, which are selectively fused/melted by a precise energy input (such as laser light or electron beams) to build the solid printed component [234, 235]. This method can be used for printing metals, alloys, glass, and plastics [236]. The main disadvantage is that this method is very time consuming, as powder heating, vacuum generation, and cooling down periods are often required [237].

Though initially concepted as a method for engineers to easily and quickly obtain prototypes, 3D-printing has greatly expanded beyond conventional engineering in recent decades and is now widely used in many areas of science, medicine, and technology. For example, in the field of prosthetics, FDM was used for printing low-cost prosthetic hands for children with upper-limb reductions [238]. In bioengineering research, multiple different 3D-printing methods have been used to print biocompatible hydrogels for biosensors and to aid and improve the growth of biological tissues [239–241]. Increasingly, trauma surgery research is working to implement 3D-printing into patient care, surgery, and recovery [242–244]. Even in the field of food science, extrusion-based 3D-printing has been utilised [245–247]. Of course, the field of energy storage devices is no exception to using 3D-printing, which will be discussed in detail in a later section (1.6).

1.5 Vat-Polymerisation and Fused Deposition Modelling

This section will outline in detail the working principles for Vat-P and FDM, the two 3D-printing methods used in this work. The advantages and disadvantages of these will be compared. The two models of 3D-printers implemented in this work will be used to explain the working principles of their respective 3D-printing type: namely the Form 2 Formlabs Vat-P printer (© Formlabs, Somerville, Massachusetts, USA) and MakerBot Replicator 2X FDM printer (© UltiMaker, Utrecht, Netherlands).

Starting with Vat-P 3D-printing, the generic working principle involves the curing of a photopolymer resin by a light source, in a process known as photopolymerisation (also known as photo-curing and photo-cross-linking). The raw material for this 3D-printing method consists of monomers/oligomers in liquid form, which are cured to form solid thermosets upon exposure to light of a specific wavelength [248]. Photopolymerisable functional groups for the monomers can include acrylates and epoxides [249] (the most common), as well as fumarates, cinnamates, and coumarins [250–252]. The polymer resin should possess several general features to improve the printing process and reduce the printing time as much as possible. Firstly, the polymers should be liquid at room temperature (or processing temperature) to allow for mobility. Low viscosity (usually between 0.25 Pa·s and 5 Pa·s [253]) is also desirable for several reasons: reactive functionalities of the resin can interact more easily, the resin self-levels more quickly, and the cleaning of excess liquid resin after printing is easier [254]. For biological implants, non-toxicity is also essential. The © Formlabs Clear V4 photopolymer resin used in this work is liquid at room temperature and possesses a viscosity of 0.9 Pa·s [255].

For this work, Vat-P 3D-printing was done by a © Formlabs Form 2 SLA printer, which uses a precise 405 nm violet laser (250 mW) as the light source [256]. The schematic for this printer can be seen in Figure 1.10. A resin cartridge is inserted into the back of the printer,

which automatically dispenses the resin into the tank until the optimum level is reached. Care must be taken to never mix different resins; therefore, the resin tank being used must either be empty, or already contain the same resin as that in the resin cartridge. When the resin tank is filled to the optimum level, the printing process begins. The build platform (mobile along the z-axis) is lowered into the resin. The laser is shone onto a scanning mirror, which directs the laser light along the x and y-axes. The laser light passes through a transparent window at the bottom of the resin tank, polymerising a thin layer of resin at the surface of the build platform. By moving around the x and y-axes (and switching on and off when necessary), the laser light polymerises an entire layer of the printed component. Once an entire layer is completed, the build platform is raised upwards by the thickness of one layer, and the process is repeated. This is done layer-by-layer until the entire component is printed, at which point the build platform is raised fully out of the resin and the printing process terminates.

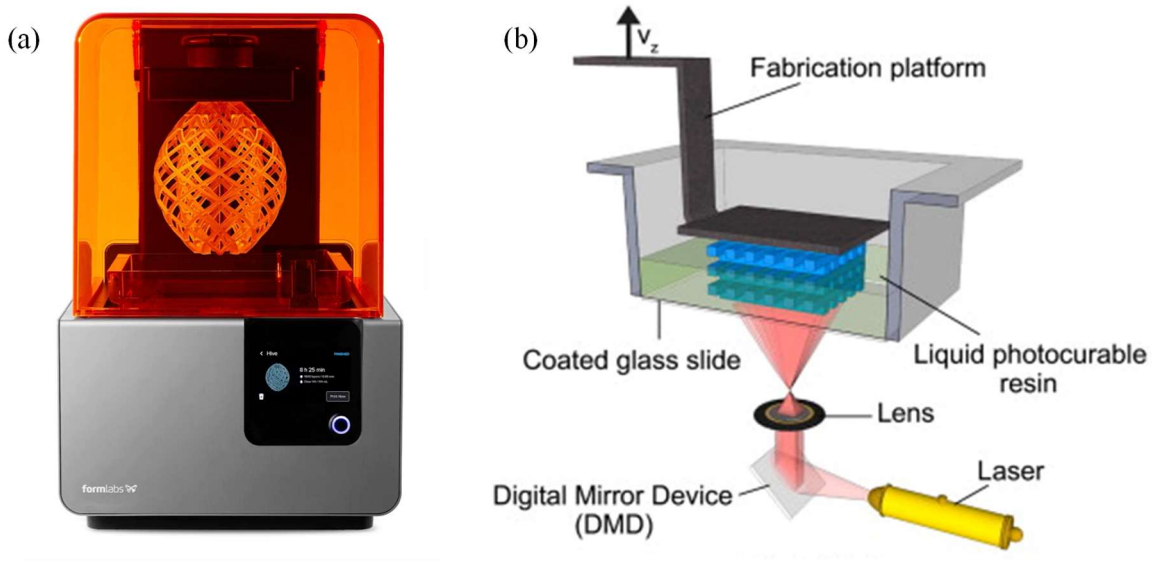

Figure 1.10 (a) © Formlabs Form 2 SLA 3D-printer, used for all Vat-P printing in this work, and (b) a schematic for this 3D-printing method. Reproduced with permission [257]. Copyright 2012, Elsevier Ltd.

For this 3D-printing method, however, the printed component is not yet finished, as several post-printing procedures must be completed. It's important to outline these, as they play

a part in the performance metrics for this 3D-printing method. Firstly, the printed part must be cleaned of any excess liquid resin remaining after the submergence in the resin tank. An isopropyl alcohol (IPA) bath is usually used for this purpose. Following this, the printed part requires further curing. The © Formlabs Form Cure or other similar curing machines can be used for this purpose. Post-print curing enhances the strength and performance of the printed part, as well as achieving the required safety standards if the printed part is biocompatible material to be used in implants or other medical purposes. If the printed part includes supports (which is advisable to prevent deformation during printing), these must be removed (by hand or using a wire cutter).

Moving onto FDM 3D-printing, the generic working principle involves the melting and extrusion of a thermoplastic via a motorised heated extruder. The raw material for this method consists of a reel of thermoplastic filament. The two most common filament materials are polylactic acid (PLA) and acrylonitrile butadiene styrene (ABS) [258]. When compared to one another, PLA requires a lower temperature (therefore less energy) for extrusion, is biocompatible and biodegradable [259], and less prone to warping during printing. However, it is also more brittle and has a higher tendency to block the printer nozzle [260]. On the other hand, ABS is stronger, more durable, and can withstand a lot more stress and heat than PLA but is prone to warping, can produce potentially hazardous fumes while printing, is non-biocompatible, and requires higher temperatures (therefore more energy) for extrusion [261]. Composite raw materials, such as the ProtoPasta Conductive PLA (© ProtoPlant, Vancouver, Washington, USA) filament (PLA mixed with conductive carbon black [262]) used in this work, are common for FDM 3D-printing (unlike Vat-P). However, ensuring that the multiple materials are compatible and extrudable within the same temperature and printing settings is essential. The intrinsic mechanical properties of the printed component may also be negatively

affected. A high concentration of conductive carbon material in PLA, for example, causes brittleness that limits mechanical strength and ability to withstand strain and bending.

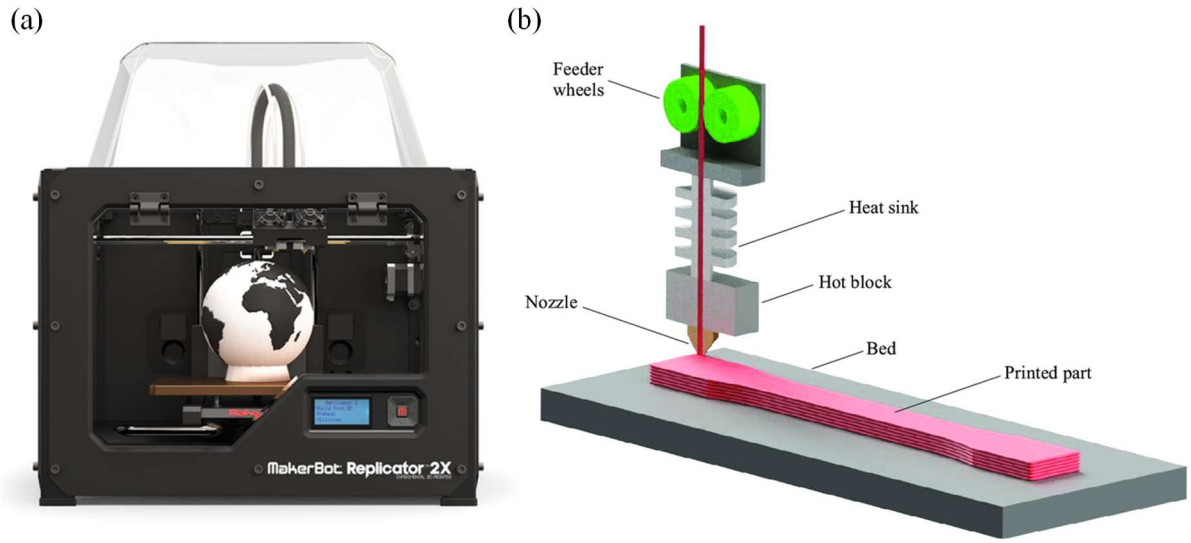

Figure 1.11 (a) © MakerBot Replicator 2X 3D-printer, used for all FDM printing in this work. Copyright 2024, B & H Foto & Electronics Corp. (b) Schematic for this 3D-printing method [263]. Copyright 2021, MDPI.

The schematic for the © MakerBot Replicator 2X FDM printer can be seen in Figure 1.11. A spool of thermo-polymer filament is inserted into the back of the printer, which is directed to the extruder by a guide tube. When the printing process begins, the extruder is heated to a pre-set temperature (optimal for melting the filament without burning it). If the filament is changed or replaced, it is essential that the extruder is set to heat to the correct temperature for that filament material. If the temperature is too low, the filament won't melt, if it's too high, the filament will burn or melt too quickly, causing a blockage. The build platform (which is also heated, but to a lower temperature than the extruder) is raised along the x-axis until it is just below the extruder nozzle, with just enough distance for one printed layer to be extruded. A motor pushes the filament into the heated extruder head, which deposits a line of melted thermo-plastic onto the build platform. The extruder is moved along the x and y-axes, with the motor controlling the flow of the extrusion (stopping and starting as

necessary), until an entire layer of the printed component is extruded. The build platform is then lowered by the thickness of one layer, and the process is repeated. This is done layer-by-layer until the entire component is printed, at which point the build platform is lowered fully and the printing process terminates. Unlike the Vat-P printer, there is very little processing to be done after printing. Supports can be printed with the component (again, to prevent deformation during printing) which must be removed, but no washing or curing processes are required for FDM printing.

Both 3D-printing methods have their pros and cons, and several factors such as the printed component's complexity, time limitation, and special requirements such as electronically conductive or watertight printed components will determine which method is best suited for that purpose. Printing resolution is a very important factor for every 3D-printing method, as the higher the resolution, the more intricate and complex the printed component can be. The minimum layer thicknesses for the Vat-P and FDM printers used in this work are 25 μm and 100 μm respectively [256, 264], making the Vat-P printer a better choice for intricate and complex printed components. In Vat-P, the print quality is much smoother, more consistent, and nominally nonporous due to the deposition method, resulting in a watertight printed component, should it be used for the purpose of holding fluids. FDM materials typically form a filamentary structure often interspersed with openings and pores in its 'woodpile' overlaid deposition, making it unsuitable for the purpose of containing fluids.

A distinct advantage of the FDM printer used in this work is the ability to print electrically conductive components using the ProtoPasta Conductive PLA filament. No such conductive raw material exists for the Vat-P printer used in this work. Conductive additives would affect the viscosity and optical properties of the photosensitive resins, likely scatter and/or absorb photons, and end up compromising the printing process [265]. Studies are being undertaken on the development of electronically conductive resins for Vat-P printing [266,

267], but these are currently beyond the scope of this work. A coating of conductive material on the surface of the Vat-P printed components is instead needed to add electrical conductivity.

Table 1.1 Summary of the 3D-printing methods and materials used in this work, outlining the advantages and disadvantages presented by each method. *Washing, curing, and removing of supports are all required for Vat-P. Curing time of 15 minutes for Clear V4 resin, but other resins could have up to 2 hours curing time. **No electronically conductive resin could be found for our Vat-P printer. Metal sputtering was used to add conductivity if it was required (e.g. for current collectors). ***Even when designed in CAD to be a completely non-porous structure and printed at the highest resolution, the filamentary woodpile structure of the FDM printed component is unable to completely retain liquids.

3D-Printing Method	Vat-Polymerisation	Fused Deposition Modelling
Model of 3D-Printer Used in Thesis	© Formlabs Form 2	© MakerBot Replicator 2X
Highest Possible Printing Resolution	25 μm Layers	100 μm Layers
3D-Printing Raw Materials Used in Thesis	© Formlabs Clear V4 Resin	ProtoPasta Conductive PLA
Post-Processing Required for Printed Components?	Yes*	No
Electronically Conductive Printing Materials?	No**	Yes
Watertight Printed Components?	Yes	No***

Printing and processing time is another factor to be considered for both printing methods. For both printer software programs used in this work (PreForm and MakerBot Desktop), a testing batch of 25 simple current collectors was designed. The resolution for both was set to 100 μm, with the current collectors at 45 º to the build platform with supports added (as is advisable to prevent deformity while printing). For the Vat-P Form 2 printer (Clear V4 resin at 100 μm) the printing time was calculated to be ~2 h 30 min. For the FDM Replicator 2X printer (Conductive PLA filament at 100 μm) the printing time was calculated to be ~2 h. The resolution of the FDM printer cannot be increased any further, but when the same test was taken for the Vat-P printer at the highest possible resolution (25 μm), the printing time predictably increased considerably, to ~5 h. What must also be accounted for is the post-

printing processing time. For the FDM printed parts there is no extra processing time, except several minutes to remove the printed supports. For the Vat-P printed parts, around 10 minutes are required for cleaning off any excess liquid resin, followed by the curing process, which takes around 30 minutes for the Clear V4 resin (curing time of 15 minutes at 60 ºC, plus around 15 minutes for the curing machine to heat up). Different resins require hugely varying cure times and cure temperatures [255] which can add considerable extra time to the process of obtaining the printed components. For example, the High Temp V2 resin requires 120 minutes of curing time at a temperature of 80 ºC.

1.6 Progress and Outlook on Additively Manufactured Supercapacitors

As discussed earlier, many fields of science and technology are now employing 3D-printing techniques in their work and research. Energy storage research is no exception to this, as 3D-printing brings a multitude of benefits to this discipline; the unmatched ease of customisation and prototyping, the elimination of waste materials, and the ability to print complex and advanced architectures within the energy storage devices.

The 3D-printing of supercapacitor devices has only been reported in the literature for around 10 years [268, 269]. An early example is a study conducted by Zhu et al. (2016) where an extrusion-based 3D-printing method was used to print a graphene-composite aerogel electrode with a periodic macroporous structure [270]. Two of these identical printed electrodes were configured into a sandwich-type symmetric supercapacitor device with gel electrolyte, which achieved a maximum specific capacitance of 4.76 F/g at a current density of 0.4 A/g. Despite the relatively thick printed electrodes (~1,000 μm each), this 3D-printed supercapacitor device achieved an exceptional rate capability (87% capacitive retention from 2 A/g to 10 A/g), outperforming most of the carbon-based symmetric supercapacitors with far thinner electrodes

reported at the time [271, 272]. Generally, ion diffusion becomes increasingly difficult with thicker electrodes, causing the rate capability and other performance metrics to suffer [273]. The ordered macroporous electrode structure (easily achievable through 3D-printing) improved the infiltration of gel electrolyte into the electrode structure and facilitated easier ion diffusion through the thick electrodes, enabling the device to achieve such an exceptional rate performance.

A report by Liu et al. (2016) showed the use of 3D metal printing (metal laser sintering) to create a stainless-steel current collector with controlled porosity to be coated in electroactive materials [274]. These printed current collectors possessed high mechanical strength and porosity. When coated in MnO_2-PEDOT:PSS electroactive material and made into a pseudo-capacitor, the device showed lower resistance and longer cycle life than the non-porous stainless-steel current collector counterparts. A thinner layer of active materials is formed over a larger surface area, improving the ion-accessible surface area and electronic conductivity. The confinement of electroactive material within the pores also prevents electrode delamination from the current collector, and reduces the strain caused by ion absorption/desorption volume expansion. Reports from the following years have detailed complex architectures for supercapacitor devices achievable through 3D-printing: selective laser melting (SLM)-printed helical-shaped stainless-steel electrode platforms [275], SLA-printed micro-architected graphene aerogels [276], extrusion-printed freestanding MXene architectures [277], and SLA-printed octet-truss polymeric lattices [278] and cellular matrices [279] are but a few examples.

With the advent of wearable electronics [280] and the advancing and expanding field of microelectronics and the Internet of Things (IoT) [281], 3D-printed micro and flexible supercapacitors are increasingly being investigated and implemented as energy storage for such systems. With these wearable applications, however, the 3D-printed supercapacitor devices

will not only have to have good electrochemical performances, but also withstand a variety of physical strains and harsh conditions (e.g. bending, stretching, tensile strain, exposure to water and heat due to weather and/or washing, etc.). In a study by Jost et al. (2013) a Shima Seiki automated knitting machine (described as "like 3D printers for garments") was used to create woven carbon fibre electrode current collectors that were subsequently loaded with carbon fibre-matte medium active materials and formed into a flexible supercapacitor device separated by a solid polymer electrolyte [282]. The device was reported to have achieved the highest areal capacitance for an all-carbon textile supercapacitor at that time (0.5 F/cm^2). Though not strictly using a 3D-printer, many details of this study would set the precedent for future studies on 3D-printed flexible wearable supercapacitors.

One such study conducted by Arier et al. (2017) used paste deposition 3D-printing to manufacture an entire flexible supercapacitor device designed to be bendable and worn around the wrist [283]. Each component of the device (casing, current collector, electrode, and gel electrolyte) consisted of a different paste material which was extruded by a 3D-printer (Ultimaker®), with the pastes being manually swapped when the next component was to be printed. The printed supercapacitor device achieved good flexibility, retaining 54-58% of its capacity when bent into a loop with a radius as small as 15 mm. When cycled at a scan rate of 80 mV/s, the device retained only 56% of its capacitance after 500 cycles.

Yang et al. (2021) also used extrusion-based 3D-printing to manufacture flexible and wearable supercapacitor devices [284]. Making use of the complex patterns achievable by 3D-printing, highly deformable, bendable, and stretchable polymer (PEDOT:PSS) electrodes with various Negative Poisson's Ratio (NPR) structures were printed. NPR (or auxetic) materials are those that stretch perpendicularly to applied stress, while conventional materials tend to contract perpendicularly to stress [285]. The printed polymer electrodes maintained their structural integrity when bent to 180º or stretched to 150% their normal length, showing

excellent mechanical properties for wearable electronics. The quasi-solid symmetric supercapacitor device assembled from these NPR electrodes and the addition of CNTs achieves high areal capacitance values of 730 mF/cm^2 at 1 mA/cm^2 and 535 mF/cm^2 at 20 mA/cm^2 and a very good cycle life stability, maintaining 74.7% of its initial capacitance after 14,000 charge-discharge cycles. The supercapacitor device also retains 93% and 97% of its capacitance when bent at 180 º and twisted, respectively, and shows negligible changes in its capacitance when stretched with strains of up to 30%.

A very recent study by Ovhal et al. used DIW to manufacture an all-3D-printed supercapacitor fibre 100 cm in length [286]. The electrodes (MXene-PEDOT:PSS), current collector (Ag), gel electrolyte (PVA/H_3PO_4), and encapsulant (NOA 63) were all made into separate paste materials and extruded along a long, narrow dialysis membrane (serving as a separator) in a particular order. The fibrous Ag current collector embedded along the length of the supercapacitor helped eliminate performance trade-offs often seen for long, fibre-shaped supercapacitors, and enabled this 100 cm 3D-printed fibrous supercapacitor device to achieve an areal capacitance of 1.062 F/cm^2, a gravimetric capacitance of 185.9 F/g, outperforming other reported fibre-shaped supercapacitors of a similar electrode thickness and lengths. The device also showed excellent cycling stability, retaining 92% of its initial capacitance after 25,000 charge-discharge cycles. The printed device also showed remarkable stability when placed in harsh conditions, retaining similar GDC profiles when bent to a radius of 4 mm, twisted around five-fold, under a tensile strain of 1 kg, and even when submerged in water.

Though a relatively new field of study, the examples presented here should give an outline as to how far 3D-printed flexible, wearable supercapacitor technologies have advanced in the last decade, and how they are emerging as a solution for powering the next-generation of wearable electronics in healthcare, sport, communication, and other applications [287–290].

Though a much more pressing concern for lithium ion-battery research (due to the relative scarcity of the raw materials and toxicity of many battery electrolytes), environmental and sustainability issues must also be addressed when it comes to 3D-printed supercapacitor devices. A recent publication by Idrees et al. (2020) details the first ever reported 3D-printed supercapacitor derived from waste materials [291]. The active material, derived from BRAN FOAM TOP-911 loose fill packaging waste, was processed into activated carbon, and mixed with PVA/H_3PO_4 electrolyte solution (~35wt% activated carbon) to form an extrudable ink active material. Both the active materials and gel electrolyte (PVA/H_3PO_4) were printed using a ©Hyrel3d 30M extrusion-based printer to form a symmetric supercapacitor device. The device achieved a capacitance of 328.95 mF/cm^2 at 2.5 mA, reported at the time as the highest amongst all solid-state supercapacitors made using extrusion-based 3D-printing.

Similarly, Aeby et al. (2021) reported a fully-3D-printed and disposable paper supercapacitor device, made of functional inks derived entirely from recyclable and non-toxic materials [292]. The current collectors (graphite, carbon black, shellac [293]), electrodes (activated carbon, nanocellulose, graphite), and electrolyte (nanocellulose, glycerol, and NaCl) were all formed into inks for DIW 3D-printing. The fully-3D-printed symmetric supercapacitor achieves a specific capacitance of 25.6 F/g at a scan rate of 1 mV/s, which, according to the study, is ten times the specific capacitance reported for any other fully printed supercapacitor device. For long-term cycling stability, the device shows less than 1% variation in capacitance over 2,000 charge-discharge cycles at 0.4 A/g. When disposed of, the device can be processed as a non-cytotoxic compostable material, losing 50% of its mass over 9 weeks. The carbon components are left behind, which can easily be collected and recycled. Even the residual waste materials left behind from 3D-printing processes themselves are intelligently used. Silva-Neto et al. (2023) recently published a report detailing a strategy to recycle residual ABS material

from FDM 3D-printing, combining the waste material with graphite flakes to form a conductive paste to be used in electrochemical sensors [294].

A huge challenge that remains for 3D-printed supercapacitor research is the ability to print all components of the device in one seamless operation [295]. In most reports on 3D-printed supercapacitor devices (including the ones in this thesis), only some components of the device is 3D-printed and/or the printed components require extensive post-processing after printing [269, 270, 296–300]. Some of the studies discussed already reported 3D-printed supercapacitors consisting entirely of 3D-printed components [283, 292, 301, 302], however, the procedures still required a certain level of processing, such as manually changing the printable inks in the 3D-printer or manually assembling the all-printed components into the final supercapacitor device. 3D-printing an entire supercapacitor device in one procedure is immensely complicated. This requires thorough understanding and intimate knowledge of the vastly different materials that will form the individual components of the supercapacitor device and the interfaces between the different materials. The materials must be compatible not just with one another, but with the 3D-printing device, settings, and environment to which they will be subjected. The 3D-printing device itself (and the printing software) must also be highly advanced, capable of accurately printing several materials with potentially different physical and chemical properties simultaneously.

These requirements were achieved by Fieber et al. (2019) who reported a novel, single-operation process to manufacture fully-3D-printed supercapacitors using a custom-made hybrid, multi-phase 3D-printer setup, fitted with two Fused Filament Fabrication and three DIW modules [303]. With this elaborate setup, up to nine different components of the device were printed in a completely automated manner, without any processing or assembly from the researchers. The fully sealed, ring-shaped supercapacitor was printed in under 30 minutes, and was immediately able to achieve an areal capacitance of ~600 mF/cm^2 at 10 mV/s. Though a

remarkable achievement, the complexity and intricacy of the custom 3D-printing setup is beyond the scope of most supercapacitor research. Further advancements in multi-material 3D-printers could make this idea more approachable and achievable in the next few years.

To conclude, it's clear that in the space of only a decade the 3D-printing of supercapacitor devices has rapidly advanced. Attracted by the potential for complex architectures, geometric freedom to explore new form-factors, ease of prototyping, reduction in part-specific tooling requirements, and the elimination of waste materials, 3D-printing methods are increasingly being used in recent years for the manufacturing of supercapacitor devices. Investigations have successfully printed supercapacitors to fulfill a wide variety of roles, including flexible, fibrous, and wearable devices, with an ever-increasing consideration for sustainable, waste-derived, and recyclable materials.

1.7 References

[1] H. Yoo, E. Markevich, G. Salitra, D. Sharon and D. Aurbach, "On the challenge of developing advanced technologies for electrochemical energy storage and conversion," *Materials Today,* vol. 17, no. 3, pp. 110-121, 2014.

[2] R. Dell and D. Rand, "Chapter 1 Energy Storage in Batteries," in *Understanding Batteries*, Cambridge, The Royal Society of Chemistry, 2001, pp. 1-5.

[3] H. Jafari and M. Rahimpour, "2 Pb Acid Batteries," in *Rechargeable Batteries: History, Progress, and Applications*, Hoboken, New Jersey, John Wiley and Sons, Inc., 2020, pp. 17-40.

[4] A. Yoshino, "The Birth of the Lithium-Ion Battery," *Angewandte Chemie,* vol. 51, no. 24, pp. 5798-5900, 2012.

[5] B. Scrosati, "History of lithium batteries," *Journal of Solid State Electrochemistry,* vol. 15, pp. 1623-1630, 2011.

[6] Y. Nishi, "The development of lithium ion secondary batteries," *The Chemical Record,* vol. 1, no. 5, pp. 406-413, 2001.

[7] G. Crabtree, E. Kócs and L. Trahey, "The energy-storage frontier: Lithium-ion batteries and beyond," *MRS Bulletin,* vol. 40, no. 12, pp. 1067-1078, 2015.

[8] N. Kularatna and K. Gunawardane, "Rechargeable battery technologies: An electronic circuit designer's viewpoint," in *Energy Storage Devices for Renewable Energy-Based Systems: Rechargeable Batteries and Supercapacitors Second Edition*, Academic Press, 2021, pp. 65-98.

[9] A. Manthiram, "An Outlook on Lithium Ion Battery Technology," *ACS Central Science,* vol. 3, no. 10, pp. 1063-1069, 2017.

[10] K. Xu, "Electrolytes and Interphases in Li-Ion Batteries and Beyond," *Chemical Reviews,* vol. 114, no. 23, pp. 11503-11618, 2014.

[11] M. Lagadec, R. Zahn and V. Wood, "Characterization and performance evaluation of lithium-ion battery separators," *Nature Energy,* vol. 4, pp. 16-25, 2019.

[12] P. Zhu, D. Gastol, J. Marshall, R. Sommerville, V. Goodship and E. Kendrick, "A review of current collectors for lithium-ion batteries," *Journal of Power Sources,* vol. 485, p. 229321, 2021.

[13] D. Deng, "Li-ion batteries: basics, progress, and challenges," *Energy Science and Engineering,* vol. 3, no. 5, pp. 385-418, 2015.

[14] A. Ferrese, "Battery Fundamentals," *GetMobile: Mobile Computing and Communications,* vol. 19, no. 3, pp. 29-32, 2015.

[15] L. C. P. Kushwaha and A. Gaikwad, "Review: Li-ion Batteries: Basics, Advancement, Challenges and Applications in Military," *International Journal for Research in Applied Science & Engineering Technology (IJRASET),* vol. 9, no. 8, 2021.

[16] A.-I. Stan, M. Świerczyński, D.-I. Stroe, R. Teodorescu and S. Andreasen, "Lithium ion battery chemistries from renewable energy storage to automotive and back-up power applications — An overview," in *2014 International Conference on Optimization of Electrical and Electronic Equipment (OPTIM)*, Bran, Romania, 2014.

[17] K. Divya and Ø. J, "Battery energy storage technology for power systems—An overview," *Electric Power Systems Research,* vol. 79, no. 4, pp. 511-520, 2009.

[18] A. Dehghani-Sanij, E. Tharumalingam, M. Dusseault and R. Fraser, "Study of energy storage systems and environmental challenges of batteries," *Renewable and Sustainable Energy Reviews,* vol. 104, pp. 192-208, 2019.

[19] C. Zhang, Y.-L. Wei, P.-F. Cao and M.-C. Lin, "Energy storage system: Current studies on batteries and power condition system," *Renewable and Sustainable Energy Reviews,* vol. 82, no. 3, pp. 3091-3106, 2018.

[20] A. Olabi, T. Wilberforce, E. Sayed, A. Abo-Khalil, H. Maghrabie, K. Elsaid and M. Abdelkareem, "Battery energy storage systems and SWOT (strengths, weakness, opportunities, and threats) analysis of batteries in power transmission," *Energy,* vol. 254, no. A, p. 123987, 2022.

[21] J. Edge, S. O'Kane, R. Prosser, N. Kirkaldy, A. Patel, A. Hales, A. Ghosh, W. Ai, J. Chen, J. Yang, S. Li, M.-C. Pang, L. Diaz, A. Tomaszewska, M. Marzook, K. Radhakrishnan, H. Wang, Y. Patel, B. Wu and G. Offer, "Lithium ion battery degradation: what you need to know," *Physical Chemistry Chemical Physics,* vol. 23, pp. 8200-8221, 2021.

[22] D. Aurbach, B. Markovsky, A. Rodkin, M. Cojocaru, E. Levi and H.-J. Kim, "An analysis of rechargeable lithium-ion batteries after prolonged cycling," *Electrochimica Acta,* vol. 47, no. 12, pp. 1899-1911, 2002.

[23] H. Zhao, J. Li, Q. Zhao, X. Huang, S. Jia, J. Ma and Y. Ren, "Si-Based Anodes: Advances and Challenges in Li-Ion Batteries for Enhanced Stability," *Electrochemical Energy Reviews,* vol. 7, no. 11, 2024.

[24] K. M. P. J. W. John Bannister Goodenough, "Electrochemical cell and method of making ion conductors for said cell". UK Patent EP0017400B1, 5th April 1979.

[25] P. Bruce, "Solid-state chemistry of lithium power sources," *Chemical Communications,* no. 19, pp. 1817-1824, 1997.

[26] K. Mizushima, P. Jones, P. Wiseman and J. Goodenough, "LixCoO2 (0<x<-1): A new cathode material for batteries of high energy density," *Materials Research Bulletin,* vol. 15, no. 6, pp. 783-789, 1980.

[27] M. Reddy, A. Mauger, C. Julien, A. Paolella and K. Zaghib, "Brief History of Early Lithium-Battery Development," *Materials,* vol. 13, no. 8, p. 1884, 2020.

[28] T. Kim, W. Song, D. Son, L. Ono and Y. Qi, "Lithium-ion batteries: outlook on present, future, and hybridized technologies," *Journal of Materials Chemistry A,* no. 7, pp. 2942-2964, 2019.

[29] G. Blomgren, "The Development and Future of Lithium Ion Batteries," *Journal of the Electrochemical Society,* vol. 164, no. 1, p. A5019, 2016.

[30] U. Gulzar, S. Goriparti, E. Miele, T. Li, G. Maidecchi, A. Toma, F. De Angelis, C. Capaglia and R. Zaccaria, "Next-generation textiles: from embedded supercapacitors to lithium ion batteries," *Journal of Materials Chemistry A,* vol. 4, no. 43, pp. 16771-16800, 2016.

[31] Y. Kado, Y. Soneda, H. Hatori and M. Kodama, "Advanced carbon electrode for electrochemical capacitors," *Journal of Solid State Electrochemistry,* vol. 23, pp. 1061-1081, 2019.

[32] T. Wulandari, D. Fawcett, S. Majumder and G. Poinern, "Lithium-based batteries, history, current status, challenges, and future perspectives," *Battery Energy,* vol. 2, no. 6, p. 20230030, 2023.

[33] M. Hossain, M. Chowdhury, N. Hossain, M. Islam and M. Mobarak, "Advances of lithium-ion batteries anode materials—A review," *Chemical Engineering Journal Advances,* vol. 16, p. 100569, 2023.

[34] P. Nzereogu, A. Omah, F. Ezema, E. Iwuoha and A. Nwanya, "Anode materials for lithium-ion batteries: A review," *Applied Surface Science Advances,* vol. 9, p. 100233, 2022.

[35] Anonymous, "Economy and Energy Shortages Impact Metal Prices," *Engineering and Mining Journal,* vol. 223, no. 9, p. 64, 2022.

[36] B. Liu, Q. Zhang, J. Liu, Y. Hao, Y. Tang and Y. Li, "The impacts of critical metal shortage on China's electric vehicle industry development and countermeasure policies," *Energy,* vol. 248, p. 123646, 2022.

[37] B. Lee, E. Paek, D. Miltin and S. Lee, "Sodium Metal Anodes: Emerging Solutions to Dendrite Growth," *Chemical Reviews,* vol. 119, no. 8, pp. 5416-5460, 2019.

[38] R. Rajagopalan, Y. Tang, X. Ji, C. Jia and H. Wang, "Advancements and Challenges in Potassium Ion Batteries: A Comprehensive Review," *Advanced Functional Materials,* vol. 30, no. 12, p. 1909486, 2020.

[39] N. Chodankar, H. Pham, A. Nanjundan, J. Fernando, K. Jayaramulu, D. Golberg, Y. Han and D. Dubal, "True Meaning of Pseudocapacitors and Their Performance Metrics: Asymmetric versus Hybrid Supercapacitors," *Small,* vol. 16, no. 37, p. 2002806, 2020.

[40] H. Helmholtz, "Ueber einige Gesetze der Vertheilung elektrischer Ströme in körperlichen Leitern, mit Anwendung auf die thierisch-elektrischen Versuche (Schluss.)," *Annalen der Physik,* vol. 165, no. 7, pp. 353-377, 1853.

[41] H. Becker, "Low Voltage Electrolytic Capacitor". United States of America Patent US2800616A, 1957.

[42] D. Dubal and Y. H. R. Wu, "Supercapacitors: from the Leyden jar to electric busses," *ChemTexts 2,* vol. 13, 2016.

[43] E. Dănilă and D. Lucache, "History of the First Energy Storage Systems," in *3rd International Symposium on the History of Electrical Engineering and of Tertiary-Level Engineering Education*, Iaşi, Romania, 2010.

[44] A. Dutta, S. Mitra, M. Basak and T. Banerjee, "A comprehensive review on batteries and supercapacitors: Development and challenges since their inception," *Energy Storage,* vol. 5, no. 1, p. e339, 2023.

[45] J. Sun, B. Luo and H. Li, "A Review on the Conventional Capacitors, Supercapacitors, and Emerging Hybrid Ion Capacitors: Past, Present, and Future," *Advanced Energy and Sustainability Research,* vol. 3, no. 6, p. 2100191, 2022.

[46] S. Yoon, J. Lee, T. Hyeon and S. Oh, "Electric Double-Layer Capacitor Performance of a New Mesoporous Carbon," *Journal of the Electrochemical Society,* vol. 147, no. 7, pp. 2507-2512, 2000.

[47] M. Endo, T. Takeda, Y. Kim, K. Koshiba and K. Ishii, "High Power Electric Double Layer Capacitor (EDLC's); from Operating Principle to Pore Size Control in Advanced Activated Carbons," *Carbon Science,* vol. 1, no. 3 and 4, pp. 117-128, 2001.

[48] J. Wu, "Understanding the Electric Double-Layer Structure, Capacitance, and Charging Dynamics," *Chemical Reviews,* vol. 122, no. 12, pp. 10821-10859, 2022.

[49] P. Sharma and T. Bhatti, "A review on electrochemical double-layer capacitors," *Energy Conversion and Management,* vol. 51, no. 12, pp. 2901-2912, 2010.

[50] V. Obreja, "On the performance of supercapacitors with electrodes based on carbon nanotubes and carbon activated material—A review," *Physica E: Low-dimensional Systems and Nanostructures,* vol. 40, no. 7, pp. 2596-2605, 2008.

[51] D. Murray and J. Hayes, "Cycle Testing of Supercapacitors for Long-Life Robust Applications," *IEEE Transactions on Power Electronics,* vol. 30, no. 5, pp. 2505-2516, 2015.

[52] Z. Qiu, Y. Wang, X. Bi, T. Zhou, J. Zhou, J. Zhao, Z. Miao, W. Yi, P. Fu and S. Zhuo, "Biochar-based carbons with hierarchical micro-meso-macro porosity for high rate and long cycle life supercapacitors," *Journal of Power Sources,* vol. 376, pp. 82-90, 2018.

[53] S. Zhang and N. Pan, "Supercapacitor Performance Evaluation," *Advanced Energy Materials,* vol. 5, no. 6, p. 1401401, 2015.

[54] M. Uno and K. Takana, "Accelerated Charge–Discharge Cycling Test and Cycle Life Prediction Model for Supercapacitors in Alternative Battery Applications," *IEEE Transactions on Industrial Electronics,* vol. 59, no. 12, pp. 4704-4712, 2012.

[55] A. Pandolfo and A. Hollenkamp, "Carbon properties and their role in supercapacitors," *Journal of Power Sources,* vol. 157, no. 1, pp. 11-27, 2006.

[56] V. Ganesh, S. Pitchumani and V. Lakshminarayanan, "New symmetric and asymmetric supercapacitors based on high surface area porous nickel and activated carbon," *Journal of Power Sources,* vol. 158, no. 2, pp. 1523-1532, 2006.

[57] Z.-F. Li, H. Zhang, Q. Liu, L. Sun, L. Stanciu and J. Xie, "Fabrication of High-Surface-Area Graphene/Polyaniline Nanocomposites and Their Application in Supercapacitors," *ACS Applied Materials and Interfaces,* vol. 5, no. 7, pp. 2685-2691, 2013.

[58] Y. Lu, S. Zhang, J. Yin, C. Bai, J. Zhang, Y. Li, Y. Yang, Z. Ge, M. Zhang, L. Wei, M. Ma, Y. Ma and Y. Chen, "Mesoporous activated carbon materials with ultrahigh mesopore volume and effective specific surface area for high performance supercapacitors," *Carbon,* vol. 124, pp. 64-71, 2017.

[59] M. Karnan, K. Subramani, N. Sudhan, N. Ilayaraja and M. Sathish, "Aloe vera Derived Activated High-Surface-Area Carbon for Flexible and High-Energy Supercapacitors," *ACS Applied Materials and Interfaces,* vol. 8, no. 51, pp. 35191-35202, 2016.

[60] R. Saliger, U. Fischer, C. Herta and J. Frickle, "High surface area carbon aerogels for supercapacitors," *Journal of Non-Crystalline Solids,* vol. 225, pp. 81-85, 1998.

[61] K. Anneser, J. Reichstein, S. Braxmeier and G. Reichenauer, "Carbon xerogel based electric double layer capacitors with polymer gel electrolytes - Improving the performance by adjusting the type of electrolyte and its processing," *Electrochimica Acta,* vol. 278, pp. 196-203, 2018.

[62] B. Pal, S. Yang, S. Ramesh, V. Thangadurai and R. Jose, "Electrolyte selection for supercapacitive devices: a critical review," *Nanoscale Advances,* vol. 1, no. 10, pp. 3807-3835, 2019.

[63] J. Gittins, K. Ge, C. Balhatchet, P.-L. Taberna, P. Simon and A. Forse, "Understanding Electrolyte Ion Size Effects on the Performance of Conducting Metal–Organic Framework Supercapacitors," *Journal of the American Chemical Society,* vol. 146, no. 18, pp. 12473-12484, 2024.

[64] K. Liu, C. Yu, W. Guo, L. Ni, J. Yu, Y. Xie, Z. Wang, Y. Ren and J. Qiu, "Recent research advances of self-discharge in supercapacitors: Mechanisms and suppressing strategies," *Journal of Energy Chemistry,* vol. 58, pp. 94-109, 2021.

[65] A. Jagadale, R. Rohit, S. Shinde and D.-Y. Kim, "Review—Mitigating Supercapacitor Self-Discharge Through Strategic Materials Modification," *Journal of the Electrochemical Society,* vol. 168, no. 9, p. 090562, 2021.

[66] D. Grahame, "Properties of the Electrical Double Layer at a Mercury Surface. I. Methods of Measurement and Interpretation of Results.," *Journal of the American Chemical Society,* vol. 63, pp. 1207-1215, 1941.

[67] P. Bhojane, "Recent advances and fundamentals of Pseudocapacitors: Materials, mechanism, and its understanding," *Journal of Energy Storage,* vol. 45, p. 103654, 2022.

[68] P. Simon, Y. Gogotsi and B. Dunn, "Where Do Batteries End and Supercapacitors Begin?," *Science,* vol. 343, pp. 1210-1211, 2014.

[69] Y. Liu, S. Jiang and Z. Shao, "Intercalation pseudocapacitance in electrochemical energy storage: recent advances in fundamental understanding and materials development," *Materials Today Advances,* vol. 7, p. 100072, 2020.

[70] S. Mahala, K. Khosravinia and A. Kiani, "Unwanted degradation in pseudocapacitors: Challenges and opportunities," *Journal of Energy Storage,* vol. 67, p. 107558, 2023.

[71] X. Zhu, "Recent advances of transition metal oxides and chalcogenides in pseudo-capacitors and hybrid capacitors: A review of structures, synthetic strategies, and mechanism studies," *Journal of Energy Storage,* vol. 49, p. 104148, 2022.

[72] A. Muzaffar, M. Ahamed, K. Deshmukh and J. Thirumalai, "A review on recent advances in hybrid supercapacitors: Design, fabrication and applications," *Renewable and Sustainable Energy Reviews,* vol. 101, pp. 123-145, 2019.

[73] D. Chatterjee and A. Nandi, "A review on the recent advances in hybrid supercapacitors," *Journal of Materials Chemistry A,* vol. 9, no. 29, pp. 15880-15918, 2021.

[74] A. Afif, S. Rahman, A. Azad, J. Zaini, M. Islan and A. Azad, "Advanced materials and technologies for hybrid supercapacitors for energy storage – A review," *Journal of Energy Storage,* vol. 25, p. 100852, 2019.

[75] M. Şahin and F. Blaabjerg, "A hybrid PV battery/supercapacitor system and a basic active power control proposal in MATLAB/Simulink," *Electronics,* vol. 9, no. 129, 2020.

[76] S. Liu, L. Wei and H. Wang, "Review on the reliability of supercapacitors in energy storage applications.," *Applied Energy,* vol. 278, p. 115436, 2020.

[77] H. Zhang, F. Zhang, L. Yang, Y. Gao and B. Jin, "Multi-Parameter Collaborative Power Prediction to Improve the Efficiency of Supercapacitor-Based Regenerative Braking System," *IEEE Transactions on Energy Conversion,* vol. 36, no. 4, pp. 2612-2622, 2021.

[78] Z. Zou, J. Cao, B. Cao and W. Chen, "Evaluation strategy of regenerative braking energy for supercapacitor vehicle," *ISA Transactions,* vol. 55, pp. 234-240, 2015.

[79] F. Naseri, E. Farjah and T. Ghanbari, "An Efficient Regenerative Braking System Based on Battery/Supercapacitor for Electric, Hybrid, and Plug-In Hybrid Electric Vehicles With BLDC Motor," *IEEE Transactions on Vehicular Technology,* vol. 66, no. 5, pp. 3724-3738, 2017.

[80] J. Miller and A. Burke, "Electrochemical Capacitors: Challenges and Opportunities for Real-World Applications," *Interface,* vol. 17, pp. 53-57, 2008.

[81] T. Sumangala, M. Sreekanth and A. Rahaman, "Applications of Supercapacitors," in *Handbook of Nanocomposite Supercapacitor Materials III. Springer Series in Materials Science*, Springer, 2021, pp. 367-393.

[82] B. Espinar and D. Mayer, "Photovoltaic Power Systems Program, The Role of Energy Storage for Mini-Grid Stabilisation," IEA PVPS Task 11; International Energy Agency, Armines, France, 2011.

[83] *Stanley Electric and Tamura Announce the Development of "Super CaLeCS," an Environment-Friendly EDLC-Powered LED Street Lamp,* Tokyo, Japan: Nippon Chemi-Con Corp., 2010.

[84] "Supercapacitors to be tested on Paris STEEM tram," *Railway Gazette International,* 08 July 2009.

[85] "Rhein-Neckar Verkehr orders more supercapacitor trams," *Railway Gazette International,* 05 April 2011.

[86] V. Herrera, H. Gaztañaga, A. Milo, A. Saez-de-Ibarra, I. Exteberria-Otadui and T. Nieva, "Optimal Energy Management and Sizing of a Battery--Supercapacitor-Based Light Rail Vehicle With a Multiobjective Approach," *IEEE Transactions on Industry Applications,* vol. 52, no. 4, pp. 3367-3377, 2016.

[87] M. Benziger, V. Dasireddy, X. Guan and G. Liu, "Advances on Emerging Materials for Flexible Supercapacitors: Current Trends and Beyond," *Advanced Functional Materials,* vol. 30, no. 40, p. 2002993, 2020.

[88] X. Chen, N. Villa, Y. Zhuang, L. Chen, T. Wang, Z. Li and T. Kong, "Stretchable Supercapacitors as Emergent Energy Storage Units for Health Monitoring Bioelectronics," *Advanced Energy Materials,* vol. 10, no. 4, p. 1902769, 2020.

[89] F. Bu, W. Zhou, Y. Xu, Y. Du, C. Guan and W. Huang, "Recent developments of advanced micro-supercapacitors: design, fabrication and applications," *npj Flexible Electronics,* vol. 4, no. 31, 2020.

[90] S. Wang, J. Ma, X. Shi and Y. Zhu, "Recent status and future perspectives of ultracompact and customizable micro-supercapacitors," *Nano Research Energy,* vol. 1, 9120018.

[91] S. He, Y. Hu, J. Wan, Q. Gao, Y. Wang, S. Xie, L. Qiu, C. Wang, G. Zheng, B. Wang and H. Peng, "Biocompatible carbon nanotube fibers for implantable supercapacitors," *Carbon,* vol. 122, pp. 162-167, 2017.

[92] Y. Su, L. Wang, R. Lin, Y. Zheng, G. Rong and M. Sawan, "Stretchable Transparent Supercapacitors for Wearable and Implantable Medical Devices," *Advanced Materials Technologies,* vol. 7, no. 1, p. 2100608, 2022.

[93] C. Meng, O. Gall and P. Irazoqui, "A flexible super-capacitive solid-state power supply for miniature implantable medical devices," *Biomedical Microdevices,* vol. 15, pp. 973-983, 2013.

[94] H. Sim, C. Choi, D. Lee, H. Kim, J.-H. Yun, J. Kim, T. Kang, R. Ovalle, R. Baughman, C. Kee and S. Kim, "Biomolecule based fiber supercapacitor for implantable device," *Nano Energy,* vol. 47, pp. 385-392, 2018.

[95] N. Chodankar, C. Padwal, H. Pham, K. Ostrikov, S. Jadhav, K. Mahale, P. Yarlagadda, Y. Huh, Y.-K. Han and D. Dubal, "Piezo-supercapacitors: A new paradigm of self-powered wellbeing and biomedical devices," *Nano Energy,* vol. 90, no. A, p. 106607, 2021.

[96] S. Mondal, S. Thakur, S. Maiti, S. Bhattacharjee and K. Chattopadhyay, "Self-Charging Piezo-Supercapacitor: One-Step Mechanical Energy Conversion and Storage," *ACS Applied Materials and Interfaces,* vol. 15, no. 6, pp. 8446-8461, 2023.

[97] B. Singh, P. Padha, S. Verma, S. Satapathi, V. Gupta and S. Arya, "Recent advances, challenges, and prospects of piezoelectric materials for self-charging supercapacitor," *Journal of Energy Storage,* vol. 47, p. 103547, 2022.

[98] M. Şahin, F. Blaabjerg and A. Sangwongwanich, "A Comprehensive Review on Supercapacitor Applications and Developments," *Energies,* vol. 15, no. 3, p. 674, 2022.

[99] J. De, J. Halder, C. Gowda, S. Kansal, S. Priya, S. Anshu, A. Chowdhury, D. Mandal, S. Biswas, B. Dubey and A. Chandra, "Role of porosity and diffusion coefficient in porous electrode used in supercapacitors – Correlating theoretical and experimental studies," *Eelctrochemical Science Advances,* vol. 3, no. 1, p. e2100159, 2023.

[100] A. Vu, Y. Qian and A. Stein, "Porous Electrode Materials for Lithium-Ion Batteries – How to Prepare Them and What Makes Them Special," *Advanced Energy Materials,* vol. 2, no. 9, pp. 1056-1085, 2012.

[101] L. Borchardt, M. Oschatz and S. Kaskel, "Tailoring porosity in carbon materials for supercapacitor applications," *Materials Horizons,* vol. 1, pp. 157-168, 2014.

[102] A. Li, Z. Li, D. Xu, G. Feng and R. Hu, "Porosity and tortuosity: Keys for accurate modeling of porous electrodes in supercapacitors," *Materials Today Physics,* vol. 36, p. 101174, 2023.

[103] K. Sing, D. Everett, R. Haul, L. Moscou, R. Pierotti and J. Rouquerol, "Reporting Physisorption Data for Gas/Solid Systems with Special Reference to the Determination of Surface Area and Porosity," *Pure and Applied Chemistry,* vol. 57, no. 4, pp. 603-619, 1985.

[104] Z. Zhai, L. Zhang, T. Du, B. Ren, Y. Xu, S. Wang, J. Miao and Z. Liu, "A review of carbon materials for supercapacitors," *Materials and Design,* vol. 221, p. 111017, 2022.

[105] C. Yuan, H. Xu, S. El-khodary, G. Ni, S. Esakkimuthu, S. Zhong and S. Wang, "Recent advances and challenges in biomass-derived carbon materials for supercapacitors: A review," *Fuel,* vol. 362, p. 130795, 2024.

[106] Y. Wang, T. Xu, K. Liu, M. Zhang, X.-M. Cai and C. Si, "Biomass-based materials for advanced supercapacitor: principles, progress, and perspectives," *Aggregate Open Access,* vol. 5, no. 1, p. e428, 2024.

[107] R. Kosheleva, A. Mitropoulos and G. Kyzas, "Synthesis of activated carbon from food waste," *Environmental Chemistry Letters,* vol. 17, pp. 429-438, 2019.

[108] B. Thomas and S. George, "Production of Activated Carbons from Natural Sources," *Trends in Green Chemistry,* vol. 1, no. 1:7, 2015.

[109] H. Marsh and F. Rodríguez Reinoso, Activated Carbons, Elsevier, 2006.

[110] R. Medhi, S. Naqvi, A. Khoja and R. Hussain, "Biomass derived activated carbon by chemical surface modification as a source of clean energy for supercapacitor application," *Fuel,* vol. 348, p. 128529, 2023.

[111] S. Tong-Xin, Z. Yue-Mei and J. Xiao-Juan, "Preparation of Disused Composite Panels-Based Activated Carbon by Microwave Induced Activation for High Performance of Electric Double-Layer Capacitors: Microwave Power Effects," *Science of Advanced Materials,* vol. 8, no. 5, pp. 1101-1107, 2016.

[112] P. Simon and A. Burke, "Nanostructured carbons: double-layer capacitance and More," *The Electrochemical Society Interface,* vol. 17, no. 1, pp. 38-44, 2008.

[113] N. Boulanger, A. Talyzin, S. Xiong, M. Hultberg and Grimm, "High surface area activated carbon prepared from wood-based spent mushroom substrate for supercapacitors and water treatment," *Colloids and Surfaces A: Physiochemical and Engineering Aspects,* vol. 680, p. 132684, 2024.

[114] J. Baptista, J. Sagu, U. KG and K. Lobato, "State-of-the-art materials for high power and high energy supercapacitors: Performance metrics and obstacles for the transition from lab to industrial scale – A critical approach," *Chemical Engineering Journal,* vol. 374, pp. 1153-1179, 2019.

[115] Y. Jiang, J. li, Z. Jiang, M. Shi, R. Sheng, Z. Liu, S. Zhang, Y. Cao, T. Wei and Z. Fan, "Large-surface-area activated carbon with high density by electrostatic densification for supercapacitor electrodes," *Carbon,* vol. 175, pp. 281-288, 2011.

[116] Y. Qing, Y. Jiang, H. Lin, L. Wang, A. Liu, Y. Cao, R. Sheng, Y. Guo, C. Fan, S. Zhang, D. Jia and Z. Fan, "Boosting the supercapacitor performance of activated carbon by constructing overall conductive networks using graphene quantum dots," *Journal of Materials Chemistry A,* vol. 7, no. 11, pp. 6021-6027, 2019.

[117] F. Cheng, X. Yang, S. Zhang and W. Lu, "Boosting the supercapacitor performances of activated carbon with carbon nanomaterials," *Journal of Power Sources,* vol. 450, p. 227678, 2020.

[118] S. Iijima, "Helical microtubules of graphitic carbon," *Nature,* vol. 354, pp. 56-58, 1991.

[119] Z. Zhen and H. Zhu, "Structure and Properties of Graphene," *Graphene,* pp. 1-12, 2018.

[120] J. Chen, S. Wei and H. Xie, "A Brief Introduction of Carbon Nanotubes: History, Synthesis, and Properties," *Journal of Physics: Conference Series,* vol. 1948, p. 012184, 2021.

[121] M. Zhang and J. Li, "Carbon nanotube in different shapes," *Materials Today,* vol. 12, no. 6, pp. 12-18, 2009.

[122] S. Iijima and T. Ichihashi, "Single-shell carbon nanotubes of 1-nm diameter," *Nature,* vol. 363, pp. 603-605, 1993.

[123] D. Bethune, C. Kiang, M. de Vries, G. Gorman, R. Savoy, J. Vazquez and R. Beyers, "Cobalt-catalysed growth of carbon nanotubes with single-atomic-layer walls," *Nature,* vol. 363, pp. 605-607, 1993.

[124] J. Chrzanowska, J. Hoffman, A. Małolepszy, M. Mazurkiewicz, T. Kowalewski, Z. Szymanski and L. Stobinski, "Synthesis of carbon nanotubes by the laser ablation method: Effect of laser wavelength," *Physica Status Solidi b,* vol. 252, no. 8, pp. 1860-1867, 2015.

[125] N. Arora and N. Sharma, "Arc discharge synthesis of carbon nanotubes: Comprehensive review," *Diamond and Related Materials,* vol. 50, pp. 135-150, 2014.

[126] Y. Chen and J. Zhang, "Chemical Vapor Deposition Growth of Single-Walled Carbon Nanotubes with Controlled Structures for Nanodevice Applications," *Accounts of Chemical Research,* vol. 47, no. 8, pp. 2273-2281, 2014.

[127] R. Hirlekar, M. Yamagar, H. Garse, M. Vij and V. Kadam, "Carbon Nanotubes and its Applications: A Review," *Asian Journal of Pharmaceutical and Clinical Research,* vol. 2, no. 4, pp. 17-27, 2009.

[128] B. Earp, D. Dunn, J. Phillips, R. Agrawal, T. Ansell, P. Aceves, I. De Rosa, W. Xin and C. Luhrs, "Enhancement of electrical conductivity of carbon nanotube sheets through copper addition using reduction expansion synthesis," *Materials Research Bulletin,* vol. 131, p. 110969, 2020.

[129] S. Demski, K. Dydek, K. Bartnicka, K. Majchrowicz, R. Kozera and A. Boczkowska, "Introduction of SWCNTs as a Method of Improvement of Electrical and Mechanical Properties of CFRPs Based on Thermoplastic Acrylic Resin," *Polymers (Basel),* vol. 15, no. 3, p. 506, 2023.

[130] N. Robertson and C. McGowan, "A comparison of potential molecular wires as components for molecular electronics," *Chemical Society Reviews,* vol. 32, no. 2, pp. 96-103, 2003.

[131] R. Thines, N. Mubarak, S. Nizamuddin, J. Sahu, E. Abdullah and P. Ganesan, "Application potential of carbon nanomaterials in water and wastewater treatment: A review," *Journal of the Taiwan Institute of Chemical Engineers,* vol. 72, pp. 116-133, 2017.

[132] C. Zheng, W. Qian, C. Cui, G. Xu, M. Zhao, G. Tian and F. Wei, "Carbon nanotubes for supercapacitors: Consideration of cost and chemical vapor deposition techniques," *Journal of Natural Gas Chemistry,* vol. 21, no. 3, pp. 233-240, 2012.

[133] A. Peigney, C. Laurent, E. Flahaut, R. Basca and A. Rousset, "Specific surface area of carbon nanotubes and bundles of carbon nanotubes," *Carbon,* vol. 39, no. 4, pp. 507-514, 2001.

[134] M. Birch, T. Ruda-Eberenz, M. Chai, R. Andrews and R. Hatfield, "Properties that Influence the Specific Surface Areas of Carbon Nanotubes and Nanofibers," *The Annals of Occupational Hygiene,* vol. 57, no. 9, pp. 1148-1166, 2013.

[135] Q. Cao, Q. Yu, D. Connell and G. Yu, "Titania/carbon nanotube composite (TiO2/CNT) and its application for removal of organic pollutants," *Clean Technologies and Environmental Policy,* vol. 15, pp. 871-880, 2013.

[136] X. Yuan, X. Zhang, L. Sun, Y. Wei and X. Wei, "Cellular Toxicity and Immunological Effects of Carbon-based Nanomaterials," *Particle and Fibre Toxicology,* vol. 16, no. 18, 2019.

[137] K. Novoselov, A. Geim, S. Morozov, M. Jiang, M. Katsnelson, I. Grigorieva, S. Dubonos and A. Firsov, "Two-dimensional gas of massless Dirac fermions in graphene," *Nature,* vol. 438, pp. 197-200, 2005.

[138] K. Bolotin, K. Sikes, Z. Jiang, M. Klima, G. Fudenberg, J. Hone, P. Kim and H. Stormer, "Ultrahigh electron mobility in suspended graphene," *Solid State Communications,* vol. 146, no. 9-10, pp. 351-355, 2008.

[139] M. Stoller, S. Park, Y. Zhu, J. An and R. Ruoff, "Graphene-Based Ultracapacitors," *Nano Letters,* vol. 8, no. 10, pp. 3498-3502, 2008.

[140] E. Siochi, "Graphene in the sky and beyond," *Nature Nanotechnology,* vol. 9, pp. 745-747, 2014.

[141] A. Geim and K. Novoselov, "The rise of graphene," *Nature Materials,* vol. 6, pp. 183-191, 2007.

[142] A. Urade, I. Lahiri and K. Suresh, "Graphene Properties, Synthesis and Applications: A Review," *The Journal of The Minerals, Metals & Materials Society,* vol. 75, pp. 614-630, 2023.

[143] P. Wick, A. Louw-Gaume, M. Kucki, H. Krug, K. Kostarelos, B. Fadeel, K. Dawson, A. Salvati, E. Vázquez, L. Ballerini and e. al., "Classification Framework for Graphene-Based Materials," *Angewandte Chemie International Edition,* vol. 53, no. 30, pp. 7714-7718, 2014.

[144] K. Yee and M. Ghayesh, "A review on the mechanics of graphene nanoplatelets reinforced structures," *International Journal of Engineering Science,* vol. 186, p. 103831, 2023.

[145] P. Cataldi, A. Athanassiou and I. Bayer, "Graphene Nanoplatelets-Based Advanced Materials and Recent Progress in Sustainable Applications," *Applied Sciences,* vol. 8, no. 9, p. 1438, 2018.

[146] A. Rahim, N. Ramli, A. Nordin and M. Wahab, "Supercapacitor performance with activated carbon and graphene nanoplatelets composite electrodes, and insights from the equivalent circuit model," *Carbon Trends,* vol. 5, p. 100101, 2021.

[147] D. Pullini, V. Siong, D. Tamvakos, B. Ortega, M. Sgroi, A. Veca, C. Glanz, I. Kolaric and A. Pruna, "Enhancing the capacitance and active surface utilization of supercapacitor electrode by graphene nanoplatelets," *Composites Science and Technology,* vol. 112, pp. 16-21, 2015.

[148] X. Sánchez-Romate, A. del Bosque García, M. Sánchez and A. Ureña, "Electrical Transport Mechanisms in Graphene Nanoplatelet Doped Polydimethylsiloxane and Application to Ultrasensitive Temperature Sensors," *ACS Applied Materials and Interfaces,* vol. 15, no. 18, pp. 22377-22394, 2023.

[149] C. Xue, M. Gao, Y. Xue, L. Zhu, L. Dai, A. Urbas and Q. Li, "Building 3D Layer-by-Layer Graphene–Gold Nanoparticle Hybrid Architecture with Tunable Interlayer Distance," *The Journal of Physical Chemistry C,* vol. 118, no. 28, pp. 15332-15338, 2014.

[150] Y. Si and E. Samulski, "Exfoliated Graphene Separated by Platinum Nanoparticles," *Chemistry of Materials,* vol. 20, no. 21, pp. 6792-6797, 2008.

[151] M. Abedi, R. Fangueiro and A. Correia, "An Effective Method for Hybrid CNT/GNP Dispersion and Its Effects on the Mechanical, Microstructural, Thermal, and Electrical Properties of Multifunctional Cementitious Composites," *Journal of Nanomaterials,* vol. 1, p. 6749150, 2020.

[152] C. Frysz, S. Xiaoping and D. Chung, "Carbon filaments and carbon black as a conductive additive to the manganese dioxide cathode of a lithium electrolytic cell," *Journal of Power Sources,* vol. 58, no. 1, pp. 41-54, 1996.

[153] H. Zhang, L. Ben, H. Yu, W. Qi, W. Zhao and X. Huang, "Ultrathin Ta2O5-coated super P carbon black as a stable conducting additive for lithium batteries charged to 4.9Vat 55°C," *Carbon,* vol. 162, pp. 519-527, 2020.

[154] D. Youn, M. Meyerson, K. Klavetter, K. Friedman, S. Coffman, J.-W. Lee, A. Heller and C. Mullins, "Mixing Super P-Li with N-Doped Mesoporous Templated Carbon Improves the High Rate Performance of a Potential Lithium Ion Battery Anode," *Journal of the Electrochemical Society,* vol. 163, p. A953, 2016.

[155] R. Gnanamuthu and C. Lee, "Electrochemical properties of Super P carbon black as an anode active material for lithium-ion batteries," *Materials Chemistry and Physics,* vol. 130, no. 3, pp. 831-834, 2011.

[156] I. Cho, J. Choi, K. Kim, M.-H. Ryou and Y. Lee, "A comparative investigation of carbon black (Super-P) and vapor-grown carbon fibers (VGCFs) as conductive additives for lithium-ion battery cathodes," *RSC Advances,* vol. 5, pp. 95073-95078, 2015.

[157] K. Wang, Y. Wu, S. Luo, X. He, J. Wang, K. Jiang and S. Fan, "Hybrid super-aligned carbon nanotube/carbon black conductive networks: A strategy to improve both electrical conductivity and capacity for lithium ion batteries," *Journal of Power Sources,* vol. 233, pp. 209-215, 2013.

[158] X. Cui, R. Lv, R. Sagar, C. Liu and Z. Zhang, "Reduced graphene oxide/carbon nanotube hybrid film as high performance negative electrode for supercapacitor," *Electrochimica Acta,* vol. 169, pp. 342-350, 2015.

[159] R. Lima, M. de Oliveira and H. de Oliveira, "Wearable supercapacitors based on graphene nanoplatelets/carbon nanotubes/polypyrrole composites on cotton yarns electrodes," *SN Applied Sciences,* vol. 1, no. 325, 2019.

[160] S. Chatterjee, F. Nafezarefi, N. Tai, L. Schlagenhauf, F. Nüesch and B. Chu, "Size and synergy effects of nanofiller hybrids including graphene nanoplatelets and carbon nanotubes in mechanical properties of epoxy composites," *Carbon,* vol. 50, no. 15, pp. 5380-5386, 2012.

[161] N. Pandit, P. Singh, S. Prasad, A. Keshri, M. Czagany, S. Hompoth, Z. Gacsi and P. Baumli, "Electrochemical behavior of GNP/CNT porous composite for supercapacitor," *Chemical Physics Letters,* vol. 827, p. 140695, 2023.

[162] Y. Jiang and J. Liu, "Definitions of Pseudocapacitive Materials: A Brief Review," *Energy & Environmental Materials,* vol. 2, no. 1, pp. 30-37, 2019.

[163] F. Shi, L. Li, X.-l. Wang, C.-d. Gu and J.-p. Tu, "Metal oxide/hydroxide-based materials for supercapacitors," *RSC Advances,* vol. 4, no. 79, pp. 41910-41921, 2014.

[164] A. Bryan, L. Santino, Y. Lu, S. Achyara and J. D'Arcy, "Conducting Polymers for Pseudocapacitive Energy Storage," *Chemistry of Materials,* vol. 28, no. 17, pp. 5989-5998, 2016.

[165] S. Trasatti and G. Buzzanca, "Ruthenium Dioxide: A New Interesting Electrode Material. Solid State Structure and Electrochemical Behaviour.," *Journal of Electroanalytical Chemistry and Interfacial Electrochemistry,* vol. 29, no. A1-A5, 1971.

[166] J. Zheng, P. Cygan and T. Jow, "Hydrous Ruthenium Oxide as an Electrode Material for Electrochemical Capacitors.," *Journal of the Electrochemical Society,* vol. 142, pp. 2699-2703, 1995.

[167] T. Liu, W. Pell and B. Conway, "Self-discharge and potential recovery phenomena at thermally and electrochemically prepared RuO2 supercapacitor electrodes," *Electrochimica Acta,* vol. 42, no. 23-24, pp. 3541-3552, 1997.

[168] V. Augustyn, P. Simon and B. Dunn, "Pseudocapacitive Oxide Materials for High-Rate Electrochemical Energy Storage.," *Energy & Environmental Science,* vol. 7, pp. 1597-1614, 2014.

[169] Umicore, "Precious Metals Management/Prices/Ruthenium," Umicore, [Online]. Available: https://pmm.umicore.com/en/prices/ruthenium/. [Accessed 09 07 2024].

[170] S. Fleischmann, J. Mitchell, R. Wang, C. Zhan, D.-E. Jiang, V. Presser and V. Augustyn, "Pseudocapacitance: From Fundamental Understanding to High Power Energy Storage Materials," *Chemical Reviews,* vol. 120, no. 14, pp. 6738-6782, 2020.

[171] H. Lee and J. Goodenough, "Supercapacitor Behavior with KCl Electrolyte," *Journal of Solid State Chemistry,* vol. 144, pp. 220-223, 1999.

[172] R. Yang, Y. Fan, R. Ye, Y. Tang, X. Cao, Z. Yin and Z. Zeng, "MnO2-Based Materials for Environmental Applications," *Advanced Materials,* vol. 33, no. 9, p. 2004862, 2021.

[173] M. Toupin, T. Brousse and D. Bélanger, "Influence of Microstucture on the Charge Storage Properties of Chemically Synthesized Manganese Dioxide," *Chemistry of Materials,* vol. 14, no. 9, pp. 3946-3952, 2002.

[174] H. Kim and B. Popov, "Synthesis and Characterization of MnO2-Based Mixed Oxides as Supercapacitors," *Journal of the Electrochemical Society,* vol. 150, no. 3, p. D56, 2003.

[175] S. Wen, J.-W. Lee, I.-H. Yeo, J. Park and S.-i. Mho, "The role of cations of the electrolyte for the pseudocapacitive behavior of metal oxide electrodes, MnO2 and RuO2," *Electrochimica Acta,* vol. 50, no. 2-3, pp. 849-855, 2004.

[176] J. Wang, H. Kim, H. Lee, Y.-J. Ko, M. Han, W. Kim, J. Baik, J.-Y. Choi, H.-S. Oh and W. Lee, "Sb incorporated into oxides enhances stability in acid during the oxygen evolution reaction by inhibiting structural distortion," *Nano Energy,* vol. 110, p. 108355, 2023.

[177] J.-G. Wang, "Engineering Nanostructured MnO2 for High Performance Supercapacitors," in *Supercapacitor Design and Applications*, IntechOpen, 2016.

[178] J. Wen, X. Ruan and Z. Zhuo, "Preparation and electrochemical performance of novel ruthenium–manganese oxide electrode materials for electrochemical capacitors," *Journal of Physics and Chemistry of Solids,* vol. 70, no. 5, pp. 816-820, 2009.

[179] D. Wu, X. Xie, Y. Zhang, D. Zhang, W. Du, X. Zhang and B. Wang, "MnO2/Carbon Composites for Supercapacitor: Synthesis and Electrochemical Performance," *Frontiers in Materials,* vol. 7, 2020.

[180] Q. Cheng, J. Tang, J. Ma, H. Zhang, N. Shinya and L.-C. Qin, "Graphene and nanostructured MnO2 composite electrodes for supercapacitors," *Carbon,* vol. 49, no. 9, pp. 2917-2925, 2011.

[181] C. Wang, J. Xu, M.-F. Yuen, J. Zhang, Y. Li, X. Chen and W. Zhang, "Hierarchical Composite Electrodes of Nickel Oxide Nanoflake 3D Graphene for High-Performance Pseudocapacitors," *Advanced Functional Materials,* vol. 24, no. 40, pp. 6372-6380, 2014.

[182] I.-H. Kim, J.-H. Kim, B.-W. Cho and K.-B. Kim, "Pseudocapacitive Properties of Electrochemically Prepared Vanadium Oxide on Carbon Nanotube Film Substrate," *Journal of the Electrochemical Society,* vol. 153, no. 8, p. A1451, 2006.

[183] L. Yang, S. Cheng, Y. Ding, X. Zhu, Z. Wang and M. Liu, "Hierarchical Network Architectures of Carbon Fiber Paper Supported Cobalt Oxide Nanonet for High-Capacity Pseudocapacitors," *Nano Letters,* vol. 12, no. 1, pp. 321-325, 2012.

[184] C.-q. Yi, J.-p. Zou, H.-z. Yang and X. Leng, "Recent advances in pseudocapacitor electrode materials: Transition metal oxides and nitrides," *Transactions of Nonferrous Metals Society of China,* vol. 28, no. 10, pp. 1980-2001, 2018.

[185] G. Snook, P. Kao and A. Best, "Conducting-polymer-based supercapacitor devices and electrodes," *Journal of Power Sources,* vol. 196, pp. 1-12, 2011.

[186] J. Campbell Scott, "History of Conductive Polymers," in *Nanostructured Conductive Polymers*, John Wiley and Sons, Ltd, 2010.

[187] C. Chiang, C. Fincher Jr., Y. Park, A. Heeger, H. Shirakawa, E. Louis, S. Gau and A. MacDiarmid, "Electrical Conductivity in Doped Polyacetylene," *Physical Review Letters,* vol. 40, p. 1472, 1978.

[188] The Nobel Prize, "The Nobel Prize in Chemistry 2000," The Nobel Prize, [Online]. Available: https://www.nobelprize.org/prizes/chemistry/2000/8961-the-nobel-prize-in-chemistry-2000/. [Accessed 10 07 2024].

[189] M. Abdelhamid, A. O'Mullane and G. Snook, "Storing energy in plastics: a review on conducting polymers & their role in electrochemical energy storage," *RSC Advances,* vol. 5, pp. 11611-11626, 2015.

[190] R. Choudhary, S. Ansari and M. Majumder, "Recent advances on redox active composites of metal-organic framework and conducting polymers as pseudocapacitor electrode material," *Renewable and Sustainable Energy Reviews,* vol. 145, p. 110854, 2021.

[191] M. Naguib, M. Kurtoglu, V. Presser, J. Lu, J. Niu, M. Heon, L. Hultman, Y. Gogotsi and M. Barosum, "Two-Dimensional Nanocrystals Produced by Exfoliation of Ti3AlC2," *Advanced Materials,* vol. 23, no. 37, pp. 4248-4253, 2011.

[192] A. Mohammadi, J. Rosen and Y. Gogotsi, "The world of two-dimensional carbides and nitrides (MXenes)," *Science,* vol. 372, no. 1165, p. eabf1581, 2021.

[193] Y. Gogotsi and B. Anasori, "The Rise of MXenes," *ACS Nano,* vol. 13, no. 8, pp. 8491-8494, 2019.

[194] M. Hu, H. Zhang, T. Hu, B. Fan, X. Wang and Z. Li, "Emerging 2D MXenes for supercapacitors: status, challenges and prospects," *Chemical Society Reviews,* vol. 49, pp. 6666-6693, 2020.

[195] C. Zhang, B. Anasori, A. Seral-Ascaso, S.-H. Park, N. McEvoy, A. Shmeliov, G. Duesberg, J. Coleman, Y. Gogotsi and V. Nicolosi, "Transparent, Flexible, and Conductive 2D Titanium Carbide (MXene) Films with High Volumetric Capacitance," *Advanced Materials,* vol. 29, no. 36, p. 1702678, 2017.

[196] K. Lim, M. Shekhirev, B. Wyatt, B. Anasori, Y. Gogotsi and Z. Seh, "Fundamentals of MXene synthesis," *Nature Synethesis,* vol. 1, pp. 601-614, 2022.

[197] M. Lukatskaya, S. Kota, Z. Lin, M.-Q. Zhao, N. Shpigel, M. Levi, J. Halim, P.-L. Taberna, M. Barsoum, P. Simon and Y. Gogotsi, "Ultra-high-rate pseudocapacitive energy storage in two-dimensional transition metal carbides," *Nature Energy,* vol. 2, p. 17105, 2017.

[198] P. Forouzandeh and S. Pillai, "MXenes-based nanocomposites for supercapacitor," *Current Opinion in Chemical Engineering,* vol. 33, p. 100710, 2021.

[199] A. Iqbal, J. Hong, T. Ko and C. Koo, "Improving oxidation stability of 2D MXenes: synthesis, storage media, and conditions," *Nano Convergence,* vol. 8, no. 9, 2021.

[200] R. Rajeswari, S. Subramanian, V. Reddy, M. Shayanti and R. Seeram, "Applications of conducting polymers and their issues in biomedical engineering," *Journal of the Royal Society Interface,* vol. 7, no. Suppl_5, pp. S559-S579, 2010.

[201] M. Pogorielov, K. Smyrnova, S. Kyrylenko, O. Gogotsi, V. Zahorodna and A. Pogrebnjak, "MXenes—A New Class of Two-Dimensional Materials: Structure, Properties and Potential Applications," *Nanomaterials,* vol. 11, no. 12, p. 3412, 2021.

[202] G. Waterhouse and M. Waterland, "Opal and inverse opal photonic crystals: Fabrication and characterization," *Polyhedron,* vol. 26, no. 2, pp. 356-368, 2007.

[203] Y. Zhang, Y. Sun, J. Liu, P. Guo, Z. Cai and J.-J. Wang, "Polymer-infiltrated SiO2 inverse opal photonic crystals for colorimetrically selective detection of xylene vapors," *Sensors and Actuators B: Chemical,* vol. 291, pp. 67-73, 2019.

[204] D. McNulty, V. Landgraf and S. Trabesinger, "Simplifying the synthesis of carbon inverse opals," *RSC Advances,* vol. 10, pp. 24108-24114, 2020.

[205] X. Zhang, B. Weinberger, S. Amrehn, X. Wu and M. Tiemann, "Synthesis of Metal Oxide Inverse Opals from Metal Nitrates by PMMA Colloidal Crystal Templating," *European Journal of Inorganic Chemistry,* vol. 2020, no. 35, pp. 3402-3407, 2020.

[206] R. Schroden, M. Al-Daous, C. Blanford and A. Stein, "Optical Properties of Inverse Opal Photonic Crystals," *Chemistry of Materials,* vol. 14, no. 8, pp. 3305-3315, 2002.

[207] S. Tabata, Y. Isshiji and M. Watanabe, "Inverse Opal Carbons Derived from a Polymer Precursor as Electrode Materials for Electric Double-Layer Capacitors," *Journal of the Electrochemical Society,* vol. 155, p. K42, 2008.

[208] K. Lee, J. Lytle, N. Ergang, S. Oh and A. Stein, "Synthesis and Rate Performance of Monolithic Macroporous CarbonElectrodes for Lithium-Ion Secondary Batteries," *Advanced Functional Materials,* vol. 15, no. 4, pp. 547-556, 2005.

[209] H. Liu, H.-M. Cho, Y. Meng and Q. Li, "Engineering Three-Dimensionally Electrodeposited Si-on-Ni Inverse Opal Structure for High Volumetric Capacity Li-Ion Microbattery Anode," *ACS Applied Materials and Interfaces,* vol. 6, no. 12, pp. 9842-9849, 2014.

[210] A. Savini and G. Savini, "A short history of 3D printing, a technological revolution just started," in *IEEE History of Telecommunications Conference, HISTELCON*, Tel Aviv, 2015.

[211] K. Sathish, S. Kumar, R. Magal, V. Selvaraj, V. Narasimharaj, R. Karthikeyan, G. Sabarinathan, M. Tiwari and A. Kassa, "A Comparative Study on Subtractive Manufacturing and Additive Manufacturing," *Advances in Materials Science and Engineering,* vol. 1, p. 6892641, 2022.

[212] H. Kodama, "Automatic method for fabricating a three-dimensional plastic model with photo-hardening polymer," *Review of Scientific Instruments,* vol. 52, no. 11, pp. 1770-1773, 1981.

[213] A. Herbert, "Solid Object Generation," *Journal of Applied Photographic Engineering,* pp. 185-188, 1982.

[214] L. Williams and L. Williams, "Additive manufacturing or 3d scanning and printing." Manufacturing Engineering Handbook, New York, USA: McGraw-Hill, 2015.

[215] C. Hull, "Apparatus for Production of Three-Dimensional Objects by Stereolithography". United States of America Patent 638905, 1984.

[216] C. Hull, "The Birth of 3D Printing," *Research-Technology Management,* vol. 58, no. 6, pp. 25-30, 2015.

[217] E. Matias and B. Rao, "3D printing: On its historical evolution and the implications for business," in *Portland International Conference on Management of Engineering and Technology (PICMET)*, Portland, Oregon, 2015.

[218] C. Groth, N. Kravitz, P. Jones, J. Graham and W. Redmond, "Three-Dimensional Printing Technologies," *Journal of Clinical Orthodontics,* vol. 48, no. 8, pp. 475-485, 2014.

[219] J. Pucci, B. Christophe, J. Sisti and E. Connolly Jr, "Three-dimensional printing: technologies, applications, and limitations in neurosurgery," *Biotechnology Advances,* vol. 35, no. 5, pp. 521-529, 2017.

[220] V. Egorov, U. Gullzar, Y. Zhang, S. Breen and C. O'Dwyer, "Evolution of 3D Printing Methods and Materials for Electrochemical Energy Storage," *Advanced Materials,* vol. 32, no. 29, p. 2000556, 2020.

[221] M. Schadt, "LIQUID CRYSTAL MATERIALS AND LIQUID CRYSTAL DISPLAYS," *Annual Review of Materials Research,* vol. 27, pp. 305-379, 1997.

[222] Z. Zhao, X. Tian and X. Song, "Engineering materials with light: recent progress in digital light processing based 3D printing," *Journal of Materials Chemistry C,* vol. 8, no. 40, pp. 13896-13917, 2020.

[223] J. Zhang, Q. Hu, S. Wang, J. Tao and M. Gou, "Digital Light Processing Based Three-dimensional Printing for Medical Applications," *International Journal of Bioprinting,* vol. 6, no. 1, p. 242, 2020.

[224] H. Quan, T. Zhang, H. Xu, S. Luo, J. Nie and X. Zhu, "Photo-curing 3D printing technique and its challenges," *Bioactive Materials,* vol. 5, no. 1, pp. 110-115, 2020.

[225] W. Moon, S. Kim, B.-S. Lim, Y.-S. Park, R.-Y. Kim and S. Chung, "Dimensional Accuracy Evaluation of Temporary Dental Restorations with Different 3D Printing Systems," *Materials,* vol. 14, no. 6, p. 1487, 2021.

[226] J. Lewis, "Direct Ink Writing of 3D FunctionalMaterials," *Advanced Functional Materials,* vol. 16, pp. 2193-2204, 2006.

[227] S. Tagliaferri, A. Paganiotopoulos and C. Mattevi, "Direct ink writing of energy materials," *Materials Advances,* vol. 2, pp. 540-563, 2021.

[228] M. Saadi, A. Maguire, N. Pottackal, M. Thakur, M. Ikram, A. Hart, P. Ajayan and M. Rahman, "Direct Ink Writing: A 3D Printing Technology for Diverse Materials," *Advanced Materials,* vol. 34, no. 28, p. 2108855, 2022.

[229] Protolabs Network by Hubs, "What is Material Jetting 3D printing?," Protolabs Network, [Online]. Available: https://www.hubs.com/knowledge-base/introduction-material-jetting-3d-printing/. [Accessed 02 07 2024].

[230] Y. Tee, P. Tran, M. Leary, P. Pille and M. Brandt, "3D Printing of polymer composites with material jetting: Mechanical and fractographic analysis," *Additive Manufacturing,* vol. 36, p. 101558, 2020.

[231] J. Yuan, C. Chen, D. Yao and G. Chen, "3D Printing of Oil Paintings Based on Material Jetting and Its Reduction of Staircase Effect," *Polymers,* vol. 12, no. 11, p. 2536, 2020.

[232] S. Mora, N. Pugno and D. Misseroni, "3D printed architected lattice structures by material jetting," *Materials Today,* vol. 59, pp. 107-132, 2022.

[233] D. Singh, T. Mahender and A. Reddy, "Powder bed fusion process: A brief review," *Materials Today: Proceedings,* vol. 46, no. 1, pp. 350-355, 2021.

[234] M. Sehhat and A. Mahdianikhotbesara, "Powder spreading in laser-powder bed fusion process," *Granular Matter,* vol. 23, p. 89, 2021.

[235] I. Yadroitsev, I. Yadroitsava and A. Du Plessis, "Basics of laser powder bed fusion," in *Fundamentals of Laser Powder Bed Fusion of Metals*, Elsevier, 2011, pp. 15-38.

[236] R. Singh, A. Gupta, O. Tripathi, S. Srivastava, B. Singh, A. Awasthi, S. Rajput, P. Sonia, P. Singhal and K. Saxena, "Powder bed fusion process in additive manufacturing: An overview," *Materials Today: Proceedings,* vol. 26, no. 2, pp. 3058-3070, 2020.

[237] A. Khorasani, I. Gibson, J. Veetil and A. Ghasemi, "A review of technological improvements in laser-based powder bed fusion of metal printers," *The International Journal of Advanced Manufacturing Technology,* vol. 108, pp. 191-209, 2020.

[238] J. Zuniga, D. Katsavelis, J. Peck, J. Stollberg, M. Petrykowski, A. Carson and C. Fernandez, "Cyborg beast: a low-cost 3d-printed prosthetic hand for children with upper-limb differences," *BMC Research Notes,* vol. 8, p. 10, 2015.

[239] T. Distler and A. Boccaccini, "3D printing of electrically conductive hydrogels for tissue engineering and biosensors–A review.," *Acta biomaterialia,* vol. 101, pp. 1-13, 2020.

[240] J. Saroia, W. Yanen, Q. Wei, K. Zhang, T. Lu and B. Zhang, "A review on biocompatibility nature of hydrogels with 3D printing techniques, tissue engineering application and its future prospective," *Bio-Design and Manufacturing,* vol. 1, pp. 265-279, 2018.

[241] A. Mironov, A. Grigoryev, L. Krotova, N. Skaletsky, V. Popov and V. Sevastianov, "3D printing of PLGA scaffolds for tissue engineering.," *Journal of Biomedical Materials Research Part A,* vol. 105, no. 1, pp. 104-109, 2017.

[242] N. Bruns and C. Krettek, "3D-printing in trauma surgery: Planning, printing and processing.," *Der Unfallchirurg,* vol. 122, pp. 270-277, 2019.

[243] L. Pugliese, S. Marconi, E. Negrello, V. Mauri, A. Peri, V. Gallo, F. Auricchio and A. Pietrabissa, "The clinical use of 3D printing in surgery," *Updates in Surgery,* vol. 70, pp. 381-388, 2018.

[244] L. Xie, C. Chen, Y. Zhang, W. Zheng, H. Chen and L. Cai, "Three-dimensional printing assisted ORIF versus conventional ORIF for tibial plateau fractures: A systematic review and meta-analysis," *International Journal of Surgery,* vol. 57, pp. 35-44, 2018.

[245] S. Hussain, S. Malakar and V. Arora, "Extrusion-Based 3D Food Printing: Technological Approaches, Material Characteristics, Printing Stability, and Post-processing," *Food Engineering Reviews,* vol. 14, pp. 100-119, 2022.

[246] Y. Liu, Y. Yu, C. Liu, J. Regenstein, X. Liu and P. Zhou, "Rheological and mechanical behavior of milk protein composite gel for extrusion-based 3D food printing.," *Lwt,* vol. 102, pp. 338-346, 2019.

[247] A. Le-Bail, B. Maniglia and P. Le-Bail, "Recent advances and future perspective in additive manufacturing of foods based on 3D printing.," *Current Opinion in Food Science,* vol. 35, pp. 54-64, 2020.

[248] A. Bagheri and J. Jin, "Photopolymerization in 3D Printing," *ACS Applied Polymer Materials,* vol. 1, no. 4, pp. 593-611, 2019.

[249] J. Crivello and E. Reichmanis, "Photopolymer Materials and Processes for Advanced Technologies," *Chemistry of Materials,* vol. 26, no. 1, pp. 533-548, 2014.

[250] E. Childers, M. Wang, M. Becker, J. Fisher and D. Dean, "3D printing of resorbable poly(propylene fumarate) tissue engineering scaffolds," *MRS Bulletin,* vol. 40, no. 2, pp. 119-126, 2015.

[251] P. Gupta, S. Trenor, T. Long and G. Wilkes, "In situ photo-cross-linking of cinnamate functionalized poly(methyl methacrylate-co-2-hydroxyethyl acrylate) fibers during electrospinning," *Macromolecules,* vol. 37, no. 24, pp. 9211-9218, 2004.

[252] R. Huyck, S. Trenor, B. Love and T. Long, "Photodimerization of coumarin functionalized poly(alkyl acrylate) and poly(alkyl methacrylate) random copolymers: influence of copolymer composition on photocrosslinking," *Journal of Macromolecular Science, Part A,* vol. 45, no. 1, pp. 9-15, 2008.

[253] F. Melchels, J. Feijen and D. Grijpma, "A poly(d,l-lactide) resin for the preparation of tissue engineering scaffolds by stereolithography," *Biomaterials,* vol. 30, no. 23-24, pp. 3801-3809, 2009.

[254] R. Mondschein, A. Kanitkar, C. Williams, S. Verbridge and T. Long, "Polymer structure-property requirements for stereolithographic 3D printing of soft tissue engineering scaffolds," *Biomaterials,* vol. 140, pp. 170-188, 2017.

[255] Formlabs, "Materials Catalog.," [Online]. Available: https://formlabs.com/eu/materials/. [Accessed 04 07 2024].

[256] Formlabs, "Form 2 Tech Specs," Formlabs, [Online]. Available: https://formlabs.com/eu/3d-printers/form-2/tech-specs/. [Accessed 04 07 2024].

[257] T. Billiet, M. Vandenhaute, J. Schelfhout, S. Van Vlierberghe and P. Dubruel, "A review of trends and limitations in hydrogel-rapid prototyping for tissue engineering," *Biomaterials,* vol. 33, no. 26, pp. 6020-6041, 2012.

[258] I. Solomon, P. Sevvel and J. Gunasekaran, "A review on the various processing parameters in FDM," *Materials Today: Proceedings,* vol. 37, no. 2, pp. 509-514, 2021.

[259] R. Kristiawan, F. Imaduddin, D. Ariawan, U. Arifin and Z. Arifin, "A review on the fused deposition modeling (FDM) 3D printing: Filament processing, materials, and printing parameters," *Open Engineering,* vol. 11, no. 1, p. 0063, 2021.

[260] A. Dey and N. Yodo, "A Systematic Survey of FDM Process Parameter Optimization and Their Influence on Part Characteristics," *Journal of Manufacturing and Materials Processing,* vol. 3, no. 3, p. 64, 2019.

[261] All3DP, "The Main 3D Printer Filament Types," All3DP, 08 10 2023. [Online]. Available: https://all3dp.com/1/3d-printer-filament-types-3d-printing-3d-filament/. [Accessed 04 07 2024].

[262] Protopasta, "Material Data Table," [Online]. Available: https://proto-pasta.com/pages/material-data-table. [Accessed 04 07 2024].

[263] M. Khosravani, J. Schüürmann, F. Berto and T. Reinicke, "On the Post-Processing of 3D-Printed ABS Parts," *Polymers,* vol. 13, no. 10, p. 1559, 2021.

[264] FutureMakers, "MAKERBOT REPLICATOR 2X EXPERIMENTAL 3D PRINTER," MakerBot, [Online]. Available: https://www.makerbot.gr/shop-makerbot-products/makerbot-replicator-2x-experimental-3d-printer/. [Accessed 05 07 2024].

[265] Y. Yan, Y. Jiang, E. Ng, Y. Zhang, C. Owh, F. Wang, Q. Song, T. Feng, B. Zhang, P. Li, X. Loh, S. Chan and B. Chan, "Progress and opportunities in additive manufacturing of electrically conductive polymer composites," *Materials Today Advances,* vol. 17, p. 100333, 2023.

[266] S.-C. Tsai, L.-H. Chen, C.-P. Chu, W.-C. Chao and Y.-C. Liao, "Photo curable resin for 3D printed conductive structures," *Additive Manufacturing,* vol. 51, p. 102590, 2022.

[267] G. Scordo, V. Bertana, L. Scaltrito, S. Ferrero, M. Cocuzza, S. Marasso, S. Romano, R. Sesana, F. Catania and C. Pirri, "A novel highly electrically conductive composite resin for stereolithography," *Materials Today Communications,* vol. 19, pp. 12-17, 2019.

[268] X. Tian, J. Jin, S. Yuan, C. Chua, S. Tor and K. Zhou, "Emerging 3D-Printed Electrochemical Energy StorageDevices: A Critical Review," *Advanced Energy Materials,* vol. 7, p. 1700127, 2017.

[269] C. Zhao, C. Wang, R. Gorkin III, S. Beirne, K. Shu and G. Wallace, "Three dimensional (3D) printed electrodes for interdigitated supercapacitors," *Electrochemistry Communications,* vol. 41, pp. 20-23, 2014.

[270] C. Zhu, T. Liu, F. Qian, T.-J. Han, E. Duoss, J. Kuntz, C. Spadaccini, M. Worsley and Y. Li, "Supercapacitors Based on Three-Dimensional Hierarchical Graphene Aerogels with Periodic Macropores," *Nano Letters,* vol. 16, no. 6, pp. 3448-3456, 2016.

[271] G. Wang, H. Wang, X. Lu, Y. Ling, M. Yu, T. Zhai, Y. Tong and Y. Li, "Solid-State Supercapacitor Based on Activated Carbon Cloths Exhibits Excellent Rate Capability," *Advanced Materials,* vol. 26, no. 17, pp. 2676-2682, 2014.

[272] H. Feng, H. Hu, H. Dong, Y. Xiao, Y. Cai, B. Lei, Y. Liu and M. Zheng, "Hierarchical structured carbon derived from bagasse wastes: A simple and efficient synthesis route and its improved electrochemical properties for high-performance supercapacitors," *Journal of Power Sources,* vol. 302, pp. 164-173, 2016.

[273] K.-C. Tsay, L. Zhang and J. Zhang, "Effects of electrode layer composition/thickness and electrolyte concentration on both specific capacitance and energy density of supercapacitor," *Electrochimica Acta,* vol. 60, pp. 428-436, 2012.

[274] X. Liu, M. Jervis, R. Maher, I. Villar-Garcia, M. Naylor-Marlow, P. Shearing, M. Ouyang, L. Cohen, N. Brandon and B. Wu, "3D-Printed Structural Pseudocapacitors," *Advanced Structural Pseudocapacitors,* vol. 1, no. 9, p. 1600167, 2016.

[275] A. Ambrosi, J. Moo and M. Pumera, "3D Printing: Helical 3D-Printed Metal Electrodes as Custom-Shaped 3D Platform for Electrochemical Devices," *Advanced Functional Materials,* vol. 26, p. 698, 2016.

[276] R. Hensleigh, H. Cui, J. Oakdale, J. Ye, P. Campbell, E. Duoss, C. Spadaccini, X. Zheng and M. Worsley, "Additive manufacturing of complex micro-architected graphene aerogels," *Materials Horizons,* vol. 5, no. 6, pp. 1035-1041, 2018.

[277] W. Yang, J. Yang, J. Byun, F. Moissinac, J. Xu, S. Haigh, M. Domingos, M. Bissett, R. Dryfe and S. Barg, "3D Printing of Freestanding MXene Architectures for Current-Collector-Free Supercapacitors," *Advanced Materials,* vol. 31, no. 37, p. 1902725, 2019.

[278] J. Xue, L. Gao, X. Hu, K. Cao, W. Zhou, W. Wang and Y. Lu, "Stereolithographic 3D Printing-Based Hierarchically Cellular Lattices for High-Performance Quasi-Solid Supercapacitor," *Nano-Micro Letters,* vol. 11, no. 46, 2019.

[279] X. Tian and K. Zhou, "3D printing of cellular materials for advanced electrochemical energy storage and conversion," *Nanoscale,* vol. 12, pp. 7416-7432, 2020.

[280] H. Peng, "Wearable Electronics," *National Science Review,* vol. 10, no. 1, p. nwac193, 2023.

[281] O. Mphale, K. Gorenjena and O. Nojila, "The Future of Things: A Comprehensive Overview of Internet of Things History, Definitions, Technologies, Architectures, Communication and beyond," *Journal of Information Systems and Informatics,* vol. 6, no. 2, pp. 1263-1286, 2024.

[282] K. Jost, D. Stenger, C. Perez, J. McDonough, K. Lian, Y. Gogotsi and G. Dion, "Knitted and screen printed carbon-fiber supercapacitors for applications in wearable electronics," *Energy and Environmental Science,* vol. 6, pp. 2698-2705, 2013.

[283] M. Arier, Y. Xu, D. Harrison and J. Fyson, "3D printing of highly flexible supercapacitor designed for wearable energy storage," *Materials Science and Engineering: B,* vol. 226, pp. 29-38, 2017.

[284] J. Yang, Q. Cao, X. Tang, J. Du, T. Yu, X. Xu, D. Cai, C. Guan and W. Huang, "3D-Printed highly stretchable conducting polymer electrodes for flexible supercapacitors," *Journal of Materials Chemistry A,* vol. 9, pp. 19649-19658, 2021.

[285] R. Lakes, "Negative-Poisson's-Ratio Materials: Auxetic Solids," *Annual Review of Materials Research,* vol. 47, pp. 63-81, 2017.

[286] M. Ovhal, H. Lee, V. Satale, B. Tyagi, S. Chowdhury and J.-W. Kang, "One-Meter-Long, All-3D-Printed Supercapacitor FibersBased on Structurally Engineered Electrode for WearableEnergy Storage," *Advanced Energy Materials,* vol. 14, p. 2303053, 2024.

[287] S. Nath, I. Patil and P. Sundriyal, "Material extrusion of electrochemical energy storage devices for flexible and wearable electronic applications," *Journal of Energy Storage,* vol. 79, p. 110129, 2024.

[288] M. Baig, S. Khan, H. Ahmad, J. Liang, G. Zhu, H. Pang and Y. Zhang, "3D printing of hydrogels for flexible micro-supercapacitors," *FlexMat,* vol. 1, no. 1, pp. 79-99, 2024.

[289] G. Zhou, X. Liu, C. Liu, Z. Li, C. Liu, X. Shi, Z. Li, C. Mei and M.-C. Li, "3D printed MXene-based films and cellulose nanofiber reinforced hydrogel electrolyte to enable

high-performance flexible supercapacitors," *Journal of Materials Chemistry A,* vol. 12, pp. 3734-3744, 2024.

[290] C. Gellrich, Y. Bräuniger, R. Schmidt, J. Grothe and S. Kaskel, "Sustainable Ketjenblack-Based Carbon Ink for 3D Extrusion Micro-Printing to Fabricate Flexible Supercapacitors," *Batteries and Supercaps,* vol. 7, no. 1, p. e202300469, 2024.

[291] M. Idrees, S. Ahmed, Z. Mohammed, N. Korivi and V. Rangari, "3D printed supercapacitor using porous carbon derived from packaging waste," *Additive Manufacuring,* vol. 36, p. 101525, 2020.

[292] X. Aeby, A. Poulin, G. Siqueira, M. Hausmann and G. Nyström, "Fully 3D printed and disposable paper supercapacitors.," *Advanced Materials,* vol. 33, no. 26, p. 2101328, 2021.

[293] N. Pearnchob, J. Siepmann and R. Bodmeier, "Pharmaceutical Applications of Shellac: Moisture-Protective and Taste-Masking Coatings and Extended-Release Matrix Tablets," *Drug Development and Industrial Pharmacy,* vol. 29, no. 8, p. 925–938, 2003.

[294] H. Silva-Neto, G. Duarte-Junior, D. Rocha, F. Bedioui, A. Varenne and W. Coltro, "Recycling 3D Printed Residues for the Development of Disposable Paper-Based Electrochemical Sensors," *ACS Applied Materials and Interfaces,* vol. 15, no. 11, pp. 14111-14121, 2023.

[295] A. Tarancón, V. Esposito, M. Torrell, M. Di Vece, J. Son, P. Norby, S. Bag, P. Grant, A. Vogelpoth and S. Linnenbrink, "2022 roadmap on 3D printing for energy," *Journal of Physics: Energy,* vol. 4, no. 1, p. 011501, 2022.

[296] M. Browne, F. Novotny, Z. Sofer and M. Pumera, "3D Printed Graphene Electrodes' Electrochemical Activation," *ACS Applied Materials and Interfaces,* vol. 10, pp. 40294-40301, 2018.

[297] B. Yao, H. Peng, H. Zhang, J. Kang, C. Zhu, G. Delgado, D. Byrne, S. Faulkner, M. Freyman, X. Lu, M. Worsley, J. Lu and Y. Li, "Printing Porous Carbon Aerogels for Low Temperature Supercapacitors," *Nano Letters,* vol. 21, pp. 3731-3737, 2021.

[298] K. Shen, J. Ding and S. Yang, "3D Printing Quasi-Solid-State Asymmetric Micro-Supercapacitors with Ultrahigh Areal Energy Density," *Advanced Energy Materials,* vol. 8, no. 20, p. 1800408, 2018.

[299] C. Foster, M. Down, Y. Zhang, X. Ji, S. Rowley-Neale, G. Smith, P. Kelly and C. Banks, "3D Printed Graphene Based Energy Storage Devices," *Scientific Reports,* vol. 7, p. 42233, 2017.

[300] Y. Jiang, Z. Xu, T. Huang, Y. Liu, F. Guo, J. Xi, W. Gao and C. Gao, "Direct 3D Printing of Ultralight Graphene Oxide Aerogel Microlattices," *Advanced Functional Materials,* vol. 28, no. 16, p. 1707024, 2018.

[301] B. Chen, Y. Jiang, X. Tang, Y. Pan and S. Hu, "Fully packaged carbon nanotube supercapacitors by direct ink writing on flexible substrates.," *ACS applied materials & interfaces,* vol. 9, no. 34, pp. 28433-28440, 2017.

[302] A. Tanwilaisiri, Y. Xu, D. Harrison, J. Fyson and M. Arier, "A Study of Metal Free Supercapacitors Using 3D Printing," *International Journal of Precision Engineering and Manufacturing,* vol. 19, no. 7, pp. 1071-1079, 2018.

[303] L. Fieber, J. Evans, C. Huang and P. Grant, "Single-operation, multi-phase additive manufacture of electro-chemical double layer capacitor devices," *Additive Manufacturing,* vol. 28, pp. 344-353, 2019.

Chapter 2

Experimental

2.1 Introduction

This chapter will serve to outline all additive manufacturing methods, experimental procedures, and characterisation techniques used during the research in this thesis project. The additive manufacturing methods used to make the supercapacitor cells studied in this work, vat-polymerisation, fused deposition modelling, will be explained in detail with background theory and the exact processes used in this work. Electrode and electrolyte preparation, and supercapacitor cell assembly will be outlined. The material characterisation techniques (Raman spectroscopy, scanning electron microscopy (SEM), and electronic resistance measurements) will be discussed, as will the electrochemical characterisation techniques used in these studies (cyclic voltammetry (CV), galvanostatic charge-discharge tests, and rate capability tests).

2.2 Design, Printing, and Processing of Additively Manufactured Components

Both vat-polymerisation (Vat-P) and fused deposition modelling (FDM) additive manufacturing were used for the printed components of the supercapacitor cells (discussed in Chapter 1.5). For all supercapacitor cells in this work the outer casings of the supercapacitor cells were made using Vat-P additive manufacturing. In Chapters 3 and 5, both Vat-P and FDM additive manufacturing methods were used to make the current collectors of the supercapacitor

cells. In Chapter 4, only FDM printing was used to make the current collectors of the supercapacitor cells.

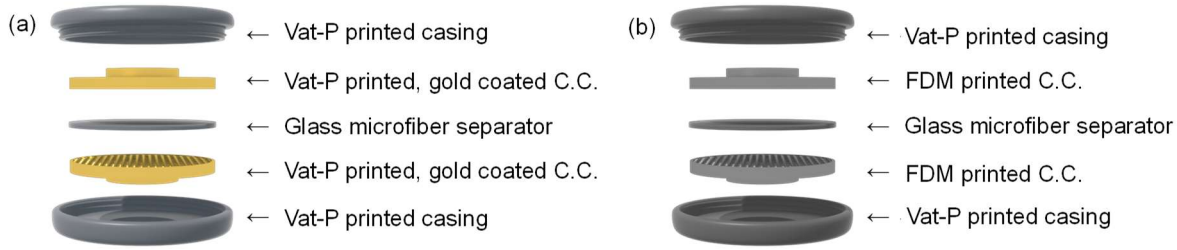

Figure 2.1 Schematic for (a) the Vat-P current collector type cell, comprised of two Vat-P printed half casings, two Vat-P printed current collectors sputtered in a 50 nm layer of gold, electrode materials loaded onto the lattice face of the current collectors, and a glass microfibre filter separator soaked in 5 drops of 6 M aqueous KOH electrolyte. The schematic for (b) the FDM current collector type cell is identical, except for the current collectors, which are made of FDM printed conductive PLA plastic.

2.2.1 Printing and Processing of Vat-P Printed Components

Following their design by FreeCAD, Vat-P components were uploaded to the Form 2 Formlabs Vat-P printer (© Formlabs, Somerville, Massachusetts, USA) via the Formlabs application. The resin used for all Vat-P components was Preform Clear V4 resin (© Formlabs, Somerville, Massachusetts, USA), always at a resolution of 0.025 mm layer thickness (the highest resolution on this printer type and model). Once uploaded, the components were printed. The printing time depended on what components needed to be printed, and how many. If both outer casings and current collectors were required, a batch of 12 outer casings and 12 current collectors (to make 6 full cells) would be printed, taking 5.25 hours at a resolution of 0.025 mm layer thickness (using a total of 24.49 mL of resin per batch, including supports). If only the outer casings were required, a batch of 12 outer casings would be printed, taking 4 hours at the highest resolution of 0.0025 mm layer thickness (using a total of 13.22 mL of resin per

batch, including supports). The Vat-P components were always printed with supports, which prevented deformation during the printed process [1, 2].

Once the printing was completed, the building platform was removed from the main printer. The printed components were removed from the building platform using a scraper, and the empty platform was washed with iso-propyl alcohol (IPA) and dried with tissue paper before being placed back into the main printer. The printed components were placed into a bath of IPA and washed manually for 10 minutes to remove any residual liquid resin. After the washed components were dried with tissue paper, they were placed within a UV-light curing machine for 15 minutes at a temperature of 60 °C (the specific time and temperature for curing this resin type). Once cured, the components were removed, and the supports were removed either by hand or using a wire cutter. Any bumps left by removing the supports were filed to smoothness with sandpaper. The entire post-processing procedure for one batch of Vat-P components took approximately 1.5 hours.

2.2.2 Printing and Processing of FDM Printed Components

FDM additive manufacturing was also used in this work, but less extensively than Vat-P. Half of the supercapacitor cells' current collectors in Chapter 3, and all the current collectors in Chapter 4 were made using FDM additive manufacturing. The current collectors for this cell type were printed using a MakerBot Replicator 2X FDM printer (© UltiMaker, Utrecht, Netherlands). The material used for these current collectors was ProtoPasta Conductive PLA (© ProtoPlant, Vancouver, Washington, USA) filament (PLA plastic loaded with graphene for conductivity). After the current collectors were designed on FreeCAD, they were uploaded to the MakerBot application to design the layout and apply the settings for the printed components. The printer platform was set to a temperature of 115°C, and the extruder to a temperature of 230°C (the ideal temperature for effective extrusion of the PLA filament without

burning). A resolution of 0.1 mm (the highest resolution possible for this printer type and model) was used for all FDM printed components. The print was uploaded to the MakerBot Replicator 2X, and printing was started. Printing a batch of 25 FDM current collectors took ~1.5 h at a resolution of 0.1 mm. Once printing was completed, any defective current collectors were recycled. No post-processing was needed for this current collector type.

2.2.3 Gold Sputtering of Vat-P Printed Current Collectors

Gold sputtering was required to add conductivity to the electronically insulating Vat-P current collectors. A Quorum Q150T S metal sputterer (Quorum Technologies, Laughton, East Sussex, UK) and 99.99% purity gold target (diameter = 57 mm, 0.2 mm thickness) purchased from Ted Pella Inc. were used, and all current collectors were coated with exactly 50 nm of gold on both sides to form a uniform metallization from outside to inside without electrical disconnection. The thickness of the gold coating is measured and regulated by the metal sputterer. The FDM current collectors required no metal sputtering and are sufficiently conductive as reported previously [3]. Following this, all current collectors were individually weighed, their masses were noted, and they were set aside for carbon slurry loading. Spare current collectors of both types were also made and set aside for materials characterisations.

2.2.4 Chemical Treatments for Chapter 4 FDM Printed Current Collectors

In Chapter 4, three different chemical treatments were utilised, with the aim of improving the conductivity of the FDM printed current collectors and the electrochemical performance of the supercapacitor cells they are used in. N,N-dimethylformamide (DMF) (>99.8%) and 6 M aqueous potassium hydroxide (KOH) solution were used as the reagents for the treatments. The KOH solution was made in bulk in the lab, using 33.66 g of KOH (≥85%, pellets) in 100 mL of water (adding a few grams of pellets at a time, and allowing them to dissolve in the water before adding more). This solution doubles as the electrolyte used in all supercapacitor cells in

this study, and is kept in a cool, dry, dark cupboard when not in use. Both the N,N-DMF and KOH pellets were purchased from Sigma Aldrich (Gillingham, UK).

The first chemical treatment (DMF (Short)) used N,N-DMF as the reagent. 12 untreated FDM current collectors were placed in individual small polystyrene vials. 1.5 mL of DMF was added to each of the vials using a 1 mL syringe, completely submerging the current collectors, and covering their surfaces in the reagent. The current collectors were left to sit in the reagent for 10 minutes, following which the vials were sonicated for 5 minutes using a Cole-Palmer 8891 Ultrasonic Cleaner (© 2023 Cole-Parmer Instrument Company, LLC), with the water bath at 20°C and a frequency output of 42 kHz. After this, the current collectors were rinsed in fresh DMF, then patted dry with tissue paper, and left in the fume hood overnight to completely dry in the air. Once completely dried, the current collectors were weighed and numbered.

The second chemical treatment (DMF (Long)) also used N,N-DMF as the reagent. 12 untreated FDM current collectors were placed in individual small polystyrene vials. 1.5 mL of DMF was added to each of the vials using a 1 mL syringe, completely submerging the current collectors, and covering their surfaces in the reagent. This time, the current collectors were left to sit in the reagent for 72 hours, following which the vials were sonicated for 5 minutes (using the same ultrasonic cleaner and settings as the DMF (Short) procedure above). After this, the current collectors were rinsed in fresh DMF, then patted dry with tissue paper, and left in the fume hood overnight to completely dry in the air. Once completely dried, the current collectors were weighed and numbered.

The final chemical treatment (KOH (Long)) used 6 M aqueous KOH solution as the reagent. 12 untreated FDM current collectors were placed in individual small polystyrene vials. 1.5 mL of KOH was added to each of the vials using a 1 mL syringe, completely submerging the current collectors, and covering their surfaces in the reagent. The current collectors were

left to sit in the reagent for 72 hours, following which the vials were sonicated for 5 minutes (using the same ultrasonic cleaner and settings as the other two chemical treatment procedures). After this, the current collectors were rinsed in fresh KOH, then rinsed in deionized water. After being patted dry with tissue paper, the current collectors were left in the fume hood to completely air-dry overnight. Once completely dried, the current collectors were weighed and numbered.

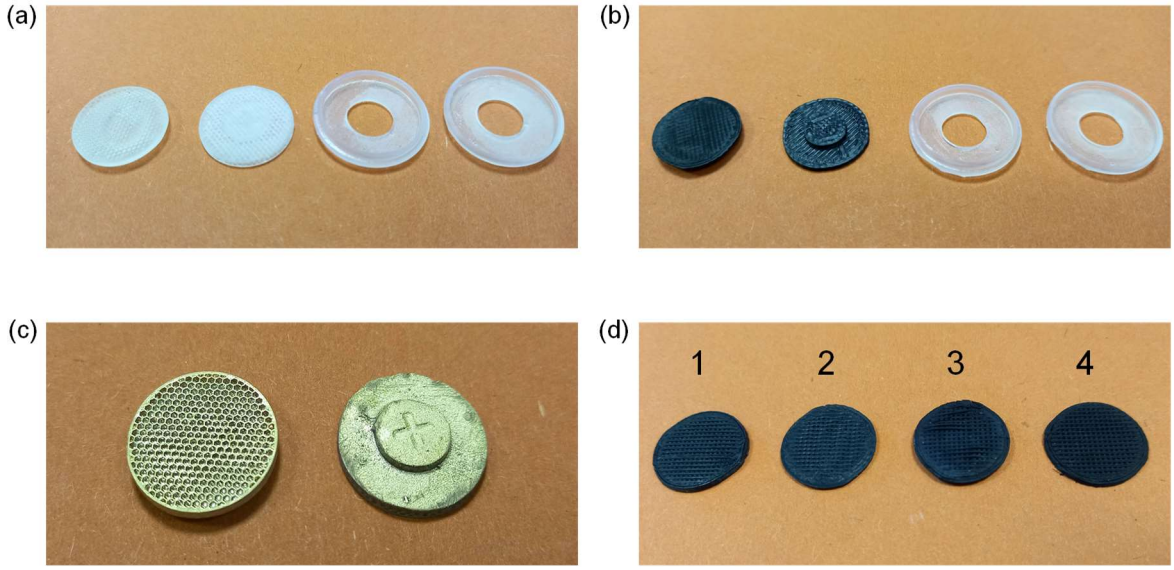

Figure 2.2 Images taken of cell components at different stages of cell assembly. (a) All 3D-printed components for one SLA current collector type cell (two half-casings and two current collectors) after post-print processing (washing, curing, removing supports, and filing to smoothness). (b) All 3D-printed components for one FDM current collector type cell. No post processing procedure is needed for the FDM current collectors, saving time at the cost of precision and overall quality of the printed parts. The difference in resolution in the two printing methods is apparent here. The pattern of melted filament lines is clearly visible in the FDM current collectors, while the layers of photopolymerized resin are invisible on the SLA components (c) 50 nm gold sputtered SLA printed current collectors (lattice face and terminal face) with the intricate detail of the current collector lattice visible. This level of complexity would not be achievable using the FDM printer, however, the FDM current collectors require no metal sputtering, saving time, and money. (d) All four types of FDM printed current collectors studied in Chapter 4 after their respective chemical treatments; namely 1) Untreated, 2) DMF-Treated (Short), 3) DMF-Treated (Long), and 4) KOH-Treated (Long). There is little visible difference between the current collectors, however, the DMF-Treated (Long) and KOH-Treated (Long) current collectors are far softer in texture.

Four groups of FDM current collectors were studied in Chapter 4 (Untreated, DMF-Treated (Short), DMF-Treated (Long), and KOH-Treated (Long)). Each group contained 12 current collectors, enough to make 6 supercapacitor cells. The Untreated current collectors were used in the supercapacitor cells as printed, without any chemical treatment. After their respective chemical treatments (or lack thereof, for the Untreated current collectors), all current collectors were loaded with active materials and assembled into supercapacitor cells, as outlined later. None of the current collectors in this study underwent more than one chemical treatment. Additionally, both current collectors within a given supercapacitor cell underwent the same treatment, or lack thereof.

2.3 Active Material Preparation

For Chapters 3 and 4, the carbon-based electrode active materials were prepared in a very straightforward manner. All materials in the carbon slurries were used as received, with no purification steps. Single-walled carbon nanotubes (SWCNTs, ≥99% carbon, ≥93% SWCNT), graphene nanoplatelets (GNPs), graphite, and polyvinylidene fluoride (PVDF, average $M_W \approx$ 534,000) were purchased from Sigma Aldrich (Gillingham, UK). Carbon black (Super P, 99+%) was purchased from Fisher Scientific (Loughborough, UK). In Chapter 5, manganese oxide inverse-opals were prepared and subsequently combined with carbon-based materials to form carbon and manganese oxide inverse-opal composite electrode active materials. All materials for the synthesis of the inverse-opals were used as received, with no purification steps. Polystyrene Polybead® Microspheres solution (2.7% solids, 0.50 μm) was purchased from Polysciences Inc. (Hirschberg an der Bergstrasse, Germany). Manganese (II) chloride tetrahydrate (99%, metals basis) was purchased from Fisher Scientific (Loughborough, UK).

2.3.1 Chapters 3 and 4 Carbon-Based Electrode Slurry Preparation

Table 2.1 Carbon-based slurries tested in Chapters 3 and 4, along with all relevant material masses and mixer volume for one standard batch of slurry. In all slurry types, the solid materials have a total mass of 0.134 g per 10 mL of EtOH.

Electrode Type	Materials for One Batch, Mixed in 10 mL EtOH				
	SWNT	GNP	Graphite	Super-P	PVDF
SWNT	0.134 g	-	-	-	-
GNP	-	0.134 g	-	-	-
50:50	0.067 g	0.067 g	-	-	-
8:1:1	-	-	0.1072 g	0.0134 g	0.0134 g
4:4:1:1	0.0536 g	0.0536 g	-	0.0134 g	0.0134 g

Five different carbon slurries were made and tested throughout Chapters 3 and 4, as shown in Table 2.1. The slurry materials were weighed and left to stir and homogenize overnight. After stirring, a 1 mL syringe was used to measure and place 50 µL of slurry onto the centre of each pre-weighed current collector. For higher viscosity slurries (those containing SWNTs), the tip of the syringe was used to spread them across the current collector surface as much as possible (while keeping the slurry as one connected "island"). Slurry samples were also placed onto a glass slide and spare current collector, for Raman spectroscopy and SEM imaging respectively. The current collectors were left to air dry overnight (applying heat can cause the plastic current collectors to burn). The glass slide and spare current collector were also allowed to air dry before any Raman spectra or SEM images were taken. Once dried, the current collectors were reweighed, and their mass loadings were measured.

2.3.2 Chapter 5 Manganese Oxide Inverse-Opal Preparation

To prepare a pristine surface for inverse-opal preparation, a glass slide was cut into 10-12 square pieces with a glass cutter. The protective film on the glass pieces was then removed. To do this the glass pieces were placed into a vial filled with acetone and sonicated for 5 minutes.

They were then placed into a vial filled with IPA and sonicated for 5 minutes. Lastly, they were placed into a vial filled with deionised water and sonicated for a final 5 minutes, then subsequently dried in an oven for approximately one hour. To prepare the sacrificial opal template, a 4 mL vial was filled with 2 mL of Polystyrene Polybead® Microspheres (2.7% solids, 0.50 μm) and 2 mL of IPA. The mixture was agitated with a syringe needle to achieve homogeneity. Using a 1 mL syringe and needle, several drops of the opal template were drop casted onto each of the prepared glass pieces, such that the glass was entirely covered in a layer of template without spilling over the sides (the needle of the syringe can be used to gently spread the template across the glass, taking care not to scratch the glass). The template-covered glass pieces are allowed to air dry for approximately three hours (or just overnight).

Next, the inverse-opal precursor material was prepared, consisting of a 0.1 M $MnCl_2.4H_2O$ in IPA solution. 0.1979 g of $MnCl_2.4H_2O$ was carefully weighed and added to a 10mL volumetric flask, followed by 10 mL of IPA. A magnetic stirring bar was added, and the solution was allowed to mix and homogenise overnight. Next, using a 1 mL syringe and needle, several drops of the precursor solution were added to each of the dried template-covered glass pieces until the entire surface is wetted (one drop near each corner of the glass piece is usually sufficient). The glass pieces were then added to the furnace and heated at 450 ºC for one hour. Following this, the glass pieces are removed from the furnace and allowed to cool. Finally, using a spatula, the final MO-IO product is scraped off the glass pieces into a labelled vial for storage.

2.3.3 Chapter 5 Carbon-MO-IO Composite Electrode Preparation

For the initial few carbon-MO-IO composites in Chapter 5 (as seen in Table 2.2) the same procedure was used for slurry formation in Chapters 3 and 4. The components were weighed out and left to stir and homogenize in EtOH overnight. After stirring, a 1 mL syringe was used

to measure and place 50 μL of slurry onto the centre of each pre-weighed current collector, gently spreading the slurry across the current collector as much as possible.

Table 2.2 Composite slurries made and tested for the first part of Chapter 5, with all relevant material masses for one standard "batch" of slurry. In all slurry types, the solid materials have a total mass of 0.134 g per 10 mL of EtOH.

Slurry Type (wt.%)	Materials Used for One Batch			
	MO-IO	SWNT	GNP	Super-P
20:40:40	0.0268 g	0.0536 g	0.0536 g	-
20:35:35:10	0.0268 g	0.0469 g	0.0469 g	0.0134 g

Table 2.3 Composite slurries made and tested for the latter part of Chapter 5, showing all relevant material masses for one "batch" of slurry. To cut down on waste, smaller batches of slurry were made (0.012 g of solid material in total), with enough to load 12 current collectors and keep two samples of slurry for characterisation.

Slurry Type (wt.%)	Materials Used for One Batch				
	MO-IO	SWNT	GNP	Super-P	PVDF
75:20:5	0.009 g	-	-	0.0024 g	0.0006 g
37.5:37.5(GNP):20:5	0.0045 g	-	0.0045 g	0.0024 g	0.0006 g
37.5:37.5(SWNT):20:5	0.0045 g	0.0045 g	-	0.0024 g	0.0006 g

After these initial slurries were prepared and tested, a different preparation method was implemented in the latter part of Chapter 5 to improve the slurry coverage across the current collector surfaces. The electrode components (as shown in Table 2.3) were individually weighed and placed into a mortar. The components were ground for several minutes until a homogenous powder was obtained. Several drops of EtOH were added to the powder, and mixed until a slurry is obtained. A small paintbrush was used to deposit a uniform layer of slurry across the entire surface of the current collectors, which resulted in better coverage than

the earlier deposition method. As before, samples of each slurry were also deposited onto a glass slide and spare current collector for materials characterisation.

2.4 Materials Characterisation Techniques

2.4.1 Raman Spectroscopy

Raman spectroscopy is a common analytical technique that obtains information on the molecular structure and vibrational modes of a sample material. The technique works by shining monochromatic laser light onto a sample material. The interaction of the photons with the molecules of the sample material results in the polarization of the molecular electron cloud, and the formation of short-lived virtual states. The molecule temporarily exists in an elevated energy state, due to the transference of the photon's energy to the molecule. This state is inherently unstable, and the photon is quickly reemitted as scattered light [4, 5].

Most photons are scattered elastically, meaning they possess the same energy as the incident radiation and the molecule electron cloud returns to its original position. This process is known as Rayleigh scattering. In a small number of cases, transference of energy from the molecule to the photon (or vice versa) results in inelastic scattering, where the reemitted photon possesses higher or lower energy than the incident photons. This higher and lower energy photon scattering is known as Raman scattering (more specifically, Raman anti-Stokes scattering and Raman Stokes scattering respectively). The technique of Raman spectroscopy analyses the difference in frequency between incident and scattered photons (the Raman shift), providing insight into the vibrational modes and molecular bond structures of a sample material [6].

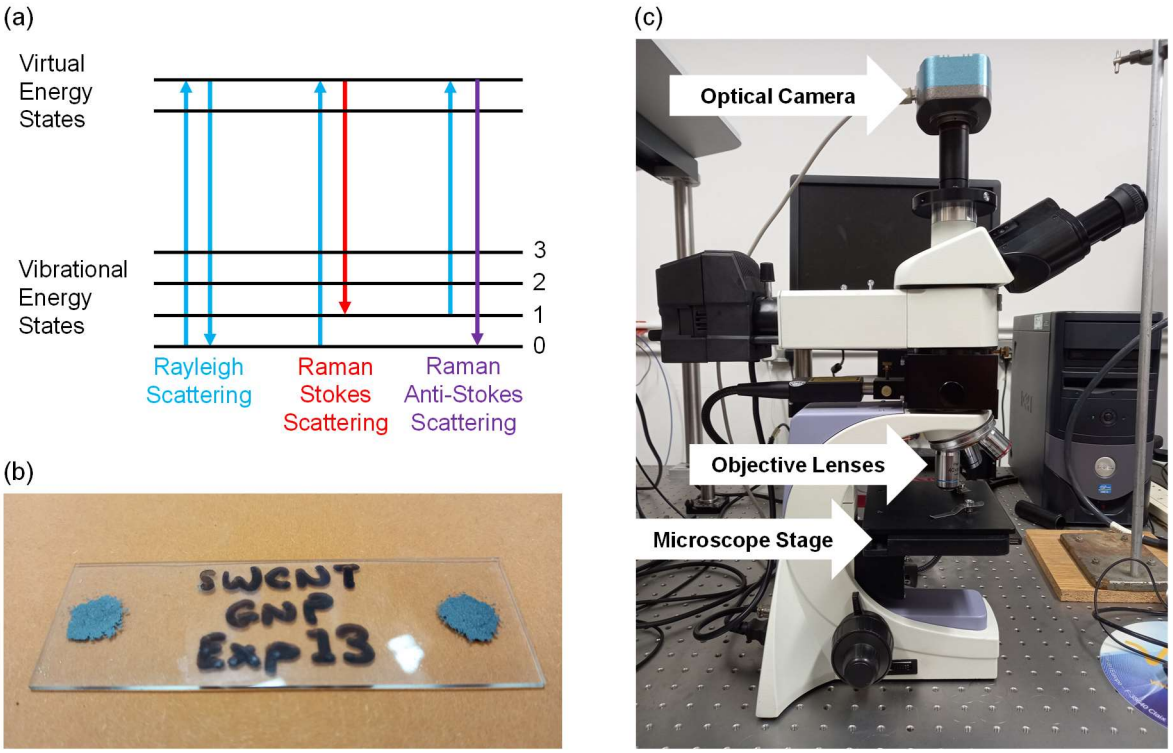

Figure 2.3 (a) Basic energy state schematic for elastic scattering (Rayleigh), and inelastic scattering (Stokes and anti-Stokes) processes occurring during Raman spectroscopy. (b) A glass slide containing slurry samples set aside for Raman spectroscopy analysis (50:50 slurry is shown in the example used here). (c) The Raman spectroscopy setup used throughout the thesis, with the sample glass slide being placed onto the microscope stage, and the laser light focused onto the sample using the objective lenses of the microscope setup.

2.4.2 Scanning Electron Microscopy and Electron Dispersive X-Ray Analysis

The surface morphology and composition of materials in this work were investigated using scanning electron microscopy (SEM), which bombards the surface of a material with a focused beam of electrons. The interactions between the electrons and the sample material emits signals which are gathered by detectors and generated into images.

The electron gun component of the SEM produces the primary electron beam (the incident electrons that first interact with the sample materials) which travels through the vacuum chamber to bombard the surface of the sample at an acceleration voltage adjustable between 0.2 and 40 kV. A variety of different interactions can occur between primary electrons

and the sample, primarily in the region of the sample surrounding the incident beam, known as the interaction volume. The size, depth, and shape of this interaction volume depends on several factors, including the atomic mass of the sample and the acceleration voltage of the primary electron beam. A higher acceleration voltage (therefore higher energy primary electron beam) can penetrate further into the sample and create a higher volume, teardrop-shaped interaction volume. Conversely, primary electrons are hindered from penetrating deep into the sample at the atomic number of the sample increases, resulting in shallower, hemispherical interaction volumes [7].

The interactions of the primary electrons with the sample atoms can largely be divided into categories of elastic and inelastic. Elastic interactions occur when the incident electrons are deflected off the sample by an atomic nucleus or by outer shell electrons of similar energy, resulting in backscattered electrons (BSEs) which have almost identical energy to the primary incident electrons [8]. Inelastic scattering occurs when there is a loss of kinetic energy from the primary electron. One such interaction is the production of secondary electrons (SE), which originate from within the sample material, but interact with the incident primary electrons such that there is a transference of kinetic energy, allowing the secondary electrons to escape the sample material. SEs are mostly formed at the surface of the sample; therefore, SE images are useful for determining surface detail of a sample [9]. BSEs occur in the deeper part of the sample surface, therefore images generated from them give insight into the sample composition, topography, crystallography, and mass thickness [10].

The resolution of the image obtained depends on the probe spot size and current density. The sample must also be adequately electronically conductive, or else charge buildup on the surface of the sample causes distortion of the images. Metal sputtering can be used to add conductivity to samples but was never used in this work due to the inherent conductivity of the samples. In Chapters 3 and 4, SEM images of Vat-P and FDM printed current collectors and

the carbon-based electrode materials were obtained using an FEI Quanta 650 SEM with accelerating voltages ranging from 5 kV to 20 kV. In Chapter 5, SEM images of pure manganese oxide inverse-opals and the carbon-MO-IO composite electrode slurries were obtained using a Zeiss Supra 40 SEM with an accelerating voltage of 15 kV.

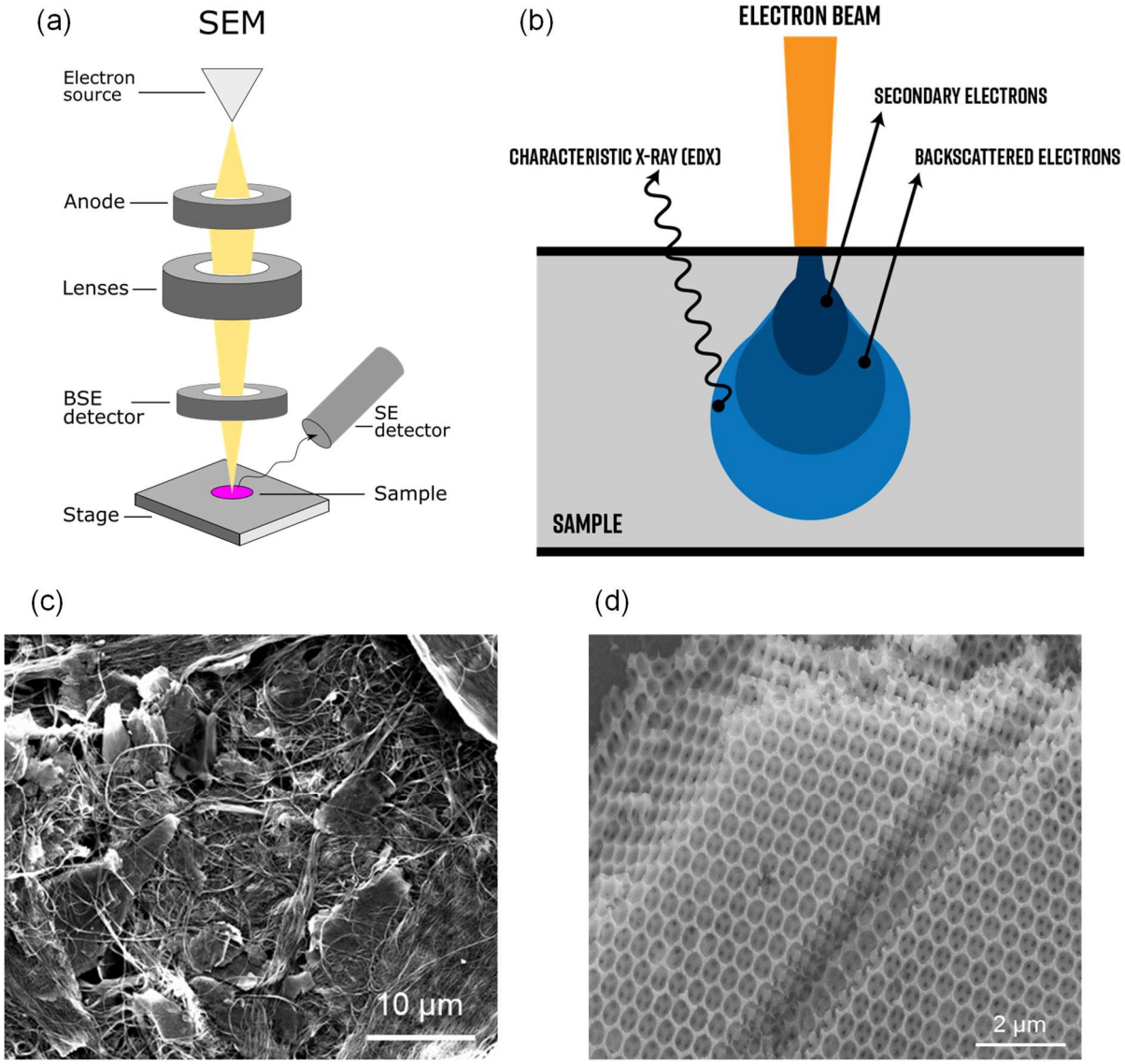

Figure 2.4 (a) Schematic for typical SEM setups [11]. Copyright 2023, AnaPath Services GmbH. (b) Schematic for the interaction of incident (primary) electrons with the sample, showing the formation of secondary electrons closer to the sample's surface and the formation of backscattering electrons deeper into the sample [12]. Copyright 2024, Nanoscience Instruments. (c) Image of 50:50 (SWNT:GNP) carbon electrode slurry taken using an FEI Quanta 650 SEM at an acceleration voltage of 5 kV. (d) Image of pure Mn_3O_4-IOs taken using a Zeiss Supra 40 SEM at an acceleration voltage of 15 kV.

2.4.3 Resistance Measurement Techniques

A core aspect of the work undertaken in this thesis involves the comparison of Vat-P and FDM printed current collectors within additively manufactured supercapacitor cells. An essential characteristic of efficient current collectors within an energy storage device is high electronic conductivity for transference of electrons to and from the external circuit [13]. As such, tests to measure the electronic resistance of the additively manufactured current collectors were designed and undertaken in Chapters 3 and 4. As seen in Figure 2.5, resistance measurements were taken in different directions and orientations of the current collectors; namely (1) across the diameter of the lattice face, (2) the centre of the lattice face to the edge of the lattice face, (3) the centre of the terminal face to the edge of the terminal face, and (4) the centre of the lattice face to the centre of the terminal face.

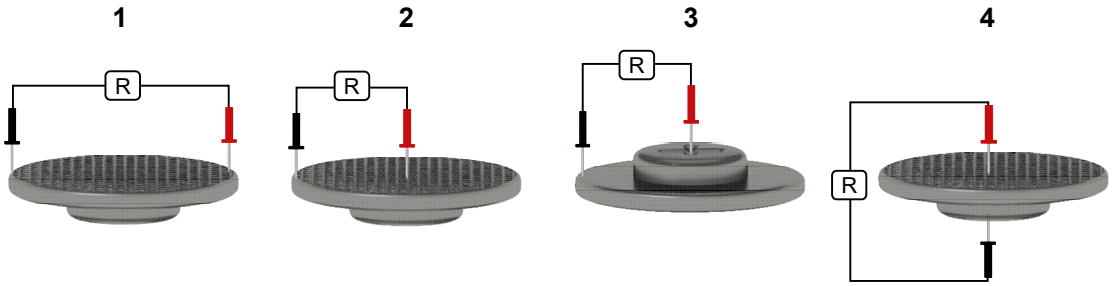

Figure 2.5 Positions of the multi-meter probes used to obtain resistance values from the 3D-printed current collectors. (1) across the diameter of the lattice face, (2) the centre of the lattice face to the edge of the lattice face, (3) the centre of the terminal face to the edge of the terminal face, and (4) the centre of the lattice face to the centre of the terminal face.

2.5 Supercapacitor Cell Assembly

We use 70 mm Whatman™ Glass Microfiber Filters as the separators for these cells. A hole puncher was used to obtain 16 mm circular separators from the larger 70 mm filters. The loaded current collectors were paired and placed within their half-casing. A separator was placed on one of the current collectors per pair.

A 6 M aqueous potassium hydroxide solution (≥85%, pellets, purchased from Sigma Aldrich (Gillingham, UK) was used as an electrolyte for all the supercapacitor cells in this work. In the fume hood, five drops of electrolyte were added to the center of each separator. The two halves of the cells were quickly placed together to prevent electrolyte from evaporating. A lining of Gorilla Epoxy glue was carefully pasted around the edge of the cells where the two half-casings meet. Care was taken that the glue does not contact the gold current collectors when assembling Vat-P current collector cells. The cells were then individually wrapped in several layers of Bemis® Parafilm "M"® laboratory film to hold the cell in place. Paper clamps were used to keep pressure on the cells as the glue cured overnight.

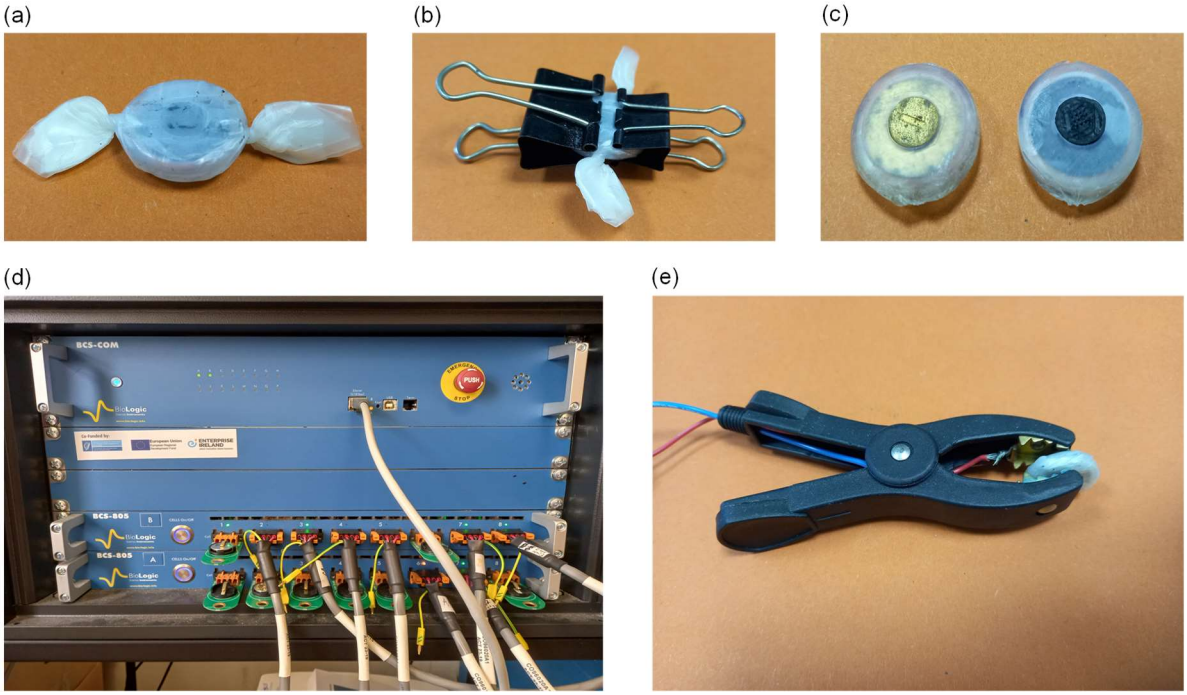

Figure 2.6 (a) Fully-assembled supercapacitor cell wrapped in Bemis® Parafilm "M"® laboratory film. (b) Fully assembled supercapacitor compressed with paper clamps. (c) SLA type current collector on the left, and FDM type current collector on the right. The difference in resolution between the two 3D-printing methods used to make the current collectors is very apparent in this image. The low resolution of the FDM current collectors allow small amounts of liquid electrolyte to leak. (d) The multichannel BioLogic BCS-805 Potentiostat/Galvanostat used for all electrochemical analyses of this work. (e) Assembled supercapacitor cell placed within alligator clips attached to Potentiostat/Galvanostat for electrochemical analysis.

Table 2.4 All cells assembled and tested in this work, listing their 3D-printed current collector type, loaded electrode materials, and voltage window used for electrochemical testing.

Chapter	Current Collector Type	Electrode Materials	Voltage Window
3 (Part 1)	Vat-P	SWNT	0.0–1.0 V
	Vat-P	GNP	0.0–1.0 V
	Vat-P	50:50	0.0–1.0 V
	FDM	SWNT	0.0–1.0 V
	FDM	GNP	0.0–1.0 V
	FDM	50:50	0.0–1.0 V
3 (Part 2)	Vat-P	50:50	0.2–0.7 V
	Vat-P	8:1:1	0.2–0.7 V
	Vat-P	4:4:1:1	0.2–0.7 V
	FDM	50:50	0.2–0.7 V
	FDM	8:1:1	0.2–0.7 V
	FDM	4:4:1:1	0.2–0.7 V
4	FDM (Untreated)	50:50	0.2–0.7 V
	FDM (DMF-Treated (Short))	50:50	0.2–0.7 V
	FDM (DMF-Treated (Long))	50:50	0.2–0.7 V
	FDM (KOH-Treated (Long))	50:50	0.2–0.7 V
5 (Part 1)	Vat-P	20:40:40	0.2–0.7 V
	Vat-P	20:35:35:10	0.2–0.7 V
5 (Part 2)	Vat-P	75:20:5	0.2–0.7 V
	Vat-P	37.5:37.5(GNP):20:5	0.2–0.7 V
	Vat-P	37.5:37.5(SWNT):20:5	0.2–0.7 V
	FDM	75:20:5	0.2–0.7 V
	FDM	37.5:37.5(GNP):20:5	0.2–0.7 V
	FDM	37.5:37.5(SWNT):20:5	0.2–0.7 V

Once the clamps were removed the next day, two circular holes were cut on either side of the cells, exposing the conductive current collector terminals for cell analysis. Due to the lower resolution of the FDM printing method, a small volume of the liquid electrolyte would

sometimes leak from the assembled cell. The details of every batch of cells studied in this work (including the current collector type, electrode slurry type, and electrochemical voltage window) can be found in Table 2.4. Figure 2.6 shows images of several steps of the cell assembly and electrochemical analysis setup.

2.6 Electrochemical Characterisation Techniques

2.6.1 Cyclic Voltammetry

Cyclic Voltammetry (CV) remains one of the most widely used and insightful techniques in electrochemistry, providing insight into the oxidation and reduction processes occurring (or in the case of EDLCs, not occurring) within a chemical system, as well as determining the contributions of faradaic and non-faradaic processes within an energy storage system.

The basic setup of a CV test involves sweeping the electrode potential between two defined potential limits, known as the voltage window. Once the upper limit of the voltage window is reached, the potential is reversed, and the potential is swept back to the lower limit of the voltage window. The scan rate (v) of a CV test refers to the rate (linearly with time) at which the potential is swept [14]. A voltammogram is generated from the CV test, plotting the current versus the potential during the CV scans. The shapes of the voltammograms (and how the shape changes relative to scan rate) and the presence/lack of anodic and cathodic peaks provides an abundance of information on the workings and processes of the studied electrochemical system.

In the case of the EDLC devices studied in this work, ideal CV voltammograms should be rectangular in shape, with a total absence of anodic and cathodic peaks [15]. The reason for this CV curve shape is the non-faradaic electrostatic charge storage mechanism (the

adsorption/desorption of electrolyte ions on the electrode material surface), which allows for the linear storage and release of charge with the potential [16]. Deviations from this shape could be indicative of excessively high scan rate, electrolyte degradation brough about by a too-wide voltage window [17, 18], high internal resistance of the EDLC device [19], and/or parasitic side reactions occurring within the cell [20]. As such, the voltammogram shapes are very useful for diagnostic purposes for poorly performing cells (as seen in Chapter 3).

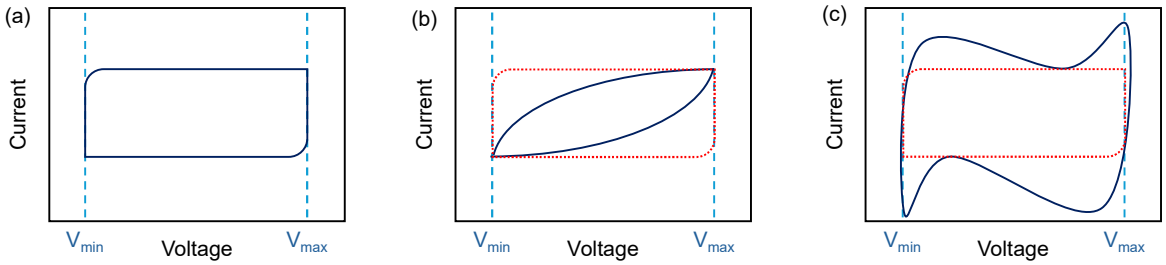

Figure 2.7 Graphical representations the CV responses of (a) an ideal, high conductivity EDLC device (distinct rectangular CV curve), (b) an EDLC device suffering from high internal resistance (skewed, leaf-shaped CV curve) [19], and (c) an EDLC device with pseudo-capacitive contributions to overall performance [21].

The generated voltammograms are also commonly used to calculate charge storage for energy storage devices, as is done throughout this thesis. Equation 3.1 was used to calculate specific capacitance from obtained CV voltammograms [22, 23], where C_m is the specific capacitance (F/g), $\int I\,dv$ is the integrated area of the entire CV curve (AV), m is the mass of electrode active material (g), ΔV is the voltage window (the voltage range bound between the lowest and highest potential, such as V_{min}–V_{max} in Figure 2.7) (V), and v is the scan rate (V/s):

$$C_m = \frac{1}{2m\Delta Vv}\int I\,\mathrm{d}v \qquad \text{Equation 2.1}$$

2.6.2 Galvanostatic Charge-Discharge

Galvanostatic charge-discharge cycling (GDC) is another ubiquitous and useful technique in electrochemistry, extensively used throughout this work. The basic workings of a GDC test

involves applying a constant applied current to an electrochemical system and recording the change in potential with respect to time. As with the CV tests, a predetermined voltage window is often applied to the test, and when the potential threshold is reached, the applied current polarity is reversed until the other potential threshold is reached. For supercapacitors, this charge-discharge process is repeated many thousands of times (even up to a million charge-discharge cycles in this work) to simulate the repeated charging and discharging of the supercapacitors' operational life [24].

For the EDLC devices studied in this work, the ideal GCD curve response would possess linear charge and discharge curves, be perfectly symmetrical, and last many tens of thousands of charge-discharge cycles before cell degradation begins to take place [25]. The isosceles triangle shape of the curves suggests ideal, fully reversible capacitive behavior caused by the formation of electronic double layers from adsorption and desorption of electrolyte ions [26]. Deviation from this shape could indicate the occurrence of electron transfer faradaic processes, which are far more apparent in pseudocapacitive systems [27, 28].

Many vital performance metrics can easily be obtained from GCD data, such as specific capacitance (the ability of the supercapacitor cell to store charge per unit loading mass), and coulombic efficiency (ratio of charge delivered versus charged stored, i.e., discharge capacitance versus charge capacitance). The presence or lack of ohmic drops in the charge-discharge curves (and their size relative to the overall voltage window) indicate the level of internal resistance within the supercapacitor cell (a metric of particular importance in Chapter 3, when comparing the electrochemical performance of 3D-printed cells containing either Vat-P printed or FDM printed current collectors), with a larger ohmic drop indicating higher internal resistance.

Two distinct forms of GCD testing were utilised in this work. The cycle life response test is the first, which cycles the supercapacitor cells many thousands of times (up to one million charge-discharge cycles in some sections of this work) while keeping the charging and discharging applied currents constant throughout the duration of the test. The purpose of this test is to simulate the working life of the supercapacitor cell, subjected to many charge-discharge cycles over a long period of time. The specific capacitance values and coulombic efficiency versus cycle number, and charge-discharge curve shapes at different points of the test are graphed to monitor any degradation or changes in electrochemical performance for the supercapacitor cells, which as discussed previously, often possess a cycle life in the range of hundreds of thousands (of not millions) of charge-discharge cycles [29].

The second form of GCD testing designed and used in this work was a rate capability test (or rate response test). Instead of testing the cycle life response over many charge-discharge cycles, this test instead analyses the response of the cell with stepwise increase in applied current over fewer numbers of charge-discharge cycles. This test determines the supercapacitor cell performance and charge transfer efficiency at higher applied currents. After subjecting the supercapacitor cell to high applied currents, the applied current is reduced to the lowest value, used at the beginning of the test. This is used to determine how well the cell recovers from the high applied currents. Good rate performance is indicative of fast and efficient ion adsorption-desorption and charge transfer within the supercapacitor cell [30, 31].

From the obtained GCD curves, Equation 2.2 was used to calculate the specific capacitance of the supercapacitor cells [32], where C_m is specific capacitance (F/g), I is applied current (A), t is discharge time (s), m is mass of electrode active material (g), and ΔV is voltage window (V):

$$C_m = \frac{It}{m\Delta V} \qquad \text{Equation 2.2}$$

From the specific capacitance (C_m) values calculated using Equations 2.1 or 2.2, the specific energy (energy stored per unit loading mass [33]) of the supercapacitor cells can be calculated using Equation 2.3 [34–36], where E is specific energy (Wh/kg), C_m is specific capacitance (F/g), and ΔV is voltage window (V). Specific energy without dividing by 3.6 gives a value in units of J/g. Multiplying by a value of 1,000 g/kg converts from J/g to J/kg. As 3,600 Joules is equivalent to 1 Watt hour, dividing by a value of 3,600 J/Wh converts from J/kg to Wh/kg. This is simplified to a division of 3.6:

$$E = \frac{(0.5)(C_m)(\Delta V)^2}{3.6} \qquad \text{Equation 2.3}$$

From the specific energy (E) calculated from Equation 2.3, the specific power (power of charge delivered per unit loading mass, a particular advantage of supercapacitors [37]) of the cells can be obtained using Equation 2.4 [34–36], where P is specific power (W/kg), E is specific energy (Wh/kg), and t is discharge time (s). Multiplying by 3,600 s/h converts the discharge time from seconds to hours:

$$P = \frac{(E)(3{,}600)}{t} \qquad \text{Equation 2.4}$$

The internal resistance of the supercapacitor cells was calculated using Equation 2.5, from the ohmic drops present in charge-discharge data under galvanostatic conditions [38]. R is total internal resistance (Ω), ΔV_{drop} is the Ohmic voltage drop (V), I is the applied charging/discharging current (A):

$$R = \frac{\Delta V_{drop}}{2I} \qquad \text{Equation 2.4}$$

The capacitance retention of the supercapacitor cells at different stages of the cycle life GCD tests was calculated using Equation 2.5, where C_{ret} is the specific capacitance retention of the cell (%), $C_{nth\ cycle}$ is the specific capacitance of the cell at a chosen cycle (F/g), and C_{max} is the maximum specific capacitance achieved by that cell (F/g):

$$C_{ret} = \frac{C_{nth\ cycle}}{C_{max}} \times 100\% \qquad \text{Equation 2.5}$$

The capacity of the supercapacitor cells was calculated with Equation 2.6, where I is the discharge current (A), and Δt is the discharge time (h). The resulting *Capacity* (Ah) can be multiplied by 1,000 mA/A or 1,000,000 µA/A to convert the final units to mAh or µAh respectively:

$$Capacity = (I)(\Delta t) \qquad \text{Equation 2.6}$$

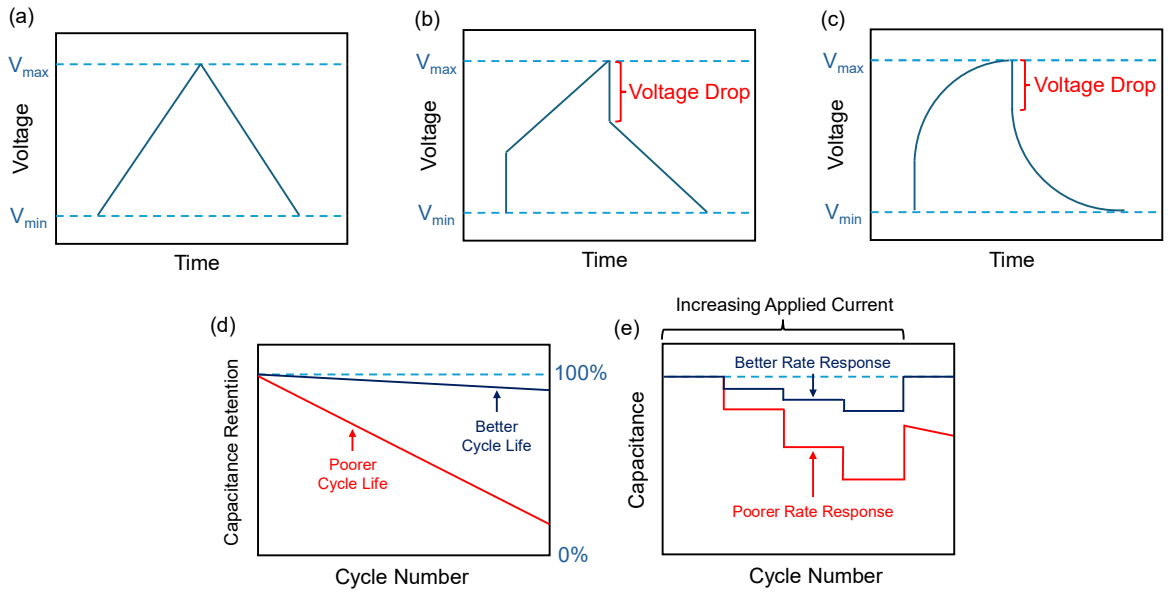

Figure 2.8 (a) An ideal, high conductivity EDLC device (linear, symmetrical charge-discharge curves), (b) an EDLC device suffering from high internal ohmic resistance (indicated by the high voltage drop), (c) a supercapacitor device including pseudo-capacitive contributions to overall charge storage (asymmetric, curved charge-discharge response). In this case, the voltage drop can include contributions from ohmic resistance and redox overpotentials. Graphical representations of (d) a cycle life test used extensively throughout this work, and (e) a rate capability test, comparing a better rate performance (retains higher portion of capacitance with increasing applied current, recovers to original performance when applied current is reduced) to a poorer one (retains lower portion of capacitance when applied current increases, and is permanently degraded because of the higher applied current).

2.6.3 Electrochemical Tests Settings

All electrochemical tests were carried out at room temperature on assembled 3D-printed supercapacitor coin cells using a multichannel BioLogic BCS-805 Potentiostat/Galvanostat (BioLogic Science Instruments, Seyssinet-Pariset, France).

For the first part of Chapter 3 (chronologically, the earliest experiments of this thesis), the electrochemical test settings are as follows. For the cyclic voltammetry tests, the cells are cycled at a voltage window of 0.0–1.0 V vs. E_{oc}, and at scan rates of 5, 10, 15, 20, 25, 30, 40, 50, 100, 250, 500, 1000, 2000, and 5000 mV/s (14 techniques). The cells are cycled for 10 cycles per scan rate, adding to 140 cycles in total.

For the cycle life tests, the cells were subjected to 100,000 cycles under galvanostatic conditions. The cells were cycled between 0.0 and 1.0 V vs. E_{oc} at an applied charging current of +500 μA (specific applied current of +0.167 A/g) and an applied discharging current of -500 μA (specific applied current of -0.167 A/g).

For the second part of Chapter 3 and the entirety of Chapters 4 and 5, the electrochemical test settings are as follows. For the cyclic voltammetry tests, the cells are cycled at scan rates of 5, 10, 15, 20, 25, 30, 40, 50, 100, 250, 500, 1000, 2000, and 5000 mV/s (14 techniques). The cells are cycled for 10 cycles per scan rate, adding to 140 cycles in total. A voltage window of 0.2–0.7 V vs. E_{oc} is used for this test.

For the cycle life tests, the cells were subjected to 1,000,000 charge-discharge cycles under galvanostatic conditions. The cells were cycled between 0.2 and 0.7 V vs. E_{oc} at an applied charging current of +500 μA (specific applied current of +0.167 A/g) and an applied discharging current of -500 μA (specific applied current of -0.167 A/g).

For the rate capability tests, the cells were cycled between 0.2 and 0.7 V vs. E_{oc} at an initial minimum charge and discharge applied current of ±100 µA (0.033 A/g) for 50 charge-discharge cycles. The 50 charge-discharge cycles were repeated for each of the following increasing applied currents ±200 µA (0.067 A/g), ±300 µA (0.100 A/g), ±400 µA (0.133 A/g), ±500 µA (0.167 A/g), ±600 µA (0.200 A/g), ±700 µA (0.233 A/g), ±800 µA (0.267 A/g), ±900 µA (0.300 A/g), ±1 mA (0.333 A/g). After 50 charge-discharge cycles at the maximum applied current of ±1 mA (0.333 A/g), the current is reduced to the minimum applied current of ±100 µA (0.033 A/g) for a final 50 charge-discharge cycles.

2.7 References

[1] V. Egorov, U. Gulzar and C. O'Dwyer, "3D Printed Rechargeable Aqueous and Non-Aqueous Lithium-Ion Batteries: Evolution of Design and Performance," *ECS Advances,* vol. 2, no. 4, p. 040508, 2023.

[2] U. Gulzar, V. Egorov, Y. Zhang and C. O'Dwyer, "Recyclable 3D-Printed Aqueous Lithium-Ion Battery," *Advanced Energy & Sustainable Research,* vol. 4, no. 10, p. 2300029, 2023.

[3] S. O'Hanlon and C. O'Dwyer, "Electrodeposition onto Conductive Additive-Impregnated 3D Printed Polylactic Acid Electrodes.," *Journal of The Electrochemical Society,* vol. 169, no. 8, p. 082514, 2022.

[4] N. Colthup, L. Daly and S. Wiberley, Introduction to Infrared and Raman Spectroscopy, New York: Academic Press, Inc., 1975.

[5] D. Le Pevelen, "NIR FT-Raman," in *Encyclopedia of Spectroscopy and Spectrometry (Third Edition)*, Academic Press, Inc., 2017, pp. 98-110.

[6] E. Smith and G. Dent, Modern Raman Spectroscopy: A Practical Approach (Second Edition), John Wiley and Sons Ltd, 2019.

[7] B. Inkson, "Scanning electron microscopy (SEM) and transmission electron microscopy (TEM) for materials characterization," in *Materials Characterization Using Nondestructive Evaluation (NDE) Methods*, Woodhead Publishing, 2016, pp. 17-44.

[8] W. Zhou, R. Apkarian, Z. Wang and D. Joy, "Fundamentals of Scanning Electron Microscopy (SEM)," in *Scanning Microscopy for Nanotechnology: Techniques and Applications*, Springer, 2007, pp. 1-40.

[9] F. Hidayanti and A. Harnovan, "Application of Scanning Electron Microscopy: A Review," *International Journal of Applied Science and Engineering Review,* vol. 1, no. 6, pp. 91-102, 2020.

[10] J. Goldstein, D. Newbury, J. Michael, N. Ritchie, J. Scott and D. Joy, "Backscattered Electrons," in *Scanning Electron Microscopy and X-Ray Microanalysis*, Springer Nature, 2017, pp. 15-28.

[11] AnaPath, "Electron Microscopy," AnaPath, [Online]. Available: https://anapath.ch/electron-microscopy-2/. [Accessed 07 August 2024].

[12] Nanoscience Instruments, "Struck by an Electron Beam: Interactions at the Surface in SEM," Nanoscience Instruments, [Online]. Available: https://www.nanoscience.com/blogs/struck-by-an-electron-beam-interactions-at-the-surface-in-sem/. [Accessed 07 August 2024].

[13] A. Abdisattar, M. Yeleuov, C. Daulbayev, K. Askaruly, A. Tolynbekov, A. Taurbekov and N. Prikhodko, "Recent advances and challenges of current collectors for supercapacitors," *Electrochemistry Communications,* vol. 142, p. 107373, 2022.

[14] N. Elgrishi, K. Rountree, B. McCarthy, E. Rountree, T. Eisenhart and J. Dempsey, " A practical beginner's guide to cyclic voltammetry.," *Journal of chemical education,* vol. 95, no. 2, pp. 197-206, 2018.

[15] D. Bograchev, Y. Volfkovich and S. Martemianov, "Diagnostics of supercapacitors using cyclic voltammetry: Modeling and experimental applications," *Journal of Electroanalytical Chemistry,* vol. 935, p. 117322, 2023.

[16] W. Dong, M. Xie, S. Zhao, Q. Qin and F. Huang, "Materials design and preparation for high energy density and high power density electrochemical supercapacitors," *Materials Science and Engineering: R: Reports,* vol. 152, p. 100713, 2023.

[17] L. Suo, O. Borodin, T. Gao, M. Olguin, J. Ho, X. Fan, C. Luo, C. Wang and K. Xu, ""Water-in-salt" electrolyte enables high-voltage aqueous lithium-ion chemistries.," *Science,* vol. 350, no. 6263, pp. 938-943, 2015.

[18] T. Mathis, N. Kurra, X. Wang, D. Pinto, P. Simon and Y. Gogotsi, "Energy Storage Data Reporting in perspective—guidelines for interpreting the performance of electrochemical energy storage systems.," *Advanced Energy Materials,* vol. 9, no. 39, p. 1902007, 2019.

[19] D. Boonpakdee, C. Yévenes and W. Surareungchai, "Exploring non-linearities of carbon-based microsupercapacitors from an equivalent circuit perspective.," *Journal of Materials Chemistry A,* vol. 6, no. 16, pp. 7162-7167, 2018.

[20] M. He, K. Fic, E. Frąckowiak, P. Novák and E. Berg, "Influence of aqueous electrolyte concentration on parasitic reactions in high-voltage electrochemical capacitors," *Energy Storage Materials,* vol. 6, pp. 111-115, 2016.

[21] Y. Jiang and J. Liu, "Definitions of Pseudocapacitive Materials: A Brief Review," *Energy and Environmental Materials,* vol. 2, no. 1, pp. 30-37, 2019.

[22] Y. Shi, M. Zhang, D. Yang and J. Li, "Study on preparation of high performance manganese dioxide supercapacitor by cyclic voltammetry.," *Ionics,* vol. 27, no. 10, pp. 4521-4529, 2021.

[23] P. Wuamprakhon, R. Crapnell, E. Sigley, N. Hurst, R. Williams, M. Sawangphruk, E. Keefe and C. Banks, "Recycled Additive Manufacturing Feedstocks for Fabricating High Voltage, Low-Cost Aqueous Supercapacitors.," *Advanced Sustainable Systems,* vol. 7, no. 2, p. 2200407, 2023.

[24] C. Masarapu, H. Zeng, K. H. Hung and B. Wei, "Effect of Temperature on the Capacitance of Carbon Nanotube Supercapacitors," *ACS Nano,* vol. 3, no. 8, pp. 2199-2206, 2009.

[25] A. Dang, T. Li, C. Xiong, T. Zhao, Y. Shang, H. Liu, X. Chen, H. Li, Q. Zhuang and S. Zhang, "Long-life electrochemical supercapacitor based on a novel hierarchically carbon foam templated carbon nanotube electrode," *Composites Part B: Engineering,* vol. 141, pp. 250-257, 2018.

[26] Y. Zhang, X. Li, Z. Li and F. Yang, "Evaluation of electrochemical performance of supercapacitors from equivalent circuits through cyclic voltammetry and galvanostatic charge/discharge," *Journal of Energy Storage,* vol. 86, no. A, p. 111122, 2024.

[27] Y. Volfkovich, A. Mikhailin, D. Bograchev, V. Sosenkin and V. Bagotsky, "Studies of Supercapacitor Carbon Electrodes eith High Pseudocapacitance," in *Recent Trend in Electrochemical Science and Technology*, InTech, 2012, pp. 159-182.

[28] S. Ingole, S. Navale, Y. Navale, I. Dhole, R. Mane, F. Stadler and V. Patil, "Galvanostatically electroplated MnO2 nanoplate-type electrode for potential electrochemical pseudocapacitor application," *Journal of Solid State Chemistry,* vol. 21, pp. 1817-1826, 2017.

[29] Z. Qiu, Y. Wang, X. Bi, T. Zhou, J. Zhou, J. Zhao, Z. Miao, W. Yi, P. Fu and S. Zhuo, "Biochar-based carbons with hierarchical micro-meso-macro porosity for high rate and long cycle life supercapacitors," *Journal of Power Sources,* vol. 376, pp. 82-90, 2018.

[30] I.-L. Tsai, J. Cao, L. Le Fevre, B. Wang, R. Todd, R. Dryfe and A. Forsyth, "Graphene-enhanced electrodes for scalable supercapacitors," *Electrochimica Acta,* vol. 257, pp. 372-379, 2017.

[31] Q. Shao, J. Tang, Y. Lin, J. Li, F. Qin, K. Zhang, J. Yuan and L.-C. Qin, "Ionic liquid modified graphene for supercapacitors with high rate capability," *Electrochimica Acta,* vol. 176, pp. 1441-1446, 2015.

[32] V. Subramanian, H. Zhu, R. Vajtai, P. Ajayan and B. Wei, "Hydrothermal synthesis and pseudocapacitance properties of MnO2 nanostructures.," *The Journal of Physical Chemistry B,* vol. 109, no. 43, pp. 20207-20214, 2005.

[33] S. Wong, J. Sunarso, B. Wong, H. Lin, A. Yu and B. Jia, "Towards enhanced energy density of graphene-based supercapacitors: Current status, approaches, and future directions," *Journal of Power Sources,* vol. 396, pp. 182-206, 2018.

[34] M. Iqbal and U. Aziz, "Supercapattery: Merging of battery-supercapacitor electrodes for hybrid energy storage devices.," *Journal of Energy Storage,* vol. 46, p. 103823, 2022.

[35] Y. Tao, X. Xie, W. Lv, D. Tang, D. Kong, Z. Huang, H. Nishihara, T. Ishii, B. Li, D. Golberg and F. Kang, "Towards ultrahigh volumetric capacitance: graphene derived highly dense but porous carbons for supercapacitors.," *Scientific reports,* vol. 3, no. 1, p. 2975, 2013.

[36] L. Fan, Q. Tu, C. Geng, J. Huang, Y. Gu, J. Lin, Y. Huang and J. Wu, "High energy density and low self-discharge of a quasi-solid-state supercapacitor with carbon nanotubes incorporated redox-active ionic liquid-based gel polymer electrolyte.," *Electrochimica Acta,* vol. 331, p. 135425, 2020.

[37] Y. Volfkovich, "High power supercapacitors. Review," *Journal of Electroanalytical Chemistry,* vol. 963, p. 118290, 2024.

[38] J. Gittins, Y. Chen, S. Arnold, V. Augustyn, A. Balducci, T. Brousse, E. Frackowiak, P. Gómez-Romero, A. Kanwade, L. Köps, P. Jha, D. Lyu, M. Meo, D. Pandey, L. Pang, V. Presser, M. Rapisarda, D. Rueda-García, S. Saeed, P. Shirage, Ślesiński and al., "Interlaboratory study assessing the analysis of supercapacitor electrochemistry data," *Journal of Power Sources,* vol. 585, p. 233637, 2023.

Chapter 3

Comparison of Symmetric Carbon Supercapacitors Made Using Different 3D-Printing Methods and Materials

Adapted from: The Influence of 3D Printing Methods and Materials on the Response of Printed Symmetric Carbon Supercapacitors https://doi.org/10.1149/2754-2734/ad71df

Abstract

We compare the electrochemical response and intrinsic limitations of symmetric carbon-based supercapacitors using two 3D-printing techniques, vat polymerization (Vat-P) and fused deposition modelling (FDM). Two cell types are made in this study, one with metallized Vat-P-printed current collectors, the other with PLA (polylactic acid) FDM-printed current collectors in a similarly designed printed coin cell. Carbon-based electrode slurry (various combinations of SWNT, GNP, Super-P, PVDF) and aqueous 6M KOH electrolyte are used in these cells. We demonstrate the influence of internal resistance of each 3D-printing method by direct comparison of cyclic voltammetry and galvanostatic charge-discharge tests. The metallized conductive Vat-P cells display better conductivity and more ideal rectangular cyclic voltammetry response but suffer from poor cycle life in initial experiments (~5,000 charge-discharge cycles before losing all specific capacitance). The FDM current collector cells using graphite-containing PLA materials have poorer conductivity, less ideal cyclic voltammetry curves, and are structurally less robust and partially porous, but offer very stable cycle life for supercapacitor cells retaining most of their specific capacitance after 100,000 charge-discharge cycles. The cycle life of the metallized Vat-P cells are improved by reducing the voltage window to 0.2 – 0.7 V to limit metal delamination and using Super-P and PVDF additives.

3.1 Introduction

With the ongoing global energy crisis, producing reliable and efficient methods of energy storage remains an integral part of cutting-edge materials research. Within this topic, 3D-printing (also known as additive manufacturing) has gained momentum over the past few years, evolving from a niche hobby to a reliable scientific tool for materials research [1–3]. Pairing energy storage with 3D-printing provides unparalleled levels of customisation [4–8] and freedom of design, while also eliminating waste material during the manufacturing process. Studies have been undertaken on 3D-printing energy storage materials, but directly comparing more than one 3D-printing method within a single energy storage study is far more seldom researched. In recent years, 3D-printing (also known as additive manufacturing), has been used extensively in many areas of science and engineering, such as prosthetic engineering [9], biological tissue engineering [10, 11], surgery [12], food science [13, 14], and PPE equipment [15]. It has similarly been implemented into the field of energy storage devices, where direct ink writing (DIW) [16, 17], fused deposition modelling (FDM) [18, 19], stereolithography (SLA) which is also generally known as vat polymerization (Vat-P) [20], and several other 3D-printing methods [6, 7] have been used for the design and manufacturing of symmetric carbon supercapacitors, and other energy storage devices for various applications [21]. Reports of supercapacitor devices consisting of only 3D-printed components are rare [22–24], but of great interest for improving the manufacturing of these devices to a single, automated 3D-printing process [18, 25]. Environmental factors should also be taken into consideration, and several studies have reported manufacturing 3D-printing carbon electrodes from recycled waste materials [26]. In a recent study by Aeby et al. a fully disposable and completely 3D-printed paper supercapacitor device is manufactured using functional inks derived from fully renewable, recyclable, and non-toxic materials, achieving a specific capacitance of 25.6 F/g at 1 mV/s (tenfold the specific capacitance of fully 3D-printed devices reported previously) [27].

Both vat polymerization stereolithography (Vat-P) and fused deposition modelling (FDM) are used in this study. Vat-P 3D-printing begins with a bed of photopolymerizable plastic resin, which is solidified [28] selectively by spatial and depth control of incident laser light. From there, layer-by-layer of resin is solidified until a complete plastic model is made. Vat-P is distinctly different from FDM prints, providing a smooth surface finish and high-resolution (~25 μm on the Vat-P printer used here). However, it suffers from long printing times and high cost for raw resin materials [29, 30]. FDM is more well known, and a common material is polylactic acid (PLA) [31], deposited in filamentary fashion by melt extrusion and thermosetting to give prints that are more porous, less uniform and lower resolution compared to Vat-P. Regardless, experimentation with different thermal polymers and printing conditions have been undertaken to maximize the effectiveness of this 3D-printing method [32–34]. These methods have proven useful in examining the possibility for energy storage devices and energy material composite formation from direct printing.

For modifying the conductivity of the added active materials, we also use various conductive carbon additives. Single-walled carbon nanotubes (SWNTs) are an ideal choice due to their ease of incorporation and their electronic conductivity [35] . In comparison to activated carbons (AC), CNTs are shown to have a lower specific capacitance [36], but higher conductivity, resulting in a better specific power performance [37]. Graphene nano-platelets (GNP) consist of several layers of graphene (one-dimensional sheets of sp^2 hybridized hexagonal carbons), usually resulting in a thickness of 1-15 nm [38] that allow very good compositing with other materials in slurries. Graphitic carbons have high conductivity, large surface area, and open porosity; all useful characteristics when it comes to energy storage materials [39, 40]. As graphene materials tend to stack on top of one another, another carbon material (such as CNTs) is often dispersed amongst the graphene sheets to separate them and increase the surface area as much as possible [41, 42]. Super-P (also known as “carbon black”)

is a carbon material produced from partial oxidation of petrochemical precursors [43]. It is a commercially available conductive carbon [44], commonly used as an additive in lithium/sodium ion battery electrodes to improve the conductivity, surface area, and electrochemical performance [45, 46]. Super-P has also been used as a conductive additive in carbon-based nanocomposites for EDLCs [47, 48]. Little information could be found within the context of 3D-printing [49]. Ketjen-black carbon inks have been shown to be printable for stable supercapacitors with consideration to rheology and conductivity [50]. Here, using super-P in slurries with conductive current collectors avoids the need to fine-tune the rheology of the underlying current collectors or printing materials.

An important consideration in 3D printed energy storage devices such as supercapacitors, is the nature, morphology and composition of the printed cells and current collectors and its influence on the overall electrochemical response of the material. FDM materials typically form a filamentary structure often interspersed with opening and pores in its 'woodpile' overlaid deposition. In Vat-P, the print quality is much smoother and consistent, nominally nonporous due to the deposition method. However, incorporation of active materials or conductive additives is limited to small volume fractions and a percolation threshold for electrical conduction. A high concentration of graphite in PLA, for example, causes brittleness that limits cell integrity, while buried materials in Vat-P resins need to be relieved at the surface or coated with metals to ensure good electronical connection to the active material or slurries deposited on top. A detailed summary of these effects can be found elsewhere [6], but a direct comparison between printing methods on identical cells has yet to be reported. Knowledge on the effect of printing methods and active materials is important when considering a technology that allow energy storage devices to be printed with shapes that are different to normal form factors. And for the proliferation of many small-scale printed batteries or supercapacitors, the material choice and their performance is important when considering recyclability and disposal

of the active materials and the entire cell. Here, we investigate the influence of these printing parameters on the overall response of cells using a range of nano-carbons and slurry mixtures for each 3D printing method. Pre- and post-mortem analysis by electron microscopy, Raman scattering spectroscopy, and compositional analysis is linked to slurry composition and the nature of the current collector for each printing method. The work presented here provides a detailed examination of the different behaviour of symmetric carbon supercapacitors made using two different printing methods, FDM and Vat-P. In doing so, we aim to provide valuable insight into the factors that influence electrochemical response and cell stability, including the nature of the printed current collectors and cells, the nature of the composite slurries and for an aqueous system, the improvement offered by reduction in the voltage window for cells that use metallized plastics as their structural components.

3.2 Experimental

A combination of Vat-P and FDM 3D-printing was implemented in this Chapter. The outer casings of the supercapacitors were printed using Vat-P, and the current collectors were printed using either Vat-P or FDM. The printing and processing of the Vat-P 3D-printed components is detailed in Chapter 2.2.1. The printing and processing of the FDM 3D-printed components is detailed in Chapter 2.2.2. The standard batch of cells printed consists of six supercapacitor cells, with 12 current collectors and 12 half-casings printed per batch. As the Vat-P current collector components are electronically insulating, a layer of 50 nm of gold is uniformly sputtered on the surface of these current collectors. The metal sputtering procedure is outlined in Chapter 2.2.3.

Table 3.1 Carbon-based slurries made and tested in this work, along with all relevant material masses and mixer volume for one standard "batch" of slurry. In all slurry types, the solid materials have a total mass of 0.134 g per 10 mL of EtOH.

Slurry Type	Materials Used for One Batch				
	SWNT	GNP	Graphite	Super-P	PVDF
SWNT	0.134 g	-	-	-	-
GNP	-	0.134 g	-	-	-
50:50	0.067 g	0.067 g	-	-	-
8:1:1	-	-	0.1072 g	0.0134 g	0.0134 g
4:4:1:1	0.0536 g	0.0536 g	-	0.0134 g	0.0134 g

Five different carbon slurries were made and tested during this study, as shown in Table 3.1. The process for making these carbon electrode slurries is explained in Chapter 2.3.1. Slurry samples were also placed onto a glass slide and spare current collector, for Raman spectroscopy and SEM imaging respectively. The current collectors were left to air dry overnight, as applying heat can cause the plastic current collectors to burn. The glass slide and spare current collector were also allowed to air dry before any Raman spectra or SEM images were taken. Once dried, the current collectors were reweighed, and their mass loadings were measured. The cells were then assembled according to the procedure outlined in Chapter 2.5.

Figure 3.1 (a) and (f) shows the design of the Vat-P and FDM current collector supercapacitor cells, respectively. Images of the Vat-P printed components for one supercapacitor cell, as well as SEM images of a gold sputtered Vat-P current collector at varying magnifications are shown in Figure 3.1 (b)–(e). Images of the Vat-P casings and FDM current collectors required for one supercapacitor cell, as well as SEM images of an FDM current collector at varying magnifications are shown in Figure 3.1 (g)–(i). Further images of the components after printing, sputtering, loading, and assembly are provided in the supplementary material (Figure 3.S.1).

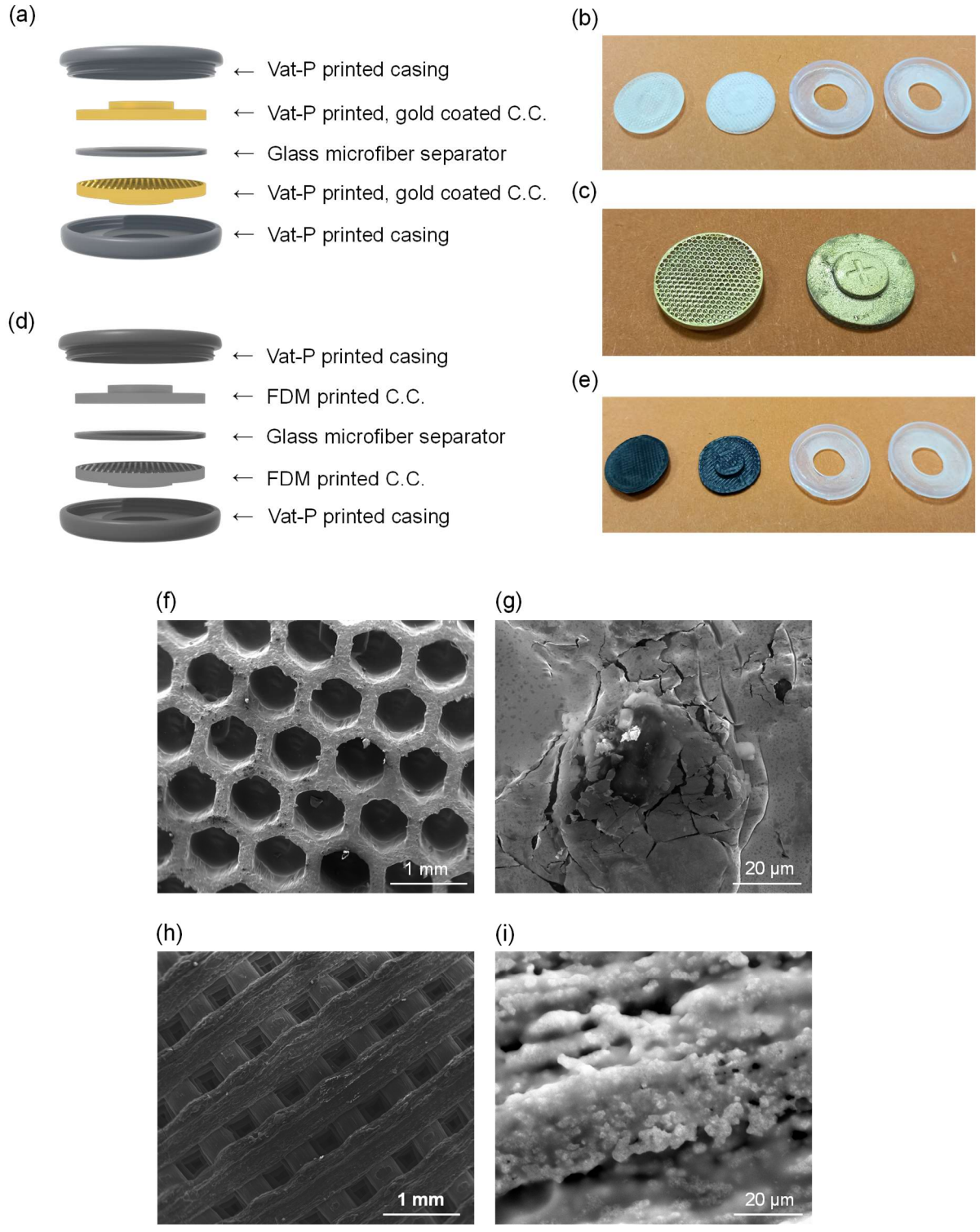

Figure 3.1 Schematic for (a) Vat-P current collector type cell, with images of (b) printed Vat-P current collectors and external casings and (c) gold-sputtered Vat-P current collectors (lattice and terminal face). Schematic for (d) FDM current collector type cell, with an image of (e) FDM-printed current collectors and Vat-P printed external casings. SEM images of bare, gold-sputtered Vat-P current collector at (f) low magnification and (g) high magnification. SEM images of bare FDM current collector at (h) low magnification and (i) high magnification.

Table 3.2 All cells assembled and tested in this Chapter, listing their 3D-printed current collector type, loaded carbon-based slurry, and voltage window used for electrochemical testing.

Current Collector Type	Carbon Slurry	Voltage Window
Vat-P	SWNT	0.0 – 1.0 V
Vat-P	GNP	0.0 – 1.0 V
Vat-P	50:50 (SWNT:GNP)	0.0 – 1.0 V
FDM	SWNT	0.0 – 1.0 V
FDM	GNP	0.0 – 1.0 V
FDM	50:50 (SWNT:GNP)	0.0 – 1.0 V
Vat-P	50:50 (SWNT:GNP)	0.2 – 0.7 V
Vat-P	8:1:1 (Gr:Super-P:PVDF)	0.2 – 0.7 V
Vat-P	4:4:1:1 (SWNT:GNP:Super-P:PVDF)	0.2 – 0.7 V
FDM	50:50 (SWNT:GNP)	0.2 – 0.7 V
FDM	8:1:1 (Gr:Super-P:PVDF)	0.2 – 0.7 V
FDM	4:4:1:1 (SWNT:GNP:Super-P:PVDF)	0.2 – 0.7 V

Samples of the carbon electrode slurries were set aside for materials characterisation. The procedures for the Raman spectroscopy and SEM imaging undertaken are detailed in Chapter 2.4.1 and Chapter 2.4.2, respectively. Resistance measurements on the unloaded gold-sputtered Vat-P and FDM current collectors were also undertaken, as is explained in Chapter 2.4.3.

The assembled supercapacitor cells were testing using a variety of cyclic voltammetry (CV) and galvanostatic charge-discharge (GCD) electrochemical tests. The procedures, theory, and electrochemical settings of these tests are detailed in Chapter 2.6. The first half of this Chapter uses a potential window of 0.0–1.0 V vs. E_{oc} for all electrochemical tests. This is changed to a potential window of 0.2–0.7 V vs. E_{oc} for the latter half of this Chapter. Table 3.2 shows the printed current collector type, carbon electrode slurry, and electrochemical test potential window used for all of the supercapacitor cells studied in this Chapter.

3.3 Results and Discussion

3.3.1 Simple Carbon Electrode Slurries and Wider Voltage Window (0.0 – 1.0 V)

To determine the baseline response of three-different carbon-based materials in aqueous electrolyte in 3D printed supercapacitors, we present the initial structural characterization of their corresponding slurries (see Experimental) on the 3D printed electrodes fabrication using metal-coated SLA printing, and conductive PLA current collectors by FDM printing. The electrochemical characterization of these cells are obtained in the wider voltage window (0.0 – 1.0 V) using consistent slurry formulation and mass loading with each carbon nanostructure. The structural characterization of the different carbon-based slurries used in our Vat-P and FDM current collector cells (see Table 3.2) is presented here in the form of Raman spectra and SEM images, clearly showing the homogeneity and consistency of each slurry type across several different batches. The electrochemical characterization of the assembled supercapacitor cells is undertaken via cyclic voltammetry and charge-discharge tests under galvanostatic conditions.

The Raman spectra for all types of Vat-P and FDM printed cells can be seen in Figure 3.2. The slurries containing SWNT in Figure 3.2 (a)–(c) have distinctive peaks, with an intense G-band (~1600 cm^{-1}) (caused by the stretching of C–C bonds in sp^2 graphitic materials) and a second intense peak in the region of 2600–2700 cm^{-1} known as the G'-band (or 2D-band) [51, 52]. The D-band (~1350 cm^{-1}) is defect-induced, arising from disorder in the sp^2 carbon structure [53, 54]. Using the ratio of intensity of the G and D-bands to indicate the ratio of ordered to disordered carbons, the nanotubes materials here are very ordered. G, G', and D-bands are present in the GNP slurry sample (which does not contain SWNT) are found at similar wavenumbers, but at a much lower intensity than those present in the SWNT containing samples [55–57]. For each slurry, Raman scattering spectra obtained in different region show

a homogenous distribution of materials and consistent modes from the respective nanocarbon after 24 h mixing.

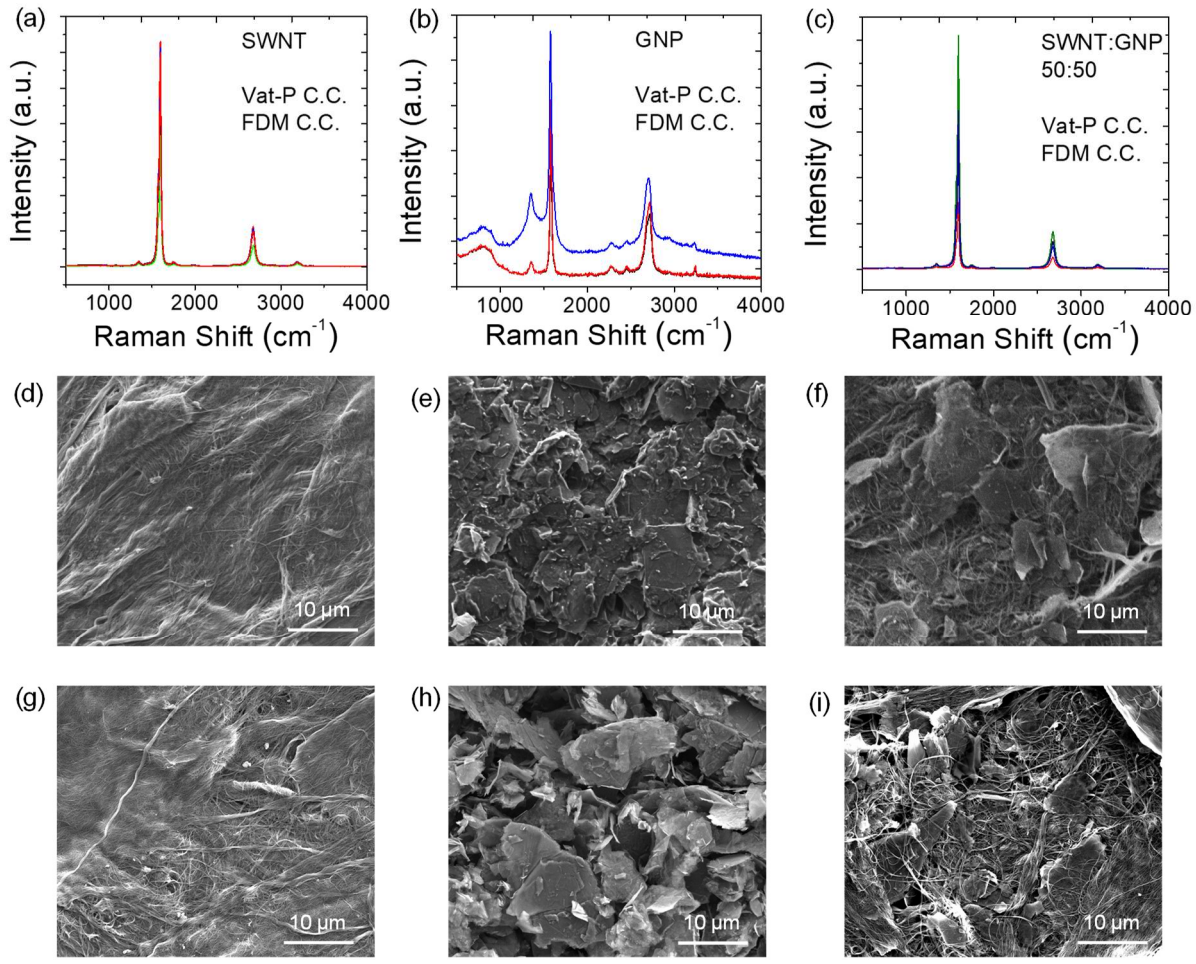

Figure 3.2 Raman scattering spectra of (a) SWNT, (b) GNP, and (c) SWNT:GNP (50:50) slurries made for use with Vat-P and FDM current collectors. Several spectra were acquired from three different regions on each slurry. (d)–(i) SEM images of each slurry morphology prepared for use with each type of printed current collector: (d) and (g) SWNT, (e) and (h) GNP, (f) and (i) SWNT:GNP mixture.

The SEM images in Figure 3.2 shows SEM images of the three carbon slurries prior to any electrochemical tests. The two different carbon types used in these slurries (SWNT and GNP) and in the 50:50 mixture are very distinctive at this magnification. The long, thin fibers of SWNTs [58] and flat, planar flakes of GNP [59] are clearly visible.

Figure 3.3 shows the CV response of cells using Vat-P and FDM printed current collectors with slurries of SWNTs, GNPs and their 50:50 mixture, at scan rates between 5 and 250 mV/s. It is clear that the cells using pure SWNT (Figure 3.3 (a) and (d)) and 50:50 SWNT/GNP mixture (Figure 3.3 (c) and (f)) carbon slurries display better electrochemical response and cumulative integrated charge in their CV curves than the pure GNP (Figure 3.3 (b) and (e)) slurry, for cells using Vat-P and FDM current collectors, indicating higher capacitance for these slurry types. The quasi-rectangular shape and lack of any distinct redox peaks for the Vat-P type cells indicate good EDLC behavior, which is expected for carbon slurry electrodes of this type [40, 60].

However, the Vat-P current collector cells (Figure 3.3 (a)–(c)) also have large, trailing tail-ends at the higher end of the potential window (1.0 V), a clear indicator of parasitic side-reactions or electrode/electrolyte degradation [61]. Though aqueous electrolytes are notorious for their narrow working potential window [62, 63], this is likely not the cause of these trailing peaks, as the upper limit of the potential window used here is still lower than that required for water electrolysis (that being at least 1.23 V) [64, 65]. A more likely explanation for this phenomenon is the reaction of the sputtered gold layer of our current collectors in alkaline electrolyte. Hydroxide ion adsorption reactions forming Au (I) hydroxide, and the formation of gold oxide species in aqueous alkaline solutions have been studied in detail and observed within the potential range used for these electrochemical tests [66–68].

These peaks are not present in the FDM current collector type cells (Figure 3.3 (d)–(f)), despite using the same electrolyte and CV test potential window. This is further evidence to suggest that reactions of the gold sputtered surface (unique to the Vat-P current collectors) in alkaline electrolyte are to blame for the non-ideal CV behaviour. However, the FDM current collector cells suffer from very high internal resistance in comparison to the metallized Vat-P current collector cells evidenced from their CV curves [61, 69]. Higher scan rate CV curves

(up to 5 V/s) for all cells can be viewed in the supplementary material, Figure 3.S.2, where cells with Vat-P printed current collectors and containing SWNTs and SWNT/GNP mixture show excellent rate capability, maintaining their quasi-rectangular shape up to a scan rate of 1 V/s. The CV curves of all other cells using FDM current collectors and Vat-P current collectors with GNP-only, quickly close to a narrow loop with increasing scan rate, which implies a high internal resistance and indicates that their respective carbon slurries and/or current collectors are not suitable for higher discharge rate applications [70, 71]. These CV results show the ordered porous Vat-P current collector cells containing SWNT (either pure SWNT or 50:50 slurry) to be the best performers, with the most ideal EDLC CV shapes, low internal resistance, and good rate capability.

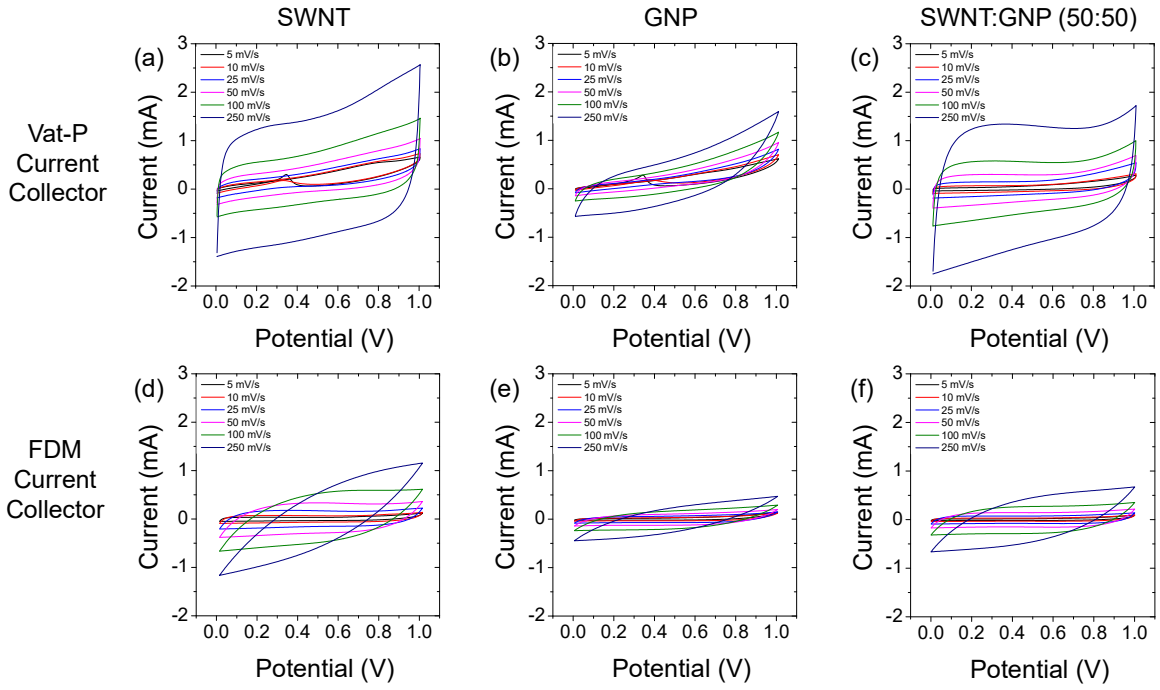

Figure 3.3 Cyclic voltammetry of printed supercapacitor cells at various scan rates in the range 5–250 mV/s. Using Vat-P printed metallized current collectors, CVs are shown for cells using (a) SWNT, (b) GNP, and (c) 50:50 SWNT:GNP carbons, also shown in (d)–(f) for the same respective carbons using FDM printed current collectors. A voltage window of 0.0 – 1.0 V was used.

A series of resistance measurements of an unloaded, as-fabricated Vat-P and FDM current collector were recorded to investigate the difference in electrical resistance between these two 3D-printed current collector types. The full results of the tests can be found in the supplementary material, Figure 3.S.3. To summarize, the resistance values of the Vat-P current collector ranged from 5.6–10.0 Ω, while the resistance of the FDM current collector varied in the range 1.15–2.85 kΩ.

The effect of the printing method on the current collector resistance and interface with each slurry over many charge-discharge cycles was also investigated. Figure 3.4 (a) shows the cycle life response for all cells discussed so far, with the specific capacitance values extracted from 100,000 galvanostatic charge-discharge cycles. The Vat-P current collector cells (using SWNT, GNP and the 50:50 mixture) lose almost all specific capacity after only 5,000 charge-discharge cycles.

The previously discussed reactions of gold in alkaline solution are likely to blame for this poor cycling stability. The trailing peaks in the anodic direction of the Vat-P cell CV curves (at the higher limit of the potential window) seem to lack a corresponding peak in the cathodic direction, suggesting that an irreversible electrochemical process is occurring. The irreversible transformation of some of the conductive gold layer into an electronically insulating species (such as gold oxides) over several thousand charge-discharge cycles would explain the poor cycling stability of the Vat-P current collector cells. Extensive delamination of the 50 nm sputtered gold layer after prolonged exposure to 6M aqueous KOH (as shown in the supplementary material, Figure 3.S.4) could also be a factor in the poor cycle life performance of these cells.

Table 3.3 Summary of integrated specific charge and specific capacitance values from cyclic voltammetry data as seen in Figure 3.3.

Current Collector Type	Carbon Slurry Type	Lower Scan Rate (5 mV/s)		Higher Scan Rate (250 mV/s)	
		Specific Charge (C/g)	Specific Capacitance (F/g)	Specific Charge (C/g)	Specific Capacitance (F/g)
Vat-P	SWNT	2.895	2.895	0.975	0.975
Vat-P	GNP	2.371	2.371	0.339	0.339
Vat-P	50:50	1.799	1.799	0.984	0.984
FDM	SWNT	3.445	3.445	0.747	0.747
FDM	GNP	0.851	0.851	0.142	0.142
FDM	50:50	1.875	1.875	0.652	0.652

The FDM current collector cells display excellent cycling stability, especially those using SWNT and the SWNT:GNP mixture, which retain ~94% and 98% of their respective specific capacitance after 100,000 cycles. Cell using an FDM printed current collector and GNP carbons showed the lowest capacitance of the three FDM printed cells, which is directly linked to the lower electrical conductivity of the nanoplatelet carbon compared to SWNT, but still maintained ~37% of its specific capacitance after 100,000 cycles. The cycle life response of each individual cell is shown in the supplementary material, Figure 3.S.5.

Figure 3.4 (b)–(g) show SEM images of the slurries of all cells after 100,000 charge-discharge cycles. Extensive formation of material impurities can be seen in the Vat-P current collector slurries (b)–(d), possibly resulting from the interactions of the sputtered gold layer with the aqueous alkaline electrolyte mentioned previously. The FDM current collector slurries (e)–(g) look very similar to their pre-cycled counterparts (Figure 3.2), with no obvious change to morphology. Figure 3.4 (h)–(m) show the charge-discharge curves of the cells at different stages of the 100,000 cycles under galvanostatic conditions. The Vat-P current collector cells initially suffer from very long charging times, resulting in very poor coulombic efficiency

(charge delivered/charge stored) for the initial thousand charge-discharge cycles. The FDM current collector cells do not suffer this same problem and show excellent coulombic efficiency from the beginning of the 100,000 cycles.

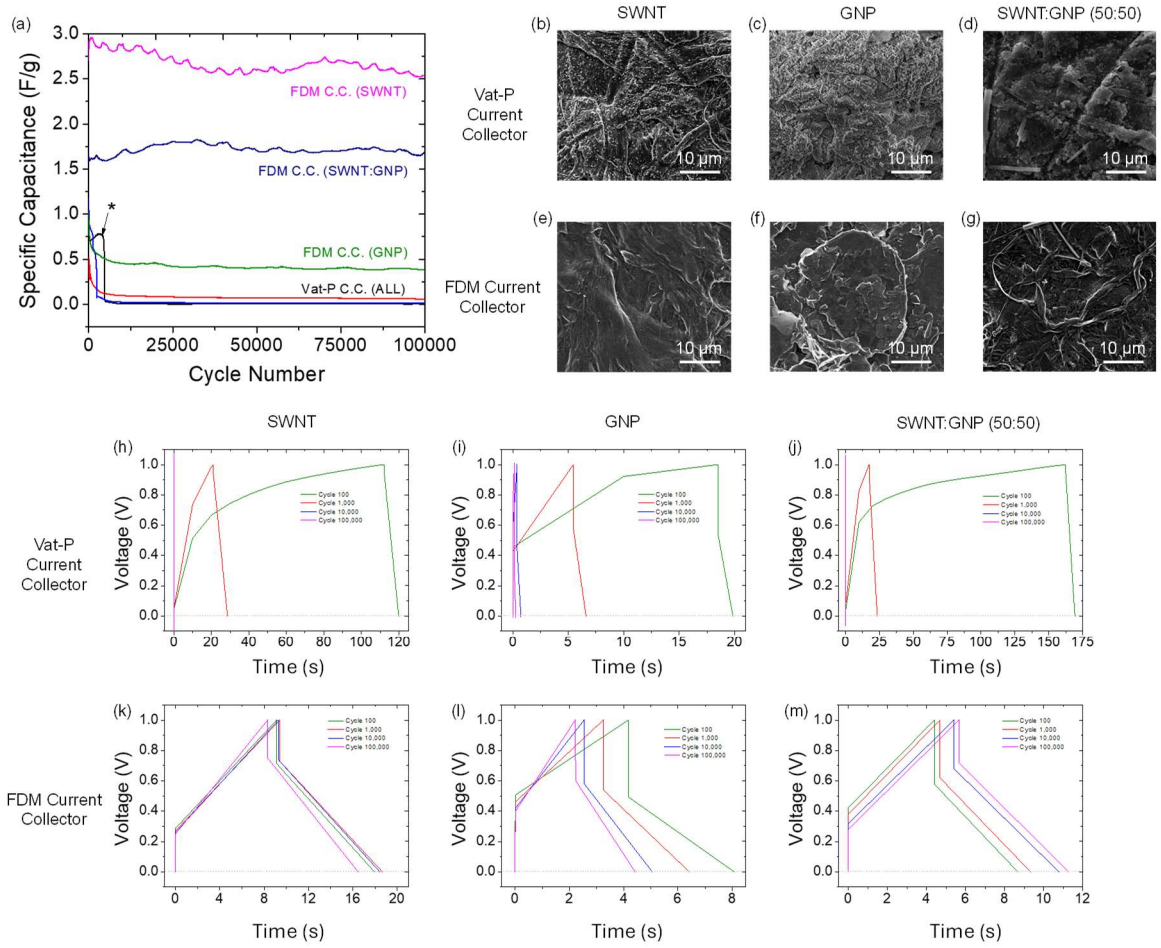

Figure 3.4 (a) Specific capacitance retention of all printed cell types in this work over 100,000 cycles under galvanostatic conditions. Cells were cycled between 0.0 and 1.0 V at an applied current of 500 µA (specific applied current of 0.167 A/g). (b)–(d) SEM images acquired after cycling for cells with Vat-P printed current collectors using SWNT, GNP and SWNT:GNP mixtures. The corresponding SEM images for cell with FDM printed current collectors are shown in (e)–(g). Charge-discharge curves of the cells at different points during the 100,000 cycles under galvanostatic conditions are shown in (h)–(m).

The SWNT-containing Vat-P current collector cells (Figure 3.4 (h) and (j)) show superior conductivity to the non-SWNT containing and FDM current collector cells (Figure 3.4 (i) and (k)–(m)), as evidenced by their far smaller ohmic drops. The other four cells all display

a significantly larger ohmic drop in their charge-discharge curves, indicating higher internal resistance than the SWNT-containing Vat-P current collector cells. Focusing on the FDM current collector cells, the SWNT-containing cells (Figure 3.4 (k) and (m)) show smaller ohmic drops than the GNP-containing FDM current collector cell (Figure 3.4 (l)), owing to the superior conductivity of the SWNT-containing carbon electrode slurries. The excellent cycle lives of the SWNT-containing FDM current collector cells is very apparent when looking at the charge-discharge curves, which remain almost the same after 100,000 charge-discharge cycles.

3.3.2 Electrode Slurry Modification and Narrowed Voltage Window (0.2 – 0.7 V)

To gauge the effect of slurry composition on the cycling behavior in FDM and Vat-P printed cells, the slurry compositions were modified to include graphite and PVDF binders to improve the uniformity of the slurry mixture and its adhesion to the printed current collectors. The masses of each material in the composite slurries are shown in Table 3.1. In addition, to minimize side reactions and any contributions from water electrolysis, we limited the voltage window to 0.2 – 0.7 V. The SWNT:GNP 50:50 slurry was used again in these experiments as the benchmark active materials to monitor the difference in performance with the reduced voltage window. While pure SWNT slurry was shown earlier to have a higher specific capacitance in the galvanostatic charge-discharge test (Figure 3.4 (a)), the 50:50 slurry was chosen as a compromise between the lower cost of the SWNT:GNP slurry materials and the lower specific capacitance values obtained. In terms of price per gram for the two carbon materials, the SWNT was approximately 60 times more expensive than the GNP.

The Raman scattering spectra for printed cells with FDM and Vat-P current collectors using SWNT:GNP mixture, a graphite-containing Gr:Super-P:PVDF (8:1:1), and a SWNT:GNP:Super-P:PVDF (4:4:1:1) slurry can be seen in Figure 3.5 . As with the earlier

experiments (Figure 3.2), the slurries containing SWNT (Figure 3.5 (a) and (c)) have an intense G-band (~1600 cm^{-1}), an intense G'-band (2D-band) in the region of 2600–2700 cm^{-1}, [51, 52] and a D-band (~1350 cm^{-1}). We note G, G', and D-bands are present in the 8:1:1 Gr:Super-P:PVDF slurry in the same positions, but at a much lower intensity than those present in the SWNT-only samples [56]. For different batches of the same slurry type there is strong correlation for the spectra peaks, their positions, and the relative intensity to other peaks in the same scan.

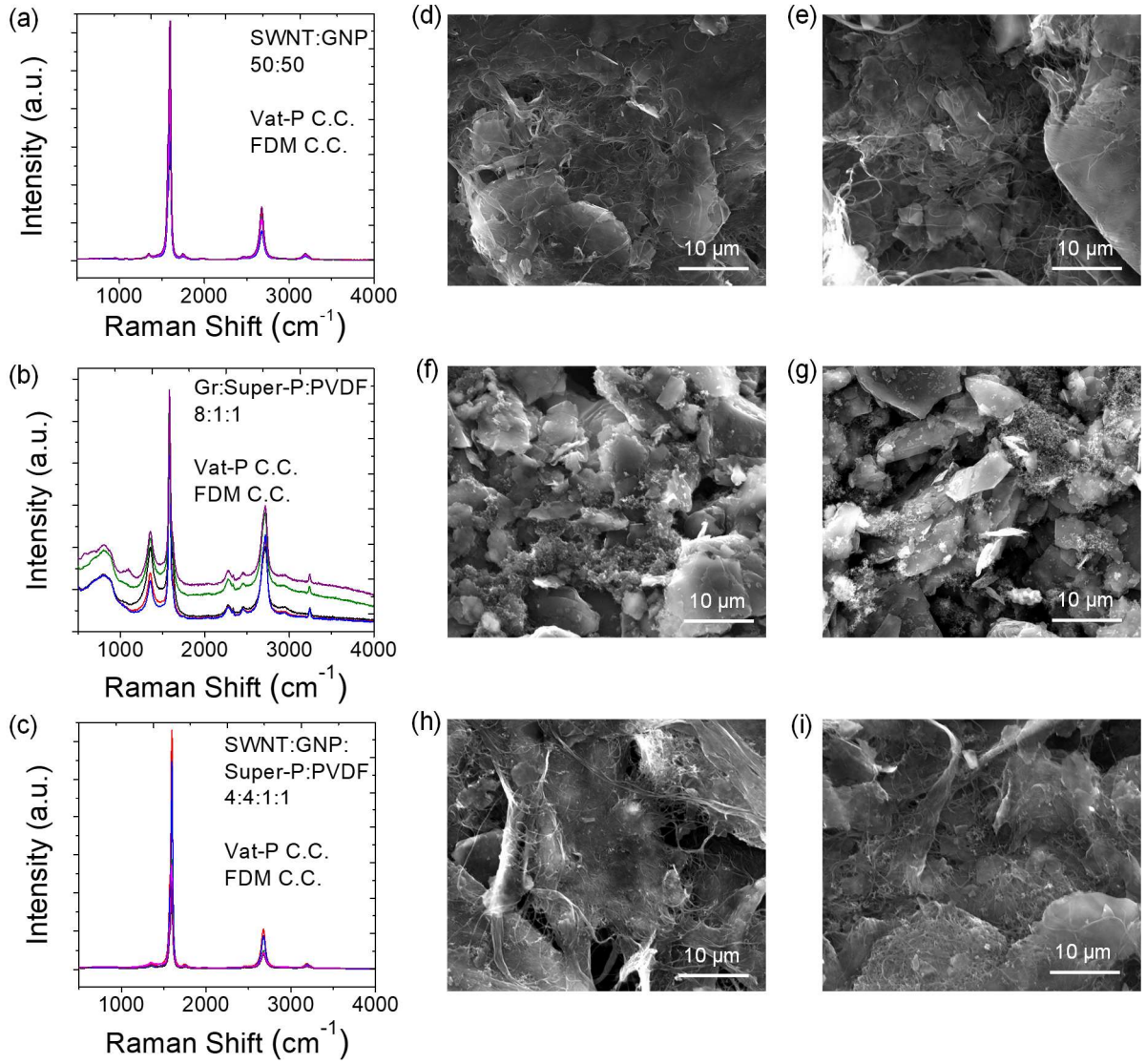

Figure 3.5 Raman scattering spectra of (a) SWNT:GNP (50:50), (b) Gr:Super-P:PVDF (8:1:1), and (c) SWNT:GNP:Super-P:PVDF (4:4:1:1) slurries prior to electrochemical testing. (d)–(i) Corresponding SEM images of the slurries on Vat-P (left) and FDM (right) current collectors.

The SEM images in Figure 3.5 show the morphology of the three carbon-containing slurries prior to any electrochemical tests. The SWNT and GNP used in the 50:50 (Figure 3.5 (d) and (e)) and 4:4:1:1 slurries in Figure 3.5 (h) and (i) (this latter one containing Super-P and PVDF) retain the relative morphologies and GNP platelets and SWNTs are relatively uniformly mixed when PVDF is used as the binder. The graphite material used in the 8:1:1 slurry (Figure 3.5 (f) and (g)) has a similar appearance to the GNPs, with the planar flakes expected of sp^2 carbon sheets [57]. Though more difficult to distinguish at these magnifications, super-P can be seen in the 8:1:1 and 4:4:1:1 slurries as a fluffy, porous material covering the graphite platelets [45, 72].

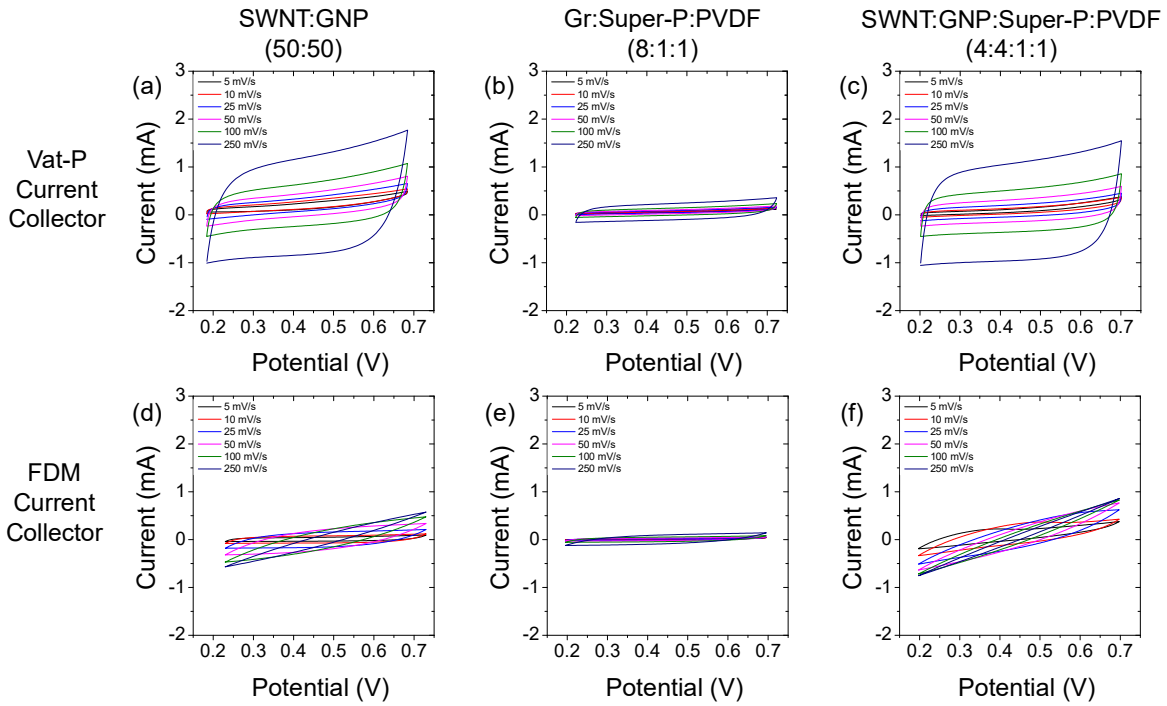

Figure 3.6 Cyclic voltammetry of printed supercapacitor cells at various scan rates in the range 5–250 mV/s. A narrower voltage window of 0.2 – 0.7 V was used. Using Vat-P printed metallized current collectors, CVs are shown for cells using (a) 50:50 SWNT:GNP, (b) Gr:Super-P:PVDF (8:1:1), and (c) SWNT:GNP:Super-P:PVDF (4:4:1:1), also shown in (d)–(f) for the same respective carbons using FDM printed current collectors.

Table 3.4 Summary of integrated specific charge and specific capacitance values from cyclic voltammetry data as seen in Figure 3.6.

Current Collector Type	Carbon Slurry Type	Lower Scan Rate (5 mV/s)		Higher Scan Rate (250 mV/s)	
		Specific Charge (C/g)	Specific Capacitance (F/g)	Specific Charge (C/g)	Specific Capacitance (F/g)
Vat-P	50:50	1.342	2.683	0.450	0.900
Vat-P	8:1:1	0.059	0.118	0.045	0.089
Vat-P	4:4:1:1	0.675	1.350	0.366	0.732
FDM	50:50	1.823	3.645	0.070	0.140
FDM	8:1:1	0.190	0.380	0.055	0.109
FDM	4:4:1:1	1.406	2.811	0.013	0.025

Examination of these active slurries in 3D printed cells containing FDM and Vat-P current collectors was also carried out. Figure 3.6 shows the CV response of all at scan rates ranging from 5 to 250 mV/s. We see that the slurries containing SWNTs (50:50 SWNT:GNP) (Figure 3.6 (a) and (d)) and 4:4:1:1 mixture also containing SWNTs (Figure 3.6 (c) and (f)) display CV curves with a higher total integrated charge compared to cells with the 8:1:1 shown in Figure 3.6 (b) and (e) slurry for both Vat-P and FDM current collector cells at higher scan rates, as shown in Table 3.4. Clearly, the interface between the metallized Vat-P and conductive FDM printed current collectors is improved in general when intraparticle conductive wiring in the form of dispersed SWNTs are used. The Vat-P current collector cells (Figure 3.6 (a)–(c)) show quasi-rectangular shape and lack any distinct redox peaks, indicating good EDLC behavior [40, 60]. Promisingly, the large, trailing tail-ends seen in the Vat-P cells in Figure 3.3 (a)–(c) in the wider voltage range are far less apparent in the Vat-P current collector cells here. This indicates that the reduction of the voltage window to 0.2 – 0.7 V avoids the unwanted side-reactions that occurred in the Vat-P current collector cell at the wider voltage window of 0.0 – 1.0 V. However, the reduction of the working potential window sacrifices some of the

capacitance and specific energy. The FDM current collector cells again suffer from very high resistance in comparison to the Vat-P current collector cells under voltammetric conditions, indicated by the distinctive, narrow leaf shape of the CV curves [61, 69].

Higher scan rate CV curves (up to 5 V/s) for all three modified slurries using both types of printed cell can be viewed in the supplementary material, Figure 3.S.6, where cells using FDM current collectors and SWNT-containing slurries show the best rate capability, similar to SWNT-containing FDM-based cells shown earlier with the wider voltage window. Vat-P current collectors containing SWNT (in this case, 50:50 and 4:4:1:1 slurries) provide the best overall response under the conditions set by the cyclic voltammetry tests, but the internal resistance limitations from printed current collectors (containing graphitic carbon or surface metallization) underwrite.

Figure 3.7 (a) shows the cycle life response for all cells under galvanostatic charge-discharge conditions at a specific applied current of 0.167 A/g (applied current of 500 μA) for 100,000 cycles. Corresponding data showing the cycling efficiency can be found in the supplementary material, Figure 3.S.7. The Vat-P current collector cells show a marked improvement in their cycle life compared to data for cells in a wider voltage window using the same active materials (the 50:50 SWNT:GNP carbon electrode slurry). The cycle lives of the Vat-P current collector cells show an even greater improvement when Super-P and PVDF is added to the 50:50 SWNT:GNP slurry mixture. The 50:50 SWNT:GNP slurry in a Vat-P cell lasts approximately 50,000 cycles before losing all specific capacity, while the 4:4:1:1 slurry Vat-P cell retains ~50% of its specific capacity after 100,000 cycles. This improvement compared to earlier Vat-P cells is likely attributed to the suppression of the side-reaction evidenced in the CV responses at the higher limit of the potential window. The charge-discharge curves of the Vat-P current collector cells (Figure 3.7 (h)–(j)) further shows the

vastly improved cycling stability of these cells, especially the cells containing 8:1:1 and 4:4:1:1 carbon slurries (Figure 3.7 (i) and (j) respectively).

As is the case with the cells examined earlier with a wider voltage window and simple slurry composition, the FDM current collector cells display excellent cycling stability. After the full 100,000 cycles, the FDM current collector with a SWNT:GNP 50:50 slurry and FDM current collector with the 4:4:1:1 slurry mixture (containing SWNTs) retained ~85% and ~58% of their initial specific capacitance, respectively. The FDM current collector cells show consistently excellent capacitance retention over many cycles under galvanostatic conditions. This was also the case with earlier FDM current collector cells tested using a wider voltage window, and simple carbon slurries without Super-P or PVDF slurry additives. All of this indicates a consistent and reliable cycling stability for FDM current collector cells, both under different voltage window conditions, and with either simple or more complex carbon-slurry electrodes.

Examination of the material morphology post-cycling for all cell slurries after 100,000 charge-discharge cycles are shown in the SEM images in Figure 3.7 (b)–(g). The formation of material impurities seen in the previous section is also present for these cells, though appearing to a lesser extent. If this impurity is linked to the gold interactions with the alkaline electrolyte, this could suggest that said interactions are still occurring in these cells (despite the reduced potential window), but to a smaller degree which does not affect the cycling stability of the cells until far later in the charge-discharge tests. The FDM current collector slurries in Figure 3.7 (e)–(g) look very similar to their pre-cycled counterparts in Figure 3.5 with no obvious formation impurities or degradation of the active material morphology.

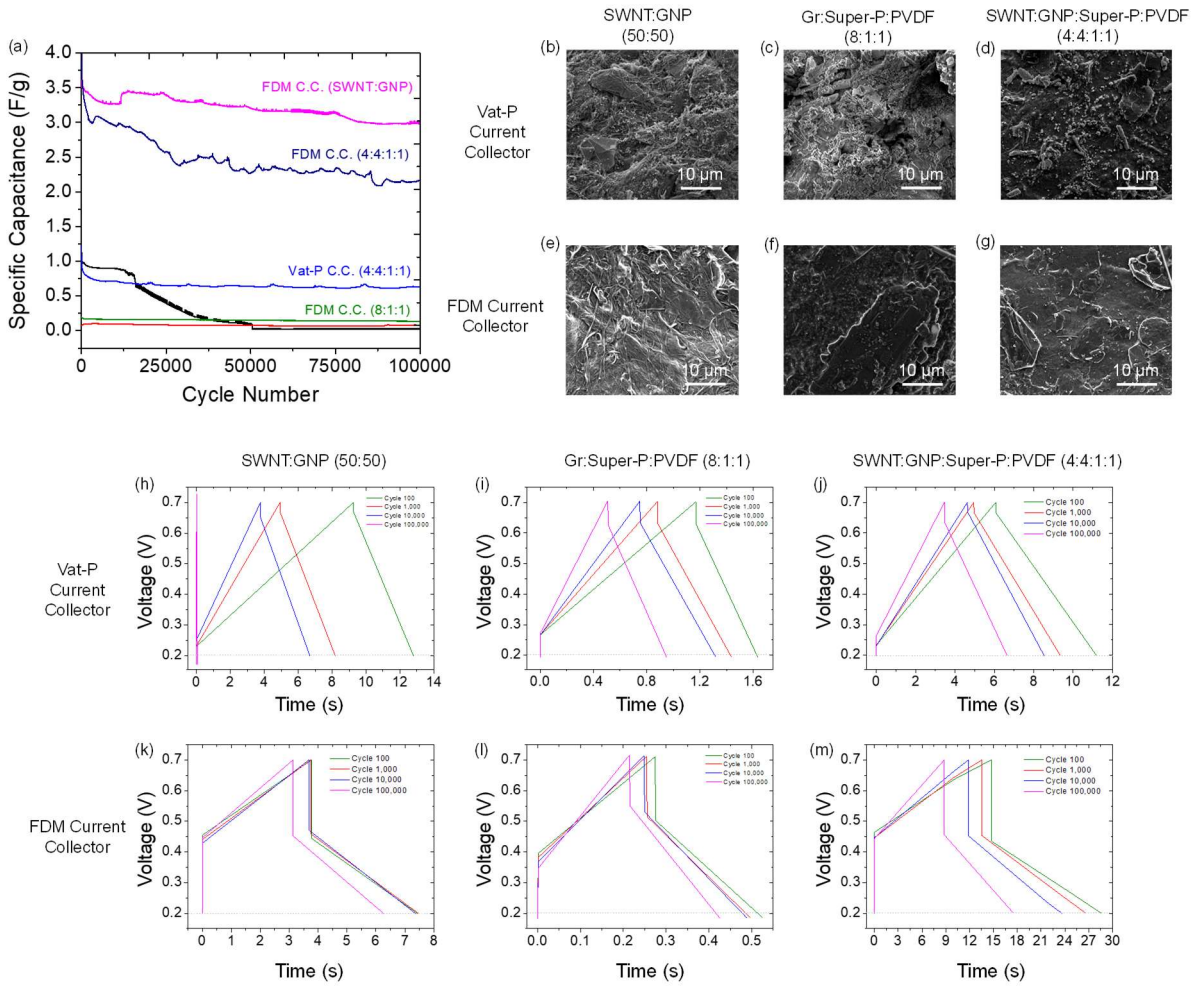

Figure 3.7 Specific capacitance retention of all printed cell types in this work over 100,000 cycles under galvanostatic conditions. Cells were cycled between 0.0 – 1.0 V at an applied current of 500 µA (specific applied current of 0.167 A/g). (b)–(d) SEM images acquired after cycling for cells with Vat-P printed current collectors using 50:50 SWNT:GNP, 8:1:1 Gr:Super-P-PVDF, and 4:4:1:1 SWNT:GNP:Super-P:PVDF slurry mixtures. The corresponding SEM images for cell with FDM printed current collectors are shown in (e)–(g). Charge-discharge curves of the cells at different points during the 100,000 cycles under galvanostatic conditions are shown in (h)–(m).

Figure 3.7 (h)–(m) show the charge-discharge curves of the cells at different stages of the 100,000 cycles under galvanostatic conditions. The Vat-P current collector cells (Figure 3.7 (h)–(j)) show a large improvement in coulombic efficiency when compared to their earlier counterparts tested at a wider voltage window and with simple carbon slurries (Figure 3.4 (h)–(j)). The SWNT-containing Vat-P current collector cells (Figure 3.7 (h) and (j)) show superior conductivity to the non-SWNT containing and FDM current collector cells (Figure 3.7

(i) and (k)–(m)), shown by their smaller ohmic drops. The other four cells all display a significantly larger ohmic drop in their charge-discharge curves, indicating higher internal resistance than the SWNT-containing Vat-P current collector cells, as was the case with the cells discussed earlier.

3.3.3 Examining Rate Response Differences in FDM and Vat-P Supercapacitors

Rate capability tests were carried out on all cells in this work using the composite slurry materials to examine the influence of printed material and resistance on the long-term stability of their interface with the active materials. Figure 3.8 shows the response of all cells using FDM and Vat-P printed current collectors extracted from galvanostatic charge-discharge tests. We find that SWNT-containing Vat-P printed supercapacitor cells with higher intrinsic slurry conductivity retain their capacitance over repeated cycling at successively higher rates (86-89% retention after tenfold increase in applied current) and recover almost all capacitance (92% recovery) after returning to the initial rate.

This behaviour mirrors the response for similar cells under voltammetric conditions shown in Figure 3.6. This can be attributed to the superior conductivity of the Vat-P current collector paired with SWNT containing electrode slurry, allowing faster and more efficient charge transfer during discharge processes at higher currents [71].

SWNT-containing FDM printed supercapacitor cells show poorer retention of capacitance over repeated cycling at successively higher rates (28-52% retention after tenfold increase in applied current), but also recover almost all capacitance (91-98% recovery) after returning to the initial rate. The poorer capacitance retention can be attributed to the inferior conductivity of the FDM current collectors, resulting in inefficient charge transfer during discharge processes at higher currents.

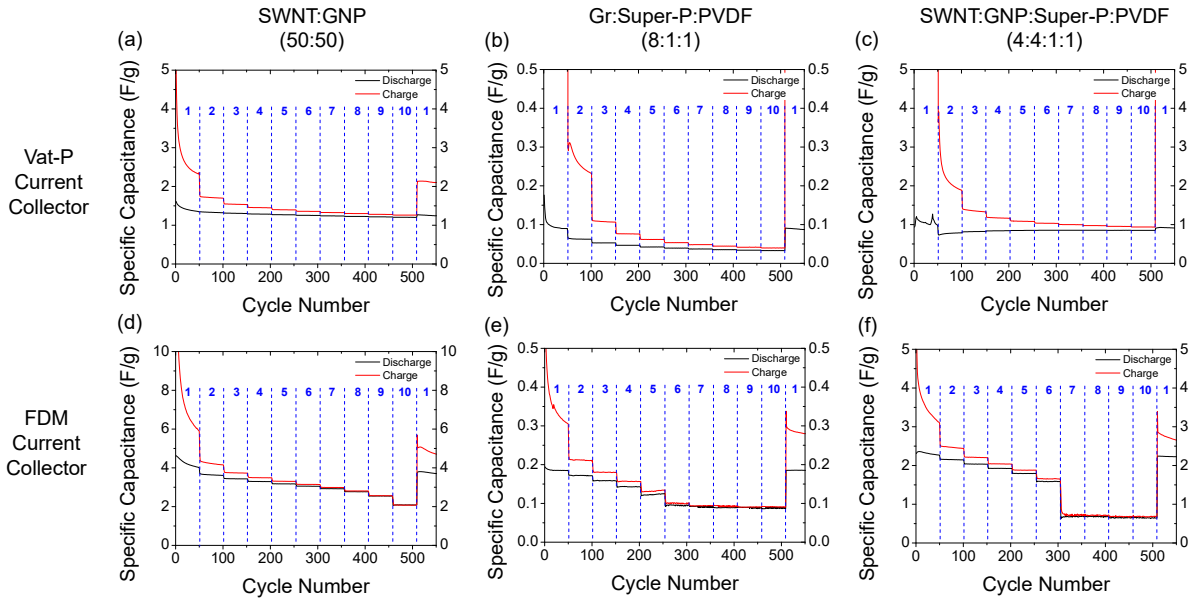

Figure 3.8 Varied-current life-cycle plot for all printed supercapacitor cell types for this work in conditions of increasing applied current. The blue numbers between the dotted lines correspond to the charging and discharging current used in that cycle period, progressing through 1 (±100 µA or 0.033 A/g), 2 (±200 µA or 0.067 A/g), 3 (±300 µA or 0.100 A/g), 4 (±400 µA or 0.133 A/g), 5 (±500 µA or 0.167 A/g), 6 (±600 µA or 0.200 A/g), 7 (±700 µA or 0.233 A/g), 8 (±800 µA or 0.267 A/g), 9 (±900 µA or 0.300 A/g), 10 (±1 mA or 0.333 A/g), then returning to 1 (±100 µA or 0.033 A/g). The cells are charged to 0.7 V, and discharged to 0.2 V.

The Vat-P current collector cells suffer from extremely long initial charging times (as can be seen in Figure 3.8), resulting in very low coulombic efficiency (charge delivered/charge stored) [73, 74] at lower applied currents. The FDM current collectors show better specific capacitance than their Vat-P counterparts, though suffer from poorer rate capability. The FDM current collector cells also display better coulombic efficiency overall (especially compared to the Vat-P cells at lower applied currents). The information extracted from the CV and rate capability tests indicate that the Vat-P current collectors paired with SWNT containing slurries, with or without binders, are the most promising for higher current density applications, but suffer from low initial coulombic efficiency, most likely due to parasitic reactions.

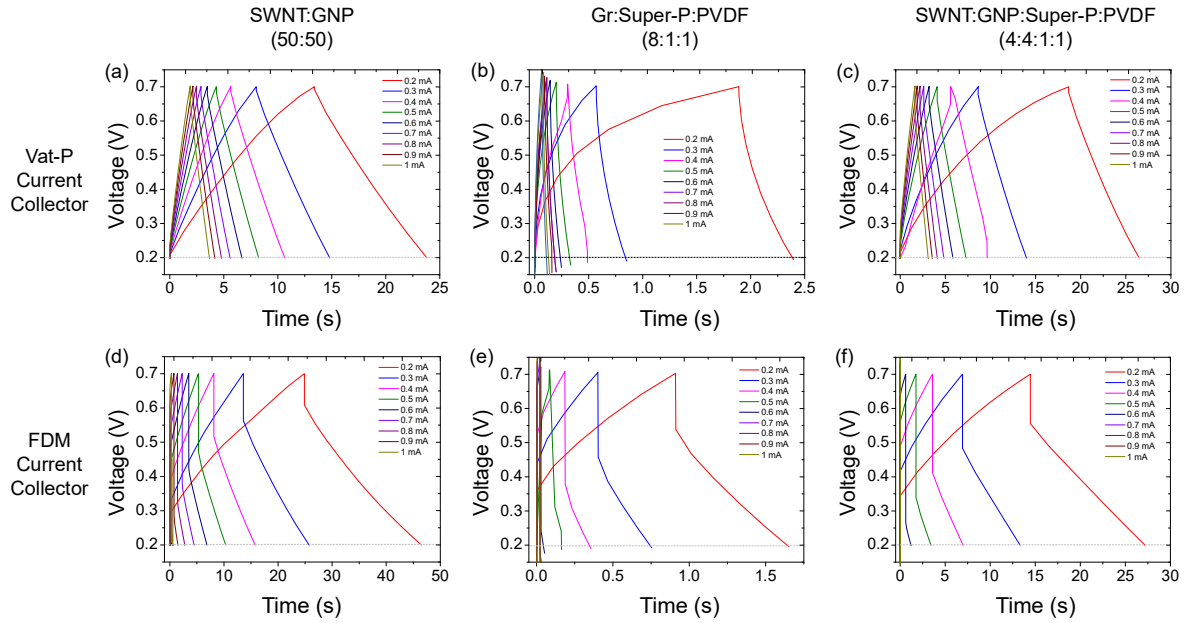

Figure 3.9 Charge-discharge curves from cycles of increasing applied current under galvanostatic conditions. ±200 µA (0.067 A/g), ±300 µA (0.100 A/g), ±400 µA (0.133 A/g), ±500 µA (0.167 A/g), ±600 µA (0.200 A/g), ±700 µA (0.233 A/g), ±800 µA (0.267 A/g), ±900 µA (0.300 A/g), ±1 mA (0.333 A/g). The cells are charged to 0.7 V, and discharged to 0.2 V. The charge-discharge curves at the applied current of ±100 µA or 0.033 A/g is omitted from these plots due to extremely long charging times rendering the rest of the graph of limited use. The plots including the charge-discharge curves at the applied current of ±100 µA or 0.033 A/g can be found in the supplementary information, Figure 3.S.8.

Figure 3.9 shows the charge-discharge curves of the cells tested in the rate capability test shown in Figure 3.8 under galvanostatic conditions with increasing applied current, ranging from ±200 µA (0.067 A/g) to ±1 mA (0.333 A/g), an overall increase of applied current by a factor of 5. As seen from Figure 3.8 (a) and (c), the SWNT-containing Vat-P printed supercapacitor cells show the best rate capability, retaining their capacitance over repeated cycling at successively higher rates. This behaviour is reflected in their charge discharge curves in Figure 3.9 (a) and (c), where the increase in applied current by a factor of 5 results in their discharge time being reduced by approximately a factor of 5. This inverse relationship between discharge time and applied current is only present for cells possessing good rate capability. For the other cells, which are shown to have inferior rate capability, increasing the applied current by a factor of 5 resulted in their discharge time being reduced by far more than a factor of 5.

This is especially apparent for FDM printed supercapacitor cells (Figure 3.9 (d)–(f)), whose discharge times quickly shrink to a small fraction of their discharge times at lower applied currents, in tandem with their poor rate capabilities shown in Figures 3.6 and 3.8. The ohmic drops of the FDM printed cells (which are far less apparent in the charge-discharge curves of the Vat-P printed cells (Figure 3.9 (a)–(c)) quickly grow with increasing applied current to encompass most of the voltage range for these tests.

For all cells with modified slurries and tested in a narrower voltage window, their specific capacitance values from Figure 3.8 were used to calculate their specific energies and specific powers at the lowest and highest applied currents, which is outlined in Table 3.5. The SWNT-containing Vat-P printed supercapacitor cells show the best rate capability, therefore maintaining their specific energy over a wider range of applied currents than the SWNT-containing FDM current collector cells, whose specific energies reduce to negligible amounts with increasing applied current. The specific powers of all cells are shown to be similar at an applied current of 0.1 mA. However, with increasing applied current, the Vat-P cells quickly outpace their FDM counterparts when it comes to specific power.

Table 3.5 Specific energies and specific powers calculated from the galvanostatic rate capability tests.

Current Collector and Carbon Slurry		Specific Energy of Electrode Material (Wh/kg)			Specific Power of Electrode Material (W/kg)		
		At 0.1 mA	At 0.5 mA	At 1 mA	At 0.1 mA	At 0.5 mA	At 1 mA
Vat-P	50:50	0.0460	0.0410	0.0362	7.76	37.61	72.32
Vat-P	8:1:1	0.0029	0.0011	0.0007	7.02	29.12	45.00
Vat-P	4:4:1:1	0.0329	0.0249	0.0207	6.00	27.89	50.49
FDM	50:50	0.1151	0.0326	0.0005	7.76	23.50	6.57
FDM	8:1:1	0.0045	0.000167	-	8.21	7.71	-
FDM	4:4:1:1	0.0578	0.0048	-	6.43	10.29	-

At the currents applied in this work, the specific energy and specific power values are very low for EDLC devices. Specific energies of 1–10 Wh/kg and specific powers of 500–10,000 W/kg are typical for EDLC devices [40, 75–77], where there are no resistance limitations from the current collector or cell itself; mitigating resistance limitations is achieved in the active materials typically for standard EDCL devices such as carbon-based supercapacitors and similar systems. The specific energies (therefore specific powers) of the devices in this study suffer from the narrow operating voltage window. The cells containing the 4:4:1:1 SWNT:GNP:Super-P:PVDF electrode slurry consistently performs slightly worse than their 50:50 SWNT:GNP counterparts in terms of specific energy and specific power. This can likely be attributed to the PVDF binder material, as other studies have found that excessive use of PVDF in carbon-based slurries can negatively affect the power and energy densities of supercapacitor performance [78].

3.4 Conclusions

We compared the fundamental response and behaviour of two different 3D-printing methods used to manufacture symmetric carbon supercapacitors. Two individual symmetric carbon supercapacitor systems were prepared (one using only Vat-P 3D-printing, the other using FDM and Vat-P 3D-printing), and their electrochemical performances were evaluated when loaded with active materials comprising several carbon types, and binder-based slurries of these carbons. The approach was designed to assess the nature of the limitation to electrochemical performance based on the material type and the 3D printing method, using unaltered and non-active material-containing materials for both printing methods.

The metallized Vat-P current collector cells are more conductive, show better EDLC CV curves, improved rate capability, and better overall structural integrity (no electrolyte

leakage). However, they initially suffered from poor cycle life stability and poor coulombic efficiency likely caused by unwanted side reactions and/or electrode degradation. This was partially alleviated by the reduction of the voltage window of further electrochemical tests (from 0.0 – 1.0 V to 0.2 – 0.7 V), resulting in an improvement in cycle life stability. The FDM current collector cells have good cycle life stability up to 100,000 charge-discharge cycles but have the disadvantages of intrinsically higher resistance of the printed material, non-ideal EDLC CV responses, poorer rate capability, and less reliable structural integrity.

While additive compositing or direct printing of the active materials is one route being explored in the literature currently, there remains a dearth of information on the basic response of simple carbon supercapacitors as a function of how they were printed, and the work here suggest that multi-modal printing techniques may be useful so that specific benefits of printing and materials can be combined to offset known issues with direct printing, e.g. brittleness with high graphite-loaded PLA thermoset materials, and poor printing definition from scattering of light in photopolymerization processes of resins containing significant randomly dispersed inorganic materials within the viscous methacrylate resin.

3.5 Appendix: Supplementary Material

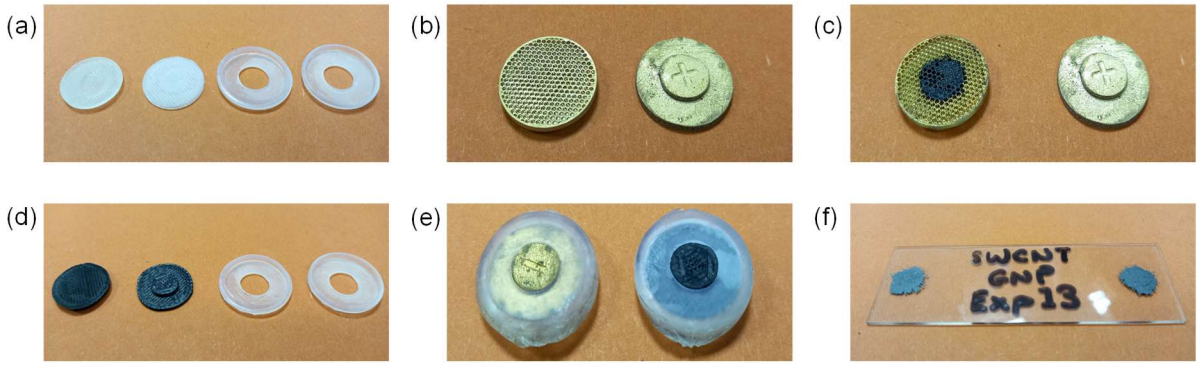

Figure 3.S.1 Images taken of cell components at different stages of cell assembly. (a) All 3D-printed components for one SLA current collector type cell (two half-casings and two current collectors) after post-print processing (washing, curing, removing supports, and filing to smoothness). (b) 50 nm gold sputtered SLA printed current collectors (top side and bottom side) with the intricate detail of the current collector lattice visible. This level of complexity would not be achievable using the FDM printer, however, the FDM current collectors require no metal sputtering, saving time, and money. (c) SLA current collectors after slurry loading (50:50 slurry is shown in the example used here). (d) All 3D-printed components for one FDM current collector type cell. No post processing procedure is needed for the FDM current collectors, saving time at the cost of precision and overall quality of the printed parts. The difference in resolution in the two printing methods is apparent here. The pattern of melted filament lines is clearly visible in the FDM current collectors, while the layers of photopolymerized resin are invisible on the SLA components. (e) Two fully assembled cells, SLA type current collector on the left, and FDM type current collector on the right. Again, the difference in resolution between the current collectors is very apparent. The low resolution of the FDM current collectors allow small amounts of liquid electrolyte to leak. (f) A glass slide containing slurry samples set aside for Raman spectroscopy analysis (again, 50:50 slurry is shown in the example used here).

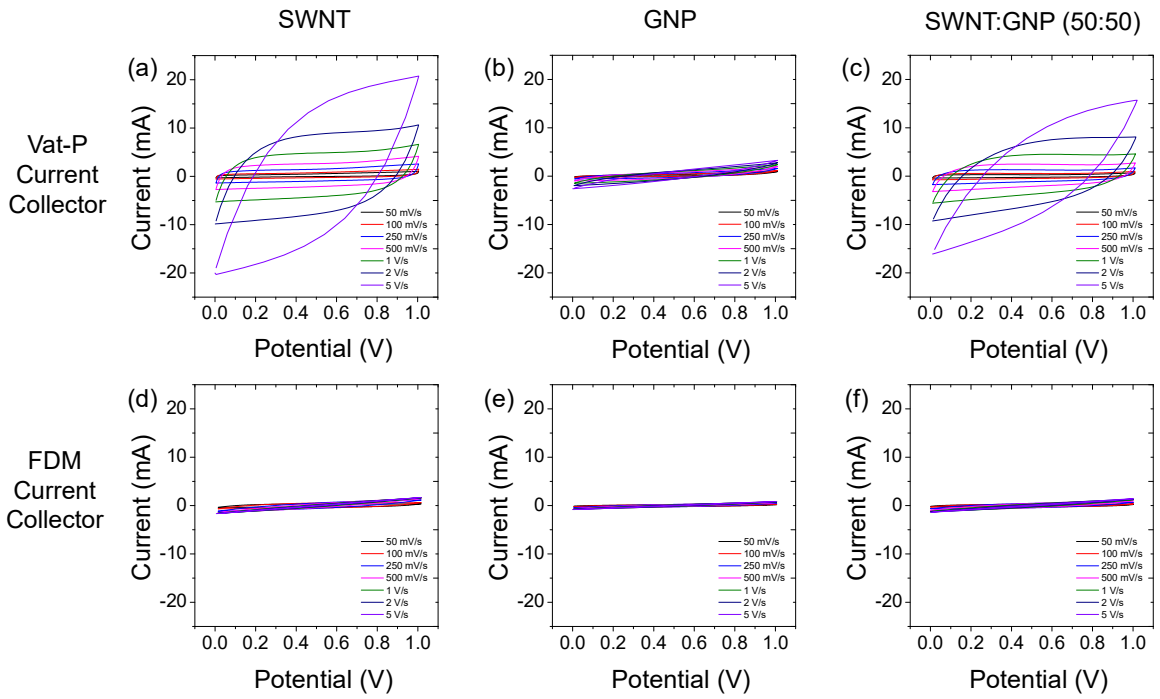

Figure 3.S.2 Cyclic voltammetry responses of printed supercapacitor cells at various scan rates in the range 50–5,000 mV/s. Using Vat-P printed metallized current collectors, CVs are shown for cells using (a) SWNT, (b) GNP, and (c) 50:50 SWNT:GNP carbons, also shown in (d)–(f) for the same respective carbons using FDM printed current collectors. A voltage window of 0.0 – 1.0 V was used.

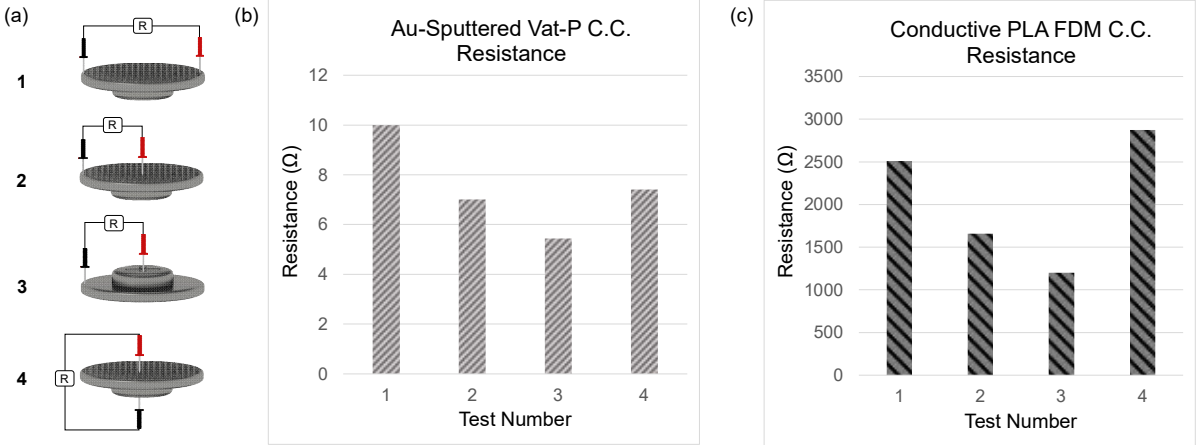

Figure 3.S.3 (a) Positions of the multi-meter probes used to obtain resistance values from an unloaded (b) Au-sputtered Vat-P current collector and (c) conductive PLA FDM current collector. The values obtained show the conductive PLA FDM current collectors to be approximately 250-300 times more resistive than the Au-sputtered Vat-P current collector collectors.

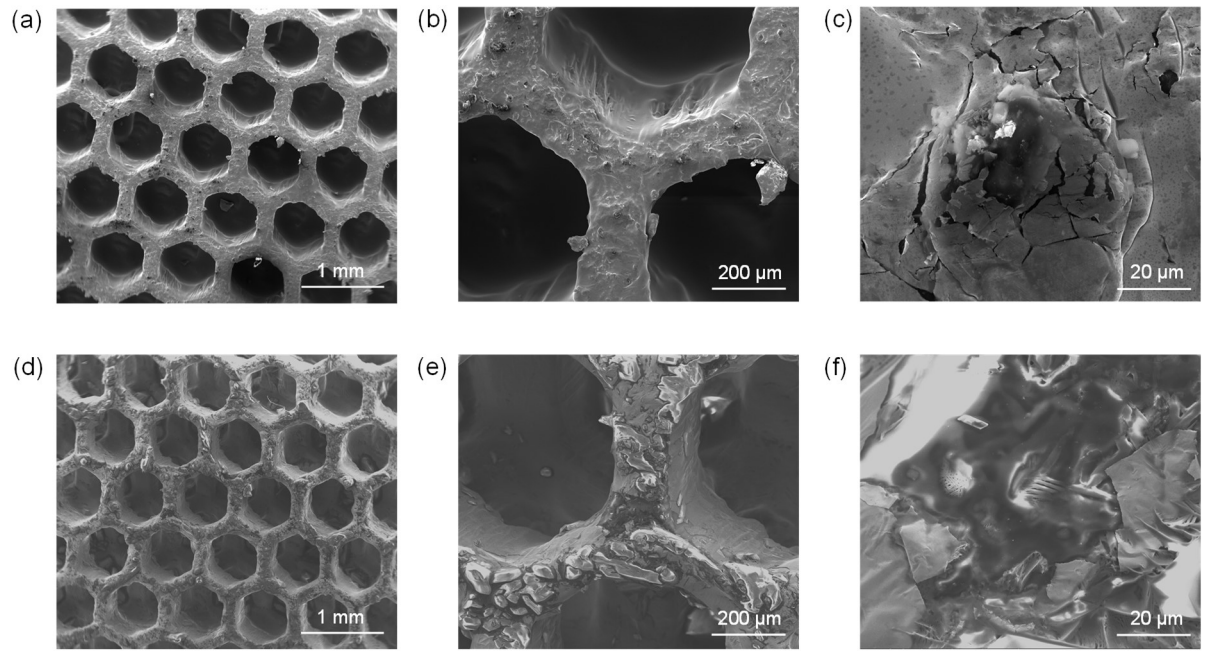

Figure 3.S.4 SEM images taken of unloaded gold-sputtered (50 nm) Vat-P printed current collectors at a variety of magnifications (a)–(c) without any chemical exposure and (d)–(f) after 72 hours of exposure to 5 drops of 6M aqueous KOH electrolyte added to the lattice side of the current collectors. Delamination of the gold is visible, especially in the higher magnification images (e) and (f).

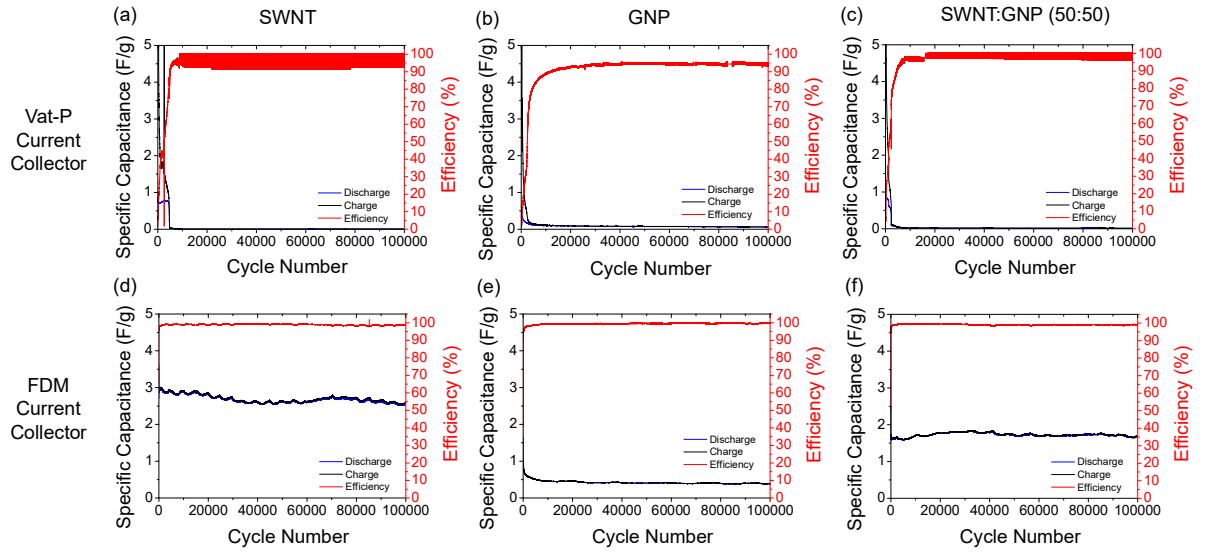

Figure 3.S.5 Specific charge and discharge capacitance retention and percentage efficiency of all printed cell types in this work over 100,000 cycles under galvanostatic conditions. Cells were cycled between 0.0 and 1.0 V at an applied current of 500 µA (specific applied current of 0.167 A/g). Using Vat-P printed metallized current collectors, CVs are shown for cells using (a) SWNT, (b) GNP, and (c) 50:50 SWNT:GNP carbons, also shown in (d)–(f) for the same respective carbons using FDM printed current collectors. Cell death occurs, for example, in (a) at ~5,000 cycles.

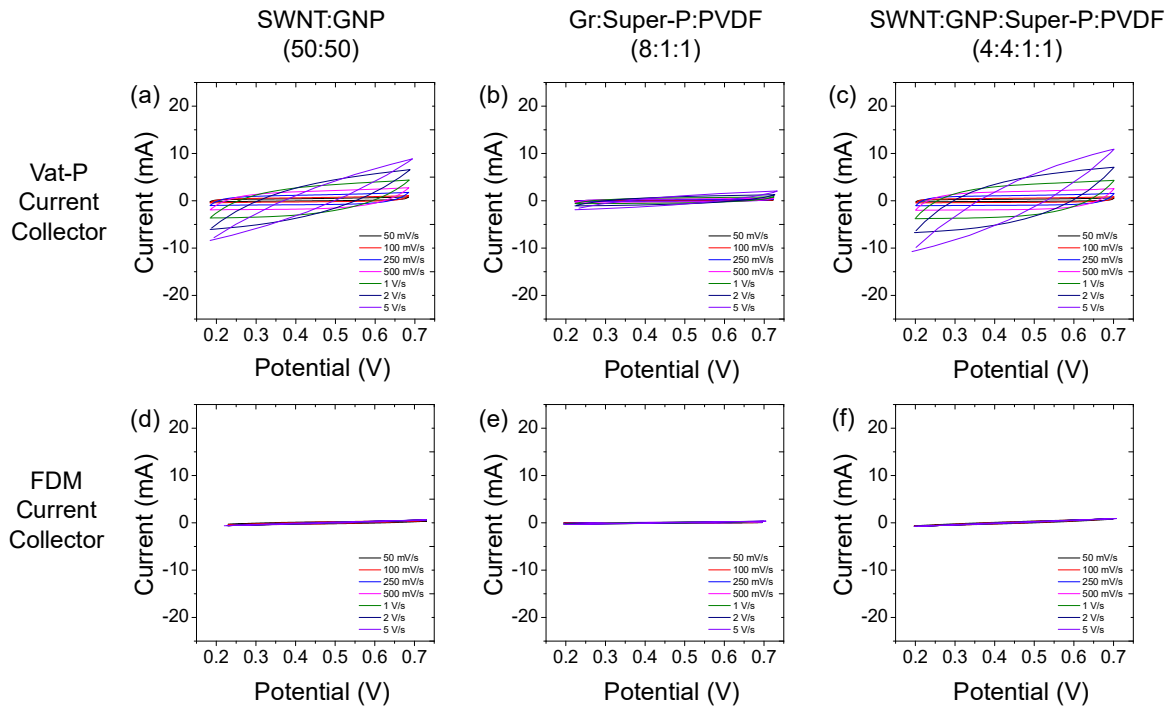

Figure 3.S.6 Cyclic voltammetry responses of printed supercapacitor cells at various scan rates in the range 50–5,000 mV/s. A narrower voltage window of 0.2 – 0.7 V was used. Using Vat-P printed metallized current collectors, CVs are shown for cells using (a) 50:50 SWNT:GNP, (b) Gr:Super-P:PVDF (8:1:1), and (c) SWNT:GNP:Super-P:PVDF (4:4:1:1), also shown in (d)–(f) for the same respective carbons using FDM printed current collectors.

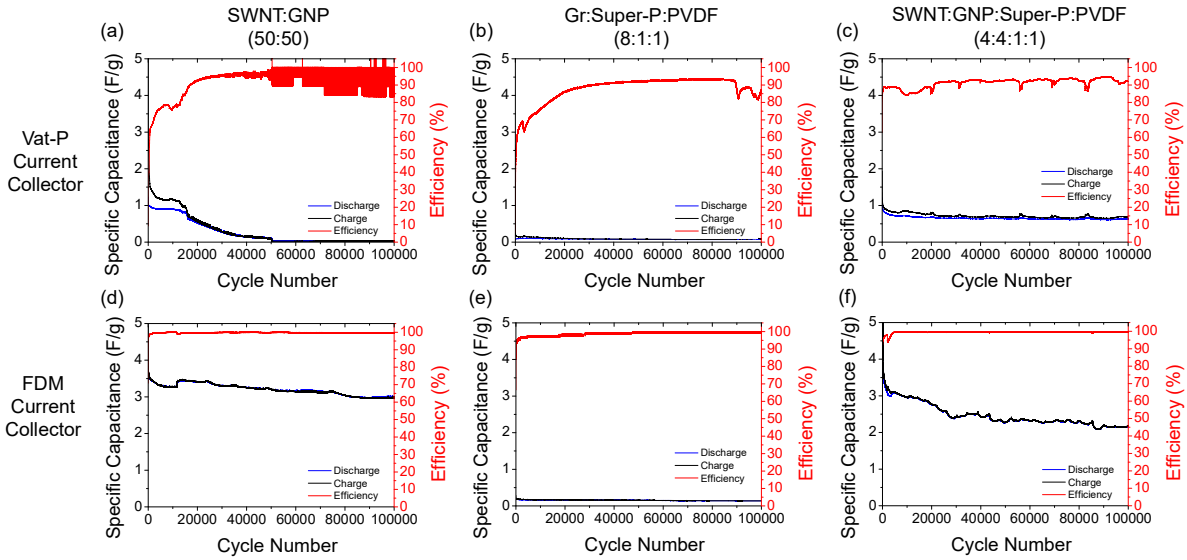

Figure 3.S.7 Specific charge and discharge capacitance retention and percentage efficiency of all printed cell types in this work over 100,000 cycles under galvanostatic conditions. Cells were cycled between 0.2 and 0.7 V at an applied current of 500 µA (specific applied current of 0.167 A/g). Using Vat-P printed metallized current collectors, CVs are shown for cells using (a) 50:50 SWNT:GNP, (b) Gr:Super-P:PVDF (8:1:1), and (c) SWNT:GNP:Super-P:PVDF (4:4:1:1), also shown in (d)–(f) for the same respective carbons using FDM printed current collectors. Cell death occurs, for example, in (a) at ~50,000 cycles.

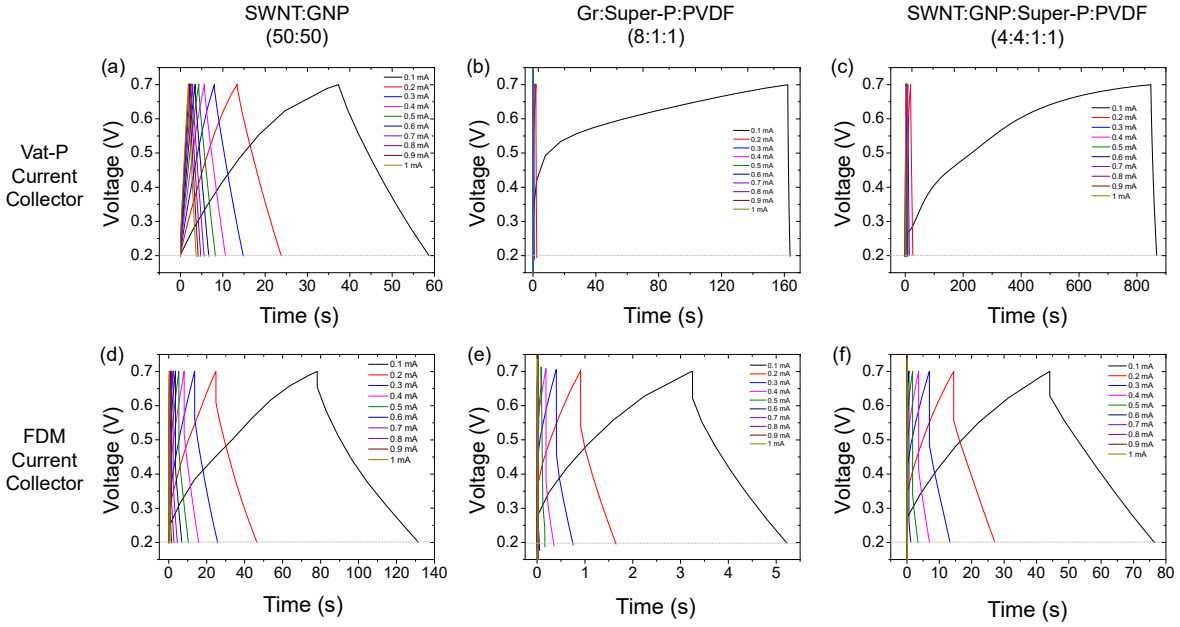

Figure 3.S.8 Charge-discharge curves from cycles of increasing applied current under galvanostatic conditions. ±100 µA (0.033 A/g), ±200 µA (0.067 A/g), ±300 µA (0.100 A/g), ±400 µA (0.133 A/g), ±500 µA (0.167 A/g), ±600 µA (0.200 A/g), ±700 µA (0.233 A/g), ±800 µA (0.267 A/g), ±900 µA (0.300 A/g), ±1 mA (0.333 A/g). The cells are charged to 0.7 V, and discharged to 0.2 V.

3.6 References

[1] J. Li, M. Leu, R. Panat and J. Park, "A hybrid three-dimensionally structured electrode for lithium-ion batteries via 3D printing.," *Materials & Design,* vol. 119, pp. 417-424, 2017.

[2] A. Ambrosi and M. Pumera, "3D-printing technologies for electrochemical applications.," *Chemical society reviews,* vol. 45, no. 10, pp. 2740-2755, 2016.

[3] A. Maurel, M. Courty, B. Fleutot, H. Tortajada, K. Pdrashantha, M. Armand, S. Grugeon, S. Panier and L. Dupont, "Highly loaded graphite–polylactic acid composite-based filaments for lithium-ion battery three-dimensional printing.," *Chemistry of Materials,* vol. 30, no. 21, pp. 7484-7493, 2018.

[4] B. Yao, S. Chandrasekaran, J. Zhang, W. Xiao, F. Qian, C. Zhu, E. Duoss, C. Spadaccini, M. Worsley and Y. Li, "Efficient 3D printed pseudocapacitive electrodes with ultrahigh MnO2 loading.," *Joule,* vol. 3, no. 2, pp. 459-470, 2019.

[5] V. Egorov and C. O'Dwyer, "Architected porous metals in electrochemical energy storage.," *Current Opinion in Electrochemistry,* vol. 21, pp. 201-208, 2020.

[6] V. Egorov, U. Gulzar, Y. Zhang, S. Breen and C. O'Dwyer, "Evolution of 3D printing methods and materials for electrochemical energy storage.," *Advanced Materials,* vol. 32, no. 29, p. 2000556, 2020.

[7] U. Gulzar, C. Glynn and C. O'Dwyer, "Additive manufacturing for energy storage: Methods, designs and material selection for customizable 3D printed batteries and supercapacitors.," *Current Opinion in Electrochemistry,* vol. 20, pp. 46-53, 2020.

[8] S. O'Hanlon and C. O'Dwyer, "Electrodeposition onto Conductive Additive-Impregnated 3D Printed Polylactic Acid Electrodes.," *Journal of The Electrochemical Society,* vol. 169, no. 8, p. 082514, 2022.

[9] A. Aimar, A. Palermo and B. Innocenti, "The role of 3D printing in medical applications: a state of the art.," *Journal of healthcare engineering,* vol. 2019, 2019.

[10] A. Mironov, A. Grigoryev, L. Krotova, N. Skaletsky, V. Popov and V. Sevastianov, "3D printing of PLGA scaffolds for tissue engineering.," *Journal of Biomedical Materials Research Part A,* vol. 105, no. 1, pp. 104-109, 2017.

[11] T. Distler and A. Boccaccini, "3D printing of electrically conductive hydrogels for tissue engineering and biosensors–A review.," *Acta biomaterialia,* vol. 101, pp. 1-13, 2020.

[12] N. Bruns and C. Krettek, "3D-printing in trauma surgery: Planning, printing and processing.," *Der Unfallchirurg,* vol. 122, pp. 270-277, 2019.

[13] A. Le-Bail, B. Maniglia and P. Le-Bail, "Recent advances and future perspective in additive manufacturing of foods based on 3D printing.," *Current Opinion in Food Science,* vol. 35, pp. 54-64, 2020.

[14] Y. Liu, Y. Yu, C. Liu, J. Regenstein, X. Liu and P. Zhou, "Rheological and mechanical behavior of milk protein composite gel for extrusion-based 3D food printing.," *Lwt,* vol. 102, pp. 338-346, 2019.

[15] K. Kumar and M. Pumera, "3D-Printing to Mitigate COVID-19 Pandemic.," *Advanced Functional Materials,* vol. 31, no. 22, p. 2100450, 2021.

[16] B. Chen, Y. Jiang, X. Tang, Y. Pan and S. Hu, "Fully packaged carbon nanotube supercapacitors by direct ink writing on flexible substrates.," *ACS applied materials & interfaces,* vol. 9, no. 34, pp. 28433-28440, 2017.

[17] X. Yun, B. Lu, Z. Xiong, B. Jia, B. Tang, H. Mao and T. W. X. Zhang, "Direct 3D printing of a graphene oxide hydrogel for fabrication of a high areal specific capacitance microsupercapacitor.," *RSC advances,* vol. 9, no. 50, pp. 29384-29395, 2019.

[18] A. Tanwilaisiri, Y. Xu, R. Zhang, D. Harrison, J. Fyson and M. Areir, "Design and fabrication of modular supercapacitors using 3D printing.," *Journal of Energy Storage,* vol. 16, pp. 1-7, 2018.

[19] X. Yan, Y. Tong, X. Wang, F. Hou and J. Liang, "Extrusion-Based 3D-Printed Supercapacitors: Recent Progress and Challenges.," *Energy & Environmental Materials,* vol. 5, no. 3, pp. 800-822, 2022.

[20] J. Xue, L. Gao, X. Hu, K. Cao, W. W. W. Zhou and Y. Lu, "Stereolithographic 3D printing-based hierarchically cellular lattices for high-performance quasi-solid supercapacitor.," *Nano-Micro Letters,* vol. 11, pp. 1-13, 2019.

[21] X. Lin, X. Li, N. Yang, X. Li, J. Yao, W. Zhang, R. Yan, J. Xu and S. Komarneni, "Design and construction of 1D/2D/3D fabric-based wearable micro-supercapacitors," *Journal of Power Sources,* vol. 560, p. 232712, 2023.

[22] M. Li, S. Zhou, L. Cheng, F. Mo, L. Chen, S. Yu and J. Wei, "3D Printed Supercapacitor: Techniques, Materials, Designs, and Applications," *Advanced Functional Materials,* vol. 33, no. 1, p. 2208034, 2023.

[23] A. Tanwilaisiri, Y. Xu, D. Harrison, J. Fyson and M. Arier, "A Study of Metal Free Supercapacitors Using 3D Printing," *International Journal of Precision Engineering and Manufacturing,* vol. 19, no. 7, pp. 1071-1079, 2018.

[24] L. Fieber, J. Evans, C. Huang and P. Grant, "Single-operation, multi-phase additive manufacture of electro-chemical double layer capacitor devices," *Additive Manufacturing,* vol. 28, pp. 344-353, 2019.

[25] M. Areir, Y. Xu, D. Harrison and J. Fyson, "3D printing of highly flexible supercapacitor designed for wearable energy storage.," *Materials Science and Engineering: B,* vol. 226, pp. 29-38, 2017.

[26] M. Idrees, S. Ahmed, Z. Mohammed, N. Korivi and V. Rangari, "3D printed supercapacitor using porous carbon derived from packaging waste.," *Additive Manufacturing,* vol. 36, p. 101525, 2020.

[27] X. Aeby, A. Poulin, G. Siqueira, M. Hausmann and G. Nyström, "Fully 3D printed and disposable paper supercapacitors.," *Advanced Materials,* vol. 33, no. 26, p. 2101328, 2021.

[28] J. Bennett, "Measuring UV curing parameters of commercial photopolymers used in additive manufacturing.," *Additive manufacturing,* vol. 18, pp. 203-212, 2017.

[29] J. Manapat, Q. Chen, P. Ye and R. Advincula, "3D printing of polymer nanocomposites via stereolithography.," *Macromolecular Materials and Engineering,* vol. 302, no. 9, p. 1600553, 2017.

[30] R. Palucci Rosa and G. Rosace, "Nanomaterials for 3D printing of polymers via stereolithography: Concept, technologies, and applications.," *Macromolecular Materials and Engineering,* vol. 306, no. 10, p. 2100345, 2021.

[31] R. Wach, P. Wolszczak and A. Adamus-Wlodarczyk, "Enhancement of mechanical properties of FDM-PLA parts via thermal annealing.," *Macromolecular Materials and Engineering,* vol. 303, no. 9, p. 1800169, 2018.

[32] E. Carlier, S. Marquette, C. Peerboom, L. Denis, S. Benali, J. Raquez, K. Amighi and J. Goole, "Investigation of the parameters used in fused deposition modeling of poly (lactic acid) to optimize 3D printing sessions.," *International Journal of Pharmaceutics,* vol. 565, pp. 367-377, 2019.

[33] U. Zaman, E. Boesch, A. Siadat, M. Rivette and A. Baqai, "Impact of fused deposition modeling (FDM) process parameters on strength of built parts using Taguchi's design of experiments.," *The international journal of Advanced Manufacturing technology,* vol. 101, pp. 1215-1226, 2019.

[34] Y. Zhou, J. Zou, H. Wu and B. Xu, "Balance between bonding and deposition during fused deposition modeling of polycarbonate and acrylonitrile-butadiene-styrene composites.," *Polymer Composites,* vol. 41, no. 1, pp. 60-72, 2020.

[35] N. Robertson and C. McGowan, "A comparison of potential molecular wires as components for molecular electronics.," *Chemical Society Reviews,* vol. 32, no. 2, pp. 96-103, 2003.

[36] C. Emmenegger, P. Mauron, P. Sudan, P. Wenger, V. Hermann, R. Gallay and A. Züttel, " Investigation of electrochemical double-layer (ECDL) capacitors electrodes based on carbon nanotubes and activated carbon materials.," *Journal of Power Sources,* vol. 124, no. 1, pp. 321-329, 2003.

[37] V. Obreja, "On the performance of supercapacitors with electrodes based on carbon nanotubes and carbon activated material—A review.," *Physica E: Low-dimensional Systems and Nanostructures,* vol. 40, no. 7, pp. 2596-2605, 2008.

[38] K. Ka Wei, T. Leng, Y. Keat, H. Osman, M. Sullivan, V. Hong, L. Ying and M. Rasidi, "Comparison study: The effect of unmodified and modified graphene nano-platelets (GNP) on the mechanical, thermal, and electrical performance of different types of GNP-filled materials.," *Polymers for Advanced Technologies,* vol. 32, no. 9, pp. 3588-3608, 2021.

[39] M. Pumera, "Graphene-based nanomaterials for energy storage.," *Energy & Environmental Science,* vol. 4, no. 3, pp. 668-674, 2011.

[40] P. Simon and Y. Gogotsi, "Materials for electrochemical capacitors.," *Nature materials,* vol. 7, no. 11, pp. 845-854, 2008.

[41] Z. Li, K. Xu and Y. Pan, "Recent development of supercapacitor electrode based on carbon materials.," *Nanotechnology Reviews,* vol. 8, no. 1, pp. 35-49, 2019.

[42] D. Yu and L. Dai, "Self-assembled graphene/carbon nanotube hybrid films for supercapacitors.," *The Journal of Physical Chemistry Letters,* vol. 1, no. 2, pp. 467-470, 2010.

[43] B. Peng, Y. Xu, X. Wang, X. Shi and F. Mulder, "The electrochemical performance of super P carbon black in reversible Li/Na ion uptake.," *Science China Physics, Mechanics & Astronomy,* vol. 60, no. 6, p. 064611, 2017.

[44] R. Gnanamuthu and C. Lee, "Electrochemical properties of Super P carbon black as an anode active material for lithium-ion batteries.," *Materials Chemistry and Physics,* vol. 130, no. 3, pp. 831-834, 2011.

[45] I. Cho, J. Choi, K. Kim, M. Ryou and Y. Lee, "A comparative investigation of carbon black (Super-P) and vapor-grown carbon fibers (VGCFs) as conductive additives for lithium-ion battery cathodes.," *Rsc Advances,* vol. 5, no. 115, pp. 95073-95078, 2015.

[46] J. Wang, J. Liu, Y. Cai, F. Cheng, Z. Niu and J. Chen, "Super P Carbon Modified Lithium Anode for High-Performance Li− O2 Batteries.," *ChemElectroChem,* vol. 5, no. 13, pp. 1702-1707, 2018.

[47] H. Chien, Y. Cheng, Y. Hao, C. Hsu, I. Cheng, S. Yu and J. Chen, "Nitrogen DC-pulse atmospheric-pressure-plasma jet (APPJ)-processed reduced graphene oxide (rGO)-carbon black (CB) nanocomposite electrodes for supercapacitor applications.," *Diamond and Related Materials,* vol. 88, pp. 23-31, 2018.

[48] M. Bavio, G. Acosta and T. Kessler, "Energy storage in symmetric and asymmetric supercapacitors based in carbon cloth/polyaniline–carbon black nanocomposites.," *International Journal of Energy Research,* vol. 39, no. 15, pp. 2053-2061, 2015.

[49] M. Ovhal, N. Kumar, H. Lee, B. Tyagi, K. Ko, S. Boud and J. Kang, "Roll-to-roll 3D printing of flexible and transparent all-solid-state supercapacitors.," *Cell Reports Physical Science,* vol. 2, no. 9, p. 100562, 2021.

[50] C. Gellrich, Y. Bräuniger, R. Schmidt, J. Grothe and S. Kaskel, "Sustainable Ketjenblack-Based Carbon Ink for 3D Extrusion Micro-Printing to Fabricate Flexible Supercapacitors," *Batteries and Supercaps,* vol. 7, no. 1, p. e202300469, 2024.

[51] M. Dresselhaus and G. J. A. Dresselhaus, "Raman spectroscopy of carbon nanotubes in 1997 and 2007.," *The Journal of Physical Chemistry C,* vol. 111, no. 48, pp. 17887-17893, 2007.

[52] M. Dresselhaus, G. Dresselhaus, R. Saito and A. Jorio, "Raman spectroscopy of carbon nanotubes.," *Physics reports,* vol. 409, no. 2, pp. 47-99, 2005.

[53] M. Dresselhaus, G. Dresselhaus, A. Jorio and A. S. R. Souza Filho, "Raman spectroscopy on isolated single wall carbon nanotubes.," *Carbon,* vol. 40, no. 12, pp. 2043-2061, 2002.

[54] A. Jorio and R. Saito, "Raman spectroscopy for carbon nanotube applications.," *Journal of Applied Physics,* vol. 129, no. 2, p. 021102, 2021.

[55] M. Shokrieh, S. Ghoreishi, M. Esmkhani and Z. Zhao, "Effects of graphene nanoplatelets and graphene nanosheets on fracture toughness of epoxy nanocomposites.," *Fatigue & Fracture of Engineering Materials & Structures,* vol. 37, no. 10, pp. 1116-1123, 2014.

[56] D. Casimir, H. Alghamdi, I. Ahmed, R. Garcia-Sanchez and P. Misra, "Chapter 2 Raman Spectroscopy of Graphene, Graphite, and Graphene Nanoplatelets," in *2D Materials*, BoD - Books on Demand, 2019, pp. 7-16.

[57] J. Shen, Y. Hu, C. Li, C. Qin, M. Shi and M. Ye, "Layer-by-layer self-assembly of graphene nanoplatelets.," *Langmuir,* vol. 25, no. 11, pp. 6122-6128, 2009.

[58] M. Itkis, D. Perea, R. Jung, S. Niyogi and R. Haddon, "Comparison of analytical techniques for purity evaluation of single-walled carbon nanotubes.," *Journal of the American Chemical Society,* vol. 127, no. 10, pp. 3439-3448, 2005.

[59] S. Kumar, K. Singh and J. Ramkumar, "Comparative study of the influence of graphene nanoplatelets filler on the mechanical and tribological behavior of glass fabric-reinforced epoxy composites.," *Polymer Composites,* vol. 41, no. 12, pp. 5403-5417, 2020.

[60] N. Elgrishi, K. Rountree, B. McCarthy, E. Rountree, T. Eisenhart and J. Dempsey, " A practical beginner's guide to cyclic voltammetry.," *Journal of chemical education,* vol. 95, no. 2, pp. 197-206, 2018.

[61] T. Mathis, N. Kurra, X. Wang, D. Pinto, P. Simon and Y. Gogotsi, "Energy Storage Data Reporting in perspective—guidelines for interpreting the performance of electrochemical energy storage systems.," *Advanced Energy Materials,* vol. 9, no. 39, p. 1902007, 2019.

[62] L. Suo, O. Borodin, T. Gao, M. Olguin, J. Ho, X. Fan, C. Luo, C. Wang and K. Xu, ""Water-in-salt" electrolyte enables high-voltage aqueous lithium-ion chemistries.," *Science,* vol. 350, no. 6263, pp. 938-943, 2015.

[63] F. Wang, O. Borodin, M. Ding, M. Gobet, J. Vatamanu, X. Fan, T. Gao, N. Edison, Y. Liang, W. Sun and S. Greenbaum, "Hybrid aqueous/non-aqueous electrolyte for safe and high-energy Li-ion batteries.," *Joule,* vol. 2, no. 5, pp. 927-937, 2018.

[64] J.-C. Liu, Z.-H. Huang and T.-Y. Ma, "Aqueous Supercapacitor with Ultrahigh Voltage Window Beyond 2.0 Volt," *Small Structures,* vol. 1, no. 1, p. 2000020, 2020.

[65] Q. Qu, P. Zhang, B. Wang, Y. Chen, S. Tian, Y. Wu and R. Holze, "Electrochemical Performance of MnO2 Nanorods in Neutral Aqueous Electrolytes as a Cathode for Asymmetric Supercapacitors," *The Journal of Physical Chemistry C,* vol. 113, no. 31, pp. 14020-14027, 2009.

[66] D. Kirk, F. Foulkes and W. Graydon, "The Electrochemical Formation of Au(I) Hydroxide on Gold in Aqueous Potassium Hydroxide," *Journal of the Electrochemical Society,* vol. 127, no. 5, pp. 1069-1076, 1980.

[67] T.-C. Wen and Y.-J. Li, "Electrochemical behavior of gold electrodeposits with and without organic compounds in KOH," *Materials Chemistry and Physics,* vol. 48, no. 3, pp. 191-198, 1997.

[68] A. Chen and J. Lipowski, "Electrochemical and Spectroscopic Studies of Hydroxide Adsorption at the Au(111) Electrode," *The Journal of Physical Chemistry B,* vol. 103, no. 4, pp. 682-691, 1999.

[69] D. Boonpakdee, C. Yévenes and W. Surareungchai, "Exploring non-linearities of carbon-based microsupercapacitors from an equivalent circuit perspective.," *Journal of Materials Chemistry A,* vol. 6, no. 16, pp. 7162-7167, 2018.

[70] B. Yoon, S. Jeong, K. Lee, H. Kim, C. Park and J. Han, "Electrical properties of electrical double layer capacitors with integrated carbon nanotube electrodes.," *Chemical Physics Letters,* vol. 388, no. 1-3, pp. 170-174, 2004.

[71] L. Zhang and G. Shi, "Preparation of highly conductive graphene hydrogels for fabricating supercapacitors with high rate capability.," *The Journal of Physical Chemistry C,* vol. 115, no. 34, pp. 17206-17212, 2011.

[72] X. Zhang, G. Xie, D. Gou, P. Luo, Y. Yao and H. Chen, "A novel enzyme-free electrochemical biosensor for rapid detection of Pseudomonas aeruginosa based on high catalytic Cu-ZrMOF and conductive Super P.," *Biosensors and Bioelectronics,* vol. 142, p. 111486, 2019.

[73] A. Laheäär, P. Przygocki, Q. Abbas and F. Béguin, " Appropriate methods for evaluating the efficiency and capacitive behavior of different types of supercapacitors.," *Electrochemistry Communications,* vol. 60, pp. 21-25, 2015.

[74] S. Sarkar, R. Akshaya and S. Ghosh, "Nitrogen doped graphene/CuCr2O4 nanocomposites for supercapacitors application: Effect of nitrogen doping on coulombic efficiency.," *Electrochimica Acta,* vol. 332, p. 135368, 2020.

[75] A. González, E. Goikolea, J. Barrena and R. Mysyk, "Review on supercapacitors: Technologies and materials.," *Renewable and sustainable energy reviews,* vol. 58, pp. 1189-1206, 2016.

[76] S. Shaheen Shan, S. Abu Nayem, N. Sultana, A. Saleh Ahammad and M. Abdul Aziz, "Preparation of sulfur-doped carbon for supercapacitor applications: a review.," *ChemSusChem,* vol. 15, no. 1, p. e202101282, 2022.

[77] A. Pandolfo and A. Hollenkamp, "Carbon properties and their role in supercapacitors.," *Journal of power sources,* vol. 157, no. 1, pp. 11-27, 2006.

[78] N. Salleh, S. Kheawhom, N. R. W. Hamid and A. Mohamad, "Electrode polymer binders for supercapacitor applications: A review," *Journal of Mateials Research and Technologies,* vol. 23, pp. 3470-3491, 2023.

Chapter 4

Solvent Pre-Soaking to Improve the Response of 3D-Printed Symmetric Carbon Supercapacitors Using FDM Printed Conductive PLA Current Collectors

Abstract

The electrochemical response of symmetric carbon-based supercapacitor devices made using two 3D-printing techniques, Vat-P (vat polymerization) and FDM (fused deposition modelling) shows how the printing method dominates the overall cell response. Though possessing excellent cycle life, the conductive polylactic acid (PLA) FDM printed current collectors suffer from relatively high resistance and suppressed capacitance linked to current collector material resistivity. Here, we examine in-situ methods to influence the interfacial conductivity of the FDM current collectors by surface modification. Both dimethylformamide (DMF) and aqueous potassium hydroxide (KOH) treatments are investigated to compare solvent decomposition and electrolyte pre-soaking for this purpose. Using a single-walled carbon nanotube and graphene nanoplatelet carbon composite slurry on FDM current collectors in Vat-P 3D-printed cells casings, the supercapacitor cells show the DMF treatment method has little benefit compared to the untreated FDM current collector cells. Pre-treatment in a solution of 6 M aqueous KOH, identical to the cell electrolyte, markedly improves the effective current collector conductivity and interface with the active material. The KOH treatment provides a tenfold reduction in the FDM current collector resistance, which correlates with the improved cyclic voltammetric response. Galvanostatic charge-discharge tests reveal a deteriorated long-term cycling stability and rate capability, despite better interfacial conductivity with the active material. In-situ pre-

soaking that allows a degree of depolymerization at the surface relieves the conductive additive within the PLA to improve electrochemical interfacial activity and identifies the failure mechanism for common electrolytes in PLA-based 3D printed aqueous supercapacitors.

4.1 Introduction

Additive manufacturing (more commonly known as 3D-printing) has seen an explosion in popularity in recent years [1–8]. Many areas of science are now extensively using 3D-printing in their research; biological engineering [9, 10, 11], healthcare [12, 13], and even food sciences [14, 15]. The field of energy storage devices (more specifically, supercapacitors) is no exception; stereolithography (SLA), also generally known as vat polymerization (Vat-P) [16], fused deposition modelling (FDM) [17, 18], direct ink writing (DIW) [19, 20], and other additive manufacturing methods [6, 7] have all been used for printing working symmetric carbon-based supercapacitors. Taking increasingly important environmental concerns into consideration, some researchers have used recycled paper, recycled conductive polylactic acid (PLA), and other carbon waste materials and sustainable waste biomass materials for making their 3D-printed electrodes [21–24]. Some studies have designed a manufacturing process that results in a functional supercapacitor device made using only 3D-printing [17, 25], though most (including this work) require some level of manual assembly. The optimal, end-stage outcome of these supercapacitor studies is a fully automated additive manufacturing process, where all supercapacitor cell components are 3D-printed into a working device with minimal external assembly or processing required. Ideally, previously mentioned environmental concerns will be met, where raw materials are obtained from renewable and/or waste biomass sources [26–28].

Our previous work involving 3D-printed supercapacitor devices details our findings for FDM printed conductive PLA current collector cells [29]. Despite possessing exceptional long-term cycling stability, the poor electronic conductivity of the FDM current collectors limited other electrochemical responses, resulting in non-ideal cyclic voltammetry responses and large ohmic drops in galvanostatic charge-discharge tests [30, 31]. As outlined in other studies, the as-printed PLA material lacks the high conductivity necessary to act as an effective electrode/current collector [5]. High electrical conductivity is essential for effective energy storage devices, to ensure efficient charge transport within the active material slurry and its interface with the 3D printed PLA current collector. As such, a post-printing treatment method is required to enhance the material's electronic conductivity, and the electrochemical performances of electrodes and current collectors made of this material. Once such method is thermal treatment via carbonisation, which both removes the insulating PLA and retains the 3D-printed structure. Redondo et al. (2020) tested the effect of carbonisation temperatures on the morphology and electrochemical performances of 3D-printed conductive PLA electrodes [32]. Though carbonisation at 300°C removed the maximum insulating PLA from the material, the same process at 500°C achieved the largest improvements in capacitance and electrochemical performances. Other studies show similar improvements in electrochemical performance, while simultaneously retaining the detail and intricacy of 3D-printed electrodes [33].

Chemical activation methods have been used extensively to improve the electronic conductivity of PLA-carbon composite materials. Gusmão et al. (2019) investigated the chemical activation ability of several common polar protic and polar aprotic solvents on 3D-printed conductive PLA electrodes [34]. Polar aprotic solvents (such as acetone and DMF) were found to be far more effective at chemical activation than polar protic solvents (DI water, MeOH, EtOH), with the DMF-activated conductive PLA electrode outperforming all other

conductive PLA electrodes in the study when it came to supercapacitor performance. Dimethylformamide (DMF) has been used in other studies for the solvent activation of polymer/graphene filaments used in 3D-printed supercapacitors [35–37]. The solvent causes the insulating PLA polymer to swell, some of which sloughs off the surface of the filament, exposing more of the filament's conductive carbon material [34]. Aqueous KOH solution (and other basic solutions, such as NaOH) have been used for chemical activation of carbon-based materials [38–40] and alkaline etching of PLA and other polymer filaments [41]. As an aliphatic polyester, PLA is susceptible to saponification, whereby it can be selectively removed using either an alkaline solution [42] or the electrolysis of water [43], which differs from the physical swelling and sloughing of PLA composites as occurs when treated with DMF or other polar aprotic solvents.

Chemical treatment is a relatively straightforward activation method which can be undertaken at room temperature, ideal for the temperature-sensitive conductive PLA current collectors. DMF and aqueous KOH were the chemicals used for these treatments. Since the 3D printed cell uses aqueous KOH-based electrolytes, we investigated electrolyte pre-soaking with the electrolyte as one of the chemical pretreatments and present a detailed examination of the different behaviours and electrochemical performances of chemically treated conductive PLA FDM printed current collectors incorporated into 3D-printed symmetric carbon supercapacitor cells. These behaviours and performances are directly compared to the FDM printed conductive PLA current collectors previously studied in Chapter 3 [29]. This study shows that electrolyte pre-soaking is effective for FDM materials such as PLA in supercapacitors under voltammetric conditions. It also demonstrates that long term cycling is relatively stable, albeit with a very low capacitance since we set out to see how the underlying PLA is depolymerized and its internal graphitic content electrically interfaces with the added active carbon slurry. At reasonably high fixed currents, we see the limitation of resistive PLA despite improved surface

conductivity, with severely suppressed capacitance during cycling a result of a failure mode in PLA exposed to electrolyte over longer periods. Changes to the PLA that improves interfacial conductivity is maintained during operation within symmetric carbon supercapacitor cells, and pre-treatment in the working electrolyte is a simple and effective was of modifying the conductive PLA, but under galvanostatic conditions it contributes to long term limitation in performance.

4.2 Experimental Procedure

A combination of Vat-P and FDM 3D-printing was implemented in this Chapter. The outer casings of the supercapacitors were printed using Vat-P, and the current collectors were printed using FDM. The printing and processing of the Vat-P 3D-printed components is detailed in Chapter 2.2.1. The printing and processing of the FDM 3D-printed components is detailed in Chapter 2.2.2. The standard batch of cells printed consists of six supercapacitor cells, with 12 current collectors and 12 half-casings printed per batch.

The procedures for the surface modification chemical treatments undertaken on the FDM current collectors are detailed in Chapter 2.2.4. A spare FDM current collector for each different treatment method was set aside for characterisation. The procedures for the Raman spectroscopy and SEM imaging undertaken on the spare FDM current collectors are detailed in Chapter 2.4.1 and Chapter 2.4.2, respectively. Resistance measurements on the FDM current collectors were also undertaken, as is explained in Chapter 2.4.3.

The treated FDM current collectors were loaded with a carbon electrode slurry consisting of SWNT and GNP in a 50:50 ratio by mass. The process for making the carbon electrode slurry is outlined in Chapter 2.3.1. The current collectors were left to air dry overnight, as applying heat can cause the plastic current collectors to burn. Once dried, the

current collectors were reweighed, and their mass loadings were measured. The cells were then assembled according to the procedure outlined in Chapter 2.5.

The assembled supercapacitor cells were testing using a variety of cyclic voltammetry (CV) and galvanostatic charge-discharge (GCD) electrochemical tests. The procedures, theory, and electrochemical settings of these tests are detailed in Chapter 2.6. The tests in this Chapter all use a potential window of 0.2–0.7 V vs. E_{oc}.

4.3 Results and Discussion

4.3.1 Material Characterisation of Chemically Treated Conductive PLA FDM Printed Current Collectors

Figure 4.1 (a) shows the schematic for the 3D-printed supercapacitor cells studied in this work, consisting of two Vat-P printed outer casings, two FDM printed conductive-PLA current collectors, and a glass microfibre filter separator soaked in 6 M aqueous KOH electrolyte. The individual 3D-printed components and fully assembled cell can be seen in Figure 4.1 (b) and Figure 4.1 (c) respectively. In our previous work with 3D-printed supercapacitor cells [29], the FDM printed conductive PLA current collectors showed poor electronic conductivity when compared to conventional stainless steel current collectors, or to Au-sputtered SLA printed current collectors also studied in that work. This resulted in high internal resistance within the 3D-printed supercapacitor cells, limiting the electrochemical performances of the cells. Simple chemical treatments were proposed as a cheap and straightforward method of improving the electronic conductivity of the FDM printed current collectors. The same cell design is used in this study, as the electrochemical performance issues did not arise from the design or assembly of the supercapacitor cell. A 3D-printed FDM conductive PLA current collector cell from Chapter 3.3.2 is used as our Untreated current collector cell (having identical electrode slurry,

electrolyte, and electrochemical tests as the chemically treated current collector cells), acting as a point of comparison to the previous work on these cells.

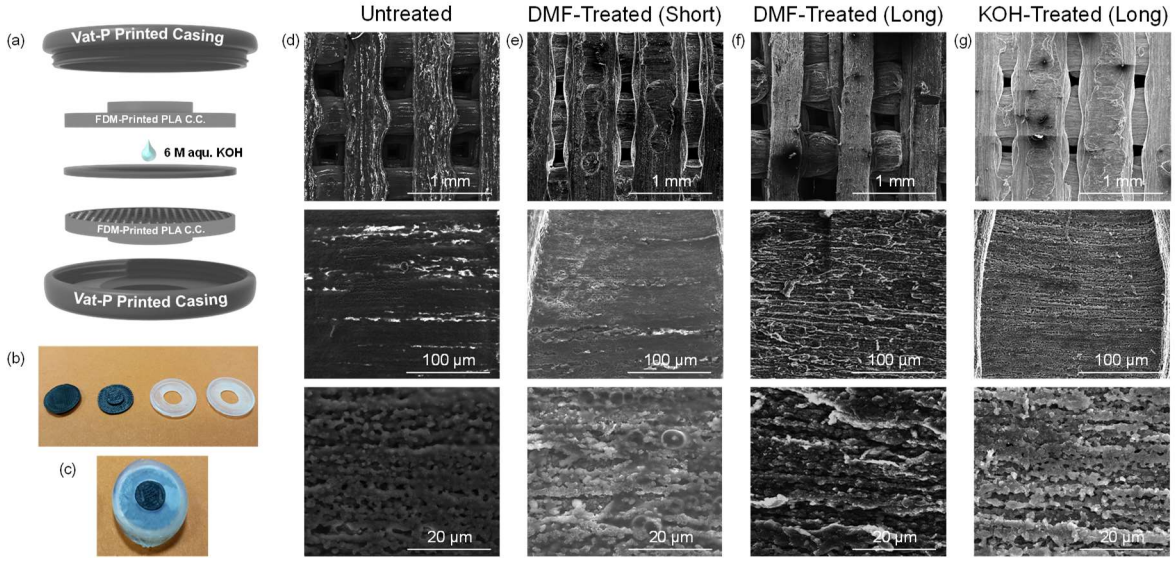

Figure 4.1 (a) Schematic for the FDM current collector symmetric supercapacitor cell made in this work, consisting of two Vat-P printed outer casings, two conductive PLA FDM printed current collectors (loaded with carbon electrode slurry after chemical treatment), and a glass microfibre filter acting as a separator soaked in 5 drops of 6 M aqueous KOH electrolyte. Images of (b) FDM printed current collectors and Vat-P printed outer casings before cell assembly and (c) one fully assembled supercapacitor cell. SEM images at varying magnifications of (d) Untreated unloaded FDM current collector, (e) DMF-Treated (Short) unloaded FDM current collector, (f) DMF-Treated (Long) unloaded FDM current collector, and (g) KOH-Treated (Long) unloaded FDM current collector.

The SEM images in Figure 4.1 and (d) and (g) show the morphologies of all four types of FDM current collectors used in these experiments after their respective chemical treatments. The filamentary/woodpile structures of the FDM-printed current collectors are clearly visible in the low magnification images. The Untreated current collector (Figure 4.1 (d)) has a smoother appearance, with a characteristic texture of smooth nodules in the conductive PLA after thermosetting. The DMF-Treated (Short) current collector (Figure 4.1 (e)) shows a rougher morphology, and the DMF-Treated (Long) and KOH-Treated (Long) current collectors (Figure 4.1 (f) and (g)) show deeper and rougher features and are porous in appearance. The smoother material present in abundance in the Untreated current collector has

clearly been removed to varying degrees by the chemical treatment methods. The depolymerization at the PLA surface relieves the internal graphitic content in the conductive PLA, and the surface roughness is cause by the random nature of the organic-inorganic composite distribution in the PLA. Excessive decomposition, however, does affect brittleness in these materials.

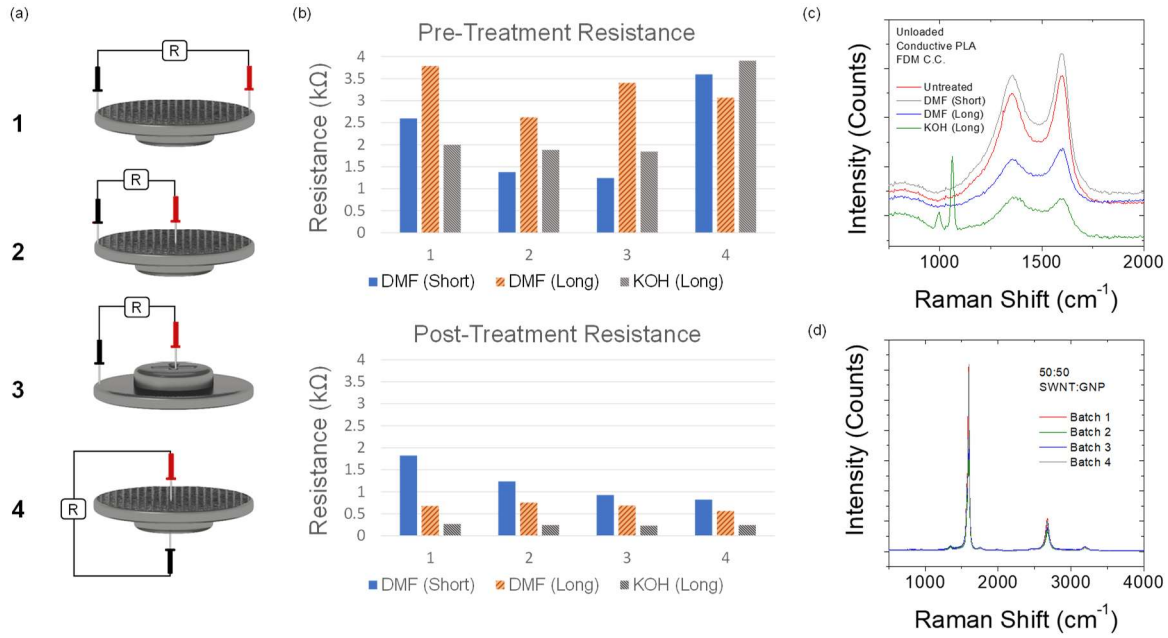

Figure 4.2 (a) Schematic for resistance measurements taken of the current collectors and the positions of the multi-meter probes. (b) bar charts of resistance measurement data before and after chemical treatments. Raman spectra of (c) chemically treated bare FDM current collectors and (d) different batches of 50:50 (SWNT:GNP) slurry used for all cells.

Resistance measurements were acquired on the different current collector types pre- and post-chemical treatment, according to Figure 4.2 (a). The resistance data shown in the bar charts in Figure 4.2 (b) show an obvious reduction in resistance for the chemically treated FDM current collectors, especially for the DMF-Treated (Long) and KOH-Treated (Long) current collectors. Correlating with the craggy and porous morphologies seen in the SEM images, the chemical treatment methods have removed some of the insulating polymer material from the conductive PLA current collectors. This has the effect of exposing more of the conductive carbon material and improving the overall conductivity of the FDM current collector interface.

Of course, the internal resistance of the FDM is unchanged, and the treatment improves the contact resistance by relieving internal graphitic components at the surface to better the interfacial conductivity with the slurry and reduce the volume of resistive polymeric material in the printed material. Both the SEM images and resistance data show that the DMF-Treated (Long) and KOH-Treated (Long) current collectors have been more extensively stripped of their insulating polymer material.

The Raman spectra for all chemically treated current collectors are shown in Figure 4.2 (c). G-bands (~1600 cm^{-1}) (arising from the stretching of C-C bonds in sp^2 graphitic materials) [44, 45] and D-bands (~1350 cm^{-1}) (arising from disorder in the sp^2 carbon structure) [46, 47] are present in all current collector types. The ratio of the G-band to D-band intensities indicate the level of disorder in a graphitic carbon structure. The KOH-Treated (Long) current collector is the only one with a more intense D-band than G-band, suggesting a more disordered graphitic structure than the other current collectors after treatment. The composition of the PLA is nominally identical in each case, and the graphitic content is randomly distributed. We rationalise the Raman scattering response by considering that the integrated signal is enhanced from the internal materials in the printed current collectors upon significant removal or surface-bound PLA. The KOH-Treated (Long) PLA is porous, rough and exhibits more of the randomly ordered graphitic structures, but a lower overall vibrational mode intensity due to scattering from the rough and porous surface. A signature of the depth of PLA removal is found in the wavenumber region 950–1100 cm^{-1}, where we see modes consistent with $C–CH_3$ and CH_3 rocking modes. These are not present on the PLA surface of untreated samples, or those pre-treated by different means or shorter times (Figure 4.2). It has been shown how NaOH can cause de-esterification and roughening of PLA [48], and this is likely caused by the K^+ ions here. The rigidity of the final porous and rough structure is maintained by the graphitic content of the filament.

The Raman spectra of the 50:50 SWNT:GNP slurry used as the electrode active material in the supercapacitor cells are shown in Figure 4.2 (d). The same G-band (~1600 cm^{-1}) and D-band (~1350 cm^{-1}) are present. The G-band in these spectra is more intense than the D-band for all batches of slurry, suggesting a very ordered graphitic carbon structure with relatively few defects present. For each slurry, Raman scattering spectra obtained in different region show a homogenous distribution of materials and consistent modes from the respective nanocarbon after 24 hours of mixing.

4.3.2 Examining Cyclic Voltammetry Response Differences of Chemically Treated FDM Printed Current Collector Supercapacitors

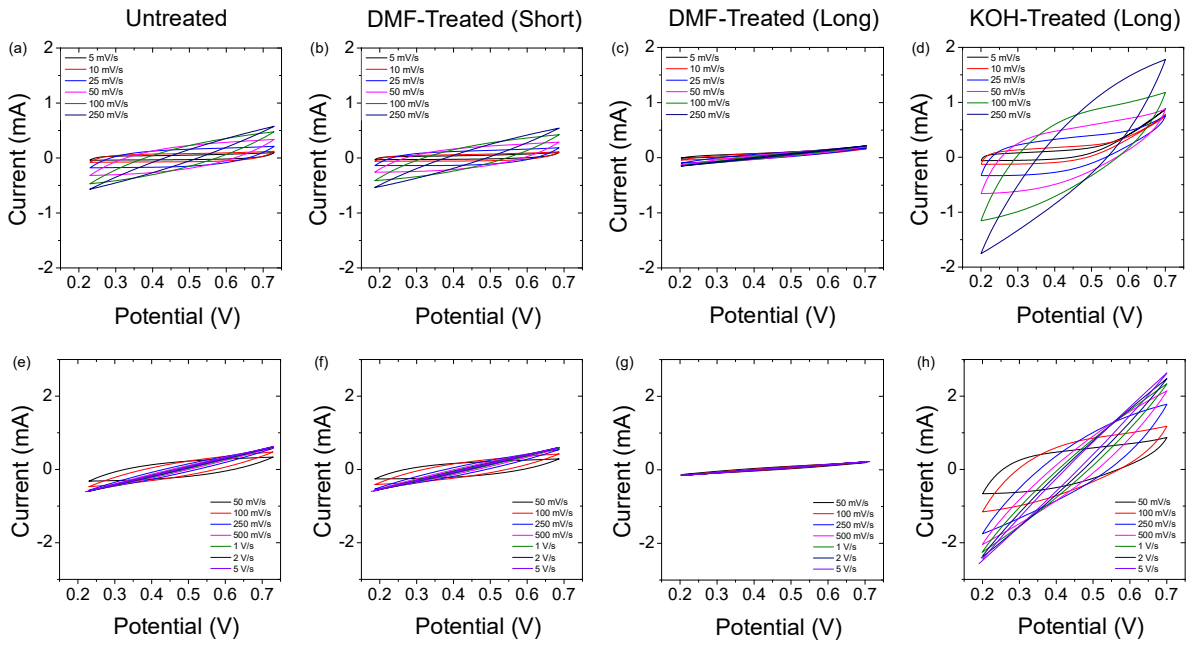

Figure 4.3 Cyclic voltammetry of conductive PLA FDM current collector printed supercapacitor cells at (a)–(d) lower scan rates in the range 5–250 mV/s, and (e)–(h) higher scan rates in the range 50–5,000 mV/s. CVs are shown for (a) and (e) Untreated current collectors, (b) and (f) DMF-Treated (Short) current collectors, (c) and (g) DMF-Treated (Long) current collectors, and (d) and (h) KOH-Treated (Long) current collectors. A voltage window of 0.2–0.7 V was used.

For all electrochemical tests, a voltage window of 0.2–0.7 V was chosen, as our previous work [29] showed signs of electrolyte degradation when using a voltage window of 0.0–1.0 V [31].

Narrow working voltage is often a disadvantage of using aqueous electrolytes [49, 50], but here allows unambiguous testing of the effect of current collector pre-treatment without parasitic reaction contributions from electrolysis.

Figure 4.3 shows the CV responses of the cells studied in this work, at lower scan rates in Figure 4.3 (a) and (d) ranging from 5–250 mV/s, and higher scan rates in Figure 4.3 (e) and (h) ranging from 50–5,000 mV/s. Looking at the shapes of the CV curves, it is immediately apparent that all cells suffers from very high internal resistance, as seen by the distinctive, narrow leaf shape of the CV curves [31, 30], rather than the pseudo-rectangular shape expected of ideal, highly-conductive EDLC behaviour [51, 52]. The CV curves presented here lack any anodic/cathodic peaks, suggesting that the energy storage mechanism within these cells is purely electronic double-layer in nature. However, the high internal resistance of the cells prevents ideal rectangular EDLC responses and hinders the optimal performance of the supercapacitor devices, which worsens with increasing scan rate. Table 4.1 summarises the integrated charge and capacitance values for each cell calculated from the cyclic voltammetry curves at a lower (5 mV/s) and higher (250 mV/s) scan rate.

Table 4.1 Summary of integrated specific charge and specific capacitance values from cyclic voltammetry data as seen in Figure 4.3.

Current Collector Chemical Treatment	Lower Scan Rate (5 mV/s)		Higher Scan Rate (250 mV/s)	
	Specific Charge (C/g)	Specific Capacitance (F/g)	Specific Charge (C/g)	Specific Capacitance (F/g)
Untreated	3.645	7.290	0.140	0.280
DMF-Treated (Short)	3.337	6.674	0.187	0.374
DMF-Treated (Long)	1.730	3.459	0.016	0.031
KOH-Treated (Long)	4.803	9.605	1.047	2.093

Both the Untreated (Figure 4.3 (a) and (e)) and the DMF-Treated (Short) (Figure 4.3 (b) and (f)) cells show very similar CV responses, both having very narrow, leaf-shaped curves caused by the high internal resistance of the cells. The curves quickly narrow further with increasing scan rate until there is negligible area within the CV curves. The values on Table 4.1 also support the similar response of these two cells, though the DMF-Treated (Short) cell shows a slight improvement over the Untreated cell at the higher scan rate (250 mV/s), with 134% the specific capacitance value of the Untreated cell. Compared to all other cells, the DMF-Treated (Long) cell (Figure 4.3 (c) and (g)) performs very poorly. The CV curves of this cell are significantly narrower than the other cells. Looking at the values on Table 4.1, the DMF-Treated (Long) cell achieves 47% of the specific capacitance of the Untreated cell at 5 mV/s, and only 11% of the specific capacitance of the Untreated cell at 250 mV/s.

The KOH-Treated (Long) cell (Figure 4.3 (d) and (h)) shows a different CV response to the other cells. Though still showing the leaf-shaped CV curves indicating high internal resistance, the area within these curves has increased, relative to the Untreated and DMF-Treated (Short) cells. Table 4.1 summarises this improvement in performance. At the lower scan rate of 5 mV/s, the KOH-Treated (Long) cell has 132% the specific capacitance value of the Untreated cell, while at the higher scan rate of 250 mV/s, it has 748% the specific capacitance value of the Untreated cell. Despite this improvement, the KOH-Treated (Long) cell still shows a CV response very different to the rectangular curves expected of high-conductivity, ideal EDLCs. However, from a plastic supercapacitor cell, the response is nonetheless improved by electrolyte soaking pre-treatment directly caused by an improvement in the current collector electrical conductivity.

4.3.3 Examining Charge-Discharge Cycle Life Differences in Chemically Treated FDM Printed Current Collector Supercapacitors

The effect of the chemical treatments on the current collector resistance and interface with the carbon slurry over many charge-discharge cycles under galvanostatic conditions was also investigated. While the capacitance values are obviously limited, the investigation examines how the PLA modification influences the cyclic stability of the charge storage process when the PLA current collectors have improved interfacial conductivity. Figure 4.4 (a)–(d) shows the cycle life response for all cells discussed so far, with the specific capacitance values extracted from 100,000 galvanostatic charge-discharge cycles. The Untreated (Figure 4.4 (a)) and DMF-Treated (Short) (Figure 4.4 (b)) cells show excellent cycle lives, retaining 81.44% and 69.39% respectively of their maximum specific capacitance values after 100,000 charge-discharge cycles. Both cells also show excellent and consistent percentage efficiency throughout this test. The cycle lives of these simple 3D-printed symmetric carbon supercapacitors compare well to other research outputs [53–55].

Following a similar pattern to the CV responses, the DMF-Treated (Long) cell (Figure 4.4 (c)) performs very poorly in this test, showing extremely low specific capacitance values and an unsteady percentage efficiency value indicative of unreliable, unstable cell performance. We surmise that DMF, often used to enhance electrospinning and thinning of PLA and other fibres, facilities rearrangement of the polymer with roughening, but without PLA decomposition to the same degree as the depolymerization and de-esterification of PLA by KOH into potassium lactates. The KOH-Treated (Long) cell (Figure 4.4 (d)) shows a worsened cycle life compared to the Untreated cell, retaining only 28.50% of specific capacitance relative to the maximum value achieved by the cell. This cell is also more sluggish in reaching its maximum percentage efficiency. The percentage efficiency begins to waver slightly after 60,000 charge-discharge cycles. These results indicate that although the KOH-Treated (Long)

current collector cells showed improved conductivity (as shown in the resistance data and CV responses), this solvent pre-treatment worsened the cycling stability of the cell.

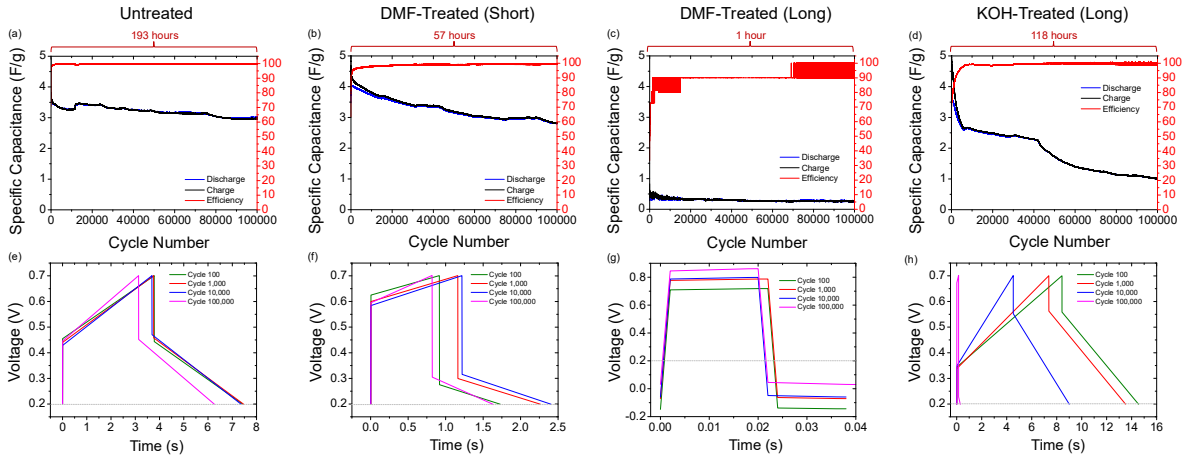

Figure 4.4 (a)–(d) Specific capacitance retention of all cell types in this work over 100,000 cycles under galvanostatic conditions. Cells were cycled between 0.2 – 0.7 V at an applied current of ±500 µA (specific applied current of 0.167 A/g). Charge-discharge curves of the cells at different points during the 100,000 cycles under galvanostatic conditions are shown in (e)–(g).

Figure 4.4 (e)–(h) shows the charge-discharge curves of the cells at different stages of the 100,000 cycles under galvanostatic conditions. Significant ohmic drops are present in all charge-discharge curves because of high internal resistance within the cells. The ohmic drop of the Untreated cell (Figure 4.4 (e)) accounts for approximately half of the voltage window, however, the exceptional cycle life stability of the cell prevents the ohmic drop from worsening. Only a slight reduction in discharge time is observed for this cell after 100,000 charge-discharge cycles. The DMF-Treated (Short) and DMF-Treated (Long) cells (Figure 4.4 (f) and (g)) show higher ohmic drops than the Untreated cell, despite the evidence for lower current collector resistance shown in the resistance data obtained in Figure 4.2 (b). The DMF-Treated (Short) cell still displays excellent cycle life stability, as the ohmic drop remains very similar after 100,000 charge-discharge cycles, with a slight reduction in charging and discharging time, as reflected in the reduction in specific capacitance.

Initially, the KOH-Treated (Long) cell (Figure 4.4 (h)) shows a smaller ohmic drop than the Untreated cell, reflecting the lower internal resistance of this cell. However, the worsened cycle life stability of the cell is also apparent, as the ohmic drop grows, and the charge and discharge times shrink throughout the charge-discharge cycles. At the 100,000 charge-discharge cycle mark, the ohmic drop has grown to nearly the entire voltage window, and the discharge time to a fraction of the starting value. The internal resistance values calculated from the charge-discharge curves are presented in Table 4.2. Thus, a failure mode is identified in PLA materials despite modification to improve interfacial conductivity that benefits faster voltammetric response. Under fixed current conditions, the internal volumetric resistance of the PLA and long-term exposure to the electrolyte over many cycles result is continued roughening that severely limits the overall performance (capacity, power) in relatively simple aqueous electrolytes. In Figure 4.5, we see cell death when the capacitance response becomes obviously noisy in Figure 4.5 (c) and (d) for example, which corresponds with the flooring of the capacitance values even though the resistance measured at the surface is not dramatically changed since its value at 100 cycles.

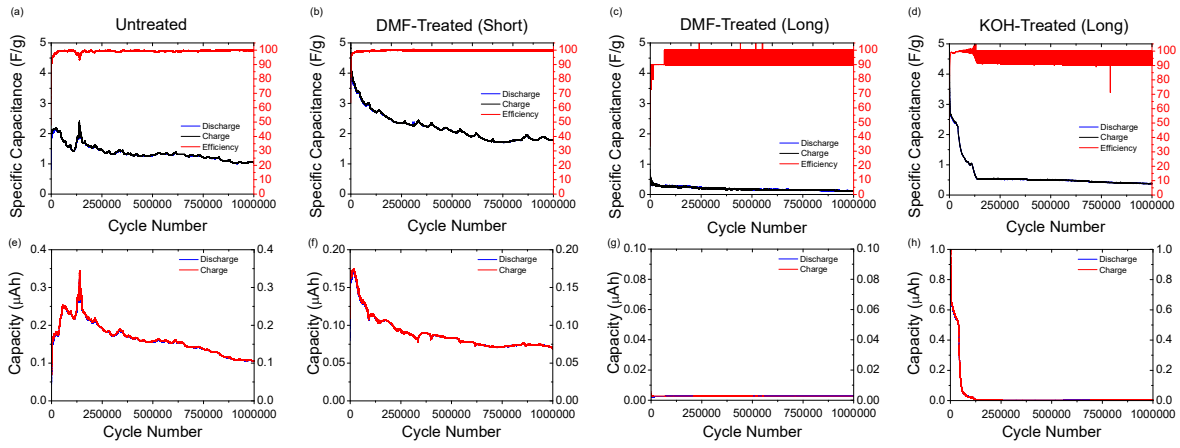

Figure 4.5 (a)–(d) Specific capacitance retention of all cell types in this work over 1,000,000 cycles under galvanostatic conditions. Cells were cycled between 0.2 and 0.7 V at an applied current of 500 μA (specific applied current of 0.167 A/g). (e)–(g) Capacity retention of all cell types in this work over 1,000,000 cycles under galvanostatic conditions. Cells were cycled between 0.2 and 0.7 V at an applied current of 500 μA (specific applied current of 0.167 A/g).

Figure 4.5 (a)–(d) shows the cycle lives of all cells across 1,000,000 charge-discharge cycles under galvanostatic conditions. The same pattern seen in the 100,000 charge-discharge cycles continues here, as both the Untreated and DMF-Treated (Short) cells (Figure 4.5 (a) and (b)) show excellent cycling stability, retaining 46.65% and 41.83% respectively of their maximum specific capacitance values after 1,000,000 charge-discharge cycles. The percentage efficiency of these cells remains steadily around 100%, with very little oscillation. The KOH-Treated (Long) cell again shows a worsened cycle-life stability, retaining 10.72% of its maximum specific capacitance, as well as an unsteady percentage efficiency for most of the test.

Table 4.2 Summary of internal resistance values calculated from charge-discharge curves under galvanostatic conditions as seen in Figure 4.4.

Current Collector Chemical Treatment	Resistance at Cycle 100 (Ω)	Resistance at Cycle 100,000 (Ω)
Untreated	257.31	249.08
DMF-Treated (Short)	425.61	396.52
KOH-Treated (Long)	141.56	474.07

Table 4.3 Maximum capacity values achieved by each cell, and capacity values at different stages of the 1,000,000 charge-discharge cycles in terms of percentages of maximum capacity.

Current Collector Chemical Treatment	Maximum Capacity (μAh)	Percentage of Maximum Capacity		
		Cycle 10,000	Cycle 100,000	Cycle 1,000,000
Untreated	0.323	49.53%	70.28%	32.20%
DMF-Treated (Short)	0.172	95.93%	65.70%	40.12%
DMF-Treated (Long)	0.00278	89.93%	100%	89.93%
KOH-Treated (Long)	0.871	71.53%	2.30%	0.287%

Figure 4.5 (e)–(h) shows the cycle lives of the cells in terms of capacity across 1,000,000 charge-discharge cycles under galvanostatic conditions. Table 4.3 shows the percentage capacity retention of the cells at different stages in the charge-discharge tests. The high cycle life stability of the Untreated and DMF-Treated (Short) cells, and the relatively low cycle life stability of the KOH-Treated (Long) cell is very apparent from these percentage values. It is quite possible that the conductive PLA current collectors, already extensively etched by the long KOH treatment, begin to lose their structural integrity upon further (even longer) exposure to the 6 M aqueous KOH electrolyte, resulting in the serious long-term stability problems seen in these results.

4.3.4 Examining Rate Response Differences in Chemically Treated FDM Printed Current Collector Supercapacitors

Rate capability tests were carried out on all cells to examine the influence of current collector chemical treatments on the stability of their interface with the active materials, but also to investigate the impact of PLA failure after longer exposure to electrolyte at fixed current. Figure 4.6 shows the response of all cells extracted from galvanostatic charge-discharge tests. The Untreated current collector FDM printed supercapacitor cell best retains its specific capacitance over repeated cycling at successively higher rates (51.87% retention after tenfold increase in applied current, 100 µA to 1 mA). The chemically treated current collector FDM printed supercapacitor cells perform worse, retaining only 25.32% (DMF-Treated (Short)), 0% (DMF-Treated (Long)), and 5.71% (KOH-Treated (Long)) of their specific capacitance after a tenfold increase in applied current. All four cells recover almost all specific capacitance (92.68-99.58%) after returning to the initial rate.

The results of these varied-current galvanostatic tests show that all the FDM current collector cells have poor rate capability and are not suited for high current density applications,

but with modification are potentially useful for low power, small cell applications where the printable materials can be readily recycled. The low capacitance retention can be attributed to the high resistance of the FDM current collectors, resulting in inefficient charge transfer during discharge processes at higher currents. In fact, the chemical treatment methods have worsened the rate capability of the cells when compared to the Untreated cell performance, despite initial improvements in capacitance. Though comparing well to other studies in terms of cycle life, these cells lack the good rate capability present with other carbon nanotube/graphene-based supercapacitors which use more conductive current collector components in their devices [56–59]. Nonetheless, this work remains instructive for understanding the nature of PLA and FDM cell components for aqueous energy storage systems.

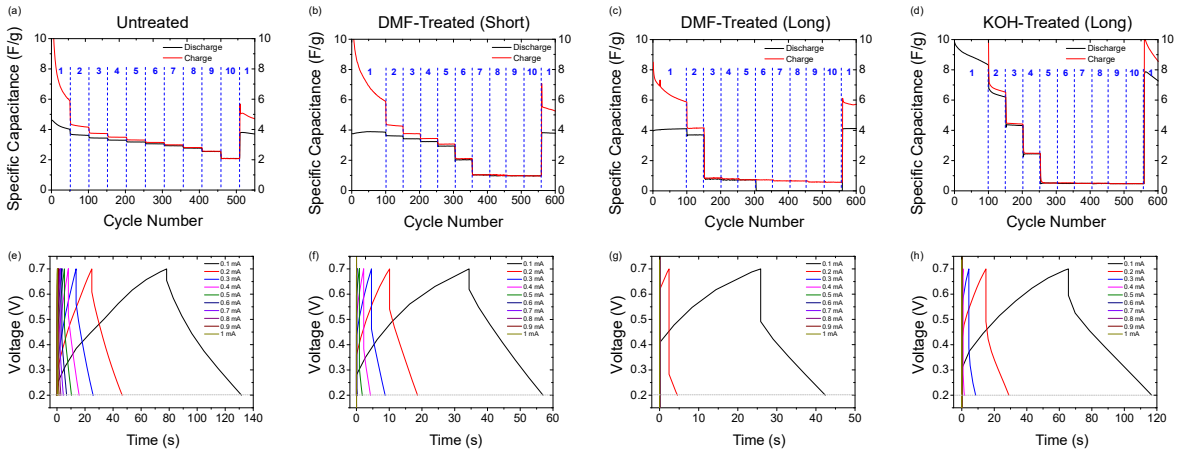

Figure 4.6 (a)–(d) Varied-current life-cycle plot for all cells studied in this work under galvanostatic conditions with increasing applied current. The blue numbers between the dotted lines correspond to the charging and discharging current used in that cycle period, progressing through 1 (±100 µA or 0.033 A/g), 2 (±200 µA or 0.067 A/g), 3 (±300 µA or 0.100 A/g), 4 (±400 µA or 0.133 A/g), 5 (±500 µA or 0.167 A/g), 6 (±600 µA or 0.200 A/g), 7 (±700 µA or 0.233 A/g), 8 (±800 µA or 0.267 A/g), 9 (±900 µA or 0.300 A/g), 10 (±1 mA or 0.333 A/g), then returning to 1 (±100 µA or 0.033 A/g). Cells were cycled between 0.2 and 0.7 V. (e)–(h) charge-discharge curves of the cells at each of the increasing applied charge-discharge currents.

For all cells tested in this work, their specific capacitance values and discharge times from Figure 4.6 were used to calculate their specific energies and specific powers applied currents of 0.1 mA, 0.5 mA, and 1 mA which is outlined in Table 4.4. Due to poor rate

performance at higher applied currents, the specific energies of the treated cells at 1 mA were unobtainable (because of distorted voltage window stretching beyond the voltage window in the settings, and miniscule discharge times).

At the currents applied in this work, the specific energy and specific power values are very low for EDLC devices. Specific energies of 1-10 Wh/kg and specific powers of 500-10,000 W/kg are typical for EDLC devices [60–63]. The specific energies (therefore specific powers) of the devices in this study suffer from the narrow operating voltage window and the resistance values that remain too high for mA-level galvanostatic cycling. Potentiodynamic responses, useful not only for some supercapacitor applications but also in electrochemical sensors for example, are much better due to electrolyte pre-soaking.

Table 4.4 Specific energies and specific powers calculated from the galvanostatic rate capability tests.

Current Collector Chemical Treatment	Specific Energy of Electrode Material (Wh/kg)			Specific Power of Electrode Material (W/kg)		
	At 0.1 mA	At 0.5 mA	At 1 mA	At 0.1 mA	At 0.5 mA	At 1 mA
Untreated	0.1151	0.0326	0.0005	7.76	23.50	6.57
DMF-Treated (Short)	0.0943	0.0045	-	15.04	18.54	-
DMF-Treated (Long)	0.0486	-	-	10.58	-	-
KOH-Treated (Long)	0.1804	0.000025	-	12.67	3.75	-

4.4 Conclusions

In this Chapter, we expanded our investigation into FDM printed current collectors, testing different solvent pre-soaking procedures with the aim to improve their interfacial conductivity, thereby mitigating some of the performance issues encountered with these FDM current collectors in Chapter 3. We showed that for hydroxide-based electrolytes, pre-soaking was

shown to improve the interfacial conductivity of conductive additive-impregnated 3D printed PLA current collectors, compared to chemical decomposition or modification using DMF. By depolymerizing the outer surface, exposed graphite improves the interfacial conductivity with the carbon-based active materials in the symmetric supercapacitor. These FDM-printed current collectors designed to fit with Vat-P printed cell show moderate electrical conductivity increase for the DMF-Treated (Short) current collectors and a significant reduction in resistance for the DMF-Treated (Long) and KOH-Treated (Long) current collectors. SEM images of the current collector morphology confirm the removal of non-conductive material from the conductive PLA current collectors via electrolyte pre-soaking. Cyclic voltammetry tests show near-identical responses from the Untreated and DMF-Treated (Short) cells, and an improved response for the KOH-Treated (Long) cell, which is useful for some voltammetric charge storage applications or electrochemical sensors where the fast response is dominated by the surface activity with current values linked to the driving voltage. Galvanostatic data, however, at higher fixed current shows stable and incrementally improve capacitance, but the higher surface conductivity PLA after long KOH pre-soaking showed a worse cycle response compared to untreated FDM. We identify a failure mode for PLA linked to decomposition the fundamentally limits its use in systems such as this with relatively simple aqueous electrolytes over longer durations. The limitation in long cycle life efficiency is fundamental to PLA current collectors and electrodes in such 3D printed aqueous supercapacitors, and future work should consider the impact of these types of electrolytes on printed passive or active materials in energy storage devices. For electrochemical sensors using printed electrodes, voltammetric responses can be improved with surface interfacial conductivity and area modification, but galvanostatic response over long durations is much less performant.

4.5 References

[1] J. Li, M. Leu, R. Panat and J. Park, "A hybrid three-dimensionally structured electrode for lithium-ion batteries via 3D printing.," *Materials & Design,* vol. 119, pp. 417-424, 2017.

[2] B. Yao, S. Chandrasekaran, J. Zhang, W. Xiao, F. Qian, C. Zhu, E. Duoss, C. Spadaccini, M. Worsley and Y. Li, "Efficient 3D printed pseudocapacitive electrodes with ultrahigh MnO2 loading.," *Joule,* vol. 3, no. 2, pp. 459-470, 2019.

[3] A. Ambrosi and M. Pumera, "3D-printing technologies for electrochemical applications.," *Chemical society reviews,* vol. 45, no. 10, pp. 2740-2755, 2016.

[4] V. Egorov and C. O'Dwyer, "Architected porous metals in electrochemical energy storage.," *Current Opinion in Electrochemistry,* vol. 21, pp. 201-208, 2020.

[5] S. O'Hanlon and C. O'Dwyer, "Electrodeposition onto Conductive Additive-Impregnated 3D Printed Polylactic Acid Electrodes.," *Journal of The Electrochemical Society,* vol. 169, no. 8, p. 082514, 2022.

[6] V. Egorov, U. Gulzar, Y. Zhang, S. Breen and C. O'Dwyer, "Evolution of 3D printing methods and materials for electrochemical energy storage.," *Advanced Materials,* vol. 32, no. 29, p. 2000556, 2020.

[7] U. Gulzar, C. Glynn and C. O'Dwyer, "Additive manufacturing for energy storage: Methods, designs and material selection for customizable 3D printed batteries and supercapacitors.," *Current Opinion in Electrochemistry,* vol. 20, pp. 46-53, 2020.

[8] A. Maurel, M. Courty, B. Fleutot, H. Tortajada, K. Pdrashantha, M. Armand, S. Grugeon, S. Panier and L. Dupont, "Highly loaded graphite–polylactic acid composite-based filaments for lithium-ion battery three-dimensional printing.," *Chemistry of Materials,* vol. 30, no. 21, pp. 7484-7493, 2018.

[9] A. Mironov, A. Grigoryev, L. Krotova, N. Skaletsky, V. Popov and V. Sevastianov, "3D printing of PLGA scaffolds for tissue engineering.," *Journal of Biomedical Materials Research Part A,* vol. 105, no. 1, pp. 104-109, 2017.

[10] A. Aimar, A. Palermo and B. Innocenti, "The role of 3D printing in medical applications: a state of the art.," *Journal of healthcare engineering,* vol. 2019, 2019.

[11] T. Distler and A. Boccaccini, "3D printing of electrically conductive hydrogels for tissue engineering and biosensors–A review.," *Acta biomaterialia,* vol. 101, pp. 1-13, 2020.

[12] K. Kumar and M. Pumera, "3D-Printing to Mitigate COVID-19 Pandemic.," *Advanced Functional Materials,* vol. 31, no. 22, p. 2100450, 2021.

[13] N. Bruns and C. Krettek, "3D-printing in trauma surgery: Planning, printing and processing.," *Der Unfallchirurg,* vol. 122, pp. 270-277, 2019.

[14] Y. Liu, Y. Yu, C. Liu, J. Regenstein, X. Liu and P. Zhou, "Rheological and mechanical behavior of milk protein composite gel for extrusion-based 3D food printing.," *Lwt,* vol. 102, pp. 338-346, 2019.

[15] A. Le-Bail, B. Maniglia and P. Le-Bail, "Recent advances and future perspective in additive manufacturing of foods based on 3D printing.," *Current Opinion in Food Science,* vol. 35, pp. 54-64, 2020.

[16] J. Xue, L. Gao, X. Hu, K. Cao, W. W. W. Zhou and Y. Lu, "Stereolithographic 3D printing-based hierarchically cellular lattices for high-performance quasi-solid supercapacitor.," *Nano-Micro Letters,* vol. 11, pp. 1-13, 2019.

[17] A. Tanwilaisiri, Y. Xu, R. Zhang, D. Harrison, J. Fyson and M. Areir, "Design and fabrication of modular supercapacitors using 3D printing.," *Journal of Energy Storage,* vol. 16, pp. 1-7, 2018.

[18] X. Yan, Y. Tong, X. Wang, F. Hou and J. Liang, "Extrusion-Based 3D-Printed Supercapacitors: Recent Progress and Challenges.," *Energy & Environmental Materials,* vol. 5, no. 3, pp. 800-822, 2022.

[19] X. Yun, B. Lu, Z. Xiong, B. Jia, B. Tang, H. Mao and T. W. X. Zhang, "Direct 3D printing of a graphene oxide hydrogel for fabrication of a high areal specific capacitance microsupercapacitor.," *RSC advances,* vol. 9, no. 50, pp. 29384-29395, 2019.

[20] B. Chen, Y. Jiang, X. Tang, Y. Pan and S. Hu, "Fully packaged carbon nanotube supercapacitors by direct ink writing on flexible substrates.," *ACS applied materials & interfaces,* vol. 9, no. 34, pp. 28433-28440, 2017.

[21] X. Aeby, A. Poulin, G. Siqueira, M. Hausmann and G. Nyström, "Fully 3D printed and disposable paper supercapacitors.," *Advanced Materials,* vol. 33, no. 26, p. 2101328, 2021.

[22] M. Idrees, S. Ahmed, Z. Mohammed, N. Korivi and V. Rangari, "3D printed supercapacitor using porous carbon derived from packaging waste.," *Additive Manufacturing,* vol. 36, p. 101525, 2020.

[23] P. Wuamprakhon, R. Crapnell, E. Sigley, N. Hurst, R. Williams, M. Sawangphruk, E. Keefe and C. Banks, "Recycled Additive Manufacturing Feedstocks for Fabricating High Voltage, Low-Cost Aqueous Supercapacitors.," *Advanced Sustainable Systems,* vol. 7, no. 2, p. 2200407, 2023.

[24] Z. Qiu, Y. Wang, X. Bi, T. Zhou, J. Zhou, J. Zhao, Z. Miao, W. Yi, P. Fu and S. Zhuo, "Biochar-based carbons with hierarchical micro-meso-macro porosity for high rate and long cycle life supercapacitors," *Journal of Power Sources,* vol. 376, pp. 82-90, 2018.

[25] M. Areir, Y. Xu, D. Harrison and J. Fyson, "3D printing of highly flexible supercapacitor designed for wearable energy storage.," *Materials Science and Engineering: B,* vol. 226, pp. 29-38, 2017.

[26] A. Abioye and F. Ani, "Recent development in the production of activated carbon electrodes from agricultural waste biomass for supercapacitors: A review," *Renewable and Sustainable Energy Reviews,* vol. 52, pp. 1282-1293, 2015.

[27] T. Kan, V. Strezov and T. Evans, "Lignocellulosic biomass pyrolysis: A review of product properties and effects of pyrolysis parameters," *Renewable and Sustainable Energy Reviews,* vol. 57, pp. 1126-1140, 2016.

[28] H. Eom, J. Kim, I. Nam and S. Bae, "Recycling Black Tea Waste Biomass as Activated Porous Carbon for Long Life Cycle Supercapacitor Electrodes," *Materials,* vol. 14, no. 21, p. 6592, 2021.

[29] M. Ferguson, V. Egorov, Y. Zhang, U. Gulzar and C. O'Dwyer, "The Influence of 3D Printing Methods and Materials on the Response of Printed Symmetric Carbon Supercapacitors," *ECS Advances,* vol. 3, no. 3, p. 032501, 2024.

[30] D. Boonpakdee, C. Yévenes and W. Surareungchai, "Exploring non-linearities of carbon-based microsupercapacitors from an equivalent circuit perspective.," *Journal of Materials Chemistry A,* vol. 6, no. 16, pp. 7162-7167, 2018.

[31] T. Mathis, N. Kurra, X. Wang, D. Pinto, P. Simon and Y. Gogotsi, "Energy Storage Data Reporting in perspective—guidelines for interpreting the performance of electrochemical energy storage systems.," *Advanced Energy Materials,* vol. 9, no. 39, p. 1902007, 2019.

[32] E. Redondo, S. Ng, J. Muñoz and M. Pumera, "Tailoring capacitance of 3D-printed graphene electrodes by carbonisation temperature," *Nanoscale,* vol. 12, pp. 19673-19680, 2020.

[33] F. Novotný, V. Urbanová, J. Plutnar and M. Pumera, "Preserving Fine Structure Details and Dramatically Enhancing Electron Transfer Rates in Graphene 3D-Printed Electrodes via Thermal Annealing: Toward Nitroaromatic Explosives Sensing," *ACS Applied Materials & Interfaces,* vol. 11, no. 38, p. 35371–35375, 2019.

[34] R. Gusmão, M. Browne, Z. Sofer and M. Pumera, "The capacitance and electron transfer of 3D-printed graphene electrodes are dramatically influenced by the type of solvent used for pre-treatment," *Electrochemistry Communications,* vol. 102, pp. 83-88, 2019.

[35] S. Srinivasan K. V, J. Santo and P. Penumakala, "Effect of surface modification of printed electrodes on the performance of supercapacitors," *Journal of Energy Storage,* vol. 56, no. B, p. 106043, 2022.

[36] G. Zhu, Y. Hou, J. Lu, H. Zhang, Z. Zhuang, M. Baig, M. Khan, M. Akram, S. Dong, P. Liu, X. Ge and Y. Zhang, "MXene decorated 3D-printed carbon black-based electrodes for solid-state micro-supercapacitors," *Journal of Materials Chemistry A,* vol. 11, no. 46, pp. 25422-25428, 2023.

[37] M. Browne, E. Renondo and M. Pumera, "3D Printing for Electrochemical Energy Applications," *Chemical Reviews,* vol. 120, no. 5, pp. 2783-2810, 2020.

[38] J. Zhou, Z. Zhang, W. Xing, J. Yu, G. Han, W. Si and S. Zhou, "Nitrogen-doped hierarchical porous carbon materials prepared from meta-aminophenol formaldehyde resin for supercapacitor with high rate performance," *Electrochimica Acta,* vol. 153, pp. 68-75, 2015.

[39] Y. Liu, Z. Shi, Y. Gao, W. An, Z. Cao and J. Liu, "Biomass-Swelling Assisted Synthesis of Hierarchical Porous Carbon Fibers for Supercapacitor Electrodes," *ACS Applied Materials and Interfaces,* vol. 8, no. 42, pp. 28283-28290, 2016.

[40] B. Xu, Y. Chen, G. wei, G. Cao, H. Zhang and Y. Yang, "Activated carbon with high capacitance prepared by NaOH activation for supercapacitors," *Materials Chemistry and Physics,* vol. 124, no. 1, pp. 504-509, 2010.

[41] R. Bernasconi, G. Natale, M. Levi and L. Magagnin, "Electroless Plating of NiP and Cu on Polylactic Acid and Polyethylene Terephthalate Glycol-Modified for 3D Printed Flexible Substrates," *Journal of the Electrochemical Society,* vol. 163, no. 9, p. D526, 2016.

[42] R. Shergill and B. Patel, "Preprinting Saponification of Carbon Thermoplastic Filaments Provides Ready-to-Use Electrochemical Sensors," *ACS Applied Electronic Materials,* vol. 5, no. 9, pp. 5120-5128, 2023.

[43] D. Wirth, M. Sheaff, J. Waldman, M. Symcox, H. Whitehead, J. Sharp, J. Doerfler, A. Lamar and G. LeBlanc, "Electrolysis Activation of Fused-Filament-Fabrication 3D-Printed Electrodes for Electrochemical and Spectroelectrochemical Analysis," *Analytical Chemistry,* vol. 91, no. 9, pp. 5553-5557, 2019.

[44] M. Dresselhaus and G. J. A. Dresselhaus, "Raman spectroscopy of carbon nanotubes in 1997 and 2007.," *The Journal of Physical Chemistry C,* vol. 111, no. 48, pp. 17887-17893, 2007.

[45] M. Dresselhaus, G. Dresselhaus, R. Saito and A. Jorio, "Raman spectroscopy of carbon nanotubes.," *Physics reports,* vol. 409, no. 2, pp. 47-99, 2005.

[46] M. Dresselhaus, G. Dresselhaus, A. Jorio and A. S. R. Souza Filho, "Raman spectroscopy on isolated single wall carbon nanotubes.," *Carbon,* vol. 40, no. 12, pp. 2043-2061, 2002.

[47] A. Jorio and R. Saito, "Raman spectroscopy for carbon nanotube applications.," *Journal of Applied Physics,* vol. 129, no. 2, p. 021102, 2021.

[48] C. Tham, Z. Hamid, Z. Ahmad and I. Hanafi, "Surface Modification of Poly(lactic acid) (PLA) via Alkaline Hydrolysis Degradation," *Advanced Materials Research,* vol. 970, pp. 324-327, 2014.

[49] F. Wang, O. Borodin, M. Ding, M. Gobet, J. Vatamanu, X. Fan, T. Gao, N. Edison, Y. Liang, W. Sun and S. Greenbaum, "Hybrid aqueous/non-aqueous electrolyte for safe and high-energy Li-ion batteries.," *Joule,* vol. 2, no. 5, pp. 927-937, 2018.

[50] L. Suo, O. Borodin, T. Gao, M. Olguin, J. Ho, X. Fan, C. Luo, C. Wang and K. Xu, "“Water-in-salt” electrolyte enables high-voltage aqueous lithium-ion chemistries.," *Science,* vol. 350, no. 6263, pp. 938-943, 2015.

[51] S. Sharma and P. Chand, "Supercapacitor and electrochemical techniques: A brief review," *Results in Chemistry,* vol. 5, p. 100885, 2023.

[52] S. Aderyani, P. Flouda, S. Shah, M. Green, J. Lutkenhaus and H. Ardebili, "Simulation of cyclic voltammetry in structural supercapacitors with pseudocapacitance behavior," *Electrochimica Acta,* vol. 390, p. 138822, 2021.

[53] M. Zhong, M. Zhang and X. Li, "Carbon nanomaterials and their composites for supercapacitors," *Carbon Energy,* vol. 4, no. 5, pp. 950-985, 2022.

[54] M. Zakaria, M. Omar, M. Abidin, H. Akil and M. Abdullah, "Recent progress in the three-dimensional structure of graphene-carbon nanotubes hybrid and their supercapacitor and high-performance battery applications," *Composites Part A: Applied Science and Manufacturing,* vol. 154, p. 106756, 2022.

[55] O. Okhay, A. Tkach, P. Staiti and F. Lufrano, "Long term durability of solid-state supercapacitor based on reduced graphene oxide aerogel and carbon nanotubes composite electrodes," *Electrochimica Acta,* vol. 353, p. 136540, 2020.

[56] N. Bardi, T. Giannakopoulou, A. Vavouliotis and C. Trapalis, "Electrodeposited Films of Graphene, Carbon Nanotubes, and Their Mixtures for Supercapacitor Applications," *ACS Applied Nano Materials,* vol. 3, no. 10, pp. 10003-10013, 2020.

[57] W. Ma, W. Li, M. Li, Q. Mao, Z. Pan, J. Hu, X. Li, M. Zhu and Y. Zhang, "Unzipped Carbon Nanotube/Graphene Hybrid Fiber with Less “Dead Volume” for Ultrahigh Volumetric Energy Density Supercapacitors," *Advanced Functional Materials,* vol. 31, no. 19, p. 2100195, 2021.

[58] Z. Ma, J. Yang, J. Zhang, G. Chen, C. Miao, L. Shi, L. Wang and Z. Zhang, "Layer-opened graphene paper with carbon nanotubes as support in a flexible electrode material for supercapacitors," *Journal of Alloys and Compounds,* vol. 775, pp. 982-989, 2019.

[59] L. Zhou, J. Wang, Z. Liu, J. Yang, M. Chen, Y. Zheng, W. Wu, Z. Gao and C. Xiong, "Facile self-assembling of three-dimensional graphene/solvent free carbon nanotubes fluid framework for high performance supercapacitors," *Journal of Alloys and Compounds,* vol. 820, p. 153157, 2020.

[60] A. González, E. Goikolea, J. Barrena and R. Mysyk, "Review on supercapacitors: Technologies and materials.," *Renewable and sustainable energy reviews,* vol. 58, pp. 1189-1206, 2016.

[61] S. Shaheen Shan, S. Abu Nayem, N. Sultana, A. Saleh Ahammad and M. Abdul Aziz, "Preparation of sulfur-doped carbon for supercapacitor applications: a review.," *ChemSusChem,* vol. 15, no. 1, p. e202101282, 2022.

[62] A. Pandolfo and A. Hollenkamp, "Carbon properties and their role in supercapacitors.," *Journal of power sources,* vol. 157, no. 1, pp. 11-27, 2006.

[63] P. Simon and Y. Gogotsi, "Materials for electrochemical capacitors.," *Nature materials,* vol. 7, no. 11, pp. 845-854, 2008.

Chapter 5

Manganese Oxide Inverse-Opal and Carbon Composite Electrodes and their Effect on the Response of 3D-Printed Symmetric Carbon Supercapacitors

Abstract

Expanding upon the 3D-printed supercapacitor framework established in the previous two chapters, this final chapter explores the inclusion of pseudo-capacitive active materials in our electrode materials, in the form of manganese oxide inverse-opals (IOs). As with Chapter 3, two different 3D-printed cell types are studied; one with metallized Vat-P-printed current collectors, the other with PLA (polylactic acid) FDM-printed current collectors in a similarly designed printed coin cell. Various mixtures of MO-IOs with previously studied carbon electrode materials and additives (SWNT, GNP, Super-P, PVDF) are analysed within these cells, using 6 M aqueous KOH as electrolyte. Cyclic voltammetry and galvanostatic charge-discharge tests are used to analyse and compare the performances of different electrode materials within the cells, as well as further comparing the performances of the two different 3D-printed current collectors. MO-IO-carbon composite slurries prepared in a similar manner and composition to previous chapters showed disappointing electrochemical response, being consistently inferior to other cells in Chapter 3. However, improved electrochemical performances were obtained by employing a different electrode slurry preparation method and exploring new compositions of MO-IO-carbon electrode slurries.

5.1 Introduction

As has been shown in the previous two chapters, carbon-based materials for EDLC devices offer exceptional cycling stabilities and inert chemistries, though suffer from lower specific energies relative to other materials used in supercapacitor devices. Pseudo-capacitive materials store energy via rapid, reversible redox reactions, which are not limited to just the surface of the electrodes [1–3]. As such, they are often used instead of (or in conjunction with) EDLC materials to boost the specific capacitance and specific energy response of supercapacitor devices. However, the reversible redox reaction energy storage mechanism could compromise the high cycle life stability and specific power of the supercapacitor device [4, 5].

As discussed in Chapter 1.3, there exists a great variety of pseudo-capacitive materials for energy storage, such as transition metal oxides (TMOs) [6–9] (as well as transition metal nitrides [10] and sulfides [11]), conductive polymers [12–15], MXenes [16, 17], and metal organic frameworks (MOFs) [18, 19]. MnO_2, a TMO-type material, will be the focus of the pseudo-capacitance studies for this chapter. Other TMO materials, such as RuO_2, possess higher specific capacitance values (720 F/g at a voltage window of 1 V in 0.5 M H_2SO_4 electrolyte solution [20]), but are extremely expensive and environmentally toxic [21, 22]. MnO_2 is far cheaper than RuO_2, environmentally inert [23], and effective in neutral electrolyte solutions [24, 25], while still offering respectably high specific capacitance values (~200 F/g in 2 M aqueous KCl electrolyte at a voltage window of 1.2 V (-0.2 and +1.0 V versus SCE)) [26]. The charge storage mechanism for MnO_2 (in neutral, aqueous KCl electrolyte) involves fast reversible redox reactions through both the potassium ions ($MnO_2 + xK^+ + xe^- \Leftrightarrow MnO_{2-x}(OK)_x$) and protons from the protic solvent ($MnO_2 + xH^+ + xe^- \Leftrightarrow MnO_{2-x}(OH)_x$), depending on availability of the cations [27]. Manganese oxides are also less electronically conductive

than RuO_2 [28, 29], but this can be mitigated by forming composites with conductive carbon materials [30, 31], which we have worked with extensively throughout this project.

One form of manganese oxide is Mn_3O_4, which exists in nature as the mineral hausmannite [32]. This material has a spinel structure (AB_2X_4), with Mn^{2+} ions in tetrahedrally coordinated voids and Mn^{3+} ions in octahedrally coordinated voids [33]. This material is of great interest to researchers in energy storage, due to its excellent theoretical capacitance, low cost, abundance, and environmental inertness [34], but is also more seldomly researched for this purpose than other manganese oxides (such as MnO_2 and MnO) [35]. As with other forms of manganese oxide, the low electronic conductivity and low SSA of Mn_3O_4 are its main drawbacks as an electrode material [36, 37].

Chapter 1.2 delves into detail about the synergistic effects of different carbon materials in electrode composites. The concept of conductive "highways" and "local roads" is highlighted, whereby long, fibrous conductive carbons (such as SWNTs), and finer, conductive carbon particles (such as Super-P) work synergistically to facilitate short-range and long-range electron transport respectively throughout the electrode active materials [38, 39]. This concept is of particular interest for forming effective electrode composites with the less conductive Mn_3O_4 active materials [37, 40], as is done in this chapter with various carbon materials (SWNTs, GNPs, and Super-P).

The Mn_3O_4 electrode materials used in this chapter have been synthesised into inverse-opal structures. As discussed in Chapter 1.3, inverse-opals (IOs) consist of face-centred cubic (fcc) packed spherical pores, with the space around these pores filled by material (in this case, Mn_3O_4) [41]. Inverse opals are obtained by depositing a sacrificial colloidal crystal opal template, such as polystyrene spheres (the size of which will determine the dimensions of the IO product's pores). The precursor material is then infiltrated into the template in fluid form

and/or dissolved in a solvent, filling the gaps between the spheres before being chemically or physically solidified. Finally, the sacrificial opal template is removed, usually via chemical and/or thermal treatment [42–44]. The highly ordered, porous structure offers extremely controllable SSA and pore size for the electrode active material. The ability to control these parameters is highly advantageous to energy storage, allowing optimisation of the SSA available for double-layer formation in supercapacitors [45], and aiding in mass transport and rate capabilities for battery and pseudo-capacitive type energy storage systems [46].

In this chapter, we formulate several different electrode composite mixtures which incorporate Mn_3O_4-IOs and a variety of carbon materials. These electrode composites are implemented into our 3D-printed current collector and outer casing components and assembled into symmetric supercapacitor devices. The responses of pseudo-capacitive Mn_3O_4-IOs compounded with different carbon materials are examined with a series of electrochemical tests, and samples of each composite electrode are characterised using electron microscopy and Raman spectroscopy. The overall aims of this chapter are to improve the SSA of the Mn_3O_4 electrode material, both through the synthesis of macroporous Mn_3O_4-IOs and the loading of this electrode material onto our previously studied complex-architecture 3D-printed current collectors, as well as to determine the most effective and efficient carbon- Mn_3O_4-IO composite for our 3D-printed cells, resulting in stable, conductive, and high-capacitance supercapacitor devices.

5.2 Experimental

A combination of Vat-P and FDM 3D-printing was implemented in this Chapter. The outer casings of the supercapacitors were printed using Vat-P, and the current collectors were printed using either Vat-P or FDM. The printing and processing of the Vat-P 3D-printed components

is detailed in Chapter 2.2.1. The printing and processing of the FDM 3D-printed components is detailed in Chapter 2.2.2. The standard batch of cells printed consists of six supercapacitor cells, with 12 current collectors and 12 half-casings printed per batch. As the Vat-P current collector components are electronically insulating, a layer of 50 nm of gold is uniformly sputtered on the surface of these current collectors. The metal sputtering procedure is outlined in Chapter 2.2.3.

The electrode active materials in this Chapter implement both pseudo-capacitive manganese oxide inverse opals (MO-IOs) and previously studied EDLC carbon nanomaterials. The MO-IOs were synthesised according to the procedure detailed in Chapter 2.3.2. A general schematic for the synthesis of inverse-opal materials is shown in Figure 5.1 (a). The obtained pure IO material was characterised via Raman spectroscopy and SEM imaging, as shown in Figure 5.1 (b) and (c) respectively. The Raman spectrum shows the presence of two minor peaks at 323 cm^{-1} and 375 cm^{-1}, and a relatively large peak at 662 cm^{-1}. The presence and relative intensities of peaks in these positions indicate the presence of hausmannite Mn_3O_4 possessing a tetragonal symmetry and a distorted spinel structure, where the Mn^{2+} ions are in tetrahedral coordination and the Mn^{3+} ions are in octahedral coordination [47, 48]. The large peak observed at 662 cm^{-1} is assigned to A_{1g} mode of vibration, caused by Mn-O breathing vibration of the divalent manganese ions (Mn^{2+}) within the tetrahedrally coordinated Mn_3O_4 crystalline structure [49, 50]. This peak is characteristic of all spinel structures [51]. The minor peaks at 323 cm^{-1} and 375 cm^{-1} are assigned to T_{2g} mode of vibration, also attributed to hausmannite Mn_3O_4 tetrahedral phase [52]. The SEM image clearly shows the IO structure of the Mn_3O_4 material with fcc packed spherical pores of a diameter of 0.5 μm, matching that of the polystyrene polyspheres used for the sacrificial opal template.

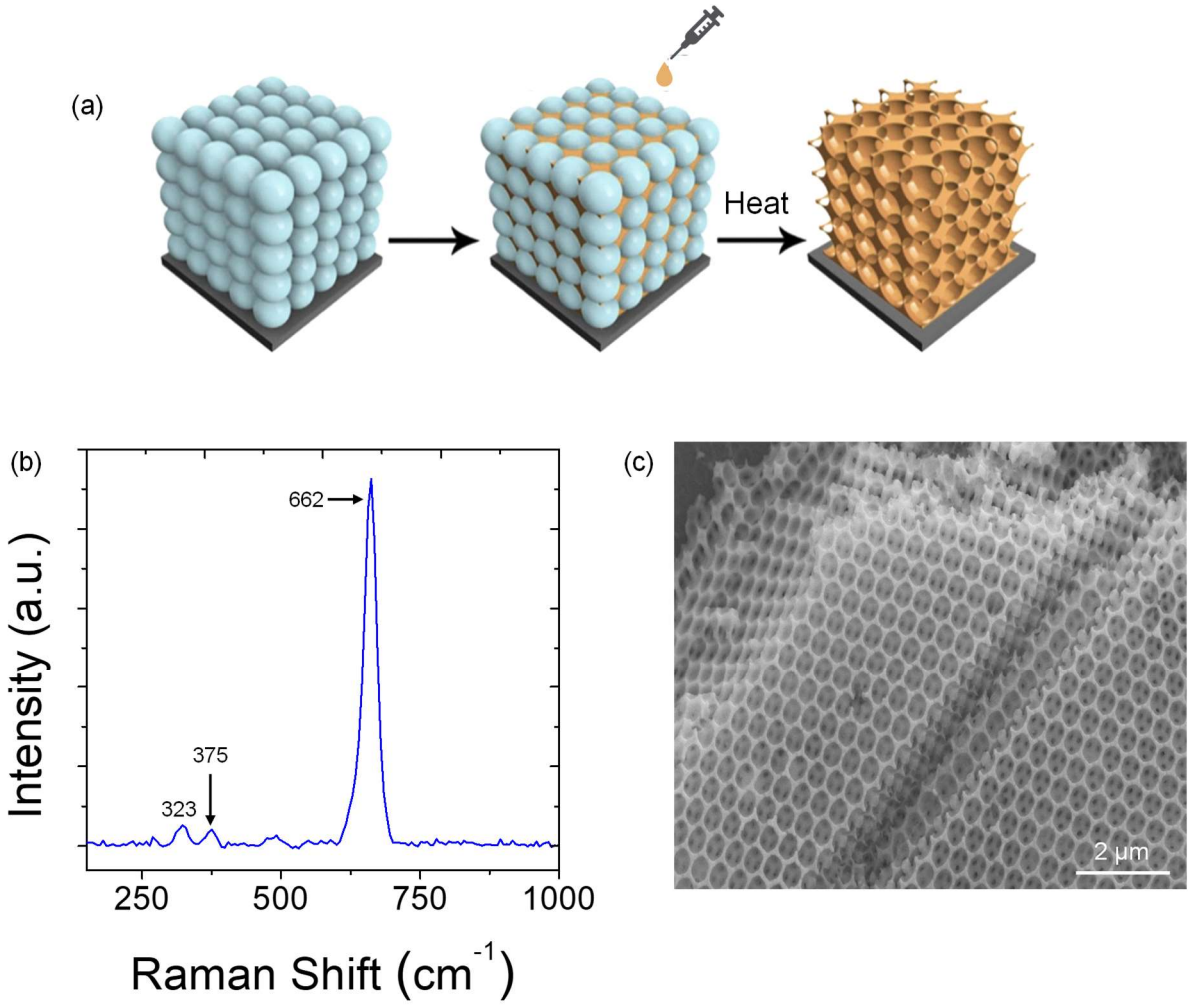

Figure 5.1 (a) Schematic for the synthesis of IO-type materials used in this work, with the sacrificial opal template represented by light blue spheres and the IO precursor and final IO-structured material represented by orange. (b) Raman spectra and (c) SEM image of the pristine MO-IO synthesised and implemented into all electrode slurries for this chapter. The ordered, IO structure of the material is clearly visible in the SEM image shown here.

For the initial few MO-IO-carbon composites of this chapter (as seen in Table 5.1), the components were weighed out and left to stir and homogenize in EtOH overnight. After stirring, a 1 mL syringe was used to measure and place 50 µL of slurry onto the centre of each pre-weighed current collector, gently spreading the slurry across the current collector as much as possible. This is the same procedure used in Chapters 3 and 4, which is detailed in Chapter 2.3.1.

Table 5.1 Composite slurries made and tested for the first part of this chapter, along with all relevant material masses and mixer volume for one standard "batch" of slurry. In all slurry types, the solid materials have a total mass of 0.134 g per 10 mL of EtOH.

Slurry Type (wt.%)	Materials Used for One Batch			
	MO-IO	SWNT	GNP	Super-P
20:40:40	0.0268 g	0.0536 g	0.0536 g	-
20:35:35:10	0.0268 g	0.0469 g	0.0469 g	0.0134 g

After these initial slurries were prepared and tested, a different preparation method was used in the latter part of this chapter to improve the slurry coverage across the current collector surfaces. This procedure is detailed in Chapter 2.3.3. The first slurry made using this method (75:20:5 wt.% MO-IO:Super-P:PVDF) is a commonly used mixture for manganese oxide electrodes [53–57]. Acetone was first tested as the mixer for the slurry components but was too volatile to form a consistent slurry. Instead, EtOH was used, as it stayed in liquid form long enough for the slurry to be deposited onto all the current collectors, while also evaporating completely overnight without having to apply any heat to the plastic current collectors (as would have been required to evaporate less volatile solvents, such as NMP). Once left to air dry overnight, the cells were then assembled according to the procedure outlined in Chapter 2.5. The materials and masses in these latter slurries are shown in Table 5.2.

Table 5.2 Composite slurries made and tested for the latter part of this chapter, showing all relevant material masses for one "batch" of slurry. To cut down on waste, smaller batches of slurry were made (0.012 g of solid material in total), with enough to load 12 current collectors, and two samples of slurry kept for characterisation.

Slurry Type (wt.%)	Materials Used for One Batch				
	MO-IO	SWNT	GNP	Super-P	PVDF
75:20:5	0.009 g	-	-	0.0024 g	0.0006 g
37.5:37.5(GNP):20:5	0.0045 g	-	0.0045 g	0.0024 g	0.0006 g
37.5:37.5(SWNT):20:5	0.0045 g	0.0045 g	-	0.0024 g	0.0006 g

Samples of the carbon electrode slurries were set aside for materials characterisation. The procedures for the Raman spectroscopy and SEM imaging undertaken are detailed in Chapter 2.4.1 and Chapter 2.4.2, respectively. The assembled supercapacitor cells were testing using a variety of cyclic voltammetry (CV) and galvanostatic charge-discharge (GCD) electrochemical tests. The procedures, theory, and electrochemical settings of these tests are detailed in Chapter 2.6. A potential window of 0.2–0.7 V vs. E_{oc} is used for each test throughout the Chapter. Table 5.3 shows the printed current collector type, electrode slurry, and electrochemical test potential window used for all of the supercapacitor cells studied in this Chapter.

Table 5.3 All cells assembled and tested in this chapter, listing their 3D-printed current collector type, loaded electrode slurry, and voltage window used for electrochemical testing. Refer to Table 5.1 and Table 5.2 for the masses of all materials used in the composite electrode slurries.

Current Collector Type	Electrode Slurry	Voltage Window
Vat-P	20:40:40	0.2 – 0.7 V
Vat-P	20:35:35:10	0.2 – 0.7 V
Vat-P	75:20:5	0.2 – 0.7 V
Vat-P	37.5:37.5(GNP):20:5	0.2 – 0.7 V
Vat-P	37.5:37.5(SWNT):20:5	0.2 – 0.7 V
FDM	75:20:5	0.2 – 0.7 V
FDM	37.5:37.5(GNP):20:5	0.2 – 0.7 V
FDM	37.5:37.5(SWNT):20:5	0.2 – 0.7 V

5.3 Results and Discussion

5.3.1 Composite Slurries as a Continuation of Chapter 3 Slurries

The first results section of this Chapter serves as a continuation of the slurries examined previously. This section directly compares the electrochemical performances of the SWNT:GNP (50:50 wt.%) electrode slurry from Chapter 3 to two carbon-IO composite slurries

made using the same procedure and incorporating similar/the same carbon materials. The purpose of this comparison is to determine the extent to which the addition of 20 wt.% Mn_3O_4-IO affects the performance of the electrode slurries. The structural characterization of the different composite slurries used in our Vat-P printed current collector cells is presented here in the form of Raman spectra and SEM images. The electrochemical characterization of the assembled supercapacitor cells is undertaken via cyclic voltammetry and charge-discharge tests under galvanostatic conditions with a voltage window of 0.2 – 0.7 V.

The Raman spectra for all initial electrode slurries can be seen in Figure 5.2 (a). All three spectra are dominated by a large, sharp peak at 1597 cm^{-1}, known as the G-band (which is assigned to the stretching of C-C bonds in sp^2 graphitic materials) and a second intense peak in the region of 2600–2700 cm^{-1} known as the G'-band (or 2D-band) [58, 59]. Another peak located at 1347 cm^{-1} is known as the D-band, which arises from disorder in the sp^2 carbon structure [60, 61]. The ratio of peak intensity of the G-band and D-band is used to show the ratio of ordered and disordered carbons in the sp^2 structure, indicating that all carbon spectra presented here are highly ordered. The Raman peaks assigned to the Mn_3O_4-IOs are not visible in these spectra due to the relatively high intensity peaks assigned to the SWNTs in the electrode composites.

The SEM images in Figure 5.2 shows the morphology of the three carbon slurries prior to any electrochemical tests. In Figure 5.2 (d) the two different carbon types used in the SWNT:GNP (50:50 wt.%) electrode are very distinctive at this magnification. The long, thin fibers of SWNTs [62] and flat, planar flakes of GNP [63] are clearly visible. In Figure 5.2 (b) and (c), the MO-IO material is visible as small, pale-coloured particles scattered throughout the electrode composite. A relatively large piece of intact MO-IO material can be seen just right of the centre point of Figure 5.2 (b).

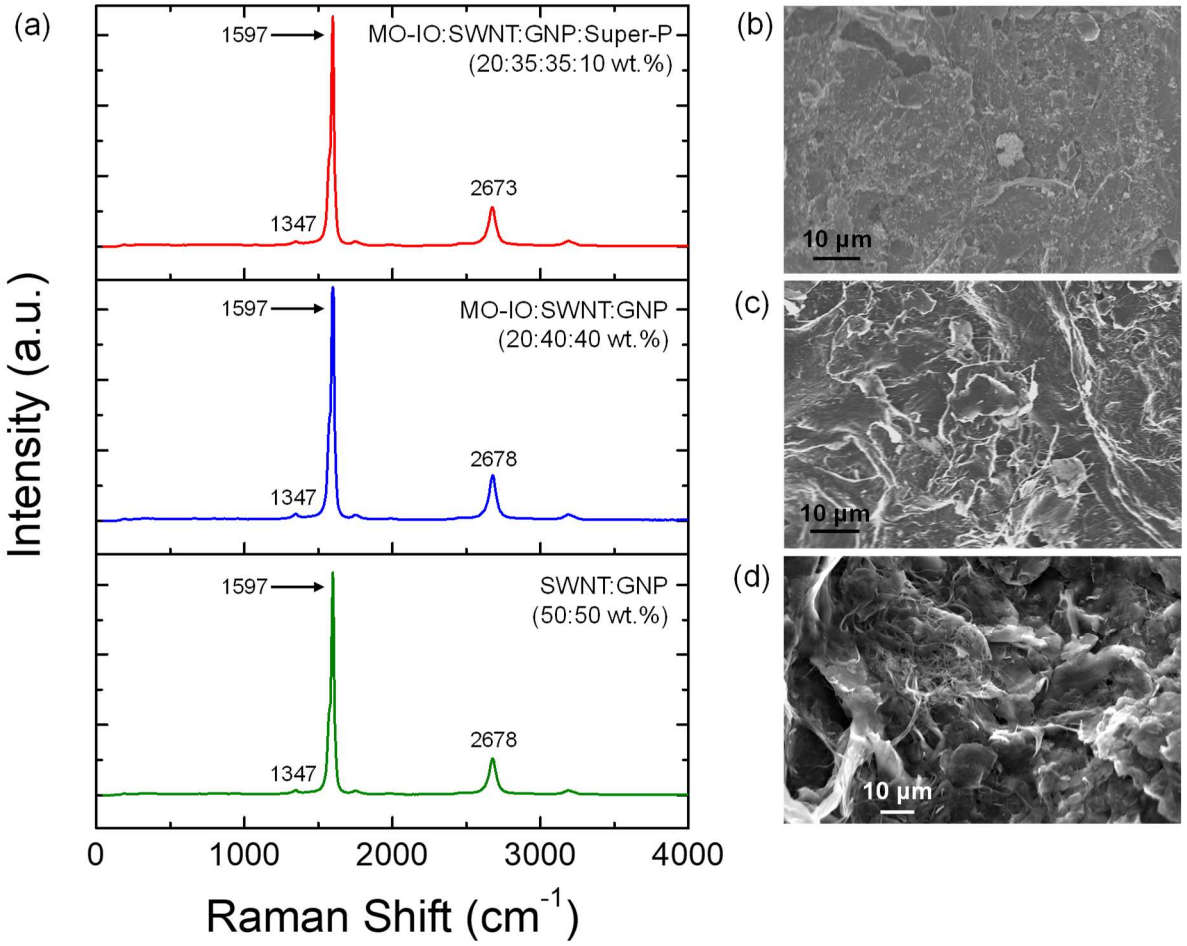

Figure 5.2 (a) Raman scattering spectra of MO-IO:SWNT:GNP:Super-P (20:35:35:10 wt.%), MO-IO:SWNT:GNP (20:40:40 wt.%), and SWNT:GNP (50:50 wt.%) electrode slurries, with their respective SEM images (b)–(d) shown to the right of the Raman spectra.

Figure 5.3 shows the CV response of cells using metallized Vat-P current collectors and the above composite electrode slurries, at scan rates between 5 and 250 mV/s. The cell using SWNT:GNP (50:50 wt.%) electrode slurry (Figure 5.3 (a)) displays better electrochemical response and cumulative integrated charge in its CV curves than the other two cells using carbon-MO-IO composite electrode slurries (Figure 5.3 (b) and (c)). While all of the cells show quasi-rectangular CV responses, the SWNT:GNP (50:50 wt.%) cell curves are closer to the ideal rectangular CV responses expected of EDLCs. As the other two cells

incorporate pseudo-capacitive materials (which give non-rectangular CV curve responses [3, 4, 64]) into their composite electrode slurries, it would make sense that their CV responses deviate more than the purely EDLC materials present in the first cell. Some of the specific capacitance and specific capacity values obtained from these CV response curves are shown in Table 5.4. Higher scan rate CV curves (up to 1 V/s) for all three of these cells can be found in the supplementary materials, Figure 5.S.1, where all the cells retain their quasi-rectangular shape, even at the highest scan rate of 1 V/s. However, as with the lower scan rate CV responses, the cell using SWNT:GNP (50:50 wt.%) from Chapter 3 displays better electrochemical response and cumulative integrated charge than the other two cells.

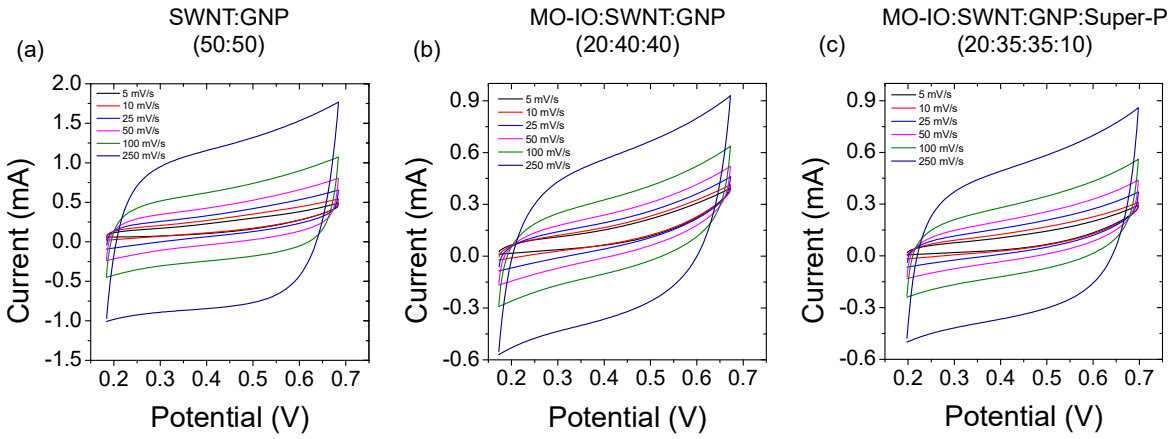

Figure 5.3 Cyclic voltammetry of printed supercapacitor cells using Vat-P printed metallized current collectors at various scan rates in the range 5–250 mV/s. CVs are shown for cells loaded with (a) SWNT:GNP (50:50 wt.%), (b) MO-IO:SWNT:GNP (20:40:40 wt.%), and (c) MO-IO:SWNT:GNP:Super-P (20:35:35:10 wt.%) electrode slurries.

Figure 5.4 (a)–(c) shows the cycle life response for the three cells under galvanostatic charge-discharge conditions at a specific applied current of 0.167 A/g (applied current of 500 µA) for 100,000 cycles, while Figure 5.4 (d)–(f) shows the charge-discharge curves of the cells at different stages of the 100,000 cycles under galvanostatic conditions. The cell containing the SWNT:GNP (50:50 wt.%) electrode slurry from Chapter 3 (Figure 5.4 (a) and (d)) displays the worst cycling stability of the three cells, losing its specific capacitance steadily, before

breaking down completely at the 50,000 charge-discharge cycle mark, as evidenced by the unstable percentage efficiency and the completely degraded charge-discharge curve at 100,000 cycles.

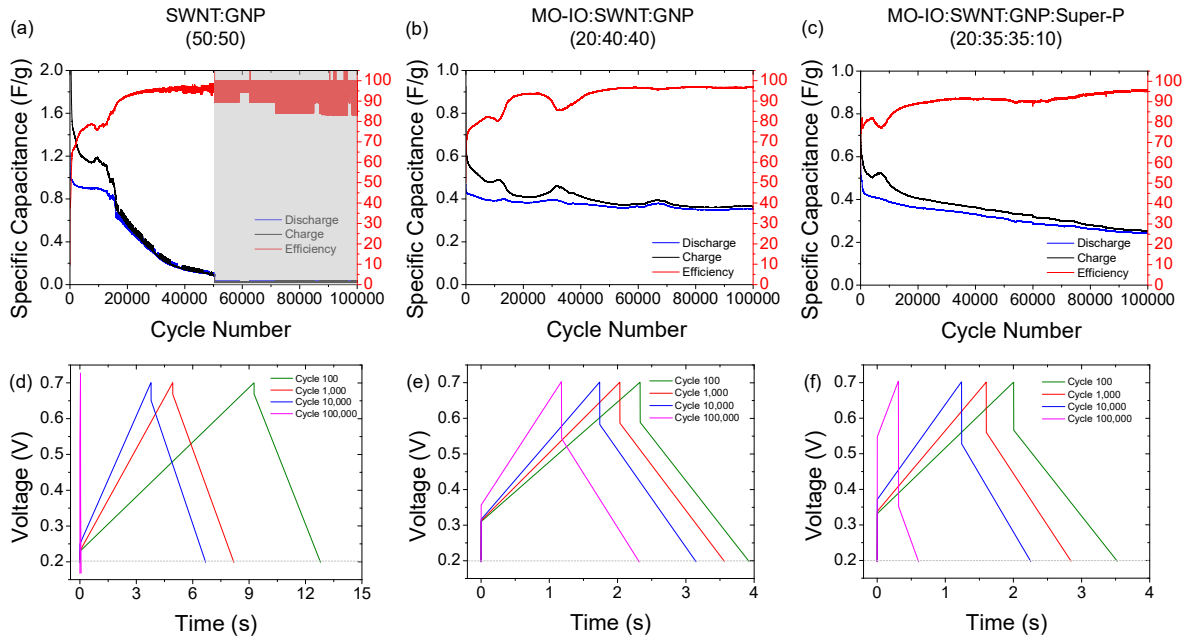

Figure 5.4 (a)–(c) Life cycle graphs of the cells in the first part of this chapter over 100,000 cycles under galvanostatic conditions, plotting the charging specific capacitance, discharging specific capacitance, and percentage efficiency of all cells. The cells were cycled between 0.2 and 0.7 V at an applied current of 500 µA (specific applied current of 0.167 A/g). Charge-discharge curves of the cells at different points during the 100,000 cycles under galvanostatic conditions are shown in (d)–(f).

The other two cells display far better cycling stability overall; however it is the cell containing the MO-IO:SWNT:GNP (20:40:40 wt.%) electrode composite slurry (Figure 5.4 (b) and (e)) that performs the best, retaining 75% of its initial specific capacitance after 100,000 charge-discharge cycles. By comparison, the cell containing the MO-IO:SWNT:GNP:Super-P (20:35:35:10 wt.%) electrode composite slurry (Figure 5.4 (c) and (f)) retains 41% of its initial specific capacitance after 100,000 charge-discharge cycles. This behaviour is also reflected in their respective charge-discharge curves (Figure 5.4 (e) and (f)), where the 100,000 cycle charge-discharge curve for the MO-IO:SWNT:GNP (20:40:40 wt.%) cell is far less degraded relative to its initial charge-discharge curves than the same charge-discharge curves for the

MO-IO:SWNT:GNP:Super-P (20:35:35:10 wt.%) cell. Both of these cells, however, display larger ohmic drops in their charge-discharge curves compared to the SWNT:GNP (50:50 wt.%) cell, which is caused by higher internal resistance. This is most likely due to the inclusion of relatively low conductivity Mn_3O_4 material in their composite electrode slurries.

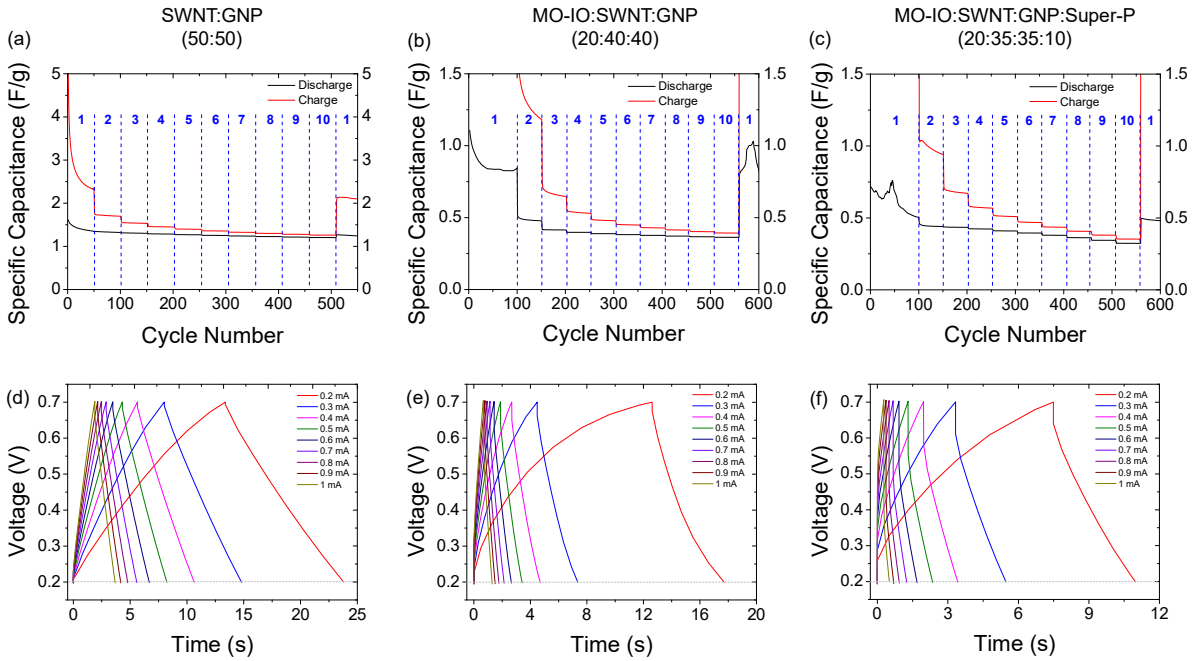

Figure 5.5 (a)–(c) Varied-current life-cycle plot for all cells in the first part of this chapter under conditions of increasing applied current. The blue numbers between the dotted lines correspond to the charging and discharging current used in that cycle period, progressing through 1 (±100 µA or 0.033 A/g), 2 (±200 µA or 0.067 A/g), 3 (±300 µA or 0.100 A/g), 4 (±400 µA or 0.133 A/g), 5 (±500 µA or 0.167 A/g), 6 (±600 µA or 0.200 A/g), 7 (±700 µA or 0.233 A/g), 8 (±800 µA or 0.267 A/g), 9 (±900 µA or 0.300 A/g), 10 (±1 mA or 0.333 A/g), then returning to 1 (±100 µA or 0.033 A/g). The cells are charged to 0.7 V and discharged to 0.2 V. (d)–(f) Charge-discharge curves from cycles of increasing applied current under galvanostatic conditions. The charge-discharge curves at the applied current of ±100 µA (0.033 A/g) is omitted from these plots due to extremely long charging times rendering the rest of the graph of limited use.

Figure 5.5 (a)–(c) shows the rate capability response of the three cells under galvanostatic charge-discharge conditions with increasing applied currents. The SWNT:GNP (50:50 wt.%) cell shows exceptional rate capability, retaining 89% of its specific capacitance after a tenfold increase in applied current, and recovering almost all capacitance (94%

recovery) after returning to the initial applied current. The other two cells do not perform as well in terms of rate capability, with the MO-IO:SWNT:GNP (20:40:40 wt.%) and MO-IO:SWNT:GNP:Super-P (20:35:35:10 wt.%) cells (Figure 5.5 (b) and (c), respectively) retaining 43% and 64%, respectively, of their specific capacitance after a tenfold increase in applied current. However, both cells also show excellent recovery upon returning to the initial applied current (94-98% recovery). The corresponding specific energies and specific powers of these cells at applied currents of 0.1 mA, 0.5 mA, and 1 mA are shown in Table 5.5.

Figure 5.5 (d)–(f) shows the charge-discharge curves of the cells tested under galvanostatic conditions with increasing applied current, ranging from ±200 μA (0.067 A/g) to ±1 mA (0.333 A/g), an overall increase of applied current by a factor of 5. As seen from Figure 5.5 (a), the SWNT:GNP (50:50 wt.%) cell shows the best rate capability, retaining the majority of its capacitance over repeated cycling at successively higher rates. This behaviour is reflected in the cell's charge discharge curves in Figure 5.5 (d), where the increase in applied current by a factor of 5 results in the discharge time being reduced by approximately a factor of 5. This inverse relationship between discharge time and applied current is only present for cells possessing good rate capability. For the other cells, which are shown to have inferior rate capability, increasing the applied current by a factor of 5 resulted in their discharge time being reduced by more than a factor of 5. The shapes of the charge-discharge curves also vary. The SWNT:GNP (50:50 wt.%) cell (Figure 5.5 (d)) shows the near-perfectly symmetrical charge and discharge curves that are a characteristic response of EDLC-type supercapacitors. The other two carbon-MO-IO cells (Figure 5.5 (e) and (f)) show more asymmetric, fin-shaped charge-discharge curves, indicative of pseudo-capacitive energy storage. The ohmic drops of the two carbon-MO-IO composite electrode cells (which are larger than that of the SWNT:GNP (50:50 wt.%) cell) grow with increasing applied current to encompass a large part of the voltage range for the higher applied currents of these tests.

5.3.2 Alternative Composite Electrode Slurry Preparation and Compositions

Though showing superior cycling stability than the SWNT:GNP (50:50 wt.%) cell (Figure 5.4), the electrochemical performances of the carbon-MO-IO cells in the previous section were disappointing. Compared to the SWNT:GNP (50:50 wt.%) cell, they displayed lower cumulative integrated charge in their CV curves (Figure 5.3), lower specific capacitance from their galvanostatic charge-discharge tests (Figure 5.4), and inferior rate capabilities (Figure 5.5). For the second results section of this Chapter, an alternative composite electrode slurry preparation method was proposed (see Section 5.2.3), whereby the composite electrode components were ground in a mortar and pestle and mixed with several drops of EtOH, resulting in a slurry paste that was easily spread across the surface of the current collectors using a small paintbrush. This preparation method thoroughly mixes the slurry components via grinding in a mortar and pestle and enables better coverage of the architected current collector surface, improving the SSA of the composite electrode materials.

The first composite electrode slurry studied in this section consists of MO-IO, Super-P, and PVDF in a percentage mass ratio of 75:20:5 %. This composition of electrode materials (or very similar variations thereof) has frequently been utilised in similar studies of manganese oxide pseudo-capacitor electrodes [53–57]. The addition of two different forms of carbon (GNPs and SWNTs) to the other two composite electrode slurries in this section serves to improve the electronically conductive interface between the two different 3D-printed current collectors (metallized Vat-P printed and conductive PLA FDM printed) and the relatively non-conductive MO-IO material. Super-P already serves this purpose to an extent by facilitating short-range electron transport, while the addition of planar GNPs or fibrous SWNTs will aid in facilitating long-range electron transport [38], with the overall aim of improving the electrochemical performance of the carbon-MO-IO composite electrode slurries studied in this section.

The Raman spectra for all latter electrode slurries in this study can be seen in Figure 5.6 (a). The spectra for the MO-IO:Super-P:PVDF (75:20:5 wt.%) and GNP:MO-IO:Super-P:PVDF (37.5:37.5:20:5 wt.%) electrode slurries are dominated by the sharp, intense peak located at 656 cm^{-1}, which, as previously discussed, is assigned to A_{1g} mode of vibration, caused by Mn-O breathing vibration of the divalent manganese ions (Mn^{2+}) within the tetrahedrally coordinated Mn_3O_4 crystalline structure [49, 50]. Both electrode slurries also show minor peaks at 323 cm^{-1} and 375 cm^{-1}, assigned to the T_{2g} mode of vibration, which is also attributed to hausmannite Mn_3O_4 tetrahedral phase [52]. All three spectra contain both the D-band (1342–1357 cm^{-1}) and G-band (1587–1607 cm^{-1}) peaks, arising from the presence of disordered and ordered carbons sp^2 graphitic materials respectively [60, 61]. The relatively low carbon content of the MO-IO:Super-P:PVDF (75:20:5 wt.%) electrode slurry results in its spectrum showing very weak D-band and G-band peaks, with their approximately equal intensities indicating a similar proportion of disordered and ordered sp^2 carbons.

The GNP:MO-IO:Super-P:PVDF (37.5:37.5:20:5 wt.%) spectrum contains more intense D-band and G-band peaks, with the respective peak heights indicating an approximately 2:3 ratio of disordered to ordered sp^2 carbons present in the electrode slurry. Similar to the Raman spectra of the slurries from the previous section, the spectrum of the SWNT:MO-IO:Super-P:PVDF (37.5:37.5:20:5 wt.%) electrode slurry is dominated by the G-band. The relatively small D-band which is also present indicates a highly ordered sp^2 carbon network in this electrode slurry. Unlike the Raman spectra from the previous section, a peak assigned to the Mn_3O_4-IO material can also be seen at 656 cm^{-1}, due to the higher wt.% of the slurry consisting of MO-IO material than in the composite electrodes in the previous section.

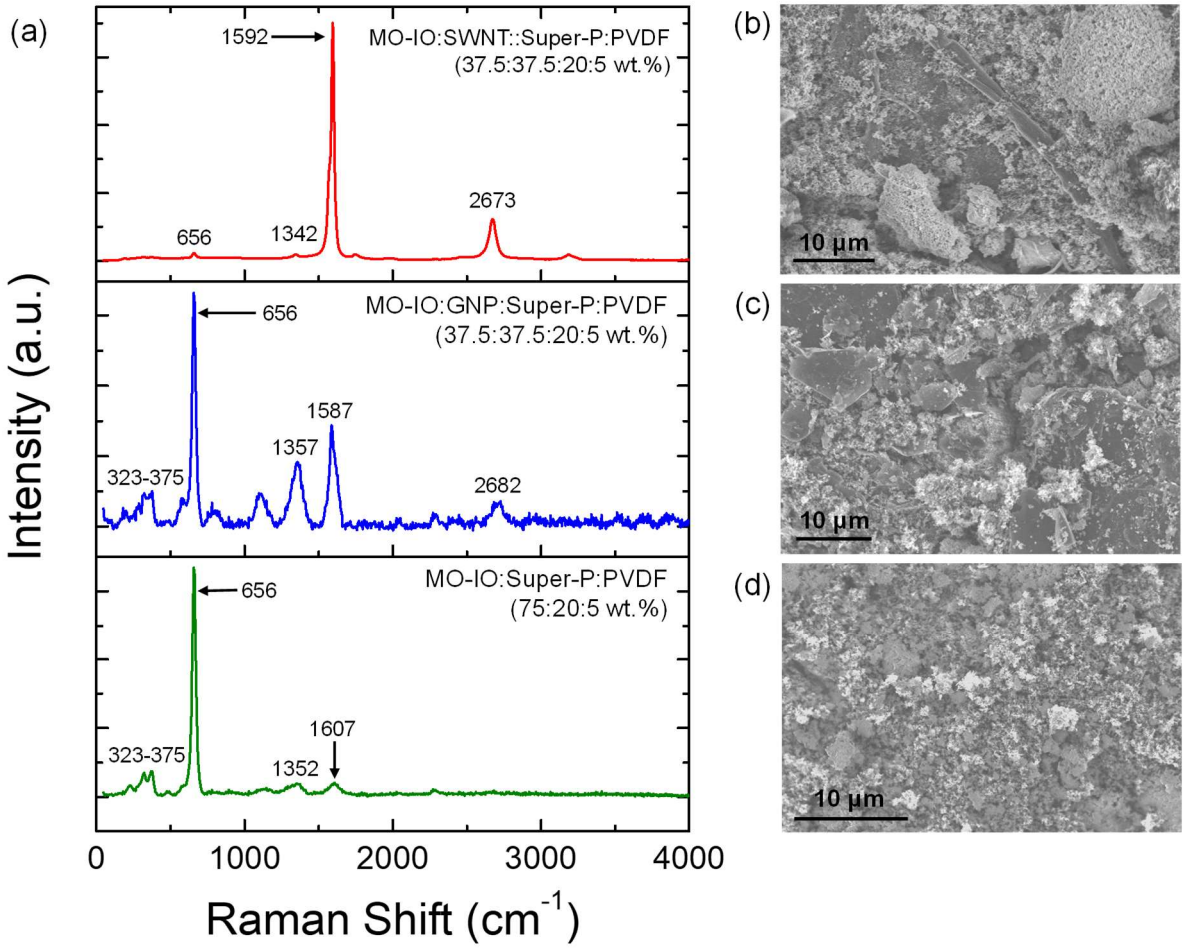

Figure 5.6 (a) Raman scattering spectra of SWNT:MO-IO:Super-P:PVDF (37.5:37.5:20:5 wt.%), GNP:MO-IO:Super-P:PVDF (37.5:37.5:20:5 wt.%), and MO-IO:Super-P:PVDF (75:20:5 wt.%) electrode slurries, with their respective SEM images (b)–(d) shown to the right of the Raman spectra.

The SEM images in Figure 5.6 show the morphology of the three composite electrode slurries prior to any electrochemical tests. The MO-IO:Super-P:PVDF (75:20:5 wt.%) electrode slurry (Figure 5.6 (d)) mostly consists of MO-IO material, which shows a rough, jagged morphology at this magnification. Super-P shows a similar morphology but is slightly more porous and hollower in appearance than the MO-IO material [65, 66]. The flat, planar flakes of GNP [67] are easily distinguished in the GNP:MO-IO:Super-P:PVDF (37.5:37.5:20:5 wt.%) electrode slurry (Figure 5.6 (c)), as are the SWNTs in the SWNT:MO-IO:Super-P:PVDF

(37.5:37.5:20:5 wt.%) electrode slurry (Figure 5.6 (b)). Fragments of the IO structure of Mn_3O_4 can most clearly be seen dispersed throughout the electrode slurry in Figure 5.6 (b).

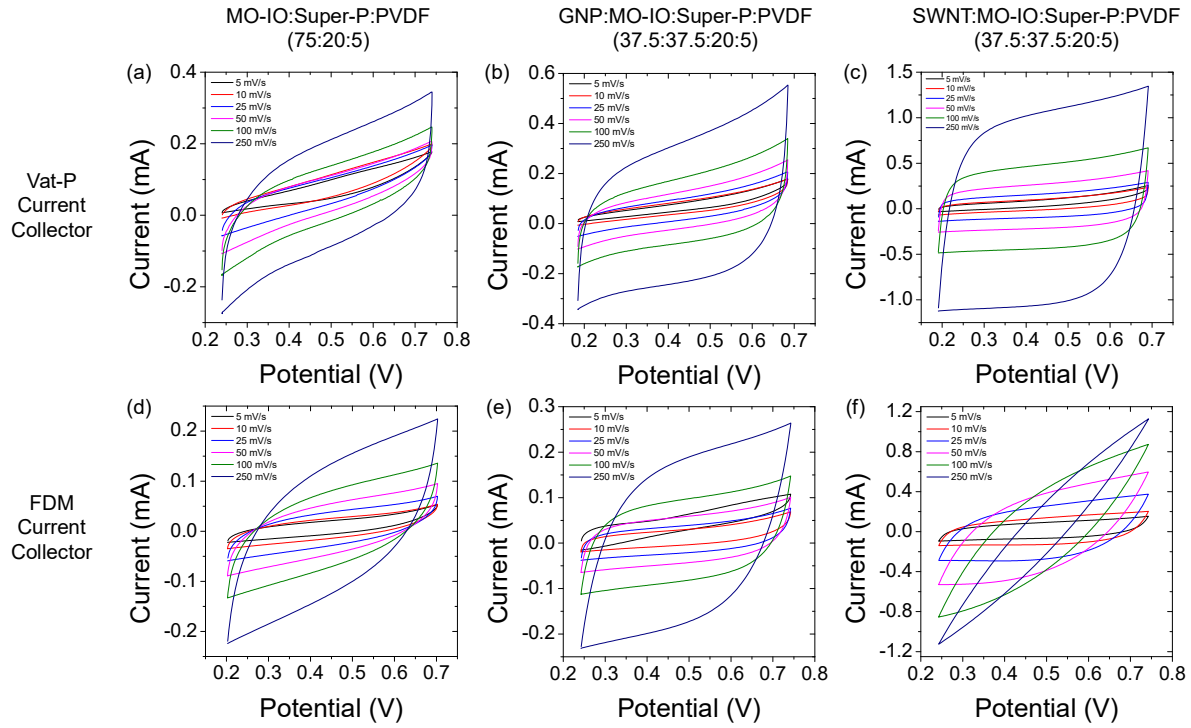

Figure 5.7 Cyclic voltammetry of printed supercapacitor cells using (a)–(c) Vat-P printed metallized current collectors and (d)–(f) FDM printed conductive PLA current collectors at various scan rates in the range 5–250 mV/s. CVs are shown for cells loaded with (a,d) MO-IO:Super-P:PVDF (75:20:5 wt.%), (b,e) GNP:MO-IO:Super-P:PVDF (37.5:37.5:20:5 wt.%), and (c,f) SWNT:MO-IO:Super-P:PVDF (37.5:37.5:20:5 wt.%) electrode slurries.

Figure 5.7 shows the CV response of the assembled cells (at scan rates ranging from 5 mV/s to 250 mV/s), which use both metallized Vat-P printed and conductive PLA FDM printed current collectors, containing the composite electrode slurries discussed in this section. Some of the specific capacitance and specific capacity values obtained from these CV response curves are shown in Table 5.4. Figure 5.S.3 in the supplementary materials shows the CV response of the same cells at higher scan rates (up to 1 V/s).

First discussing the MO-IO:Super-P:PVDF (75:20:5 wt.%) slurry (Figure 5.7 (a) and (d)), both of the cells containing this electrode give the lowest total integrated charge compared to the other two cells using the same current collector type. The shapes of the CV responses

also deviate the most from the rectangular EDLC response, likely due to a combination of the lower electronic conductivity and pseudo-capacitive nature of the MO-IO material, which makes up most of the mass of these electrodes (75%). Both of the cells containing the GNP:MO-IO:Super-P:PVDF (37.5:37.5:20:5 wt.%) slurry (Figure 5.7 (b) and (e)) respond with CV curves possessing both a larger integrated area (especially at higher scan rates) and more rectangular shape than their MO-IO:Super-P:PVDF (75:20:5 wt.%) slurry counterparts. The improved interfacial conductivity and added cumulative integrated charge contributions caused by the EDLC GNP material explains this response.

Table 5.4 Summary of integrated specific charge and specific capacitance values from cyclic voltammetry data in this Chapter. Values of similar cells from Chapter 3 are also included in the bottom four rows of the table (shaded) for comparison.

Current Collector and Electrode Slurry		Lower Scan Rate (5 mV/s)		Higher Scan Rate (250 mV/s)	
		Specific Charge (C/g)	Specific Capacitance (F/g)	Specific Charge (C/g)	Specific Capacitance (F/g)
Vat-P	20:40:40	0.861	1.721	0.176	0.351
Vat-P	20:35:35:10	0.837	1.674	0.209	0.418
Vat-P	75:20:5	0.391	0.781	0.057	0.114
Vat-P	37.5:37.5(GNP):20:5	0.382	0.764	0.134	0.268
Vat-P	37.5:37.5(SWNT):20:5	0.830	1.659	0.438	0.876
FDM	75:20:5	0.505	1.010	0.095	0.189
FDM	37.5:37.5(GNP):20:5	1.07	2.140	0.169	0.337
FDM	37.5:37.5(SWNT):20:5	1.827	3.654	0.096	0.192
Vat-P	50:50	1.342	2.683	0.450	0.900
Vat-P	4:4:1:1	0.675	1.350	0.366	0.732
FDM	50:50	1.823	3.645	0.070	0.140
FDM	4:4:1:1	1.406	2.811	0.013	0.025

Finally, the SWNT:MO-IO:Super-P:PVDF (37.5:37.5:20:5 wt.%) electrode cells give a response of CV curves showing the highest cumulative integrated charge compared to the other cells of the same current collector type. This result was expected, as our previous work has already shown the superior CV response of SWNT compared to GNP in similar supercapacitor cells (see Chapter 3.3.1). Chapter 3 also compares the two different 3D-printed current collector behaviours at length, but to summarise, the superior conductivity of the metallized Vat-P current collector facilitates quick and efficient charge storage, resulting in CV responses that are not distorted by the internal resistance of the cell. The conductive PLA FDM current collectors, however, are far poorer electronic conductors, resulting in narrowed, leaf-shaped CV responses that limit the cumulative integrated charge of the cell. This same behaviour studied previously is apparent in the CV responses of the cells studied in this section, which utilise the same two 3D-printed current collector types.

Figure 5.8 (a) shows the cycle life response for all latter cells under galvanostatic charge-discharge conditions at a specific applied current of 0.167 A/g (applied current of 500 μA) for 100,000 cycles. Corresponding data also showing the cycling efficiency can be found in the supplementary material, Figure 5.S.4. For both current collector types, the MO-IO:Super-P:PVDF (75:20:5 wt.%) electrode cells (Figure 5.8 (b) and (e)) achieve the lowest specific capacitance values, while the SWNT:MO-IO:Super-P:PVDF (37.5:37.5:20:5 wt.%) electrode cells (Figure 5.8 (d) and (g)) achieve the highest specific capacitance values. This is a very similar pattern to the specific capacitance values derived from the CV responses of the same cells (Figure 5.7 and Table 5.4). All cells possess exceptional cycling stability, retaining 51-97% of their initial specific capacitance values after the full 100,000 charge-discharge cycles. The shapes of the charge-discharge curves at various points of the 100,000 charge-discharge cycles (Figure 5.8 (b)–(g)) highlight this excellent cycling stability, while also revealing the effect of the different 3D-printed current collectors on the charge-discharge behaviour of the

cells. The relatively small ohmic drops present in the metallized Vat-P current collector cells (Figure 5.8 (b)–(d)) show the superior electronic conductivity of this current collector type relative to the PLA FDM current collector cells (Figure 5.8 (e)–(g)).

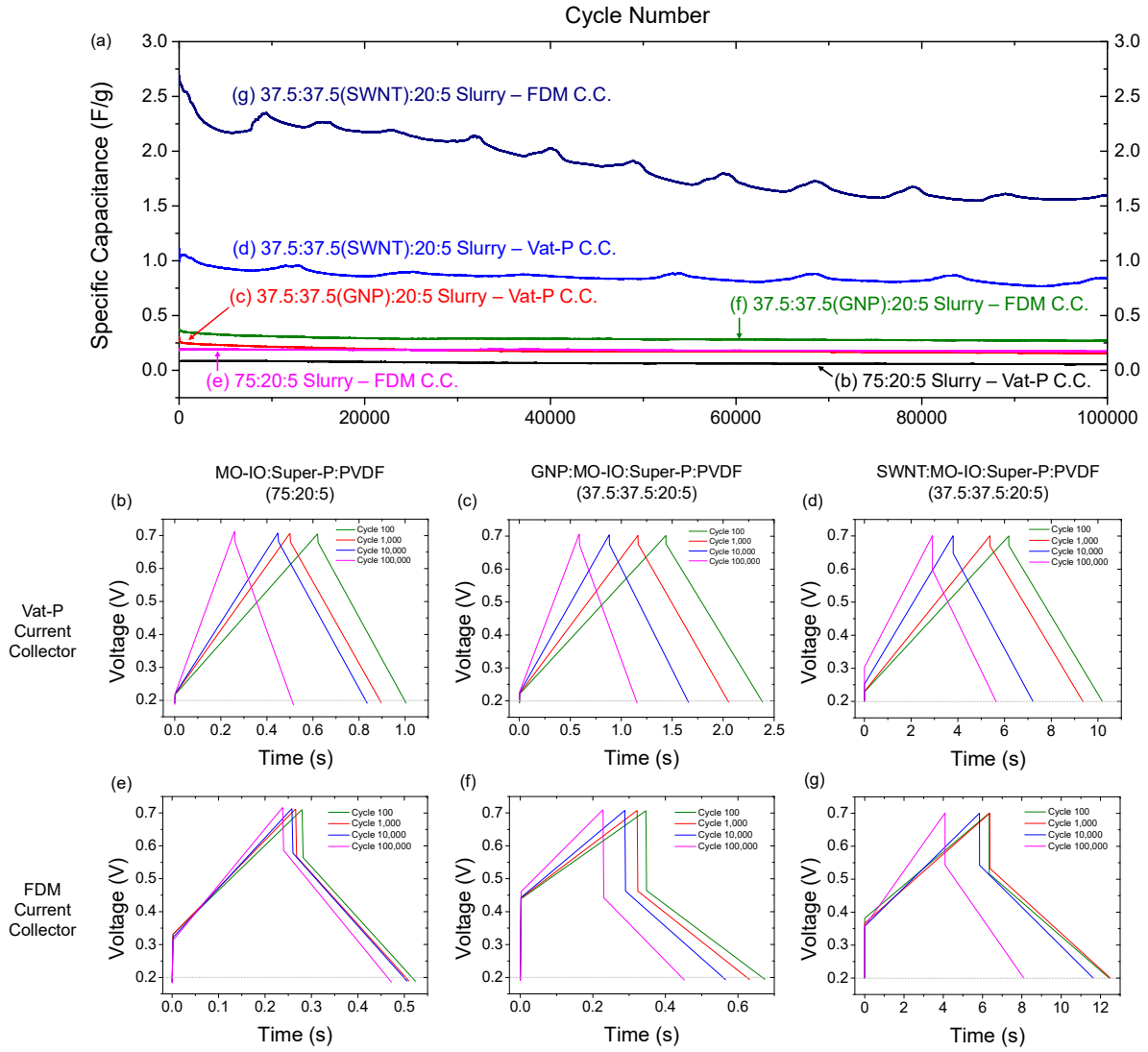

Figure 5.8 (a) Specific capacitance retention of all printed cells in the second part of this chapter over 100,000 cycles under galvanostatic conditions. Cells were cycled between 0.0 – 1.0 V at an applied current of 500 µA (specific applied current of 0.167 A/g). (b)–(g) Charge-discharge curves of the cells at different points during the 100,000 cycles under galvanostatic conditions, with the cells containing Vat-P printed metallized current collectors shown in (b)–(d), and cells containing FDM printed conductive PLA current collectors shown in (e)–(g). After 100,000 charge-discharge cycles, the cells retain: (b) 66.75%, (c) 51.23%, (d) 75.77%, (e) 97.47%, (f) 74.53%, and (g) 59.93% of their specific capacitance relative to their starting values.

Figure 5.9 (a)–(f) shows the rate capability response of the cells under galvanostatic charge-discharge conditions with increasing applied currents. A similar pattern seen throughout the Chapter is observed again in the rate response data, with the MO-IO:Super-P:PVDF (75:20:5 wt.%) electrode cells (Figure 5.9 (a) and (c)) showing the lowest specific capacitance response and a poorer rate response.

Meanwhile, the SWNT:MO-IO:Super-P:PVDF (37.5:37.5:20:5 wt.%) electrode cells display both the highest specific capacitance values and the best rate response, with the Vat-P and FDM current collector cells (Figure 5.9 (c) and (f)) retaining 64% and 73%, respectively, of their specific capacitance after a tenfold increase in applied current. This highlights the benefits to both specific capacitance and rate response obtained by the addition of highly conductive fibrous carbon networks interspersed amongst the lower electronic conductivity Mn_3O_4-IO material, aiding in both long-range electron transfer and interfacial conductivity with the current collectors. All the cells recover most of their capacitance (89-100% recovery) after returning to the initial rate.

Focusing more on each current collector type, although the Vat-P cell containing the SWNT:MO-IO:Super-P:PVDF (37.5:37.5:20:5 wt.%) electrode slurry (Figure 5.9 (c)) shows a superior rate response to its MO-IO:Super-P:PVDF (75:20:5 wt.%) electrode counterpart (Figure 5.9 (a)), it still does not perform as well as the earlier Vat-P SWNT:GNP (50:50 wt.%) electrode cell (see Figure 3.8 (a) and Figure 5.5 (a)), which retains 89% of its specific capacitance under the same conditions. The inclusion of significant amounts of relatively poorly conducting pseudo-capacitive material to the SWNT:MO-IO:Super-P:PVDF (37.5:37.5:20:5 wt.%) electrode slurry is likely the reason for this behaviour.

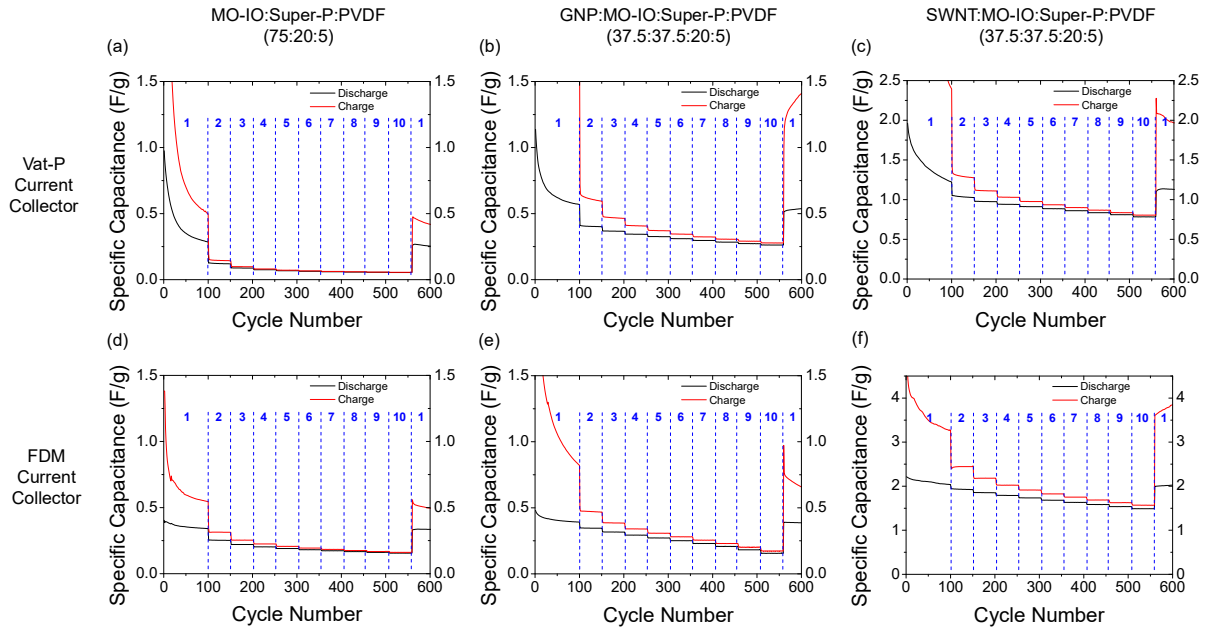

Figure 5.9 Varied-current life-cycle plot for all cells in the second part of this chapter under conditions of increasing applied current. The blue numbers between the dotted lines correspond to the charging and discharging current used in that cycle period, progressing through 1 (±100 µA or 0.033 A/g), 2 (±200 µA or 0.067 A/g), 3 (±300 µA or 0.100 A/g), 4 (±400 µA or 0.133 A/g), 5 (±500 µA or 0.167 A/g), 6 (±600 µA or 0.200 A/g), 7 (±700 µA or 0.233 A/g), 8 (±800 µA or 0.267 A/g), 9 (±900 µA or 0.300 A/g), 10 (±1 mA or 0.333 A/g), then returning to 1 (±100 µA or 0.033 A/g). The cells are charged to 0.7 V and discharged to 0.2 V. Comparing their specific capacitance values at applied currents of 100 µA (cycle 100) and 1 mA (cycle 559), the cells show a capacitance retention of (a) 18.85%, (b) 46.07%, (c) 64.02%, (d) 45.60%, (e) 39.64%, and (f) 73.11%. Upon returning to the lowest applied current of 100 µA, the cells recover (a) 89.43%, (b) 90.48%, (c) 90.12%, (d) 97.57%, (e) 99.98%, and (f) 97.98% of their original specific capacitance values.

Interestingly, this is not the case for the FDM current collector cells. In this Chapter, the FDM cell containing SWNT:MO-IO:Super-P:PVDF (37.5:37.5:20:5 wt.%) electrode slurry (Figure 5.9 (f)) actually shows a better rate response than the FDM carbon-based electrode slurry cells from Chapter 3 (see Figure 3.8 (d)–(f) and Figure 3.9 (d)–(f)), with these cells retaining only 28-52% of their specific capacitance after the tenfold increase in applied current. This is a promising result for the FDM current collector cells, as it shows that despite the overall poorer rate response than metallized Vat-P current collector cells, a respectable rate response is still achievable via the utilisation of the appropriate composite electrode materials.

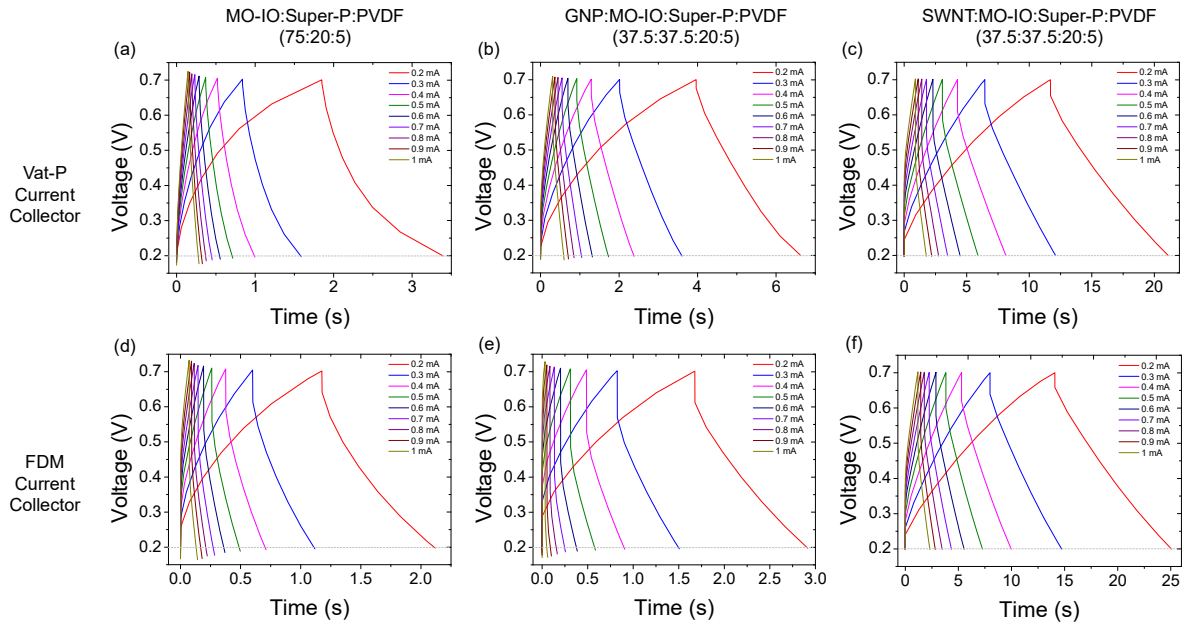

Figure 5.10 Charge-discharge curves from cycles of increasing applied current under galvanostatic conditions. ±200 µA (0.067 A/g), ±300 µA (0.100 A/g), ±400 µA (0.133 A/g), ±500 µA (0.167 A/g), ±600 µA (0.200 A/g), ±700 µA (0.233 A/g), ±800 µA (0.267 A/g), ±900 µA (0.300 A/g), ±1 mA (0.333 A/g). The cells are charged to 0.7 V, and discharged to 0.2 V. The charge-discharge curves at the applied current of ±100 µA (0.033 A/g) is omitted from these plots due to extremely long charging times rendering the rest of the graph of limited use.

Figure 5.10 shows the charge-discharge curves of the cells tested in the rate capability test shown in Figure 5.9. The distinctive fin-shape of the charge-discharge curves, especially for the MO-IO:Super-P:PVDF (75:20:5 wt.%) cells (Figure 5.10 (a) and (d)) are characteristic of pseudo-capacitive energy storage. As explained earlier, a cell possessing a very good rate response will retain the shape of its charge-discharge curve over a range of applied currents, except that the charge-discharge time will decrease with increasing applied current in an inversely proportional relationship. This is most apparent in the Vat-P SWNT:GNP (50:50 wt.%) cell shown in Figure 5.5 (d).

These charge-discharge curves further highlight the significant improvement in rate response seen for the FDM current collector cells (Figure 5.10 (d)–(f)) compared to the earlier cells studied in Chapter 3 (Figure 3.9 (d)–(f)). For these earlier cells, increasing the applied current causes the charge-discharge times to shrink to small fractions of their original values,

while the ohmic drops of the curves grow and the voltage window expands beyond the limits set by the electrochemical test. Many of the charge-discharge curves of these earlier cells are so distorted and degraded as to be unreadable (in particular, Figure 3.9 (e) and (f)). These signs of poor rate performance are present to a much smaller degree in the FDM current collector cells shown in Figure 5.10 (d)–(f), especially for the FDM SWNT:MO-IO:Super-P:PVDF (37.5:37.5:20:5 wt.%) electrode cell, which surpasses any other FDM current collector cell studied in this thesis in terms of rate performance.

The rate test specific capacitance values (Figure 5.5 (a)–(c) and Figure 5.9) and rate test discharge times (Figure 5.5 (d)–(f) and Figure 5.10) were used to calculate the corresponding specific energies and specific powers of the cells studied in this Chapter at applied currents of 0.1 mA, 0.5 mA, and 1 mA. This data is shown in Table 5.5, along with corresponding data for similar cells from Chapter 3 for comparison. As with the data from previous chapters, the supercapacitor devices presented here fall short of what is typically expected for the specific energies and powers for supercapacitor devices [68–70].

The narrow working voltage achievable by aqueous KOH acts as a serious hinderance to achieving the highest possible specific energies and specific powers for these electrode materials [71]. This is especially the case for the cells possessing poorer rate responses, as the larger ohmic drops at higher applied currents further limit the working voltage window when the specific energies and powers are calculated. Despite these shortcomings, improvements in the rate response of the FDM current collector cells is also reflected in the specific energies and specific powers, especially for the SWNT:MO-IO:Super-P:PVDF (37.5:37.5:20:5 wt.%) electrode cell, which far surpasses the specific energies and specific powers of the FDM cells studied in Chapters 3 and 4 at higher applied currents (see Table 3.5 and Table 4.4).

Table 5.5 Specific energies and specific powers at a given applied current calculated from the galvanostatic rate capability tests in this Chapter. Values of similar cells from Chapter 3 are also included in the bottom four rows of the table (shaded) for comparison.

Current Collector and Electrode Slurry		Specific Energy of Electrode Material (Wh/kg)			Specific Power of Electrode Material (W/kg)		
		0.1 mA	0.5 mA	1 mA	0.1 mA	0.5 mA	1 mA
Vat-P	20:40:40	0.0278	0.0102	0.0069	5.41	24.00	40.06
Vat-P	20:35:35:10	0.0154	0.0070	0.0018	6.52	24.09	27.23
Vat-P	75:20:5	0.0097	0.0021	0.0015	4.70	21.85	38.57
Vat-P	37.5:37.5(GNP):20:5	0.0188	0.0087	0.0051	8.74	38.67	62.88
Vat-P	37.5:37.5(SWNT):20:5	0.0386	0.0188	0.0080	5.91	23.76	33.10
FDM	75:20:5	0.0104	0.0032	0.0008	13.85	48.40	41.14
FDM	37.5:37.5(GNP):20:5	0.0113	0.0029	0.0001	13.15	37.83	12.00
FDM	37.5:37.5(SWNT):20:5	0.0648	0.0383	0.0185	9.61	39.87	59.15
Vat-P	50:50	0.0460	0.0410	0.0362	7.76	37.61	72.32
Vat-P	4:4:1:1	0.0329	0.0249	0.0207	6.00	27.89	50.49
FDM	50:50	0.1151	0.0326	0.0005	7.76	23.50	6.57
FDM	4:4:1:1	0.0578	0.0048	-	6.43	10.29	-

5.4 Conclusions

In this Chapter, the electrochemical responses of pseudo-capacitive manganese-oxide inverse-opals (MO-IOs) and carbon composite electrodes were examined. Characterisation proved the MO-IO material to consist of hausmannite Mn_3O_4. A series of MO-IO-carbon composites were prepared (including carbon nanomaterials studied in previous Chapters, such as SWNT, GNP, and Super-P), with the aim to optimise the synergistic performance of the pseudo-capacitive MO-IO and EDLC conductive carbon electrode materials. The electrode slurries were loaded

onto the metallized Vat-P and conductive PLA FDM 3D-printed current collectors studied in previous Chapters.

The initial composite electrode slurries in this Chapter were made using a similar method to previous Chapters, resulting in poor coverage of the high surface area architected current collectors. These composite electrode cells also showed inferior electrochemical responses (CV cumulative charge, rate response) compared to the previously studied purely EDLC carbon slurries.

A different preparation method was used for the latter part of this Chapter, resulting in better slurry coverage of the current collectors (therefore improved SSA of the electrode materials). New MO-IO-carbon composite slurries were also tested. The composite electrode consisting of SWNT:MO-IO:Super-P:PVDF (37.5:37.5:20:5 wt.%) consistently outperformed all others tested in this Chapter, showing the best CV cumulative charges, highest specific capacitance values, best rate performances, and highest specific energies. This was the case when tested in both Vat-P and FDM current collector cells, though the FDM cell performed especially well, showing a superior rate performance to any other FDM current collector cell studied throughout the entire thesis.

The implementation of multi-modal 3D-printing techniques proved a useful approach for this work, allowing the performances of pseudo-capacitive electrode composites within architected porous current collectors to be directly compared. The performances of the cells are presented here with respect to both the active materials composition, and as a function of 3D-printing method.

5.5 Appendix: Supplementary Materials

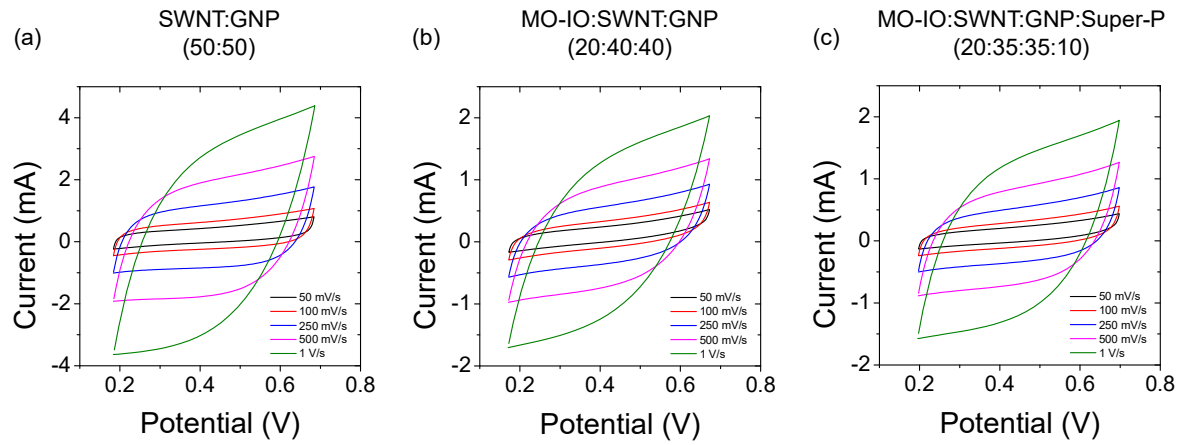

Figure 5.S.1 Cyclic voltammetry of printed supercapacitor cells using Vat-P printed metallized current collectors at various scan rates in the range 250–1,000 mV/s. CVs are shown for cells loaded with (a) SWNT:GNP (50:50 wt.%), (b) MO-IO:SWNT:GNP (20:40:40 wt.%), and (c) MO-IO:SWNT:GNP:Super-P (20:35:35:10 wt.%) electrode slurries.

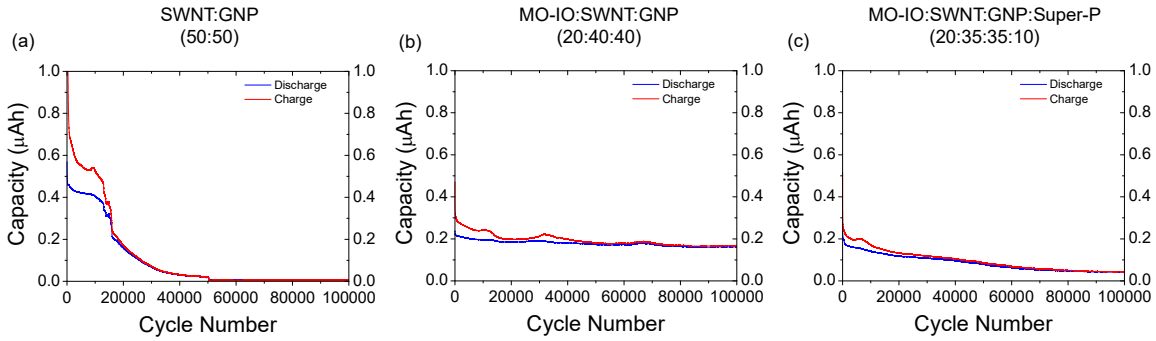

Figure 5.S.2 Capacity retention of all cells in the first part of this chapter over 100,000 cycles under galvanostatic conditions. Cells were cycled between 0.2 and 0.7 V at an applied current of 500 μA (specific applied current of 0.167 A/g).

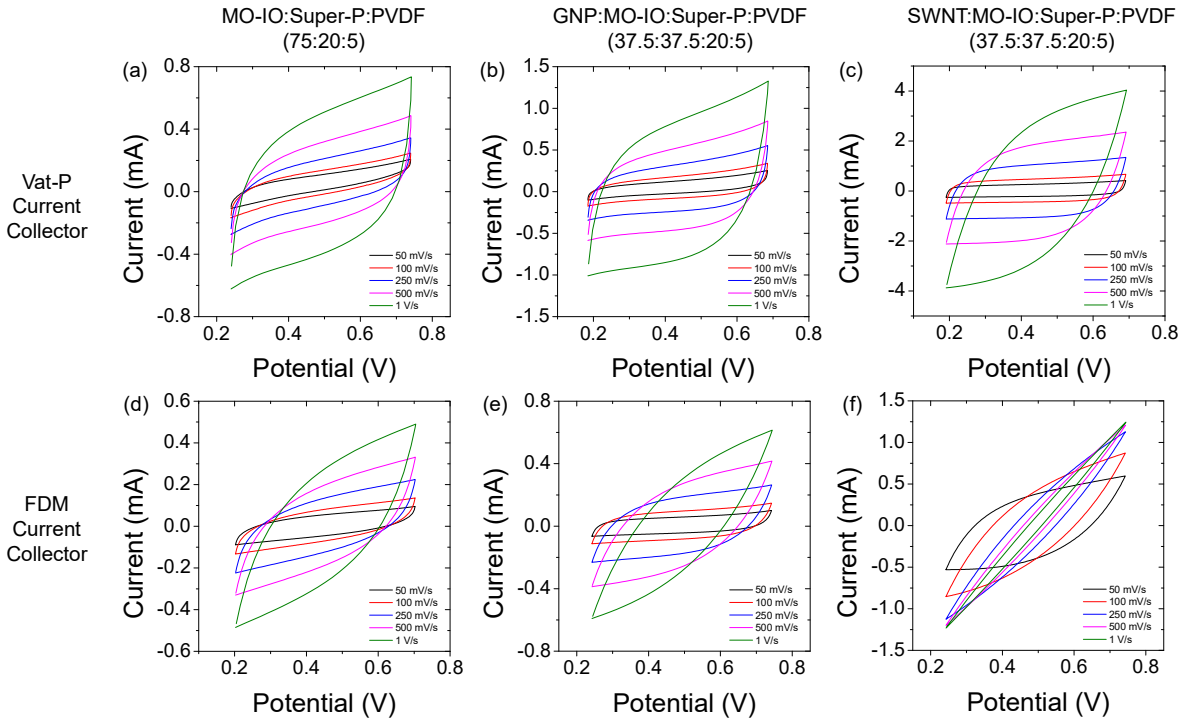

Figure 5.S.3 Cyclic voltammetry of printed supercapacitor cells using (a)–(c) Vat-P printed metallized current collectors and (d)–(f) FDM printed conductive PLA current collectors at various scan rates in the range 250–1,000 mV/s. CVs are shown for cells loaded with (a,d) MO-IO:Super-P:PVDF (75:20:5 wt.%), (b,e) GNP:MO-IO:Super-P:PVDF (37.5:37.5:20:5 wt.%), and (c,f) SWNT:MO-IO:Super-P:PVDF (37.5:37.5:20:5 wt.%) electrode slurries.

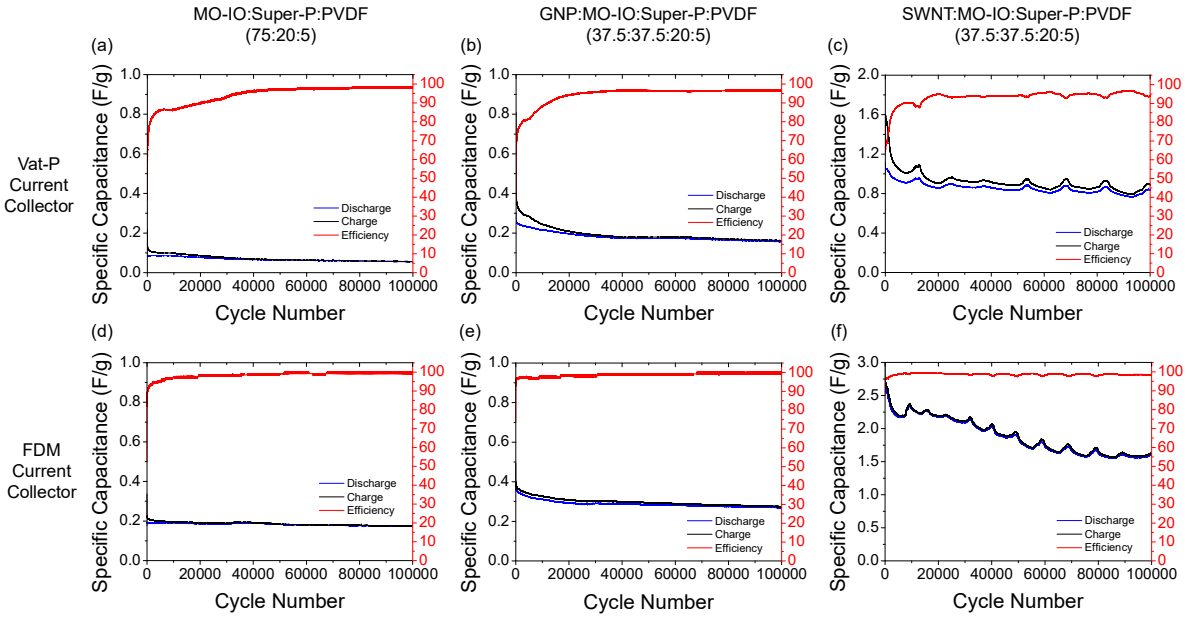

Figure 5.S.4 Life cycle graphs of the (a)–(c) Vat-P printed metallized current collector and (d)–(f) FDM printed conductive PLA current collector cells in the second part of this chapter over 100,000 cycles under galvanostatic conditions, plotting the charging specific capacitance, discharging specific capacitance, and percentage efficiency of all cells. The cells were cycled between 0.2 and 0.7 V at an applied current of 500 µA (specific applied current of 0.167 A/g).

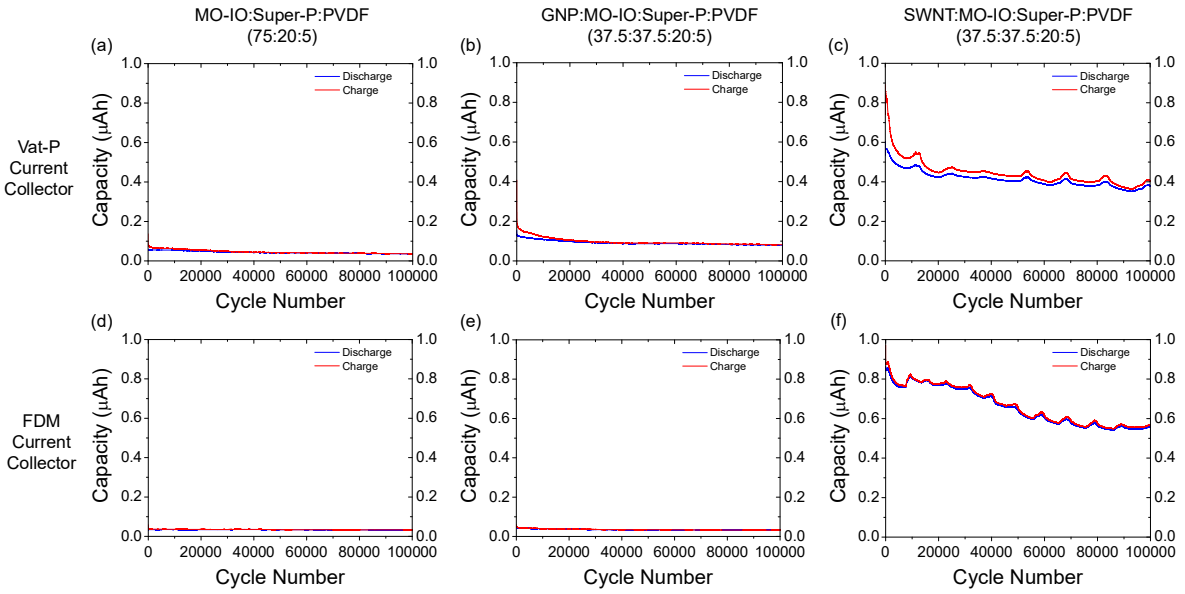

Figure 5.S.5 Capacity retention of the (a)–(c) Vat-P printed metallized current collector and (d)–(f) FDM printed conductive PLA current collector cells in the second part of this chapter over 100,000 cycles under galvanostatic conditions. Cells were cycled between 0.2 and 0.7 V at an applied current of 500 μA (specific applied current of 0.167 A/g).

5.6 References

[1] P. Bhojane, "Recent advances and fundamentals of Pseudocapacitors: Materials, mechanism, and its understanding," *Journal of Energy Storage,* vol. 45, p. 103654, 2022.

[2] Y. Liu, S. Jiang and Z. Shao, "Intercalation pseudocapacitance in electrochemical energy storage: recent advances in fundamental understanding and materials development," *Materials Today Advances,* vol. 7, p. 100072, 2020.

[3] P. Simon, Y. Gogotsi and B. Dunn, "Where Do Batteries End and Supercapacitors Begin?," *Science,* vol. 343, pp. 1210-1211, 2014.

[4] Y. Jiang and J. Liu, "Definitions of Pseudocapacitive Materials: A Brief Review," *Energy & Environmental Materials,* vol. 2, no. 1, pp. 30-37, 2019.

[5] S. Mahala, K. Khosravinia and A. Kiani, "Unwanted degradation in pseudocapacitors: Challenges and opportunities," *Journal of Energy Storage,* vol. 67, p. 107558, 2023.

[6] F. Shi, L. Li, X.-l. Wang, C.-d. Gu and J.-p. Tu, "Metal oxide/hydroxide-based materials for supercapacitors," *RSC Advances,* vol. 4, no. 79, pp. 41910-41921, 2014.

[7] L. Yang, S. Cheng, Y. Ding, X. Zhu, Z. Wang and M. Liu, "Hierarchical Network Architectures of Carbon Fiber Paper Supported Cobalt Oxide Nanonet for High-Capacity Pseudocapacitors," *Nano Letters,* vol. 12, no. 1, pp. 321-325, 2012.

[8] C. Wang, J. Xu, M.-F. Yuen, J. Zhang, Y. Li, X. Chen and W. Zhang, "Hierarchical Composite Electrodes of Nickel Oxide Nanoflake 3D Graphene for High-Performance Pseudocapacitors," *Advanced Functional Materials,* vol. 24, no. 40, pp. 6372-6380, 2014.

[9] I.-H. Kim, J.-H. Kim, B.-W. Cho and K.-B. Kim, "Pseudocapacitive Properties of Electrochemically Prepared Vanadium Oxide on Carbon Nanotube Film Substrate," *Journal of the Electrochemical Society,* vol. 153, no. 8, p. A1451, 2006.

[10] C.-q. Yi, J.-p. Zou, H.-z. Yang and X. Leng, "Recent advances in pseudocapacitor electrode materials: Transition metal oxides and nitrides," *Transactions of Nonferrous Metals Society of China,* vol. 28, no. 10, pp. 1980-2001, 2018.

[11] Y. Gao and L. Zhao, "Review on recent advances in nanostructured transition-metal-sulfide-based electrode materials for cathode materials of asymmetric supercapacitors," *Chemical Engineering Journal,* vol. 430, no. Part 2, p. 132745, 2022.

[12] A. Bryan, L. Santino, Y. Lu, S. Achyara and J. D'Arcy, "Conducting Polymers for Pseudocapacitive Energy Storage," *Chemistry of Materials,* vol. 28, no. 17, pp. 5989-5998, 2016.

[13] G. Snook, P. Kao and A. Best, "Conducting-polymer-based supercapacitor devices and electrodes," *Journal of Power Sources,* vol. 196, pp. 1-12, 2011.

[14] R. Choudhary, S. Ansari and M. Majumder, "Recent advances on redox active composites of metal-organic framework and conducting polymers as pseudocapacitor electrode material," *Renewable and Sustainable Energy Reviews,* vol. 145, p. 110854, 2021.

[15] M. Abdelhamid, A. O'Mullane and G. Snook, "Storing energy in plastics: a review on conducting polymers & their role in electrochemical energy storage," *RSC Advances,* vol. 5, pp. 11611-11626, 2015.

[16] M. Lukatskaya, S. Kota, Z. Lin, M.-Q. Zhao, N. Shpigel, M. Levi, J. Halim, P.-L. Taberna, M. Barsoum, P. Simon and Y. Gogotsi, "Ultra-high-rate pseudocapacitive energy storage in two-dimensional transition metal carbides," *Nature Energy,* vol. 2, p. 17105, 2017.

[17] P. Forouzandeh and S. Pillai, "MXenes-based nanocomposites for supercapacitor," *Current Opinion in Chemical Engineering,* vol. 33, p. 100710, 2021.

[18] K. Choi, H. Jeong, J. Park, Y.-B. Zhang, J. Kang and O. Yaghi, "Supercapacitors of Nanocrystalline Metal–Organic Frameworks," *ACS Nano,* vol. 8, no. 7, pp. 7451-7457, 2014.

[19] L. Niu, T. Wu, M. Chen, L. Yang, J. Yang, Z. Wang, A. Kornyshev, H. Jiang, S. Bi and G. Feng, "Conductive Metal–Organic Frameworks for Supercapacitors," *Advanced Materials,* vol. 34, no. 52, p. 2200999, 2022.

[20] J. Zheng, P. Cygan and T. Jow, "Hydrous Ruthenium Oxide as an Electrode Material for Electrochemical Capacitors.," *Journal of the Electrochemical Society,* vol. 142, pp. 2699-2703, 1995.

[21] Umicore, "Precious Metals Management/Prices/Ruthenium," Umicore, [Online]. Available: https://pmm.umicore.com/en/prices/ruthenium/. [Accessed 09 07 2024].

[22] S. Fleischmann, J. Mitchell, R. Wang, C. Zhan, D.-E. Jiang, V. Presser and V. Augustyn, "Pseudocapacitance: From Fundamental Understanding to High Power Energy Storage Materials," *Chemical Reviews,* vol. 120, no. 14, pp. 6738-6782, 2020.

[23] R. Yang, Y. Fan, R. Ye, Y. Tang, X. Cao, Z. Yin and Z. Zeng, "MnO2-Based Materials for Environmental Applications," *Advanced Materials,* vol. 33, no. 9, p. 2004862, 2021.

[24] M. Toupin, T. Brousse and D. Bélanger, "Influence of Microstucture on the Charge Storage Properties of Chemically Synthesized Manganese Dioxide," *Chemistry of Materials,* vol. 14, no. 9, pp. 3946-3952, 2002.

[25] H. Kim and B. Popov, "Synthesis and Characterization of MnO2-Based Mixed Oxides as Supercapacitors," *Journal of the Electrochemical Society,* vol. 150, no. 3, p. D56, 2003.

[26] H. Lee and J. Goodenough, "Supercapacitor Behavior with KCl Electrolyte," *Journal of Solid State Chemistry,* vol. 144, pp. 220-223, 1999.

[27] S. Wen, J.-W. Lee, I.-H. Yeo, J. Park and S.-i. Mho, "The role of cations of the electrolyte for the pseudocapacitive behavior of metal oxide electrodes, MnO2 and RuO2," *Electrochimica Acta,* vol. 50, no. 2-3, pp. 849-855, 2004.

[28] J. Wen, X. Ruan and Z. Zhuo, "Preparation and electrochemical performance of novel ruthenium–manganese oxide electrode materials for electrochemical capacitors," *Journal of Physics and Chemistry of Solids,* vol. 70, no. 5, pp. 816-820, 2009.

[29] J.-G. Wang, "Engineering Nanostructured MnO2 for High Performance Supercapacitors," in *Supercapacitor Design and Applications*, IntechOpen, 2016.

[30] Q. Cheng, J. Tang, J. Ma, H. Zhang, N. Shinya and L.-C. Qin, "Graphene and nanostructured MnO2 composite electrodes for supercapacitors," *Carbon,* vol. 49, no. 9, pp. 2917-2925, 2011.

[31] D. Wu, X. Xie, Y. Zhang, D. Zhang, W. Du, X. Zhang and B. Wang, "MnO2/Carbon Composites for Supercapacitor: Synthesis and Electrochemical Performance," *Frontiers in Materials,* vol. 7, 2020.

[32] S. Zhang, H. Li, Z. Wu, J. Post, B. Lanson, E. Elzinga, Y. Liu, H. Li, M. Hong, F. Liu and H. Yin, "Effects of Co doping on the structure and physicochemical properties of hausmannite (Mn3O4) and its transformation during aging," *Chemical Geology,* vol. 582, p. 120448, 2021.

[33] T. Shahanas, G. Harichandran and B. Muthuraaman, "Controllable synthesis of nano-spherical and spinel structure hausmannite for asymmetric supercapacitor electrode

application with long-term cyclic stability and its photocatalytic activity," *Materials Chemistry and Physics,* vol. 296, p. 127028, 2023.

[34] A. Yadav, S. Jadhav, D. Chougule, P. Patil, U. Chavan and Y. Kolekar, "Spray deposited Hausmannite Mn3O4 thin films using aqueous/organic solvent mixture for supercapacitor applications," *Electrochimica Acta,* vol. 206, pp. 134-142, 2016.

[35] S. Beknalker, A. Teli, T. Bhat, K. Pawar, S. Patil, N. Harale, J. Shin and P. Patil, "Mn3O4 based materials for electrochemical supercapacitors: Basic principles, charge storage mechanism, progress, and perspectives," *Journal of Materials Science and Technology,* vol. 130, pp. 227-248, 2022.

[36] D. Dubal and R. Holze, "All-solid-state flexible thin film supercapacitor based on Mn3O4 stacked nanosheets with gel electrolyte," *Energy,* vol. 51, pp. 407-412, 2013.

[37] L. Cuéllar-Herrera, E. Arce-Estrada, D. Pacheco-Catalán, L. Vivas, J. Ortiz-Landeros, C. Jiménez-Lugos and A. Romero-Serrano, "Chemical synthesis and electrochemical performance of Hausmannite Mn3O4/rGO composites for supercapacitor applications," *International Journal of Electrochemical Science,* vol. 19, no. 9, p. 100737, 2024.

[38] K. Wang, Y. Wu, S. Luo, X. He, J. Wang, K. Jiang and S. Fan, "Hybrid super-aligned carbon nanotube/carbon black conductive networks: A strategy to improve both electrical conductivity and capacity for lithium ion batteries," *Journal of Power Sources,* vol. 233, pp. 209-215, 2013.

[39] I. Cho, J. Choi, K. Kim, M.-H. Ryou and Y. Lee, "A comparative investigation of carbon black (Super-P) and vapor-grown carbon fibers (VGCFs) as conductive additives for lithium-ion battery cathodes," *RSC Advances,* vol. 5, pp. 95073-95078, 2015.

[40] K. Makgopa, K. Raju, P. Ejikeme and K. Ozoemena, "High-performance Mn3O4/onion-like carbon (OLC) nanohybrid pseudocapacitor: Unravelling the intrinsic properties of OLC against other carbon supports," *Carbon,* vol. 117, pp. 20-32, 2017.

[41] R. Schroden, M. Al-Daous, C. Blanford and A. Stein, "Optical Properties of Inverse Opal Photonic Crystals," *Chemistry of Materials,* vol. 14, no. 8, pp. 3305-3315, 2002.

[42] D. McNulty, V. Landgraf and S. Trabesinger, "Simplifying the synthesis of carbon inverse opals," *RSC Advances,* vol. 10, pp. 24108-24114, 2020.

[43] Y. Zhang, Y. Sun, J. Liu, P. Guo, Z. Cai and J.-J. Wang, "Polymer-infiltrated SiO2 inverse opal photonic crystals for colorimetrically selective detection of xylene vapors," *Sensors and Actuators B: Chemical,* vol. 291, pp. 67-73, 2019.

[44] X. Zhang, B. Weinberger, S. Amrehn, X. Wu and M. Tiemann, "Synthesis of Metal Oxide Inverse Opals from Metal Nitrates by PMMA Colloidal Crystal Templating," *European Journal of Inorganic Chemistry,* vol. 2020, no. 35, pp. 3402-3407, 2020.

[45] S. Tabata, Y. Isshiji and M. Watanabe, "Inverse Opal Carbons Derived from a Polymer Precursor as Electrode Materials for Electric Double-Layer Capacitors," *Journal of the Electrochemical Society,* vol. 155, p. K42, 2008.

[46] K. Lee, J. Lytle, N. Ergang, S. Oh and A. Stein, "Synthesis and Rate Performance of Monolithic Macroporous CarbonElectrodes for Lithium-Ion Secondary Batteries," *Advanced Functional Materials,* vol. 15, no. 4, pp. 547-556, 2005.

[47] S. Bernardini, F. Bellatreccia, A. Municchia, G. Ventura and A. Sodo, "Raman spectra of natural manganese oxides," *Journal of Raman Spectroscopy,* vol. 50, pp. 873-888, 2019.

[48] M.-C. Bernard, A. Hugot-Le Goff and B. Thi, "Electrochromic Reactions in Manganese Oxides: I. Raman Analysis," *Journal of the Electrochemical Society,* vol. 140, no. 11, pp. 3065-3070, 1993.

[49] C. Julien, M. Massot and C. Poinsignon, "Lattice vibrations of manganese oxides: Part I. Periodic structures," *Spectrochimica Acta Part A; Molecular and Biomolecular Spectroscopy,* vol. 60, no. 3, pp. 689-700, 2004.

[50] H. Xu, S. Xu, X. Li, H. Wang and H. Yan, "Chemical bath deposition of hausmannite Mn3O4 thin films," *Applied Surface Science,* vol. 252, no. 12, pp. 4091-4096, 2006.

[51] L. Li, Z. Hu, Y. Yang, P. Liang, A. Lu, H. Xu, Y. Hu and H. Wu, "Hydrothermal Self-Assembly Synthesis of Mn3O4/Reduced Graphene Oxide Hydrogel and Its High Electrochemical Performance for Supercapacitors," *Chinese Journal of Chemistry,* vol. 31, pp. 1290-1298, 2013.

[52] B. Rani, M. Ravina, G. Ravi, S. Ravichandran, V. Ganesh and R. Yuvakkumar, "Synthesis and characterization of hausmannite (Mn3O4) nanostructures," *Surfaces and Interfaces,* vol. 11, pp. 28-36, 2018.

[53] A. Roberts and R. Slade, "Effect of specific surface area on capacitance in asymmetric carbon/α-MnO2 supercapacitors," *Electrochimica Acta,* vol. 55, no. 25, pp. 7460-7469, 2010.

[54] N. Tang, X. Tian, C. Yang and Z. Pi, "Facile synthesis of α-MnO2 nanostructures for supercapacitors," *Materials Research Bulletin,* vol. 44, no. 11, pp. 2062-2067, 2009.

[55] L. Coustan, A. Le Comte, T. Brousse and F. Favier, "MnO2 as ink material for the fabrication of supercapacitor electrodes," *Electrochimica Acta,* vol. 152, pp. 520-529, 2015.

[56] P. Ragupathy, H. Vasan and N. Munichandraiah, "Synthesis and Characterization of Nano- MnO2 for Electrochemical Supercapacitor Studies," *Journal of the Electrochemial Society,* vol. 155, no. A34, 2007.

[57] S. Meher and G. Rao, "Enhanced activity of microwave synthesized hierarchical MnO2 for high performance supercapacitor applications," *Journal of Power Sources,* vol. 215, pp. 317-328, 2012.

[58] M. Dresselhaus and G. J. A. Dresselhaus, "Raman spectroscopy of carbon nanotubes in 1997 and 2007.," *The Journal of Physical Chemistry C,* vol. 111, no. 48, pp. 17887-17893, 2007.

[59] M. Dresselhaus, G. Dresselhaus, R. Saito and A. Jorio, "Raman spectroscopy of carbon nanotubes.," *Physics reports,* vol. 409, no. 2, pp. 47-99, 2005.

[60] M. Dresselhaus, G. Dresselhaus, A. Jorio and A. S. R. Souza Filho, "Raman spectroscopy on isolated single wall carbon nanotubes.," *Carbon,* vol. 40, no. 12, pp. 2043-2061, 2002.

[61] A. Jorio and R. Saito, "Raman spectroscopy for carbon nanotube applications.," *Journal of Applied Physics,* vol. 129, no. 2, p. 021102, 2021.

[62] M. Itkis, D. Perea, R. Jung, S. Niyogi and R. Haddon, "Comparison of analytical techniques for purity evaluation of single-walled carbon nanotubes.," *Journal of the American Chemical Society,* vol. 127, no. 10, pp. 3439-3448, 2005.

[63] S. Kumar, K. Singh and J. Ramkumar, "Comparative study of the influence of graphene nanoplatelets filler on the mechanical and tribological behavior of glass fabric-reinforced epoxy composites.," *Polymer Composites,* vol. 41, no. 12, pp. 5403-5417, 2020.

[64] S. Sharma and P. Chand, "Supercapacitor and electrochemical techniques: A brief review," *Results in Chemistry,* vol. 5, p. 100885, 2023.

[65] I. Cho, J. Choi, K. Kim, M. Ryou and Y. Lee, "A comparative investigation of carbon black (Super-P) and vapor-grown carbon fibers (VGCFs) as conductive additives for lithium-ion battery cathodes.," *Rsc Advances,* vol. 5, no. 115, pp. 95073-95078, 2015.

[66] X. Zhang, G. Xie, D. Gou, P. Luo, Y. Yao and H. Chen, "A novel enzyme-free electrochemical biosensor for rapid detection of Pseudomonas aeruginosa based on high catalytic Cu-ZrMOF and conductive Super P.," *Biosensors and Bioelectronics,* vol. 142, p. 111486, 2019.

[67] J. Shen, Y. Hu, C. Li, C. Qin, M. Shi and M. Ye, "Layer-by-layer self-assembly of graphene nanoplatelets.," *Langmuir,* vol. 25, no. 11, pp. 6122-6128, 2009.

[68] A. Pandolfo and A. Hollenkamp, "Carbon properties and their role in supercapacitors," *Journal of Power Sources,* vol. 157, no. 1, pp. 11-27, 2006.

[69] S. Shaheen Shan, S. Abu Nayem, N. Sultana, A. Saleh Ahammad and M. Abdul Aziz, "Preparation of sulfur-doped carbon for supercapacitor applications: a review.," *ChemSusChem,* vol. 15, no. 1, p. e202101282, 2022.

[70] K. Wang, S. Gao, Z. Du, A. Yuan, W. Lu and L. Chen, "MnO2-Carbon nanotube composite for high-areal-density supercapacitors with high rate performance," *Journal of Power Sources,* vol. 305, pp. 30-36, 2016.

[71] X. Liu, M. Zhong, Z. Fu, X. Xu, C. Wang, L. Yuan and Y. Tang, "From hierarchically porous carbon to Mn3O4/Carbon composites for high voltage aqueous supercapacitors," *Journal of Power Sources,* vol. 485, p. 229111, 2021.

Chapter 6

Outlook and Future Work

6.1 Outlook and Future Work

The primary objective of this thesis was to examine in detail the behaviour and electrochemical performance of symmetric supercapacitors made using two different 3D-printing methods (Vat-P and FDM). Two cell types are made in this study, one with metallized Vat-P-printed current collectors, the other with conductive PLA (polylactic acid) FDM-printed current collectors in a similarly designed printed coin cell. In Chapter 3, an array of carbon-based active materials was made and tested in both cell types. Chapter 4 focuses on the FDM printed current collectors, examining how solvent pre-soaking effects the electrochemical performance and cycle life of the 3D-printed supercapacitor cells containing these treated current collectors. Chapter 5 introduces pseudo-capacitive Mn_3O_4-inverse opal electrodes to the 3D-printed supercapacitor cells and highlights the enhanced performance of these electrodes when composited with conductive nanocarbons.

Chapter 3 compared the electrochemical response and intrinsic limitations of symmetric carbon-based supercapacitors made using Vat-P and FDM 3D-printing. Carbon-based electrode slurry (various combinations of SWNT, GNP, Super-P, PVDF) and aqueous 6M KOH electrolyte were used in these cells. The influence of internal resistance of each 3D-printing method was illustrated by direct comparison of cyclic voltammetry and galvanostatic charge-discharge tests. The metallized conductive Vat-P cells displayed better conductivity and more ideal rectangular cyclic voltammetry response but suffered from poor cycle life in initial

experiments (~5,000 charge-discharge cycles before losing all specific capacitance). The FDM current collector cells using graphite-containing PLA materials showed poorer conductivity, less ideal cyclic voltammetry curves, and were structurally less robust and partially porous, but offered very stable cycle life for supercapacitor cells, retaining most of their specific capacitance after 100,000 charge-discharge cycles. A major improvement in the cycle life of the metallized Vat-P cells was observed by reducing the voltage window to 0.2 – 0.7 V to limit metal delamination, as well as incorporating Super-P and PVDF additives into the electrodes. The work presented in Chapter 3 provided much needed insight into electrochemical response of supercapacitors as a function of 3D-printing method used, as many studies in the literature instead focus on direct printing of the active materials. The approach used in this work allows for the benefits of 3D-printing of supercapacitor components and direct addition of the active materials to be combined. Known issues with the 3D-printing of active materials can be avoided in this way.

Chapter 4 focuses on the conductive PLA FDM current collectors, which showed far lower electronic conductivity than the metallized Vat-P current collectors, negatively affecting the capacitance and rate responses of the FDM cells in Chapter 3. To address this issue, several solvent pre-soaking treatments were proposed with the aim of improving the interfacial electronic conductivity (therefore electrochemical performance) of the FDM current collector cells. We showed that for hydroxide-based electrolytes, pre-soaking was shown to improve the interfacial conductivity of conductive additive-impregnated 3D printed PLA current collectors, compared to chemical decomposition or modification using DMF. By depolymerizing the outer surface, exposed graphite improves the interfacial conductivity with the carbon-based active materials in the symmetric supercapacitor. Little change was observed in the cyclic voltammetry responses of the Untreated and DMF-Treated (Short) cells. The KOH-Treated (Long) cell showed an improved cyclic voltammetry response, useful for some voltammetric

charge storage applications or electrochemical sensors where the fast response is dominated by the surface activity with current values linked to the driving voltage. Galvanostatic charge-discharge tests initially showed smaller ohmic drops and improved capacitance for the KOH-Treated (Long) cell compared to the Untreated cell. However, the higher surface conductivity PLA after long KOH pre-soaking showed a worse cycle response compared to untreated FDM. This work into solvent pre-soaking illustrates the limitations of the rate response and long-term cycling stability (up to 1,000,000 charge-discharge cycles) of printed PLA energy storage systems in aqueous electrolytes. This Chapter shows that for electrochemical sensors using printed electrodes, voltammetric responses can be improved with surface interfacial conductivity and area modification, but galvanostatic response over long durations is much less performant.

Chapter 5 introduced pseudo-capacitive active material to our 3D-printed supercapacitor cell setup, in the form of manganese-oxide inverse-opals (MO-IOs). Characterisation of the MO-IO showed it to consist of hausmannite Mn_3O_4. A series of MO-IO-carbon composite electrodes were prepared (with the aim to optimise the synergistic performance of the pseudo-capacitive MO-IO and EDLC conductive carbon electrode materials) and loaded onto our 3D-printed supercapacitor cells (both the Vat-P and FDM current collector cell designs). A different slurry preparation method than that used previously was proposed, after initial composites showed poor coverage across the current collector and disappointing electrochemical performances. The new preparation method resulted in better slurry coverage across the current collector, therefore improving the SSA of the electrode materials. The composite electrode consisting of SWNT:MO-IO:Super-P:PVDF (37.5:37.5:20:5 wt.%) consistently outperformed all others tested in this Chapter, showing the best CV cumulative charges, highest specific capacitance values, best rate performances, and highest specific energies. The FDM cell loaded with this electrode performed especially well,

showing a superior rate performance to any other FDM current collector cell studied throughout the entire thesis. The variety of electrode slurries tested in this work further improves our knowledge of the synergistic energy storage behaviours of nanocarbon allotropes and inverse-opal structured metal oxides.

Though a variety of carbon-based electrode materials were tested in this work (SWNT, GNP, Super-P, graphite), there remains a plethora of carbon nanomaterials that could be investigated in a future study within our 3D-printed supercapacitor cells. Though a very commonly investigated carbon electrode material, activated carbons (ACs) were not implemented in any of the electrode slurries in this thesis. The material is cheap, eco-friendly, made from abundant sources [1–3], and possessing an exceptionally high SSA [4]. The drawbacks of poorer electronic conductivity can easily be ameliorated by forming composites with more highly conductive forms of carbon [5, 6]. More novel forms of carbon, such as carbon nano-dots [7, 8] and carbon nano-onions [9, 10] could also be investigated for their feasibility as electrode materials within our complex architecture 3D-printed current collectors. Furthering to this point, many of the non-carbon energy storage materials discussed in Chapter 1.3 could yet be implemented into the 3D-printed framework established in this work. Relatively novel materials, such as MXenes, are gaining the interest of energy storage researchers [11, 12] because of their high SSA, tuneable interlayer-distance, exceptional electronic conductivity, and rich surface chemistry [13–15]. Future 3D-printed supercapacitor studies could incorporate these active materials, furthering our knowledge of their energy storage response (both alone and within composite electrodes) within the context of architected 3D-printed current collectors.

The same electrolyte (6 M aqueous KOH) was used throughout the work presented here. As such, further studies which vary the electrolyte used within our 3D-printed supercapacitor cells can easily be undertaken, and address some of the issues encountered in

this work. Aqueous electrolytes are cheap, non-toxic, and highly conductive, but suffer from narrow voltage windows [16], which limited the capacitance and specific energy response of the supercapacitors studied here. Organic electrolytes, on the other hand, tend to be less conductive than aqueous electrolytes and are often toxic, but possess a far wider voltage window (resulting in improved capacitance and specific energy values) [17]. Gel electrolytes are of great interest for future investigations, as their semi-solid state would mitigate the liquid electrolyte leakage encountered with the woodpile structure FDM printed current collectors [18, 19]. Additionally, gel electrolytes of the correct rheological properties can be formed into 3D-printable ink [20, 21].

One of the biggest advantages of 3D-printed energy storage devices is their independence from predetermined form factors. This allows an unprecedented level of customisation and freedom of design, which is of particular interest to the field of wearable electronics [22–24]. Tying into the increasing demand for customised and unobtrusive energy storage devices, a future study could investigate the electrochemical performance of our 3D-printed supercapacitor devices made into an array of shapes and dimensions, to test their feasibility for a range of applications beyond the usual coin cell form.

Another consideration for future expansions of this work is the direct printing of the active materials of our supercapacitor devices, along with the casing and current collector components printed in this work (and potential for printable gel electrolytes as mentioned earlier). It was discussed previously in the thesis that our method avoids known issues with the direct printing of active materials (e.g. brittleness with high graphite-loaded PLA thermoset materials, and poor printing definition for methacrylate resins containing significant randomly dispersed inorganic materials). However, as the field constantly grows and matures, the prospect of facile direct printing of active materials becomes ever more achievable. Recent publications on printable hydrogels [25], MXene inks [26, 22], ceramics and glass 3D-printing

[27], and metal-embedded elastomers [28] show a promising indication of ever-improving printable electrode materials that overcome the issues discussed here and in other more detailed reviews [29]. Simultaneously, the pioneering work into multi-material 3D-printing (and the increasingly advanced knowledge of varying interfacial materials that it requires [30, 31]) brings the eventual objective of seamless, production line level capability to additively manufacture alternative form-factor energy storage devices ever closer to everyday reality.

6.2 References

[1] N. Boulanger, A. Talyzin, S. Xiong, M. Hultberg and Grimm, "High surface area activated carbon prepared from wood-based spent mushroom substrate for supercapacitors and water treatment," *Colloids and Surfaces A: Physiochemical and Engineering Aspects,* vol. 680, p. 132684, 2024.

[2] R. Medhi, S. Naqvi, A. Khoja and R. Hussain, "Biomass derived activated carbon by chemical surface modification as a source of clean energy for supercapacitor application," *Fuel,* vol. 348, p. 128529, 2023.

[3] S. Tong-Xin, Z. Yue-Mei and J. Xiao-Juan, "Preparation of Disused Composite Panels-Based Activated Carbon by Microwave Induced Activation for High Performance of Electric Double-Layer Capacitors: Microwave Power Effects," *Science of Advanced Materials,* vol. 8, no. 5, pp. 1101-1107, 2016.

[4] P. Simon and A. Burke, "Nanostructured carbons: double-layer capacitance and More," *The Electrochemical Society Interface,* vol. 17, no. 1, pp. 38-44, 2008.

[5] F. Cheng, X. Yang, S. Zhang and W. Lu, "Boosting the supercapacitor performances of activated carbon with carbon nanomaterials," *Journal of Power Sources,* vol. 450, p. 227678, 2020.

[6] Y. Qing, Y. Jiang, H. Lin, L. Wang, A. Liu, Y. Cao, R. Sheng, Y. Guo, C. Fan, S. Zhang, D. Jia and Z. Fan, "Boosting the supercapacitor performance of activated carbon by constructing overall conductive networks using graphene quantum dots," *Journal of Materials Chemistry A,* vol. 7, no. 11, pp. 6021-6027, 2019.

[7] V. Kumar, A. Borenstein, B. Markovsky, D. Aurbach, A. Gedanken, M. Talianker and Z. Porat, "Activated Carbon Modified with Carbon Nanodots as Novel Electrode Material for Supercapacitors," *The Journal of Physical Chemistry C,* vol. 120, no. 25, pp. 13406-13413, 2016.

[8] V. Strauss, K. Marsh, M. Kowal, M. El-Kady and R. Kaner, "A Simple Route to Porous Graphene from Carbon Nanodots for Supercapacitor Applications," *Advanced Materials,* vol. 30, no. 8, p. 1704449, 2018.

[9] S. Kaur, A. Krishnan and S. Chakraborty, "Recent advances and challenges of carbon nano onions (CNOs) for application in supercapacitor devices (SCDs)," *Journal of Energy Storage,* vol. 71, p. 107928, 2023.

[10] H. Jin, S. Wu, T. Li, Y. Bai, X. Wang, H. Zhang, H. Xu, C. Kong and H. Wang, "Synthesis of porous carbon nano-onions derived from rice husk for high-performance supercapacitors," *Applied Surface Science,* vol. 488, pp. 593-599, 2019.

[11] P. Forouzandeh and S. Pillai, "MXenes-based nanocomposites for supercapacitor," *Current Opinion in Chemical Engineering,* vol. 33, p. 100710, 2021.

[12] J. Xu, J. You, L. Wang, Z. Wang and H. Zhang, "MXenes serving aqueous supercapacitors: Preparation, energy storage.," *Sustainable Materials and Technologies,* vol. 33, p. e00490, 2022.

[13] M. Lukatskaya, S. Kota, Z. Lin, M.-Q. Zhao, N. Shpigel, M. Levi, J. Halim, P.-L. Taberna, M. Barsoum, P. Simon and Y. Gogotsi, "Ultra-high-rate pseudocapacitive energy storage in two-dimensional transition metal carbides," *Nature Energy,* vol. 2, p. 17105, 2017.

[14] K. Lim, M. Shekhirev, B. Wyatt, B. Anasori, Y. Gogotsi and Z. Seh, "Fundamentals of MXene synthesis," *Nature Synethesis,* vol. 1, pp. 601-614, 2022.

[15] C. Zhang, B. Anasori, A. Seral-Ascaso, S.-H. Park, N. McEvoy, A. Shmeliov, G. Duesberg, J. Coleman, Y. Gogotsi and V. Nicolosi, "Transparent, Flexible, and Conductive 2D Titanium Carbide (MXene) Films with High Volumetric Capacitance," *Advanced Materials,* vol. 29, no. 36, p. 1702678, 2017.

[16] T. Guo, D. Zhou, L. Pang, S. Sun, T. Zhou and J. Su, "Perspectives on Working Voltage of Aqueous Supercapacitors," *Small,* vol. 18, no. 16, p. 2106360, 2022.

[17] T. Bhat, P. Patil and R. Rakhi, "Recent trends in electrolytes for supercapacitors," *Journal of Energy Storage,* vol. 50, p. 104222, 2022.

[18] Y. Xie and J. Wang, "Capacitance performance of carbon paper supercapacitor using redox-mediated gel polymer electrolyte.," *Journal of Sol-Gel Science and Technology,* vol. 86, pp. 760-772, 2018.

[19] K. Anneser, J. Reichstein, S. Braxmeier and G. Reichenauer, "Carbon xerogel based electric double layer capacitors with polymer gel electrolytes–improving the performance by adjusting the type of electrolyte and its processing.," *Electrochimica Acta,* vol. 278, pp. 196-203, 2018.

[20] M. Idrees, S. Ahmed, Z. Mohammed, N. Korivi and V. Rangari, "3D printed supercapacitor using porous carbon derived from packaging waste," *Additive Manufacuring,* vol. 36, p. 101525, 2020.

[21] M. Ovhal, H. Lee, V. Satale, B. Tyagi, S. Chowdhury and J.-W. Kang, "One-Meter-Long, All-3D-Printed Supercapacitor FibersBased on Structurally Engineered Electrode for WearableEnergy Storage," *Advanced Energy Materials,* vol. 14, p. 2303053, 2024.

[22] G. Zhou, X. Liu, C. Liu, Z. Li, C. Liu, X. Shi, Z. Li, C. Mei and M.-C. Li, "3D printed MXene-based films and cellulose nanofiber reinforced hydrogel electrolyte to enable high-performance flexible supercapacitors," *Journal of Materials Chemistry A,* vol. 12, pp. 3734-3744, 2024.

[23] S. Nath, I. Patil and P. Sundriyal, "Material extrusion of electrochemical energy storage devices for flexible and wearable electronic applications," *Journal of Energy Storage,* vol. 79, p. 110129, 2024.

[24] J. Yang, Q. Cao, X. Tang, J. Du, T. Yu, X. Xu, D. Cai, C. Guan and W. Huang, "3D-Printed highly stretchable conducting polymer electrodes for flexible supercapacitors," *Journal of Materials Chemistry A,* vol. 9, pp. 19649-19658, 2021.

[25] M. Baig, S. Khan, H. Ahmad, J. Liang, G. Zhu and H. Pang, "3D printing of hydrogels for flexible micro-supercapacitors," *FlexMat,* vol. 1, no. 1, pp. 79-99, 2024.

[26] Y. Zhu, Q. Zhang, J. Ma, P. Das, L. Zhang, H. Liu, S. Wang, H. Li and Z.-S. Wu, "Three-dimensional (3D)-printed MXene high-voltage aqueous micro-supercapacitors with ultrahigh areal energy density and low-temperature tolerance," *Carbon Energy,* vol. 6, no. 8, p. e481, 2024.

[27] D. Moore, L. Barbera, K. Masania and A. Studart, "Three-dimensional printing of multicomponent glasses using phase-separating resins," *Nature Materials,* vol. 19, pp. 212-217, 2019.

[28] P. Won, C. Valentine, M. Zadan, C. Pan, M. Vinciguerra, D. Patel, S. Ko, L. Walker and C. Majidi, "3D Printing of Liquid Metal Embedded Elastomers for Soft Thermal and Electrical Materials," *ACS Applied Materials and Interfaces,* vol. 14, no. 49, pp. 55028-55038, 2022.

[29] V. Egorov, U. Gulzar, Y. Zhang, S. Breen and C. O'Dwyer, "Evolution of 3D Printing Methods and Materials for Electrochemical Energy Storage," *Advanced Materials,* vol. 32, no. 29, p. 2000556, 2020.

[30] M. Skylar-Scott, J. Mueller, C. Visser and J. Lewis, "Voxelated soft matter via multimaterial multinozzle 3D printing," *Nature,* vol. 575, pp. 330-335, 2019.

[31] L. Fieber, J. Evans, C. Huang and P. Grant, "Single-operation, multi-phase additive manufacture of electro-chemical double layer capacitor devices," *Additive Manufacturing,* vol. 28, pp. 344-353, 2019.